

University of Alberta

**NONLINEAR MICROMECHANICAL ANALYSIS OF COMPOSITE  
MATERIALS UNDER MULTIAXIAL LOADING**

by



Yunfa Zhang

A thesis submitted to the Faculty of Graduate Studies and Research  
in partial fulfillment of the requirements for the degree of  
Doctor of Philosophy

Department of Mechanical Engineering

Edmonton, Alberta

Spring 2006



Library and  
Archives Canada

Bibliothèque et  
Archives Canada

Published Heritage  
Branch

Direction du  
Patrimoine de l'édition

395 Wellington Street  
Ottawa ON K1A 0N4  
Canada

395, rue Wellington  
Ottawa ON K1A 0N4  
Canada

*Your file* *Votre référence*  
*ISBN: 0-494-14072-0*  
*Our file* *Notre référence*  
*ISBN: 0-494-14072-0*

#### NOTICE:

The author has granted a non-exclusive license allowing Library and Archives Canada to reproduce, publish, archive, preserve, conserve, communicate to the public by telecommunication or on the Internet, loan, distribute and sell theses worldwide, for commercial or non-commercial purposes, in microform, paper, electronic and/or any other formats.

The author retains copyright ownership and moral rights in this thesis. Neither the thesis nor substantial extracts from it may be printed or otherwise reproduced without the author's permission.

#### AVIS:

L'auteur a accordé une licence non exclusive permettant à la Bibliothèque et Archives Canada de reproduire, publier, archiver, sauvegarder, conserver, transmettre au public par télécommunication ou par l'Internet, prêter, distribuer et vendre des thèses partout dans le monde, à des fins commerciales ou autres, sur support microforme, papier, électronique et/ou autres formats.

L'auteur conserve la propriété du droit d'auteur et des droits moraux qui protègent cette thèse. Ni la thèse ni des extraits substantiels de celle-ci ne doivent être imprimés ou autrement reproduits sans son autorisation.

---

In compliance with the Canadian Privacy Act some supporting forms may have been removed from this thesis.

Conformément à la loi canadienne sur la protection de la vie privée, quelques formulaires secondaires ont été enlevés de cette thèse.

While these forms may be included in the document page count, their removal does not represent any loss of content from the thesis.

Bien que ces formulaires aient inclus dans la pagination, il n'y aura aucun contenu manquant.

  
**Canada**

## ABSTRACT

In this thesis, a 3D approach based on the micro/meso repeated unit cell (RUC) model for composite laminates is established which incorporates material nonlinearity, damage initiation and growth, and multiaxial loading. A unified form of periodic boundary conditions for RUC models subjected to multiaxial loads is first presented. The implementation into the finite element scheme and the calculations of the average stress/strain are discussed. The periodic boundary conditions for the off-axis loading of a one-quarter RUC are further derived considering the symmetries of the geometry, material and load. A rhombohedral two cell model has been developed to facilitate the analysis of angle-ply and cross-ply laminates.

A differential form of nonlinear viscoelastic constitutive model for thermoset matrix materials is introduced and has been implemented into the FEM code ADINA through its user-defined subroutine. To model the damage of the fibre/matrix interface, a new type of interphase element is proposed and its stress-strain relation is derived based on a cohesive law. The model can handle both the normal and tangential separations, thus mixed mode of interphase damage can be predicted. In addition, a viscous term is added to the cohesive law to overcome the convergence difficulty in numerical iterations. To model the progress of matrix-cracking, a 'smeared crack approach' is employed. This approach permits a crack description in terms of stress-strain relations. In particular, the proposed post-damage stress-strain relation allows that only normal and shear stress components in the cracked plane tend to zero.

For different loading cases, composite laminates with various fibre architectures and constituent material properties are analyzed as application examples. Detailed numerical results are presented and are found to be in good agreement with the available experimental results or similar theoretical predictions in the literature.

## **ACKNOWLEDGEMENTS**

I would like to thank Dr. Zihui Xia for his invaluable guidance, stimulating discussion and consistent support throughout the course of this degree. I would also like to thank Dr. Fernand Ellyin and all the members of the Advanced Composite Materials Engineering group, who provided great encouragement, technical expertise and the occasional critique.

I wish to express my appreciation to the members of my thesis examination committee: Dr. R. L. Eadie, Dr. F. Ellyin, Dr. P.-Y. B. Jar, Dr. C. Ru and Dr. R. Vaziri (external examiner), for their time, effort and an excellent feedback to my thesis.

My special thanks go to my wife, Hong Ye, and my daughter, Lulu, to whom this thesis is dedicated, for their love, understanding and patience throughout my study.

## TABLE OF CONTENTS

<b>CHAPTER 1</b>	<b>INTRODUCTION</b>	<b>1</b>
1.1	APPLICATION OF COMPOSITE MATERIALS	1
1.2	MECHANICAL PROPERTIES OF COMPOSITE MATERIALS	2
1.2.1	Mechanical Properties	2
1.2.2	Inherent Scales Involved in the Analysis of Composite Materials	6
1.3	MICROMECHANICAL ANALYSIS OF COMPOSITE MATERIALS	7
1.4	OBJECTIVES OF THE STUDY	11
1.5	LITERATURE REVIEW	13
1.5.1	Micromechanical Analysis	13
1.5.2	Micromechanical Analysis with Damage Evolution	15
1.5.3	Current Status	17
1.6	SCOPE AND ORGANIZATION OF THE DISSERTATION	19
1.7	SUMMARY OF MAIN CONTRIBUTIONS THROUGH THIS RESEARCH PROJECT	22
<b>BIBLIOGRAPHY</b>		<b>25</b>
<b>CHAPTER 2</b>	<b>FINITE ELEMENT ANALYSIS FOR PERIODIC COMPOSITES UNDER MULTIAXIAL LOADING</b>	<b>34</b>
2.1	INTRODUCTION	34
2.2	PERIODIC BOUNDARY CONDITIONS OF A UNIT CELL	36
2.2.1	Unit Cell of Composite with Periodic Microstructure	36
2.2.2	Formulation of the Problem	37
2.2.3	Unified Periodic Boundary Conditions	39
2.2.4	Calculation of Average Stress and Strain	43
2.2.5	Implementation into a FEM Scheme and Examples	46
2.2.6	Illustrative Examples	52
2.3	SYMMETRY CONSIDERATIONS OF A SQUARE RUC	55
2.3.1	General Procedure and Examples	55
2.3.2	Off-axis Loading	59

2.3.3	Generalized Plane Strain Conditions	71
2.4	ILLUSTRATIVE EXAMPLES OF MICROMECHANICAL ANALYSIS	73
2.4.1	Example 1	74
2.4.2	Example 2 (Prediction of Effective Elastic Constants of a UDC)	78
2.5	CONCLUDING REMARKS	81
	<b>BIBLIOGRAPHY</b>	84
	<b>CHAPTER 3 MODELING VISCOELASTICITY OF MATRIX AND</b>	
	INTRALAMINAR DAMAGE	88
3.1	INTRODUCTION	88
3.2	NONLINEAR VISCOELASTIC MATERIAL MODEL FOR EPOXY	90
3.2.1	Nonlinear Visoelastic Model for Epoxy Matrix	90
3.2.2	Implementation into ADINA and Verification Examples	95
3.3	COHESIVE DEBONDING LAW AND COHESIVE INTERPHASE ELEMENT	98
3.3.1	Cohesive Law	98
3.3.2	Cohesive Interphase Element	102
3.3.3	Snap-back Instability	103
3.4	MODELING OF MATRIX CRACKING	107
3.4.1	Initiation of a Crack	108
3.4.2	Post-damage Constitutive Model	109
3.4.3	Coordinate System Transformation	111
3.5	CONCLUDING REMARKS	113
	<b>BIBLIOGRAPHY</b>	114
	<b>CHAPTER 4 MICROMECHANICAL ANALYSIS OF OFF-AXIS</b>	
	UNIDIRECTIONAL LAMINATES WITH INTRALAMINAR DAMAGE	117
4.1	INTRODUCTION	117
4.2	OFF-AXIS TENSILE LOADING OF UNIDIRECTIONAL LAMINATES	119
4.2.1	Unit Cell of a Unidirectional Laminate	119
4.2.2	Periodic Boundary Conditions	120
4.2.3	Off-axis Loading Algorithm	121

4.2.4	Finite Element Analysis of the Unit Cell	123
4.3	ANALYSIS OF GLASS/EPON 828 LAMINATES	126
4.3.1	Test Results	126
4.3.2	Material Constants	128
4.3.3	Numerical Results for Glass/Epon 828 Laminates	128
4.4	ANALYSIS OF GLASS/EPON 815 LAMINATES	136
4.4.1	Test Results	136
4.4.2	Material Constants	138
4.4.3	Numerical Results	138
4.5	CONCLUDING REMARKS	142
	<b>BIBLIOGRAPHY</b>	144
	<b>CHAPTER 5 MICRO/MESO-MECHANICAL ANALYSIS OF ANGLE-PLY AND CROSS-PLY LAMINATES</b>	146
5.1	INTRODUCTION	146
5.2	MESO SCALE MODELING FOR ANGLE-PLY LAMINATES	148
5.2.1	Meso Scale Unit Cell Modeling	148
5.2.2	Prediction of In-plane Moduli	154
5.3	MESO/MICRO-MECHANICAL ANALYSIS OF THREE LAMINATES	156
5.3.1	RUC/MUC Model and Loading	156
5.3.2	Boundary Conditions	158
5.3.3	Models for Material and Damage and Constants	159
5.3.4	Prediction of Stress-strain Curves of the Three Types of Laminates	160
5.3.5	Prediction of the Ply Level Response	162
5.3.6	Microscopic Response	165
5.3.7	Evolution of Matrix Damage	168
5.4	ANALYSIS OF RESIDUAL STRESS AND ITS INFLUENCES	173
5.4.1	Temperature Dependent Material Constants	173
5.4.2	Generation and Evolution of Thermal Residual Stresses and Strains	175
5.4.3	Mechanical Part of the Total Strain	181
5.4.4	Results of Subsequent Uniaxial Tensile Loading	183

5.5	CONCLUDING REMARKS	185
	<b>BIBLIOGRAPHY</b>	187
	<b>CHAPTER 6</b>	
	SUMMARY	190
6.1	SUMMARY AND CONCLUSIONS	190

## LIST OF FIGURES

Fig. 1-1	Response of composite materials: (a)Unidirectional laminate[5]; (b)Different lay-ups [5-6].	3
Fig. 1-2	Transverse damage of UDC: (a) Mixed matrix cracking and interface debonding; (b) Fractograph of transverse damage.	5
Fig. 1-3	Viscoelasticity.	6
Fig. 1-4	Micro-scale and macro-scale analysis (after Suquet [20]).	9
Fig. 2-1	Possible choice of unit cells of a unidirectional composite.	37
Fig. 2-2	RUC from a periodic composite.	38
Fig. 2-3	Node labeling on the boundary: (a) Periodic conditions; (b) Constrained plane.	47
Fig. 2-4	Illustrative example 1: (a)Meshed RUC; (b) Total deformation; (c) Periodic part of deformation.	53
Fig. 2-5	Dimensions of an asymmetric RUC.	54
Fig. 2-6	Stress distributions at the two opposite sides of a RUC.	54
Fig. 2-7	Reduction of RUC under extensions in three directions.	57
Fig. 2-8	Combined shear loading.	59
Fig. 2-9	Reduce to one-quarter of the RUC under off-axis loading.	59
Fig. 2-10	Verification models <i>A</i> and <i>B</i> : (a)Full-size RUC; (b) Quarter-size RUC.	66
Fig. 2-11	Comparison of the distributions of stress: (a) Distribution of $\sigma_{zz}$ in the full RUC and quarter RUC; (b) Distribution of $\sigma_{xy}$ in the full RUC and quarter RUC.	68
Fig. 2-12	Selected points for comparison.	69
Fig. 2-13	Generalized plane strain.	72
Fig. 2-14	Deformed shape and shear stress distribution of a two dimensional RUC model with different applied boundary conditions: (a) Eqn. (2.98); (b) Eqn. (2.100).	75

Fig. 2-15	Resultant boundary forces and distribution of stress components by applying homogeneous boundary conditions: (a) Distribution of stress component $\sigma_{xx}$ ; (b) Distribution of stress component $\sigma_{yy}$ .	77
Fig. 2-16	(a) The Finite element mesh of the RUC model for the unidirectional laminate; (b) Deformed shape under shear.	78
Fig. 3-1	A uniaxial viscoelastic model represented by a finite series of Kelvin elements coupled with an elastic spring.	92
Fig. 3-2	Stress-strain curve of viscoelastic matrix including unloading.	96
Fig. 3-3	Stress-strain curve of Epon 828 and Epon 815.	96
Fig. 3-4	Transverse loading of unidirectional laminate at different orientations: (a) Direction of global loading; (b) FEM mesh.	97
Fig. 3-5	Transverse response of a unidirectional laminate.	97
Fig. 3-6	Interface coordinate system.	98
Fig. 3-7	Combined mode debonding criterion.	99
Fig. 3-8	Normal cohesive law.	101
Fig. 3-9	One dimensional interphase model.	104
Fig. 3-10	Global stress vs. global strain.	105
Fig. 3-11	Interface separation vs. global strain.	106
Fig. 3-12	Response with artificial viscosity.	107
Fig. 3-13	Global and local coordinate systems of a crack.	109
Fig. 3-14	The response of a matrix element including damage process.	111
Fig. 4-1	Unidirectional laminates and unit cell model: (a) A unidirectional laminate under off-axis loading; (b) Unit cell for a square fibre array; (c) Quarter of a unit cell.	120
Fig. 4-2	Finite element mesh of the RUC model.	123
Fig. 4-3	Finer mesh for RUC (Mesh B).	124
Fig. 4-4	Comparison of the results of two meshes and the test.	125
Fig. 4-5	Fractographs of glass/Epon 828 coupon specimens under off-axis loadings: (a) 90° loading; (b) 45° loading; (c) 20° loading (adopted from [15]).	127

Fig. 4-6	Global stress-strain curve of glass/Epon 828 laminates.	129
Fig. 4-7	Strength of unidirectional laminates vs. off-axis orientations.	130
Fig. 4.8	Deformed shape of the RUC and interphase damage for different off-axis angles: (a) 90° loading; (b) 45° loading.	131
Fig. 4-9	Distribution of $T_3$ (Epon 828 laminates).	133
Fig. 4-10	Distribution of $T_2$ (Epon 828 laminates).	133
Fig. 4-11	Distribution of $T_1$ (Epon 828 laminates).	134
Fig. 4-12	Distribution of the first principal strain near the interphase (Epon 828).	134
Fig. 4-13	Traction distributions in interphase prior to and after damage: (a) Traction $T_3$ ; (b) Traction $T_2$ .	135
Fig. 4-14	Fractographs of glass/Epon 815 coupon specimens under off-axis loadings: (a) 90° loading; (b) 45° loading; (c) 20° loading (adopted from [15]).	137
Fig. 4-15	Global stress-strain curve of glass/Epon 815 laminates.	139
Fig. 4-16	Distribution of $T_3$ (Epon 815 laminates).	140
Fig. 4-17	Distribution of $T_2$ (Epon 815 laminates).	140
Fig. 4-18	Distribution of $T_1$ (Epon 815 laminates).	141
Fig. 4-19	Distribution of the first principal strain near the interphase (Epon 815 laminates).	141
Fig. 5-1	Meso-scale cell models for angle-ply laminates: (a) Angle-ply laminates; (b) Meso scale unit cell model.	149
Fig. 5-2	The two coordinate systems.	150
Fig. 5-3	Meshed MUC for angle-ply laminates: (a) Meshed MUC for $\pm 15^\circ$ ( $\pm 75^\circ$ ); (b) Meshed MUC for $\pm 30^\circ$ ( $\pm 60^\circ$ ).	153
Fig. 5-4	$E_x \sim \theta$ curves for angle-ply laminates.	155
Fig. 5-5	$G_{xy} \sim \theta$ curves for angle-ply laminates.	156
Fig. 5-6	Two types of laminates under uniaxial tensile loading : (a) A unidirectional laminate; (b) A $[\pm 45^\circ]_n$ s angle-ply laminate.	156
Fig. 5-7	RUC/MUC models of two composite laminates: (a) A unidirectional laminate; (b) A $[\pm 45^\circ]_n$ s angle-ply laminate.	157
Fig. 5-8	Predicted global stress-strain curve of a unidirectional laminate.	160

Fig. 5-9	Predicted global stress-strain curves of a $[0/90^\circ]_{ns}$ cross-ply laminate and a $[\pm 45^\circ]_{ns}$ angle-ply laminate.	162
Fig. 5-10	Global stress-strain curve at the laminate level and ply level stresses (angle-ply).	164
Fig. 5-11	Global stress-strain curve at the laminate level and ply level stresses (cross-ply).	164
Fig. 5-12	First principal strain distribution in the unit cell.	165
Fig. 5-13	Distribution of the local shear stress, $\tau_{xy}$ in a $[\pm 45^\circ]_{ns}$ laminate.	166
Fig. 5-14	Distribution of the maximum principal strain in a $[\pm 45^\circ]_{ns}$ laminate.	166
Fig. 5-15	Change in the fibre orientation resulting from load application.	167
Fig. 5-16	Fibre orientation change vs. the applied global strain.	168
Fig. 5-17	Evolution of the damaged zone (unidirectional laminate).	170
Fig. 5-18	Evolution of the damaged zone (cross-ply laminate).	171
Fig. 5-19	Evolution of the damaged zone (angle-ply laminate).	172
Fig. 5-20	Residual stress ( $\sigma_{zz}$ ) distribution in the model.	176
Fig. 5-21	Evolution of the maximum tensile stress in the matrix for various cooling rates and material properties.	177
Fig. 5-22	Evolution of the maximum compressive stress in the fibre for various cooling rates and material properties.	178
Fig. 5-23	Evolution of the global (average) stress $\bar{\sigma}_{xx}$ and $\bar{\sigma}_{zz}$ in the $90^\circ$ ply.	179
Fig. 5-24	The evolution of shrinkage strain $\bar{\epsilon}^L$ for two cooling rates and two material properties.	181
Fig. 5-25	The distribution of the first principal strain.	182
Fig. 5-26	The evolution of the maximum principal strain in the matrix.	182
Fig. 5-27	Damage evolution in cross-ply laminates: (a) With residual stress/strain; (b) Without residual stress/strain.	184

## LIST OF TABLES

Table 2-1 Stress at arbitrarily selected locations	70
Table 2-2 Material properties of fibre and matrix [4]	78
Table 2-3 Results and comparison for unidirectional boron/aluminum laminate ( $V_f = 0.47$ )	81
Table 3-1 Material properties and constants of constitutive model	95
Table 5-1 Properties of constituents [5]	155
Table 5-2 Properties of a lamina [7]	155

## NOMENCLATURE

$\alpha$	coefficient of linear thermal expansion ( $m/m/^\circ C$ )
$\alpha_g$	CTE at glass transition temperature
$\beta$	constants in smeared crack model
$\beta_v$	volumetric coefficient of thermal expansion
$\chi$	constants in smeared crack model
$\Delta$	increment or difference
$\delta$	ratio of the micro scale to macro scale character length
$\delta_{ij}$	Kronecker's $\delta$
$\delta_n, \delta_{t1}, \delta_{t2}$	critical displacement jumps in cohesive law
$\varepsilon_1, \varepsilon_2, \varepsilon_3$	principal strains
$\varepsilon_{33}^c, \gamma_{23}^c, \gamma_{13}^c$	critical strain of cohesive element
$\varepsilon_{cr}$	critical strain in matrix damage model
$\varepsilon_{ij}$	strain tensor ( $i, j = 1, 2, 3$ or $i, j = x, y, z$ )
$\bar{\varepsilon}_{ij}$	global strain tensor
$\dot{\varepsilon}_{ij}$	strain rate tensor
$\Delta\varepsilon_{ij}$	strain increment tensor
$\{\varepsilon\}$	strain vector: $\{\varepsilon_{11}, \varepsilon_{22}, \varepsilon_{33}, \varepsilon_{12}, \varepsilon_{23}, \varepsilon_{31}\}$
$\{\varepsilon_t\}$	total strain vector
$\{\varepsilon_e\}$	elastic strain vector
$\{\varepsilon_c\}$	creep strain vector
$\{\varepsilon_m\}$	mechanical strain vector
$\{\varepsilon_{th}\}$	thermal strain vector
$\phi$	angle
$\gamma_{ij}$	engineering shear strain ( $i, j = 1, 2, 3$ or $i, j = x, y, z$ but $i \neq j$ )

$\eta_n, \eta_{t2}, \eta_{t1}$	artificial viscous coefficient in cohesive law
$\lambda$	parameter in cohesive law
$\lambda_i$	Lagrange's multipliers
$\nu$	Poisson's ratio
$\nu_{xy}$	effective in-plane Poisson's ratio of laminates
$\Pi$	potential energy of a finite element system
$\theta$	off-axis angle
$\sigma_{eq}$	equivalent stress
$\sigma_{max}$	strength parameter of the cohesive law
$\sigma_{ij}$	stress tensor ( $i, j = 1, 2, 3$ or $i, j = x, y, z$ )
$\bar{\sigma}_{ij}$	global stress tensor
$\dot{\sigma}_{ij}$	stress rate tensor
$\Delta\sigma_{ij}$	stress increment tensor
$\{\sigma\}$	stress vector: $\{\sigma_{11}, \sigma_{22}, \sigma_{33}, \sigma_{12}, \sigma_{23}, \sigma_{31}\}$
$\tau_{ij}$	shear stress component ( $i, j = 1, 2, 3$ or $i, j = x, y, z$ but $i \neq j$ )
$\tau_i$	constants in viscoelastic model
$[A]$	matrix determined by Poisson's ratio
$a, b, c$	sides of a rectangular parallelepiped unit cell
$[B], [B']$	coefficient matrix in smeared crack model
$\{C\}$	constants of constraint equations
$C_{ijkl}$	elastic constants
$c_i^j$	constants related to the global strain loading
$D$	characteristic length of a structure
$[D]$	coefficient matrix of constraint equations
$[D']$	coefficient matrix in smeared crack model
$d$	characteristic length of a unit cell
$E$	Young's modulus

$E'$	Modulus parameter in one-dimensional cohesive law
$E_t$	modulus prior to damage
$E_x, E_y$	effective modulus of laminates
$E_1(\sigma_{eq})$	functional in the viscoelastic model
$\{F\}$	global nodal load vector
$F(\lambda)$	function of cohesive law
$f$	subscript for fibre
$f_m^\sigma$	function to describe the stress memory surface
$G$	shear modulus
$G_{xy}$	in-plane effective shear modulus of laminates
$h$	thickness of cohesive interphase element, thickness of a MUC
$I_1$	first invariant of stress tensor
$[I]$	identity matrix
$i$	subscript index $i = 1, 2, 3$ or $i = x, y, z$
$[J]$	a matrix to describe the constraint equations of a constrained plane
$J_2$	second invariant of deviatoric stress tensor
$j$	subscript index $j = 1, 2, 3$ or $j = x, y, z$
$[K]$	stiffness matrix
$k_1, k_2$	coefficients in the function of temperature dependent material constants
$L_1, L_2, L_3$	dimension of a parallelepiped unit cell
$\ell$	side length of a MUC
$l_i, m_i, n_i$	direction cosines in the coordinate transformation matrix
$m$	subscript for matrix
$m, n$	numbers, numbering subscripts
$\mathbf{n}, n_j$	unit outward normal vector and its components
$P$	resultant reaction at boundary
$R$	radius of fibre; material constants in viscoelastic model

$R_{mem}$	radius of memory surface
$S, S_1$	area
$[S]$	compliance matrix
$s$	subscript for skew coordinate system
$s_{ij}$	deviatoric stress tensor
$T_g$	glass transition temperature
$T_i$	traction
$T_r$	room temperature
$[T]$	coordinate transformation matrix
$U$	strain energy stored in a heterogeneous media
$U'$	strain energy stored in a homogenized media
$\{U\}$	vector of global degree of freedom
$u_i$	displacement components
$[u_i]$	displacement jump across the interface
$u_i^*$	periodic displacement
$\bar{u}_i$	prescribed displacement
$V$	volume
$V_f$	fibre volume fraction
$X_i$	macroscopic coordinates
$x_i$	microscopic coordinates
$Z_1, Z_2, Z_3$	constants in the smeared crack model

## CHAPTER 1

### INTRODUCTION

#### 1.1 APPLICATION OF COMPOSITE MATERIALS

Composite materials are becoming an essential part of present engineered materials because they offer advantages such as higher specific stiffness and strength, better fatigue strength and improved corrosion-resistance compared to conventional materials. The advanced composite materials usually consist of high performance fibres as reinforcing phase and polymers or metals as matrices. Examples of advanced fibrous composite materials are carbon or graphite fibre/epoxy, glass fibre/epoxy, boron fibre/aluminum, etc. The utilization of fibre reinforced composites in various fields of application has progressed significantly over past decades. They are used in a variety of applications from making aircraft structures to golf clubs, from electronic packaging to medical equipment, and from space vehicles to home building. By using composite materials, designers are able to locate and orient the reinforcement to withstand the anticipated loads. However, in spite of the superior properties of composite materials, the use of composite materials in critical load bearing members is still limited. One of the main reasons for this limited application is the difficulty in reliable prediction of the behaviour of composite materials. For example, the time- and temperature-dependent behaviour of polymer matrices and the mechanical degradation (damage) make the accurate prediction difficult, e.g. see the comments in References [1-4].

## 1.2 MECHANICAL PROPERTIES OF COMPOSITE MATERIALS

### 1.2.1 *Mechanical Properties*

We mainly discuss the properties of continuous fibre reinforced polymeric composites. The high specific stiffness and strength of composite come from the high strength of the fibres. Compared to bulk materials, continuous fibres produced from the same material have different microstructures and much less defects. However, an individual fibre or fibre bundle is difficult to use in an engineering structure. To utilize the superior performance of fibres, the key is to support them in a matrix. The mechanical properties of composites depend not only on the properties of the constituents but also on the arrangement of the constituents (contents and distributions of fibres, etc.)[1-3]. Composite materials are therefore heterogeneous and anisotropic (orientation-dependent) materials. Furthermore, mainly due to the properties of the matrix phase, composite materials exhibit time-dependence, and their behaviour is influenced by damage or degradation that frequently exists in the material system. For practical design and analysis, the orientation dependence, damage sensitivity and time-dependence of composite materials are significant factors to be considered.

#### *(a) Orientation dependence*

The most significant characteristic of composite material is the orientation dependence (anisotropy). Figure 1-1(a) shows, for example, the stiffness of a typical E-glass/epoxy unidirectional composite (UDC) at fibre direction ( $0^\circ$ ) and transverse direction ( $90^\circ$ ) [5]. It can be seen from the figure that for the same unidirectional laminates, the stiffness is saliently different in the longitudinal and transverse directions.

Experimental results also show that even under the same uniaxial loading the fibrous composite laminates with different fibre architecture have quite different stress-strain response and damage behaviour [6]. Figure 1-1(b), for example, shows different responses for: (1) a unidirectional laminate under  $45^\circ$  off-axis loading; (2) a  $[0^\circ/90^\circ]$  cross-ply laminate under tensile loading in  $0^\circ$  direction; and (3) a  $[\pm 45^\circ]$  angle-ply laminate under uniaxial tensile loading. The drastically different stress/strain response and the stress/strain level at final failure are clearly demonstrated in this figure. This implies that the location and orientation of the reinforcement can be tailored by the designer to withstand the anticipated loads. However, it also brings up a challenge to the researchers to accurately predict and analyze the highly nonlinear stress-strain curves and the deformation mechanisms involved.

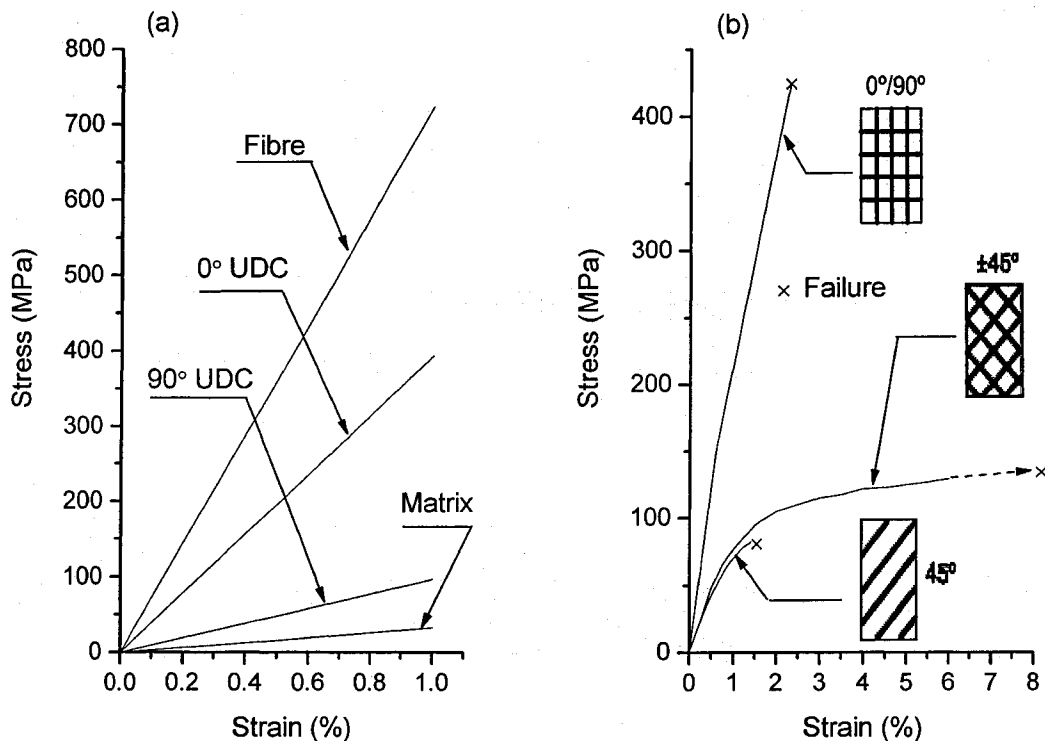


Fig.1-1. Response of composite materials:

(a) Unidirectional laminate [5]. (b) Different lay-ups [5-6].

*(b) Influence of Damage*

In many cases, the mechanical response of composite laminates are accompanied with and influenced by damage. The most important damage modes in a multi-layer laminate are fibre breaking, matrix cracking, interphase/interface separation and delamination [3]. Among them, the first three modes are the primary intralaminar damage modes [7], and the matrix cracking and interface debonding are greatly influenced by the matrix properties. For instance, the damage process in a unidirectional composite laminate may initiate by matrix cracking or interface debonding at certain locations, this damage then propagates and finally breaks the laminate. For multidirectional laminates, matrix cracking or interface debonding may exist at loading level much lower than the final failure load or even during the material curing process. However, these damages may be confined to certain laminae, thus the entire laminate can still hold loads until final fracture occurs, as in the case of a cross-ply laminate [6]. Thus for an accurate analysis, it is imperative to consider the prevailing damage mechanisms, especially the intralaminar ones. The features of matrix cracking and interfacial damage are dominated by the properties of the matrix and the fibre/matrix interface.

An adverse effect of using a matrix phase in the composite is its influences on the damage properties of the composite. In a glass/epoxy composite, for example, epoxies are usually weak and flaw sensitive compared to the fibre, under tensile loading, most epoxies fail in a brittle manner [8]. Because of the brittleness of the epoxy, matrix cracking becomes one of the most important damage mechanisms of a composite.

In most advanced composite materials, there is invariably an interphase between the two main constituents of the reinforced composites. The scale of the interphase may be

very small of the order of several microns [3]. Therefore, in many studies the interphase can be treated as an interface. The interphase/interface determines the stress transfer between the reinforcement and matrix, and thus it influences the damage process of laminates if the bonding is weak.

In practice, damage usually evolves in mixed modes. Figure 1-2, for example, displays the damage of a unidirectional laminate under transverse tensile loading. Figure 1-2(a) shows that the final failure is the mixed mode of matrix cracking and interphase damage [3] and Fig.1-2(b) shows the fractograph of the fractured specimen [9].

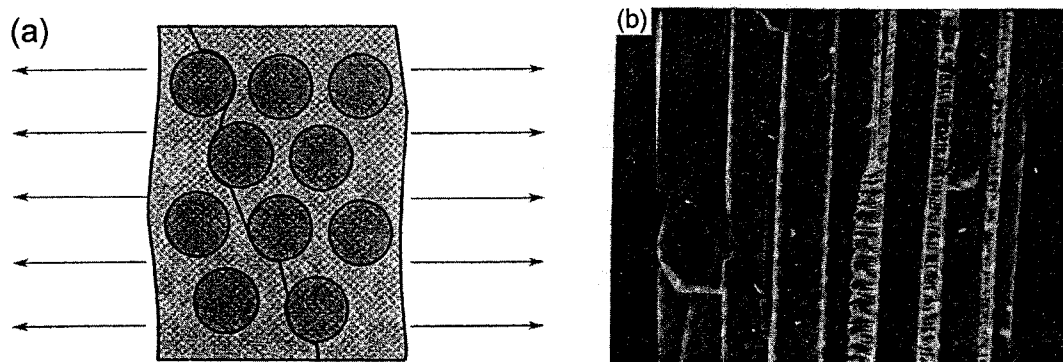


Fig. 1-2 Transverse damage of UDC.

(a) Mixed matrix cracking and interface debonding; (b) Fractograph of transverse damage (adopted from [9]).

### (c) *Time-dependence*

Epoxies are polymerization products with a highly crosslinked network. They are extensively used as the matrix phase in high performance composite materials. Their specific properties depend upon their particular formulation [8-10]. However, the epoxy matrix, like other thermoset polymers, exhibits time dependence (viscoelasticity). This is manifested by the increase of deformation with time under constant load, which is called

creep, and, conversely, by the decrease of stresses with time under constant strain, which is called relaxation (Fig. 1-3). Although the fibres, such as E-glass fibre, behave elastically for most of their stress-strain range, composites still exhibit viscoelasticity. The analysis of Hashin [11] showed that the viscoelastic effect in a unidirectional fibre composite is significant for axial shear, transverse shear and transverse uniaxial stress, for which the influence of the matrix is dominant. This implies that for multiaxial loading cases, influences of viscoelasticity will be inevitable. Furthermore, in many cases, the viscoelasticity of the matrix and the composite will be nonlinear and the damage in composite laminates would also evolve with time. This increases the complexity of the analysis.

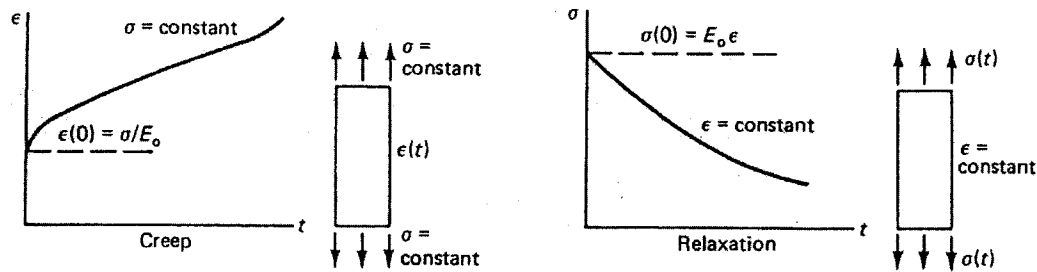


Fig. 1-3 Viscoelasticity (after Hashin [11]).

### 1.2.2 Inherent Scales Involved in the Analysis of Composite Materials

When analyzing a composite structure, one should be aware of different scales involved in the structure. There are at least three scales explicitly manifested in the composite structure (composite laminates, for instance, can be regarded as a simple structure or structural element), viz. (a) the macro-scale of the entire laminate, (b) meso-scale of individual plies and (c) microstructural length scales of individual fibres, matrix, coatings or interphases. The specific scales depend on the particular composite material

systems. In a typical glass-fibre reinforced polymeric composite, the diameter of each fibre is of the order of a few microns, and the thickness of the layers is of the order of  $100 \mu\text{m}$ .

### 1.3 MICROMECHANICAL ANALYSIS OF COMPOSITE MATERIALS

From the above discussion, the mechanical responses of composite materials are not only influenced by the properties of their constituents, but also greatly influenced by their microstructures. And in many cases, the influence of time and damage should be considered in the analysis. Therefore it is desirable to conduct a full micromechanical analysis for the entire composite structure where *both the properties and structures* of the reinforcement, matrix, and interphase/interface are explicitly presented in the model. If sufficient computing power and adequate solution procedure are provided to handle the full microscopic model of composite structures, many advantages can be ensured. However, from a practical point of view, it is very difficult to analyze full microscopic models, since the required computing resources are tremendous if numerical solution methods are used [12-13]. Due to this reason, full microscopic modeling of a whole composite structure has rarely been dealt with. Instead, in the analysis of composite materials, the object of a micromechanical analysis is usually confined to a small size of material sample, which is called representative volume element (RVE). And usually, a macromechanical approach is combined with the micromechanical approach to analyze the whole structure.

The applications of the micromechanical and macromechanical analyses can be very well demonstrated by the analysis of multi-layer laminates. First the micromechanical

analysis is conducted, in which a micro-scale model is established according to the microstructure of the composite lamina. (This is usually called a representative volume element (RVE). For a composite with periodic structures, the micro-scale model reduces to a repeated unit cell (RUC).) The properties of the constituents are then input to the RVE or RUC model to obtain the mechanical response, and effective modulus (EM) of the lamina can be defined considering each ply as a homogenized but anisotropic material [14].

The homogenized laminates are then analyzed by the macromechanical approach, e.g. classical laminate theory or similar theories which are based on the effective properties obtained by the above micromechanical analysis. (Of course, the effective properties can also be obtained from a test. However, in some situations, for example during the design stage, the material may not be available yet, then the micromechanical analysis becomes the main source). Thus macroscopic stress fields can be evaluated and non-critical and critical regions be identified from macroscopic computations using homogenized constitutive relations. This macromechanical approach is similar to that for a conventional material, except for composite materials, usually anisotropic constitutive models should be used.

Upon the identification of critical points according to the macroscopic response, key microscopic stresses may then be recovered in local regions by detailed micromechanical solution using a RVE and the boundary conditions from the macroscopic solution. Therefore, through these global-local computations, it is possible to overcome shortcomings of pure macroscopic analyses that are inaccurate and pure micromechanical

modeling of the entire laminate which is computationally prohibitive. Examples of effective multiscale global-local techniques can be found in [15-19].

It can be seen that the micromechanical modeling of heterogeneous material involves two procedures for efficient computing and for accurate representation of variables at different scales. First is ‘from micro to macro’, and usually referred to as ‘homogenization’ procedure [14, 20]. In this step, homogenized material behaviour at a macroscopic point  $X$  is determined as a function of microstructural parameters but independent of applied load. In this homogenization procedure, an isolated representative volume element is identified at the microstructural scale of heterogeneities (See Fig. 1-4). The dimensions of the RVE are typically very small in comparison with the structural dimensions  $D$ . Homogenized (averaged) variables are obtained by volume averaging the continuous variables in the RVE. The macroscopic material constants can then be determined using the effective modulus, and the entire structure can be analyzed macroscopically under different loadings.

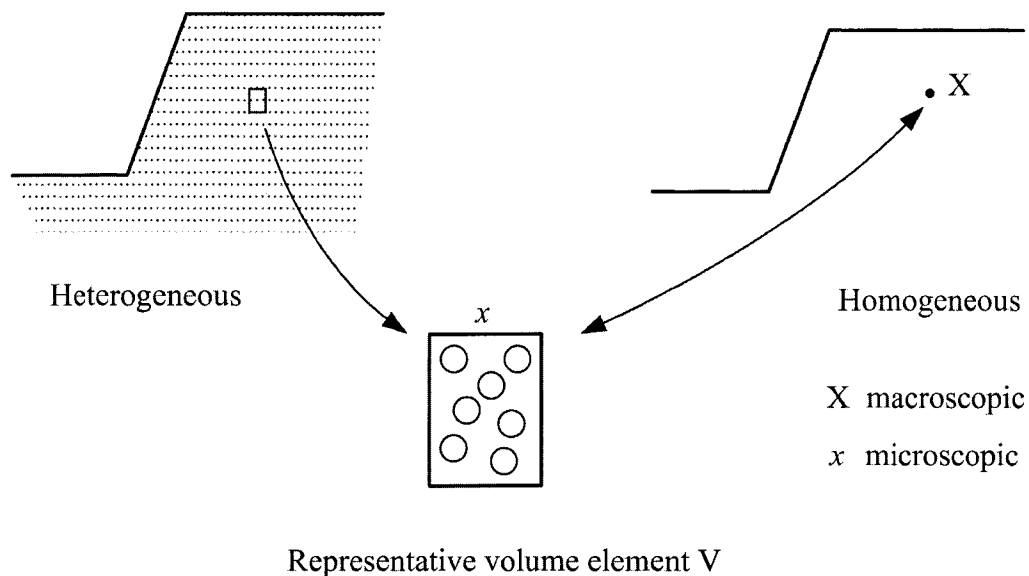


Fig.1-4 Micro-scale and macro-scale analysis (after Suquet [20]).

The reverse of this process, termed as ‘localization’, is a ‘top down approach’ where the evolution of variables is evaluated in the microstructure from known macroscopic variables. In those regions, where the microstructure admits an RVE, the microscopic variables can be evaluated by solving a boundary value problem with imposed macroscopic strains and the local periodicity conditions.

Thus an effective and accurate micromechanical approach is the critical element for both the ‘homogenization’ and ‘localization’ for the composite materials. Micromechanical analysis for linear elastic composites has been addressed extensively in the literature, e.g., in Hashin [1] and Christensen [2] and the references therein. However, with the increasing use of composite materials as major load-bearing parts, for meaningful design of structural materials and accurate analysis, it is very important that micromechanical analysis should robustly incorporate details of real morphology, nonlinear constituent properties and damage models.

For fibre reinforced polymeric composite (FRPC), the following two factors should be considered in developing micromechanical models:

- *Viscoelastic behaviour of polymer matrices:* All polymers are viscoelastic materials (Some thermoplastics may also be viscoelastic-viscoplastic). The viscoelastic response of a polymer becomes more pronounced under conditions of high temperature, sustained loading, and/or high stress level. Owing to the viscoelasticity of the polymer matrix, the composite material also presents viscoelastic behaviour. The viscoelastic effect in a unidirectional laminate is significant for the axial shear, transverse shear, and transverse uniaxial loadings, for which the influence of matrix is dominant [11].

- *Matrix dominated damage*: Basically, there are four damage modes in a composite laminate: (1) Matrix cracking; (2) Interfacial debonding; (3) Fibre breaking; and (4) Delamination. Among them, the matrix cracking and the fibre/matrix interface debonding are two primary damage modes in composite laminates [7, 21]. These intralaminar damages could occur during the manufacturing process or at a relatively low applied load. In most cases, damage in composite laminates initiates in these two forms. Obviously, these damage behaviours are also evolved from the micro scale, thus a micromechanical analysis is preferred.

#### 1.4 OBJECTIVES OF THE STUDY

The objective of this study is to develop a unified micromechanical model for periodic composite laminates which incorporates the material nonlinearity of the matrix and damage models of matrix cracking and interface debonding. To this end, the study concentrated on the following aspects:

- (1) *The development of a unified three-dimensional micromechanical analysis model under general multiaxial loading*. This includes primarily how to establish a RUC model, and the formulation of the appropriate periodic boundary conditions to be applied. The incorporation of the nonlinear viscoelastic model for the matrix and ease of implementation into a commercial FEM scheme are also important factors.
- (2) *Microscopic damage models*. For the requirement of performing micromechanical analyses with capability to simulate entire evolving damage process including matrix cracking, interface debonding, and fibre fracture, more realistic failure criteria and

post-failure constitutive relations for the matrix and the interface need to be developed.

- (3) *Meso-scale modeling of multi-layer laminates.* Meso-scale approaches for cross-ply and angle-ply laminates will be investigated. The micromechanical approach for a unidirectional RUC will be extended to a meso-scale model in which the fibres in a ply are represented by a homogenized fibre. This provides an alternate procedure to obtain the response of the laminates directly from the properties of the constituents. And the damage evolution in the laminates can be simulated more accurately.
- (4) *Numerical issues.* For time-dependent multiaxial loading cases, to specify the direction of the global stress or strain vector, as to simulate the strain controlled test of off-axis unidirectional laminates or angle-ply laminates, a special iteration algorithm is to be established. Other considerations such as imposing and implementing proper boundary conditions accounting for the symmetry of a RUC, mesh convergence, and strategies to overcome the snap-back instability for equilibrium iterations in a nonlinear FEM solution, will be investigated.
- (5) *Application and verification examples.* A number of numerical analyses will be conducted to show the wide application potential of the proposed micromechanical approaches, which include: 1) The elastic analysis of unidirectional laminates and angle-ply laminates. 2) Nonlinear analysis of unidirectional laminates with evolution of interface debonding under general off-axis loading. 3) Nonlinear analysis of unidirectional laminates and angle-ply laminates with evolution of matrix cracking. And 4) Residual stress/strain analysis of cross-ply laminates. All the results will be compared with the available experimental and theoretical results in the literature.

## 1.5 LITERATURE REVIEW

### 1.5.1 *Micromechanical Analysis*

The main and important motivation of micromechanical analysis is the prediction of homogenized material properties from the microstructure of a composite material. Since 1960s, many analytical and numerical studies have been carried out. Based on the approaches (mechanics of material, theory of elasticity) adopted, there are several types of micromechanical methods. In particular, upper and lower bounds for elastic moduli have been derived using energy variational principles, and closed-form analytical expressions have been obtained [22-23]. For example, based on an energy balance approach with the aid of elasticity theory, Whitney and Riley [24] obtained closed-form analytical expressions for a composite's elastic moduli. Unfortunately, the generalization of this method to viscoelastic, elastoplastic and nonlinear composites is very difficult. The solutions of composite cylinder assemblage (CCA) model, self-consistent scheme (SCS), and generalized self-consistent scheme (GSCS) models are from the theory of elasticity, thus usually give more accurate results [25-27]. However, the solutions of the above models may not be accurate for high fibre volume fractions or high rigidity of the fibre [28]. Aboudi [29] has developed a unified micromechanical theory based on the study of interacting periodic cells, and it was used to predict the overall behaviour of composite materials both for elastic and inelastic constituents [30]. As in reference [29], homogeneous boundary conditions were applied to the RVE or unit cell models. In fact, this is only valid for those cases in which normal tractions are applied on the boundaries. For a shear loading case, many researchers, e.g., Suquet [20], Yuan and Pagano [28], and Sun [31], among others, have indicated that the 'plane-remains-plane' boundary

conditions are over-constrained boundary conditions. Xia, et al. [32] further demonstrated that homogeneous boundary conditions are not only over-constrained boundary conditions but may also violate the stress/strain periodicity conditions.

The above micromechanical models can be regarded as mechanical or engineering models. A mathematical counterpart to such engineering methods appeared in the 1970's under the general heading of the 'asymptotic homogenization theory'. The fundamentals of this theory can be found, e.g. in [20, 33-37], among others. Asymptotic homogenization theory has explicitly used periodic boundary conditions in modeling of linear and nonlinear composite materials. These results have clearly shown that characteristic modes of deformation do not result in plane boundaries after deformation [20]. Guedes and Kikuchi [38] discussed the application of finite element method (FEM) to composite problems. It showed that usually a special FEM code should be developed or modified to solve the basic equations of the homogenization theory. Recent development and applications of homogenization theory for various aspects of composite analysis are given, for instance, in Ref. [15-19, 38-42].

Suquet [20], Hori and Nemat-Nasser [40] presented universal inequalities which indicate that the predicted effective elastic modulus can vary depending on the applied conditions on the boundary  $\partial V$  of a unit cell, and the homogeneous displacement and homogeneous traction boundary conditions will give the upper and lower bounds of the effective modulus. Hollister and Kikuchi [41] have given a very good comparison of the homogenization theory and the mechanical methods (it is called average field theory in [41]), concluding that the homogenization theory, which uses the periodic boundary conditions, yields more accurate results. It is shown in [40] that the homogenization

theory and mechanical methods can be related to each other and a more applicable hybrid theory was established.

Note that from the compatibility and continuity of displacement and traction along the cell boundaries, the periodic boundary conditions can also be obtained for a unit cell, see for example, Ref. [28, 31, 43].

The direct extension of elastic micromechanical analysis is in predicting the nonlinear response of a composite caused by the nonlinearity of the constituents. In [42, 44] the rate-independent plastic response of a unidirectional laminate were studied, while in [45-46] viscoplastic model of matrix were used. Examples of viscoelastic response of a composite can be found in [47-50]. A few investigators have also applied the micromechanical analysis to the cross-ply laminates (laminates containing only  $0^\circ$  and  $90^\circ$  plies) [46, 48-52], by which the thermal residual stresses, viscoelastic response and matrix damage have been studied. There are very few studies extending the micromechanical approach to angle-ply laminates [30, 32].

In addition to analytical approaches, the finite element method, the boundary element method [53-55], and the fast Fourier transformation method [36] have been used in the micromechanical analysis. However, in most cases, the finite element method was explored to conduct the numerical micromechanical analysis [41-42, 56-58].

### ***1.5.2 Micromechanical Analysis with Damage Evolution***

Within the framework of continuum mechanics, two distinct approaches, namely the phenomenological and micromechanical approaches have evolved. Motivated by experimental observations, the phenomenological theories introduce a set of internal

scalar or tensor damage variables, whose growth is determined by appropriate evolution laws. Although these models have been popular for their relative simplicity in representing underlying physical complexities, the empirical treatment makes their applications to different materials questionable [39]. The micromechanical approach enables one to investigate damage/failure behaviour of laminates at the fibre, matrix and interface level, and it can be directly related to the micro-scale structure and the properties of constituents. There are many investigations incorporating the damage models (we confined our attention mainly to matrix cracking and interfacial debonding) in the micromechanical analysis. Usually, the entire response of laminates including damage evolution and failure mechanisms can be simulated. Micromechanical analyses including damage/failure analysis can be found, among others, in [28-29, 46, 49-50, 53-57, 59-65].

According to the approaches used and applications, the mechanical analysis with damage/failure can be grouped into: (1) Prediction of the strength of laminates [59-60]; (2) Analysis of the response of composites with assumed known damage [28, 53-55, 61-62]; and (3) Prediction and analysis of composites with evolving damage [49-50, 56-57, 63-65].

In [60], for instance, Aboudi presented a micromechanical analysis for the prediction of ultimate stresses of unidirectional fibre composites under combined loadings. The approach is based on micro-failure criteria applied to the fibre and matrix phases as well as to the fibre/matrix interface. The advantage of a micromechanical analysis for the strength of laminates is that one can gain some insight into the failure mechanisms of composite materials.

The analyses of composites with assumed known damage mostly relate the influences of imperfect bonding across the fibre/matrix interface. In [28], for example, Yuan and Pagano have carried out an analysis of fibre reinforced brittle matrix composites in order to predict the influence of the debonded interface on “effective” elastic moduli of the composites. The debonded interface is assumed to be completely separated and the extent of the debonded interface is simulated by assumed debonding geometries. Hashin [61-62] also studied the influence of the imperfect interface where the interface conditions are discussed and formulated.

Examples of predicting the entire evolution process of damage can be found, e.g., in [46, 57]. The key for predicting both the initiation of propagation of damage is that proper damage criteria and propagation rule and appropriate numerical techniques should be adopted, since the damage location and path is unknown prior to the analysis. It is worthwhile to note that several researchers have introduced the cohesive interphase damage models into the micromechanical RUC analysis. A significant advantage of the cohesive damage model is that both the initiation and propagation can be properly simulated, e.g., see [56-57, 64]. Also in the modeling of matrix cracking, smeared crack method is used in [63, 65]. This approach permits a description of crack in terms of stress-strain relations; therefore, it is convenient to implement into a FEM code [66-67].

### ***1.5.3 Current Status***

Both standard mechanical approach and asymptotic homogenization theory are extensively used in the micromechanical analysis. Generally, homogenization theory, using periodic boundary conditions, gives more accurate results [41]. Finite element

method is widely used in both approaches. However, for homogenization theory, standard structural finite element analysis codes can not be directly used to implement the periodic boundary conditions [32, 42], especially for multiaxial loading cases.

It is noted that most of the aforementioned micromechanical analysis of composites, with or without damage modeling, has been confined to unidirectional laminate under uniaxial loading applied along the material principal directions, see, for example, the review by Pagano and Yuan [14]. The micromechanical approach can be applied also to multi-angle laminates and to unidirectional laminates under general off-axis loading [45, 60, 63, 68]. However, works on off-axis loading analyses including damage modeling are very limited [60, 63].

For cross-ply and angle-ply laminates, several researchers use simplified unit/multi-cell models, where the cross-sections of fibre are represented by squares, as in [29]. And damage is usually not included in the analysis [51].

The prediction and analysis of composites with the entire evolution process of damage is a challenge to researchers, especially in combined loading cases. In these types of analyses, proper damage initiation criteria and propagation rule are an essential prerequisite. The cohesive interphase damage model and smeared cracking approach for matrix crack modeling are two main approaches which are successfully used in the micromechanical analysis. These two approaches are also convenient to implement in a FEM code.

Two issues arise in the numerical solution of micromechanical problems when material nonlinearity is involved. First, to specify the direction of the global stress or strain vector, as to simulate the stress controlled or strain controlled tests of a laminate, a

specific iteration algorithm is needed [36, 63]. Second, in strongly nonlinear problems, convergence of equilibrium iterations of the FEM solution is frequently an important concern. In general, special algorithms, for example, arc length method, are needed to overcome the convergence difficulties [40, 69-71].

## 1.6 SCOPE AND ORGANIZATION OF THE DISSERTATION

*In chapter 2*, a three-dimensional micromechanical analysis model is proposed. A unified, explicit form of periodic boundary conditions suitable for FEM analyses of RUC models subjected to multiaxial loads is presented. The proposed model and implementation into the finite element scheme are discussed in detail. With the aid of Gauss' theorem, a formula is derived to calculate the average stress/strain based on periodic boundary conditions. Using the method of Lagrange's multipliers, it is demonstrated that in a FEM scheme, imposing periodic displacement constraints to a RUC will guarantee the traction continuity conditions automatically. It is also shown that by using effective properties of a 'homogenized' media, the strain energy stored in the effective media is equal to the strain energy stored in the composite material.

The use of symmetry to reduce the computational effort in the RUC analysis under *off-axis loading conditions* is presented in detail. The procedure is first illustrated through two examples for square array RUC under triaxial extension/compression, combined in-plane shear and axial shear loadings. Then periodic boundary conditions for off-axis loading on a one-quarter RUC are obtained. The comparison with a full-size RUC model demonstrated the validity of the formulation.

Examples of elastic analysis by using the FEM code ANSYS [72] are also provided in this chapter. The first two examples show that: (1) The periodic part of deformation can be retrieved after the solution of the RUC using the proposed unified periodic boundary conditions; (2) An asymmetric RUC is analyzed which demonstrated that the present model can apply to general inclusion geometries. In another 2-D example, the results of the present method and those obtained by applying homogeneous boundary conditions are compared. The results clearly show that homogeneous boundary conditions are not only over constraints to the deformation of a periodic laminate, but also will violate the traction continuity conditions. In the last 3-D example, it is demonstrated that all the nine effective constants of an orthotropic unidirectional laminate can be predicted simultaneously by the present approach.

*In chapter 3*, models for the matrix viscoelasticity, fibre/matrix interphase damage, and matrix cracking are presented. The matrix behaviour is described by a recently developed nonlinear viscoelastic constitutive model [73]. A brief description of the model is provided in Section 3.2 and the model is implemented into the FEM code ADINA [74].

To model the damage (separation) of the fibre/matrix interface, an interphase/interface separation model is proposed which can be directly applied to a unit cell analysis. The stress-strain relation of the interphase element is derived based on a cohesive law, which characterizes the dependence of the tractions on the displacement discontinuities across the interface. The model can handle both the normal and tangential separations of the interphase, thus mixed mode interphase damage can be predicted. In addition, an 'artificial' viscous term is added to the cohesive law to overcome the convergence

difficulty induced by the so-called snap-back instability in the equilibrium iterations (Section 3.3).

To model the matrix cracking, a 'smeared crack approach' is employed. In this approach, the cracked solid is assumed to be a continuum that permits a crack description in terms of stress-strain relations. In particular, the proposed post-damage stress-strain relation allows that only normal and in-plane shear stress components (corresponding to crack orientations) tend to zero (Section 3.4).

*In Chapter 4*, the initiation and evolution of the intralaminar damage and its effect on the global stress-strain relation of composite laminates are predicted by finite element micromechanical analysis. As application examples, two unidirectional laminates (glass fibre/Epon 828 and glass/Epon 815) under off-axis tensile loading are analyzed. Results show that the initiation and evolution of the intralaminar damage can be well simulated. And the predicted global stress-strain curves are also in good agreement with the experimental results.

*In Chapter 5*, the analysis of three laminates with different lay-ups is described. The finite element predictions of the three types of laminates subject to uniaxial tensile loading are presented, viz. (1) a unidirectional laminate under  $45^\circ$  off-axis loading, (2) a  $[0^\circ/90^\circ]_{ns}$  cross-ply laminate under transverse loading and, (3) a  $[\pm 45^\circ]_{ns}$  angle-ply laminate under tensile loading.

To facilitate the micromechanical analysis for angle-ply and cross-ply laminates, a meso/micro rhombohedral two cell model has been developed for the  $[\pm\theta]_n$  angle-ply laminates. The in-plane elastic moduli for  $[\pm\theta]_n$  angle-ply laminates are predicted to verify the model (Section 5.2).

For the three laminates involved in Chapter 5, studies show that the bonding between the fibre and matrix is strong and perfect bonding conditions can be assumed. Thus matrix cracking remains the main intralaminar damage mechanism. The ‘smeared crack approach’ presented in Chapter 3 is employed to simulate the matrix cracking in the three laminates. The numerical results characterizing the local and global responses of the laminates including the damage evolution are presented and the predicted results are compared with the experimental data with similar composite lay-ups (Section 5.3).

Residual stress/strain may lead to the development of damage and may also have an adverse effect on the mechanical behaviour of the composites. In Section 5.4, the initiation and evolution of the residual stress/strain are analyzed using *time-dependent* and *temperature-dependent* material constants. A subsequent mechanical loading is imposed to the cross-ply RUC to investigate the influence of the residual stress/strain.

Conclusions from this study are summarized *in Chapter 6*.

## **1.7 SUMMARY OF MAIN CONTRIBUTIONS THROUGH THIS RESEARCH PROJECT**

- The proposed three-dimensional micromechanical model and the unified form of periodic boundary conditions are suitable for RUC models subjected to general multiaxial loads. The approach applies not only to linear elastic but also to nonlinear viscoelastic problems. It has rigorously demonstrated that imposing the suggested periodic displacement constraints on the RUC can guarantee the traction continuity conditions across the neighbouring cells. The proposed approach can also be easily implemented into a commercial FEM code.

- The proposed meso/micro rhombohedral two cell models for the  $[\pm\theta]_n$  angle-ply laminates provide an alternative way to the analysis of multi-directional laminates. Thus the mechanical properties of the laminates can be directly related to the properties of the constituents. To the author's best knowledge, no similar work has been reported.
- Considering the symmetries of geometry, material and loading, appropriate boundary conditions for combined normal and shear loading (off-axis loading) on a one-quarter RUC are further derived. An iteration algorithm is proposed to simulate the off-axis loading under strain control conditions.
- A cohesive interphase element is developed which can be directly applied to a unit cell analysis. The model can handle both the normal and tangential separations of the interphase, thus mixed mode interphase damage can be predicted. The interphase element can be conveniently inserted into a FEM scheme since an equivalent stress-strain relationship is used. A simple strategy has been introduced to overcome the convergence difficulty induced by the so-called snap-back instability in the interface damage analysis.
- A 'smeared crack approach' is employed to model the matrix cracking. The approach has been used in the analyses for concrete structure; however, its application to the fibrous composite materials is rather limited. In addition, in the present research, the proposed post-damage stress-strain relation allows that only preferred stress components tend to zero.
- The application examples demonstrated that the present model can distinguish the damage modes of fibre breaking, matrix cracking and interface separating based on

---

the properties of the constituents, without the need to prescribe the prevailing damage mode. Evolving damage analysis is also extended to a meso-scale model of angle-ply laminates.

- The initiation and evolution of the residual stress/strain are analyzed using time- and temperature-dependent material constants. Especially, the temperature-dependence of both the Young's modulus and the coefficient of thermal expansion are considered for the entire range from curing temperature to room temperature. The meso/micro-mechanical analysis of a cross-ply laminate reveals that the damage initiation and evolution under subsequent mechanical loading are greatly influenced by the residual stress/strain.

**BIBLIOGRAPHY**

1. Hashin, Z. (1983). Analysis of composite materials—a survey. *ASME Journal of Applied Mechanics*, **53**, 550-560.
2. Christensen, R. M. (1979). *Mechanics of Composite Materials*. Wiley, New York.
3. Daniel, I. M., Ishai, O. (1994). *Engineering Mechanics of Composite Materials*. Oxford University Press, New York, Oxford.
4. Raghavan, P., Moorthy, S., Ghosh, S., Pagano, N. J., 2001. Revisiting the composite laminate problem with an adaptive multi-level computational model. *Composites Sciences and Technology*, **61**, 1017-1040.
5. 3M Minnesota Mining & Manufacturing CO., Technical data of ‘Scotchply’ reinforced plastic type 1002 & 1003. St. Paul, Minnesota, USA.
6. Ellyin, F., Kujawski, D. (1995). Tensile and fatigue behaviour of glass fibre/epoxy laminates. *Construction and Building Materials*, **9**, 425-430.
7. Smith, Brian W. (1987). Fractography for continuous fiber composites, in *Engineered Materials Handbook, Volume 1, Composites*. ASM International, Ohio, USA, pp786-793.
8. Bandyopadhyay, S. (1990). Review of the microscopic and macroscopic aspects of fracture of unmodified and modified epoxy resins. *Materials Science and Engineering*, **A125**, 157-184.
9. Ishai, O. (1971). Failure of unidirectional composites in tension. *Journal of the Engineering Mechanics Division, Proceedings of the ASCE*, **97**, 205-222.
10. Lorenzo, L., Hahn, H. T. (1986). Effect of ductility on the fatigue behaviour of epoxy resins. *Polymer Engineering and Science*, **26**, 274-284.

11. Hashin, Z. (1966). Viscoelastic fiber reinforced materials. *AIAA Journal*, **4**, 1141-1147.
12. Kim, S. J., Lee, C. S., Yeo, H. J. (2002). Direct numerical simulation of composite structures. *Journal of Composite Materials*, **36**, 2765-2785.
13. Nemat-Nasser S., Hori, M. (1999). On two micromechanics theories for determining micro-macro relations in heterogeneous solids. *Mechanics of Materials*, **31**, 667-682.
14. Pagano, N. J., Yuan, F. G. (2000). The significance of effective modulus theory (homogenization) in composite laminate mechanics. *Composites Science and Technology*, **60**, 2471-2488.
15. Ghosh, S., Lee, K., Moorthy, S. (1995). Multiple scale analysis of heterogeneous elastic structures using homogenization theory and Voronoi cell finite element method. *International Journal of Solids and Structures*, **32**, 27-62.
16. Raghavan, P., Moorthy, S. Ghosh, S., Pagano, N. J. (2001). Revisiting the composite laminate problem with an adaptive multi-level computational model. *Composites Science and Technology*, **61**, 1017-1040.
17. Fish, J., Shek, K. (2000). Multiple scale analysis of composite materials and structures. *Composites Science and Technology*, **60**, 2547-2556.
18. Robbins, D. H., Reddy, J. N. (1996). An efficient computational model for the stress analysis of smart plate structures. *Smart Material Structures*, **5**, 353-360.
19. Oden, J. T., Vemaganti, K., Moes, N. (1999). Hierarchical modelling of heterogeneous solids. *Computer Methods in Applied Mechanics and Engineering*, **172**, 3-25.

20. Suquet, P. (1987). Elements of homogenization theory for inelastic solid mechanics. In: Sanchez-Palencia, E., Zaoui, A., (eds.). *Homogenization Techniques for Composite Media*, Springer-Verlag, Berlin. 194-275.
21. Wang, A. S. D., (1987). Strength, failure, and fatigue analysis of laminates, in *Engineered Materials Handbook, Volume 1, Composites*. ASM International, Ohio, USA, pp236-251.
22. Hashin, Z., Shtrikman, S. (1963). A variational approach to the theory of elastic behaviour of multiphase materials. *Journal of Mechanics and Physics of Solids*, **11**, 127-140.
23. Hashin, Z. (1962). The elastic moduli of heterogeneous materials. *ASME Journal of Applied Mechanics*, **30**, 143–150.
24. Whitney, J. M., Riley, M. B. (1966). Elastic properties of fiber reinforced composite materials. *AIAA Journal*, **4**, 1537-1542.
25. Hashin, Z., Rosen, B. W. (1964). The elastic moduli of fiber-reinforced materials. *ASME Journal of Applied Mechanics*, **31**, 223-232.
26. Hill, R. (1965). A self consistent mechanics of composite materials. *Journal of Mechanics and Physics of Solids*, **13**, 213-222.
27. Christensen, R. M., Lo, K. M. (1979). Solutions for effective shear properties of three-phase sphere and cylinders. *Journal of Mechanics and Physics of Solids*, **37**, 315-330.
28. Yuan, F., Pagano, N. J., Cai, X. (1997). Elastic moduli of brittle matrix composites with interfacial debonding. *International Journal of Solids and Structures*, **34**, 177–201.

- 
29. Aboudi, J. (1991). *Mechanics of Composite Materials, a Unified Micromechanical Approach*. Elsevier Science Publishers, Amsterdam.
  30. Aboudi, J. (1996). Micromechanical analysis of composites by the method of cells-update. *Applied Mechanics Review, ASME*, **49**(10), part 2, S83-S91.
  31. Sun, C. T., Vaidya, R. S. (1996). Prediction of composite properties from a representative volume element. *Composites Science and Technology*, **56**, 171-179.
  32. Xia Z., Zhang, Y., Ellyin, F. (2003). A unified periodical boundary condition for representative volume elements of composites and applications. *International Journal of Solids and Structures*, **40**, 1907-1921.
  33. Benssousan, A., Lions, J. L., Papanicoulau, G. (1978). *Asymptotic Analysis for Periodic Structures*, Amsterdam, North Holland.
  34. Sanchez-Palencia, E. (1980). *Non-homogeneous Media and Vibration Theory*, Lecture notes in physics, **127**. Springer-Verlag, Berlin.
  35. Bakhvalov, N. S., Panasenko, G. P. (1984). *Homogenization in Periodic Media, Mathematical Problems of the Mechanics of Composite Materials*. Nauka, Moscow.
  36. Michel, J. C., Moulinec, H., Suquet, P. (1999). Effective properties of composite materials with periodic microstructure: a computational approach. *Computer Methods in Applied Mechanics and Engineering*, **172**, 109-143.
  37. Aboudi, J., Pindera, M.-J., Arnold, S. M. (2001). Linear thermoelastic higher-order theory for periodic multiphase materials. *ASME Journal of Applied Mechanics*, **68**, 697-707.

38. Guedes, J. M., Kikuchi, N. (1991). Preprocessing and postprocessing for materials based on the homogenization method with adaptive finite element methods. *Computer Methods in Applied Mechanics and Engineering*, **83**, 143-198.
39. Moorthy, S., Ghosh, S. (1998). Particle cracking in discretely reinforced materials with the Voronoi cell finite element model. *International Journal of Plasticity*, **14**, 805-827.
40. Hori, M., Nemat-Nasser, S. (1999). On two micromechanics theories for determining micro-macro relations in heterogeneous solids. *Mechanics of Materials*, **31**, 667-682.
41. Hollister, S. J., Kikuchi, N. (1992). A comparison of homogenization and standard mechanics analysis for periodic porous composites. *Computational Mechanics*, **10**, 73-95.
42. Jansson, S. (1992). Homogenized nonlinear constitutive properties and local stress concentrations for composites with periodic internal structure. *International Journal of Solids and Structures*, **29**, 2181-2200.
43. Li, S. (2000). General unit cells for micromechanical analysis of unidirectional composites. *Composites, Part A: Applied Science and Manufacturing*, **32**, 815-826.
44. Brockenbrough, J. R., Suresh, S., Wienecke, H. A. (1991). Deformation of metal-matrix composites with continuous fibers: geometrical effects of fiber distribution and shape. *Acta metallurgica et Materialil*, **39**, 735-752.
45. Zhu, C., Sun, C. T. (2003). Micromechanical modelling of fibre composites under off-axis loading. *Journal of Thermoplastic Composite Materials*, **16**, 333-344.

46. Ellyin, F., Xia, Z. (2001). Rate-dependent constitutive modelling and micro-mechanical analysis of fibre-reinforced metal-matrix composites. *Journal of Mechanics and Physics of Solids*, **49**, 2543-2555.
47. Zhang, L., Ernst, L. J., Brouwer, H. R. (1998). Transverse behavior of a unidirectional composite (glass fibre reinforced unsaturated polyester), part II: influence of shrinkage strains. *Mechanics of Materials*, **27**, 37-61.
48. Chen, Y., Xia, Z., Ellyin, F. (2001). Evolution of residual stresses induced during curing processing using a viscoelastic micro-mechanical model. *Journal of Composite Materials*, **35**, 522-542.
49. Xia, Z., Chen, Y., Ellyin, F. (2000). A meso/micro-mechanical model for damage progression in glass-fiber/epoxy cross-ply laminates by finite-element analysis. *Composite Science and Technology*, **60**, 1171-1179.
50. Ellyin, F., Xia, Z., Chen, Y. (2002). Viscoelastic micromechanical modelling of free edge and time effects in glass fiber/epoxy cross-ply laminates. *Composites: Part A*, **33**, 399-409.
51. Bigelow, C. A. (1993). Thermal residual stresses in a silicon-carbide/titanium [0/90] laminate. *Journal of Composite Technology and Research*, **15**, 304-310.
52. Zhang, Y., Xia, Z., Ellyin, F. (2004). Evolution and influence of residual stresses/strains of fiber reinforced laminates. *Composites Science and Technology*, **64**, 1613-1621.
53. Achenbach, J. D., Zhu, H. (1989). Effect of interfacial zone on mechanical behaviour and failure of fibre-reinforced composites. *Journal of the Mechanics and Physics of Solids*, **37**, 381-393.

- 
54. Achenbach, J. D., Zhu, H. (1990). Effect of interphases on micro and macromechanical behaviour of hexagonal-array fibre composites. *ASME Journal of Applied Mechanics*, **57**, 956-963.
55. Zhu, H., Achenbach, J. D. (1991). Radial matrix cracking and interphase failure in transversely loaded fiber composites. *Mechanics of Materials*, **11**, 347-356.
56. Tvergaard, V. (1990). Analysis of tensile properties for a whisker-reinforced metal-matrix composite. *Acta Metallurgica*, **38**, 185-194.
57. Tvergaard, V. (1990). Effect of fibre debonding in a Whisker-reinforced metal, *Material Science and Engineering*, **A125**, 203-213.
58. Adams, D. F., Crane D. A. (1984). Finite element micromechanical analysis of a unidirectional composite including longitudinal shear loading. *Computers and Structures*, **18**, 1153-65.
59. Zhu, H., Sankar B.V., Marney R. V. (1998). Evaluation of failure criteria for fibre composites using single element micromechanics. *Journal of Composite Materials*, **32**, 766-782.
60. Aboudi, J. (1988). Micromechanical analysis of the strength of unidirectional fibre composites. *Composites Science and Technology*, **33**, 79-96.
61. Hashin, Z. (1991). The spherical inclusion with imperfect interface conditions. *ASME Journal of Applied Mechanics*, **58**, 444-449.
62. Hashin, Z. (2002). Thin interphase/imperfect interface in elasticity with application to coated fiber composites. *Journal of the Mechanics and Physics of Solids*, **50**, 2509-2537.

- 
63. Zhang, Y., Xia, Z., Ellyin, F. (2005). Nonlinear viscoelastic micromechanical analysis of fibre reinforced polymer laminates with damage evolution. *International Journal of Solids and structures*, **42**, 591-604.
64. Legarth, B. N. (2004). Unit cell debonding analyses for arbitrary orientation of plastic anisotropy. *International Journal of Solids and structures*, **41**, 7267-7285.
65. Jadhav, V. R., Sridharan, S. (2002). Micro-mechanical modelling of polymer based unidirectional composites: use of bulk properties of matrix with the smeared crack model. *Journal of Composite Materials*, **36**, 2735-2762.
66. Rots, J.G., Borst, R. D. (1989). Analysis of concrete fracture in “direct” tension. *International Journal of Solids and Structures*, **25**, 1381-1394.
67. Rots, J. G. (1991). Smeared and discrete representations of localized fracture. *International Journal of Fracture*, **51**, 45-59.
68. Aghdam, M. M., Pavier, M. J., Smith, D. J. (2001). Micro-mechanics of off-axis loading of metal matrix composites using finite element analysis. *International Journal of Solids and Structures*, **38**, 3905-3925.
69. Gao, Y. F., Bower, A. F., (2004). A simple technique for avoiding convergence problems in finite element simulations of crack nucleation and growth on cohesive interfaces. *Modelling and Simulation in Materials Science and Engineering*, **12**, 453-463.
70. Yang, Z. J., Proverbs, D. (2004). A comparative study of numerical solutions to non-linear discrete crack modelling of concrete beams involving sharp snap-back. *Engineering Fracture Mechanics*, **71**, 81-105.
71. Crisfield, M. A. (1981). A fast incremental/iteration solution procedure that handles

- 
- 'snap-through'. *Computers and Structures*, **13**, 55-62.
72. ANSYS User's Manual. (2002). Swanson Analysis System, Inc. Huston, PA, USA.
73. Xia, Z., Hu, Y., Ellyin, F. (2000). Mechanical behaviour of an epoxy resin under multiaxial loadings, part II: comparison of viscoelastic constitutive model predictions. *Polymers and Polymer Composites*, **8**, 157-166.
74. ADINA User's Manual. (1984). ADINA Engineering, Watertown, MA, USA.

## **CHAPTER 2**

### **FINITE ELEMENT ANALYSIS FOR PERIODIC COMPOSITES UNDER MULTIAXIAL LOADING**

#### **2.1 INTRODUCTION**

In the following Section 2.2, a micromechanical model of periodic fibrous composites under multi-axial loading conditions is presented. A unified, explicit form of periodic boundary conditions for a repeated unit cell (RUC) is proposed which satisfies the periodicity conditions and is suitable for any combination of multi-axial loads. The implementation of the boundary conditions into a finite element analysis scheme is described. It is shown that the traction continuity conditions across adjacent cells can be satisfied automatically through the FEA solution. A method to simplify the calculation of average stress and average strain over the RUC subjected to periodic boundary conditions is presented. It is proved that by using effective properties of a ‘homogenized’ media, the strain energy stored in the effective media is equivalent to the strain energy stored in the composite material. Finally through a 2-D example, it is shown that the periodic part of deformation can be retrieved after the solution of the RUC, although the periodic deformation is not explicitly presented in the proposed periodic boundary conditions. Another 2-D example shows that the proposed boundary conditions also apply to an asymmetric RUC.

Section 2.3 discusses the symmetries of a RUC. When a three dimensional unit cell exhibits planes or axes of symmetry, the micromechanical analysis with periodic boundary conditions can be performed on a reduced-size RUC and with standard boundary conditions on the plane of symmetry. However, the reduction of the RUC depends not only on the geometry and material of the RUC, but also on the loading applied to the RUC. For multiaxial loading cases, only for some loading combinations could symmetry conditions be exploited to reduce the RUC analysis and the procedure is usually complicated. In this chapter, for a unidirectional composite (UDC) under off-axis loading, from the symmetric conditions of geometry, material and loading, the boundary conditions for a one-quarter RUC are derived from the general periodic boundary conditions. The one-quarter RUC and the original full-size RUC under the periodic boundary conditions are solved and comparison of the results of the two RUCs verifies the proposed boundary conditions for the one-quarter model.

In Section 2.4, examples are provided to illustrate the validity and application of the proposed approach. Starting from a simple 2-D example, the results of the present method and those obtained by applying homogeneous boundary conditions are compared. The results clearly show that homogeneous boundary conditions are not only over constraints to the deformation of a periodic laminate, but also will violate the traction continuity conditions. In the second example, based on a three-dimensional RUC, it is shown that all the nine effective constants of an orthotropic unidirectional laminate can be predicted simultaneously by the present approach. The predicted results are in good agreement with

the experimental and theoretical results available in the literature.

## **2.2 PERIODIC BOUNDARY CONDITIONS OF A UNIT CELL**

### ***2.2.1 Unit Cell of Composite with Periodic Microstructure***

A composite with periodic reinforcement distributions can be envisioned as a structure generated by periodically repeating a unit cell in three directions [1-3]. In a real fibre composite, the fibre is usually straight in the axial direction, thus the fibre distribution in the cross-section determines the microstructure. Although in reality the fibre distribution may be quite random, assuming a perfectly periodic distribution will greatly reduce the complexity and cost of the analysis. In micromechanics of fibrous composites, the frequently used fibre array is square array or hexagonal array [4-7]. The unit cell is not uniquely defined as illustrated in Fig. 2-1 for the square fibre array. However, the effective behaviour of the composite computed from different unit cells should coincide since they generate the same microstructure [8-9]. The choice of the unit cell is often motivated by the differences in geometrical symmetries which can be used to simplify the numerical solution of the problem [8, 10-11]. In this thesis, the square array of fibre distribution is assumed, resulting in a repeated unit cell (RUC) in the shape of a cube. Note that the length of side  $d$  is the space between the centers of the neighbouring fibres, and in the fibre direction, an arbitrary length can be used. The volume fraction of a RUC is the volume fraction of the laminate.

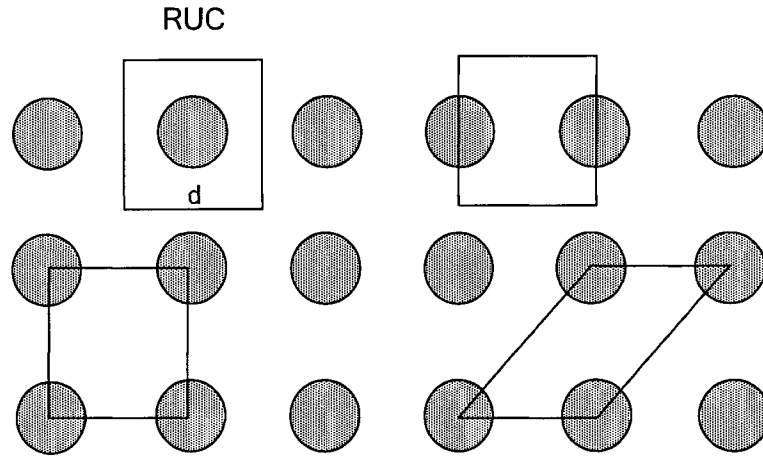


Fig. 2-1 Possible choice of unit cells of a unidirectional composite.

### 2.2.2 Formulation of the Problem

Consider a large sample of periodic inhomogeneous body (composite) as shown in Fig. 2-2. The body has two length scales, a global length scale,  $D$ , which is of the order of the size of the body, and a local length scale,  $d$ , which is proportional to the wavelength of the variation of the microstructure. The size of RUC is of the order of  $d$ , which is typically very small in comparison with the structural dimension  $D$ . Consequently,

$$\delta = \frac{d}{D} \ll 1 \quad (2.1)$$

Obviously, any function  $f$  in the body depends on two variables,  $X_i$  and  $x_i$ , and the relation between the *global coordinates*  $X_i$  for the body and the *local coordinates*  $x_i$  for the unit cell can then be written as

$$x_i = \frac{X_i}{\delta} \quad (2.2)$$

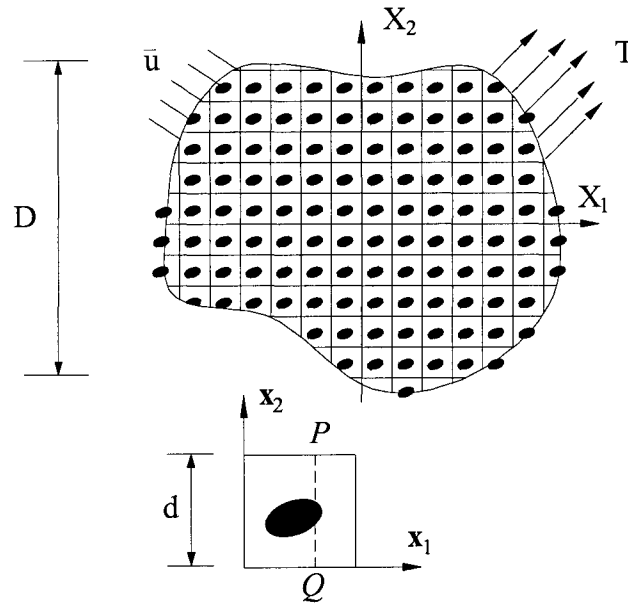


Fig. 2-2 RUC from a periodic composite.

At each macroscopic point,  $X_i$ , there is a RUC whose microstructure and properties can be repeated to construct the whole body. A small change on the global scale corresponds to a very large movement on the local scale. For small strain elasticity, the boundary value problem for the composite body can be defined as the following, from which the unknown field quantities, stress  $\sigma_{ij}$ , strain  $\varepsilon_{ij}$  and displacements  $u_i$  can be solved:

$$\sigma_{ij,j} = 0 \quad (2.3)$$

$$\sigma_{ij} = C_{ijkl} \varepsilon_{kl} \quad (2.4)$$

$$\varepsilon_{kl} = \frac{1}{2} (u_{k,l} + u_{l,k}) \quad (2.5)$$

$$\sigma_{ij} n_j = T_i \quad \text{on } \partial_\sigma, \quad u_i = \bar{u}_i \quad \text{on } \partial_u \quad (2.6)$$

The boundary value problem has the feature that  $C_{ijkl}$  varies very rapidly within a

short wavelength (order of  $d$ ) on the global length scale  $X_i$ , and therefore it is difficult to find a solution that solves the global problem and accounts for the local oscillation at the same time [6]. For example, in a FEM solution, assuming roughly each unit cell should have several hundred elements to accurately capture the large variations due to the heterogeneous nature of the microstructure, then for the whole composite laminate or a real composite structure, the elements needed will be increased by orders of magnitude. Hence, there is a motivation to seek a simplified solution.

### ***2.2.3 Unified Periodic Boundary Conditions***

The composite body can be envisioned as a periodical array of the RUCs. This implies that beyond a boundary layer of the composite body, each RUC in the composite has the same deformation mode and there is no separation or overlap between the neighbouring RUCs. That is, the stress and strain fields are periodic as the microstructure. Therefore it is adequate to obtain a solution based on the RUC, except for the boundary layer of the body [8].

Since the whole body and thus each unit cell is in balance, the equilibrium equation, Eqn.(2.3) and the relations in Eqns.(2.4-2.5) still apply in a RUC with volume  $V$ . However, the boundary conditions on the boundary of the RUC,  $\partial$ , should be properly determined. In the case of periodic media, the microscopic fields have to fulfill suitable periodicity conditions ensuring continuity of boundary displacements and tractions across adjacent cells.

For a periodic array, the displacement field can be expressed as [1]:

$$u_i(x_1, x_2, x_3) = \bar{\varepsilon}_{ij}x_j + u_i^*(x_1, x_2, x_3) \quad (2.7)$$

In the above,  $\bar{\varepsilon}_{ij}$  is the global strain tensor of the periodic structure and the first term on the right-hand side represents a linear distributed displacement field, which is true for homogeneous materials. The second term on the right-hand side is a periodic function from one RUC to another (it corresponds to the microscopic perturbation of the displacement field due to the heterogeneity of the microstructure [1], also see Eqn. 2.22 later). In addition, for a periodic RUC, the tractions on the opposite boundary surfaces should also meet the continuity condition, i.e.

$$\sigma_{ij}(P)n_j(P) = -\sigma_{ij}(Q)n_j(Q) \quad (2.8)$$

where  $P$  and  $Q$  are periodic points (with the same in-plane coordinates) on the two opposite boundary surfaces,  $\mathbf{n}$  is the unit outward normal vector to the surfaces, see Fig. 2-2. Thus for a RUC, Eqns. (2.3) – (2.5) and Eqns. (2-7)-(2.8) define the boundary value problem. This problem is well-posed as shown, for example, in Ref. [1].

The global (macroscopic) strain  $\bar{\varepsilon}_{ij}$  in Eqn. (2.7) and hence the global stress  $\bar{\sigma}_{ij}$  can be defined as the averages over the RUC volume  $V$ :

$$\bar{\sigma}_{ij} = \frac{1}{V} \int_V \sigma_{ij} dV \quad (2.9)$$

$$\bar{\varepsilon}_{ij} = \frac{1}{V} \int_V \varepsilon_{ij} dV \quad (2.10)$$

Imagine a homogenized media with the same volume  $V$  as that of the unit cell, upon applying a constant  $\bar{\varepsilon}_{ij}$  to this homogenized media, a uniform stress  $\bar{\sigma}_{ij}$  will be produced,

thus the strain energy in the volume is  $U = (1/2)\bar{\sigma}_{ij}\bar{\varepsilon}_{ij}V$ . On the other hand, the strain energy in a RUC is  $U' = \int_V (1/2)\sigma_{ij}\varepsilon_{ij}dV$ . It can be shown (see Section 2.2.4) that under periodic boundary conditions,

$$U' = U \quad (2.11)$$

Therefore for a homogenized media, effective material properties can be defined which describe the relation between  $\bar{\sigma}_{ij}$  and  $\bar{\varepsilon}_{ij}$ , and by doing so it ensures that for the same global loading  $\bar{\varepsilon}_{ij}$ , the strain energy of the homogenized media is the same as the strain energy of the heterogeneous media [1, 4, 12-13].

Generally,  $u_i^*(x_1, x_2, x_3)$  is unknown prior to the solution, therefore, Eqn. (2.7) is not convenient to apply in a commercial structure FEM code, and usually a FEA code should be modified [6, 14-15]. A more explicit form of periodic boundary conditions, suitable for the FEM analysis of RUC models can be derived from the above general expression.

For brevity, we start from a rectangular parallelepiped RUC as shown in Fig. 2-2, the displacements on a pair of opposite boundary surfaces whose normals are along the  $x_j$  axis are

$$u_i^{j+} = \bar{\varepsilon}_{ik}x_k^{j+} + u_i^* \quad (2.12)$$

$$u_i^{j-} = \bar{\varepsilon}_{ik}x_k^{j-} + u_i^* \quad (2.13)$$

where index “ $j+$ ” means along the positive  $x_j$  direction and “ $j-$ ” means along the negative  $x_j$  direction. The difference between the above two equations is

$$u_i^{j+} - u_i^{j-} = \bar{\varepsilon}_{ik}(x_k^{j+} - x_k^{j-}) = \bar{\varepsilon}_{ik}\Delta x_k^j. \quad (2.14)$$

For any parallelepiped RUC models  $\Delta x_k^j$  is constant, therefore the following unified periodic boundary conditions are obtained:

$$u_i^{j+}(x_1, x_2, x_3) - u_i^{j-}(x_1, x_2, x_3) = c_i^j \quad (i, j = 1, 2, 3) \quad (2.15)$$

The constants,  $c_1^1, c_2^2$  and  $c_3^3$ , represent the average stretch or contraction of the RUC model due to the action of the three normal traction components, whereas the other three pairs of constants,  $c_1^2, c_2^1$ ;  $c_1^3, c_3^1$  and  $c_2^3, c_3^2$ , correspond to the shear deformations due to the three shear traction components. This form of boundary conditions meets the requirement of displacement periodicity and continuity. It can be seen from Eqn. (2.15) that although the difference of the displacements for the corresponding points on the two opposite boundary surfaces are specified, the individual displacement component is still a function of the coordinates, i.e. a plane does not necessarily remain a plane after the deformation. Also since Eqn. (2.15) does not contain the periodic part of the displacement, which is unknown, it becomes easier to adopt this form in a finite element procedure, instead of applying Eqn. (2.7) directly as the boundary conditions. The application of Eqn (2.15) can be realized by the constraint equation options in many FEM codes, for example, ADINA [16], or ANSYS [17]. Examples can be seen in Ref. [15, 18-19].

In the later Section 2.2.5 we will show that when we apply Eqn. (2.15) to a RUC using a displacement based FEM procedure, the traction continuity condition in Eqn. (2.8) will be met automatically, therefore, in a finite element analysis, only Eqn. (2.15) needs to be applied.

### 2.2.4 Calculation of Average Stress and Strain

#### Calculation of average stress and strain

The calculation of average strain and stress defined in Eqns. (2.9) and (2.10) can be simplified. By using the Gauss' theorem, the average strain in the RUC can be expressed as an integral around the boundary surfaces [1, 4]

$$\bar{\varepsilon}_{ij} = \frac{1}{V} \int_V \varepsilon_{ij} dV = \frac{1}{2V} \int_S (u_i n_j + u_j n_i) dS. \quad (2.16)$$

Since all the boundary surfaces in Fig.2-2 are perpendicular to one of the coordinate axis, the unit normal vector  $\mathbf{n}$  has only one non-zero component on these surfaces with a value of unity. Therefore, using the symbols defined in Eqns. (2.12) and (2.13); the above integral can be reduced to

$$\begin{aligned} \bar{\varepsilon}_{ij} &= \frac{1}{2V} \left[ \int_{S_j} (u_i^{j+} - u_i^{j-}) n_j dS + \int_{S_i} (u_j^{i+} - u_j^{i-}) n_i dS \right] \\ &= \frac{1}{2V} (c_i^j S_j + c_j^i S_i) = \frac{c_i^j \Delta x_i \Delta x_k + c_j^i \Delta x_j \Delta x_k}{2 \Delta x_i \Delta x_j \Delta x_k} \end{aligned}$$

Therefore,

$$\bar{\varepsilon}_{ij} = \frac{1}{2} \frac{c_i^j \Delta x_i + c_j^i \Delta x_j}{\Delta x_i \Delta x_j} \quad (2.17)$$

Note that the suffixes  $i$  and  $j$  in the above expressions are not dummy suffixes.

Similarly, by using the Gauss' theorem and equilibrium equation  $\sigma_{ij,j} = 0$ , the average stress can be expressed as [2, 15]

$$\bar{\sigma}_{ij} = \frac{1}{V} \int_S \sigma_{ik} x_j n_k dS \quad (2.18)$$

Since the traction distributions at the boundaries must satisfy the periodicity condition expressed in Eqn. (2.8), the two corresponding points on the two opposite planes (with the

same in-plane coordinates) must have the same normal and shear stresses. By using the same argument as in the derivation of Eqn. (2.17), Eqn. (2.18) is reduced to

$$\bar{\sigma}_{ij} = \frac{1}{V} \int_S \sigma_{ik} x_j n_k dS = \frac{1}{V} \left( \int_{S_m^+} \sigma_{im}^+ x_j^+ dS - \int_{S_m^-} \sigma_{im}^- x_j^- dS \right) = \frac{1}{V} \int_{S_m^+} \sigma_{im}^+ (x_j^+ - x_j^-) dS$$

In the above the suffix  $m$  is a dummy suffix. However, when  $m \neq j$ , the coordinates  $x_j^+ = x_j^-$  and when  $m = j$ ,  $x_j^+ - x_j^- = \Delta x_j$ , therefore,

$$\bar{\sigma}_{ij} = \frac{\Delta x_j}{V} \int_{S_j} \sigma_{ij} dS = \frac{P_{ij}}{S_j} \quad (\text{no summation over } j) \quad (2.19)$$

The above equation indicates that the average stresses can be simply obtained from the ratio of resultant tractions on the boundary surfaces to the areas of the corresponding boundary surfaces.

### **Strain energy relations**

If the composite is homogenized with effective properties, the total strain energy stored in a volume  $V$  of the effective media is

$$U = \frac{1}{2} \bar{\sigma}_{ij} \bar{\varepsilon}_{ij} V \quad (2.20)$$

The strain energy in the heterogeneous RUC of the same volume is

$$U' = \frac{1}{2} \int_V \sigma_{ij} \varepsilon_{ij} dV \quad (2.21)$$

Since  $u_i = \bar{\varepsilon}_{ik} x_k + u_i^*$ , using the definition of strain, we have

$$\varepsilon_{ij} = \bar{\varepsilon}_{ij} + \frac{1}{2} \left( \frac{\partial u_i^*}{\partial x_j} + \frac{\partial u_j^*}{\partial x_i} \right) \quad (2.22)$$

Substituting Eqn. (2.22) into Eqn. (2.21), and noting  $\sigma_{ij}$  is a symmetric tensor, i.e.,

$\sigma_{ij} = \sigma_{ji}$ , we get

$$\begin{aligned}
U' &= \frac{1}{2} \int_V \sigma_{ij} (\bar{\varepsilon}_{ij} + \frac{1}{2} \frac{\partial u_i^*}{\partial x_j} + \frac{1}{2} \frac{\partial u_j^*}{\partial x_i}) dV \\
&= \frac{1}{2} \int_V \sigma_{ij} \bar{\varepsilon}_{ij} dV + \frac{1}{4} \int_V (\sigma_{ij} \frac{\partial u_i^*}{\partial x_j} + \sigma_{ji} \frac{\partial u_j^*}{\partial x_i}) dV \\
&= \frac{1}{2} \bar{\sigma}_{ij} \bar{\varepsilon}_{ij} V + \frac{1}{2} \int_V \sigma_{ij} \frac{\partial u_i^*}{\partial x_j} dV
\end{aligned} \tag{2.23}$$

Designating the second integral in the last step as  $I_2$ , Noting the equilibrium equation,  $\frac{\partial \sigma_{ij}}{\partial x_j} = 0$ , and using the Gauss' theorem, we reach

$$\begin{aligned}
2I_2 &= \int_V \frac{\partial}{\partial x_j} (\sigma_{ij} u_i^*) dV - \int_V \frac{\partial \sigma_{ij}}{\partial x_j} u_i^* dV \\
&= \int_S \sigma_{ij} u_i^* n_j dS
\end{aligned}$$

Where  $S$  is the boundary of the RUC volume  $V$ . For a periodic media,  $S$  can always be divided into two parallel parts,  $S^+$  and  $S^-$ ,  $S = S^+ \cap S^-$ . For two arbitrary corresponding points on  $S^+$  and  $S^-$ , we have: (1) the out normal vectors  $\mathbf{n}$  are opposite; (2)  $u_i^*$  is the same since it is the periodic part of displacement; and (3) traction  $\sigma_{ij} n_j$  are anti-periodic from Eqn. (2.8). Thus

$$\begin{aligned}
2I_2 &= \int_{S^+} \sigma_{ij}^+ u_i^* n_j^+ dS + \int_{S^-} \sigma_{ij}^- u_i^* n_j^- dS \\
&= \int_{S^+} \sigma_{ij}^+ n_j^+ (u_i^* - u_i^*) dS \\
&= 0
\end{aligned} \tag{2.24}$$

Therefore, from Eqn. (2.23) we conclude

$$U' = U \tag{2.25}$$

Thus we showed that *the strain energy stored in a heterogeneous RUC of volume  $V$  and that stored in an equivalent homogeneous media of volume  $V$  are equal if the two are*

subjected to the same periodic boundary conditions.

### 2.2.5 Implementation into a FEM Scheme and Examples

#### Periodic boundary conditions:

In a FEM scheme, the displacement constraint equations, Eqn. (2.15), can be imposed by Lagrange multipliers [20-21]. Lagrange's method of undetermined multipliers is used to find the maximum or minimum of a function whose variables are not independent but have some prescribed relations. In structural mechanics the function is potential energy  $\Pi$  and the variables are displacements in  $\{U\}$ . System unknowns become  $\{U\}$  and the Lagrange multipliers.

In a discrete (finite element) system, let  $[K]$ ,  $\{U\}$ , and  $\{F\}$  be the global stiffness matrix, displacement vector and nodal load vector, respectively, then the potential energy of the system is

$$\Pi = \frac{1}{2} \{U\}^T \{K\} \{U\} - \{U\}^T \{F\} \quad (2.26)$$

And the system of constraint equations can be written in a general matrix form as

$$[D]\{U\} - \{C\} = 0 \quad (2.27)$$

We are seeking a solution of  $\{U\}$  which minimizes  $\Pi$  under the constraints in Eqn. (2.27).

To this end, for each constraint equation in Eqn. (2.27), we introduce a Lagrange multiplier  $\lambda_i$ , thus for  $m$  independent constraint equations, we have

$$\{\lambda\}^T = \{\lambda_1, \lambda_2, \dots, \lambda_m\}^T \quad (2.28)$$

Multiplying the left-hand side of Eqn. (2.27) by Eqn. (2.28) and adding the result to Eqn.

(2.26), we obtain the modified potential energy function (Lagrangian) as

$$\Pi = \frac{1}{2} \{U\}^T \{K\} \{U\} - \{U\}^T \{F\} + \{\lambda\}^T ([D]\{U\} - [C]) \quad (2.29)$$

The stationary condition is

$$\begin{aligned} \frac{\partial \Pi}{\partial u_i} &= 0 \\ \frac{\partial \Pi}{\partial \lambda_i} &= 0 \end{aligned} \quad (2.30)$$

Thus from Eqn. (2.29) we get the system of equations for the finite element system [20-21]

$$\begin{bmatrix} K & D^T \\ D & 0 \end{bmatrix} \begin{Bmatrix} U \\ \lambda \end{Bmatrix} = \begin{Bmatrix} F \\ C \end{Bmatrix} \quad (2.31)$$

After the solution of  $\{U\}$  and  $\{\lambda\}$ , the nodal reactions can be obtained by

$$\{R\} = [K]\{U\} = \{F\} - [D]^T \{\lambda\} \quad (2.32)$$

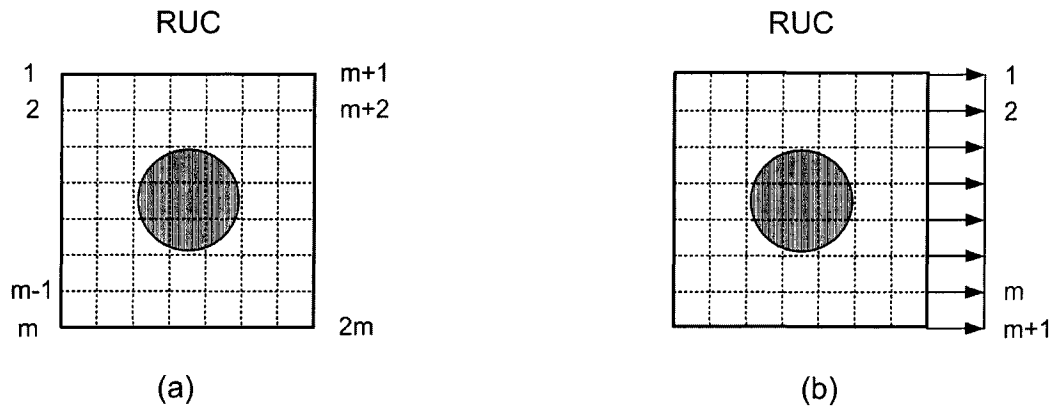


Fig. 2-3 Node labeling on the boundary:

(a) Periodic conditions; (b) Constrained plane.

Now let us regroup the  $n$  unknowns in  $\{U\}$  in the following manner (see Fig. 2-3a):

$$\{U\} = \begin{Bmatrix} U_1 \\ U_2 \\ U_3 \end{Bmatrix} = \begin{Bmatrix} \begin{pmatrix} u_1 \\ \vdots \\ u_m \end{pmatrix} \\ \begin{pmatrix} u_{m+1} \\ \vdots \\ u_{2m} \end{pmatrix} \\ \begin{pmatrix} u_{2m+1} \\ \vdots \\ u_n \end{pmatrix} \end{Bmatrix} \quad (2.33)$$

Where  $\{U_3\}$  is unconstrained degrees of freedom,  $\{U_1\}$  and  $\{U_2\}$  are constrained by the  $m$  constraint equations

$$[I \quad -I] \begin{Bmatrix} U_1 \\ U_2 \end{Bmatrix} = \{C\} \quad (2.34)$$

Where  $[I]$  is the  $m$ -th order identity matrix,  $\{C\}$  is determined from the  $c_i^j$  in Eqn. (2.15).

Thus Eqn. (2.34) is equivalent to Eqn. (2.15). And the nodal force vector is also regrouped correspondingly.

Using Eqn. (2.33) and Eqn. (2.34), the system equation, Eqn. (2.31) can be written in a partitioned matrix form

$$\begin{bmatrix} K_{11} & K_{12} & K_{13} & I \\ K_{12}^T & K_{22} & K_{23} & -I \\ K_{13}^T & K_{23}^T & K_{33} & 0 \\ I & -I & 0 & 0 \end{bmatrix} \begin{Bmatrix} U_1 \\ U_2 \\ U_3 \\ \lambda \end{Bmatrix} = \begin{Bmatrix} F_1 \\ F_2 \\ F_3 \\ C \end{Bmatrix} \quad (2.35)$$

If only constraint equations Eqn. (2.15), or Eqn. (2.34) are imposed,  $\{F_1\} = \{F_2\} = \{0\}$ , thus for two arbitrary corresponding nodes  $p$  and  $p+m$  on the boundary (see Fig. 2-3a), the reactions induced by the constraints are

$$\begin{cases} t_p = -\lambda_p \\ t_{p+m} = \lambda_p \end{cases} \quad \forall p \in \{1, \dots, m\} \quad (2.36)$$

Note if we only apply  $\lambda_i$  as the load to the original finite element system ( $\{F_1\} = \{F_2\} = \{0\}$ ), then

$$\begin{bmatrix} K_{11} & K_{12} & K_{13} \\ K_{12}^T & K_{22} & K_{23} \\ K_{13}^T & K_{23}^T & K_{33} \end{bmatrix} \begin{Bmatrix} U_1 \\ U_2 \\ U_3 \end{Bmatrix} = \begin{Bmatrix} \lambda \\ -\lambda \\ F_3 \end{Bmatrix} \quad (2.37)$$

will give the solution of displacement that satisfies the constraint equations [20]. In other words, if we (only) apply the displacement constraint equations,  $\lambda_i$  are the tractions on the corresponding boundary nodes, and they satisfy Eqn. (2.36).

Therefore it can be concluded *that in a finite element scheme, upon applying the displacement constraint equations (periodic displacement boundary conditions), Eqn. (2.15), the tractions at the corresponding nodes will be solved and the traction condition, Eqn. (2.8) will be satisfied automatically.*

To impose the displacement constraints, Eqn. (2.15) or (2.34), in FEM, it is a requirement to produce the same meshing at each paired boundary surfaces; this can always be done since the geometry of the RUC should satisfy the periodic conditions.

Some micromechanical analyses [1, 22] use  $u_i^*(x_1, x_2, x_3)$  as unknowns to be solved. In the present approach, although Eqn. (2.15) does not explicitly include the periodic part of the displacement  $u_i^*$ , their values can easily be retrieved after the solution, as shown in the illustrative example 1 in the following Section 2.2.6.

It can be seen that the above derivation does not assume a particular inclusion shape,

thus the boundary conditions also apply to any inclusion shapes. This also indicates that for an asymmetric RUC, the displacement boundary conditions will guarantee the traction continuity conditions (see illustrative example 2 in Section 2.2.6).

One can also see that the derivation and proof procedures for the proposed unified periodic boundary conditions are not dependent on the properties of the constituent materials of the composites. Therefore, they can be applied to nonlinear micromechanical analyses of the composites under any combination of multiaxial loads.

**Constrained plane:**

In the micromechanical analysis of a RUC, another type of boundary condition frequently encountered is the constrained plane. See, e.g., in [4, 6], or examples in the following Section 2.3. On this plane, the displacement components in the normal direction are coupled, while the resultant traction in the normal direction vanishes. Referring to Fig. 2-3b, on the right-hand side surface  $s$  of the square RUC, the boundary condition can be stated as:

$$u|_s = \delta \quad (2.38)$$

$$\int_s \sigma_{11} dS = 0 \quad (2.39)$$

Note that in a finite element analysis, only Eqn. (2.38) will be applied as constrained nodal displacement conditions, i.e., the normal displacements of all nodes in this boundary surface are equal to each other. The value of  $\delta$  is not specified when applying the boundary conditions, its value is to be determined by the solution. We will show that in the finite element analysis, upon applying Eqn. (2.38), Eqn. (2.39) will be satisfied automatically. If

the plane has  $m+1$  nodes, then Eqn. (2.38) can be equivalently expressed as  $m$  constraint equations (see Fig. 2-3b)

$$\begin{aligned} u_1 &= u_{m+1} \\ \cdots &= u_{m+1} \\ u_m &= u_{m+1} \end{aligned} \tag{2.40}$$

which in a matrix form is

$$[I \quad -J] \begin{Bmatrix} U_1 \\ U_2 \end{Bmatrix} = \{0\} \tag{2.41}$$

where  $[I]$  is  $m$ -th order identity matrix,  $[J] = \{1, 1, \dots, 1\}^T$  ( $m$  components), and

$$\begin{aligned} \{U_1\} &= \{u_1, u_2, \dots, u_m\}^T \\ \{U_2\} &= \{u_{m+1}\} \\ \{U_3\} &= \{u_{m+2}, \dots, u_n\}^T \text{ (unconstrained degrees of freedom)} \end{aligned} \tag{2.42}$$

Again, assuming the degrees of freedom of the system are labeled as

$$\{U\} = \begin{Bmatrix} U_1 \\ U_2 \\ U_3 \end{Bmatrix} \tag{2.43}$$

Hence, by introducing  $m$  Lagrange multipliers, the system of equations can be written in

the partitioned form

$$\begin{bmatrix} K_{11} & K_{12} & K_{13} & I \\ K_{12}^T & K_{22} & K_{23} & -J^T \\ K_{13}^T & K_{23}^T & K_{33} & 0 \\ I & -J & 0 & 0 \end{bmatrix} \begin{Bmatrix} U_1 \\ U_2 \\ U_3 \\ \lambda \end{Bmatrix} = \begin{Bmatrix} F_1 \\ F_2 \\ F_3 \\ 0 \end{Bmatrix} \tag{2.44}$$

Since  $\{F_1\} = \{F_2\} = \{F_3\} = \{0\}$ , the resultant reactions of d.o.fs.  $u_1, u_2, \dots, u_m$  are

$$\sum_m t_i = t_1 + \dots + t_m = -(\lambda_1 + \dots + \lambda_m) = -\sum_m \lambda_i \quad (2.45)$$

While the reaction of  $u_{m+1}$  is

$$t_{m+1} = \{J\}^T \{\lambda\} = \lambda_1 + \dots + \lambda_m = \sum_m \lambda_i \quad (2.46)$$

Thus the resultant traction on the plane

$$\int_S \sigma_{11} dS = \sum_m t_i + t_{m+1} = -\sum_m \lambda_i + \sum_m \lambda_i = 0 \quad (2.47)$$

And from Eqn. (2.19) we get the average stress in the RUC,  $\bar{\sigma}_{11} = 0$ . Applications of this type of boundary conditions will be shown in Section 2.3.

Finally, it should be noted that other approaches such as transformation and penalty functions can also be used to impose constraint equations on a FEM system [20, 23]. However, from the uniqueness of the solution (the proof of the uniqueness of the solution can be seen, e.g., in [21, 24]), the conclusions of this section hold for any approach.

### 2.2.6 Illustrative Examples

In the following, illustrative example 1 shows that the periodic displacement  $u_i^*$  can be easily retrieved from the FEM solution and example 2 shows that the present approach applies to an asymmetric RUC. For these two examples, the materials of the inclusion and matrix are assumed to be elastic and the material constants used are  $E_f = 72400 \text{ MPa}$ ,  $\nu_f = 0.22$  for inclusion and  $E_m = 2600 \text{ MPa}$ , and  $\nu_m = 0.4$  for matrix. And for simplicity, only two-dimensional RUCs are used.

### Example 1

Figure 2-4(a) shows a RUC for a unidirectional laminate of E-glass/epoxy composite based on square fibre array. The meshed model is established with four noded elements with 1632 elements and 1681 nodes. The volume fraction of the RUC is  $V_f=50\%$  and the side of the square (space between the centres of neighbouring fibres) is unity. The RUC under a general multiaxial loading (in-plane biaxial tension and shear) is solved. Note that for the square RUC shown in Fig. 2-4a,  $\Delta x_1 = \Delta x_2 = 1$ , therefore the constants in Eqn. (2-15) applied are:  $c_1^1=0.0012$ ,  $c_2^2=0.0016$ ,  $c_1^2 = c_2^1=0.0018$ .

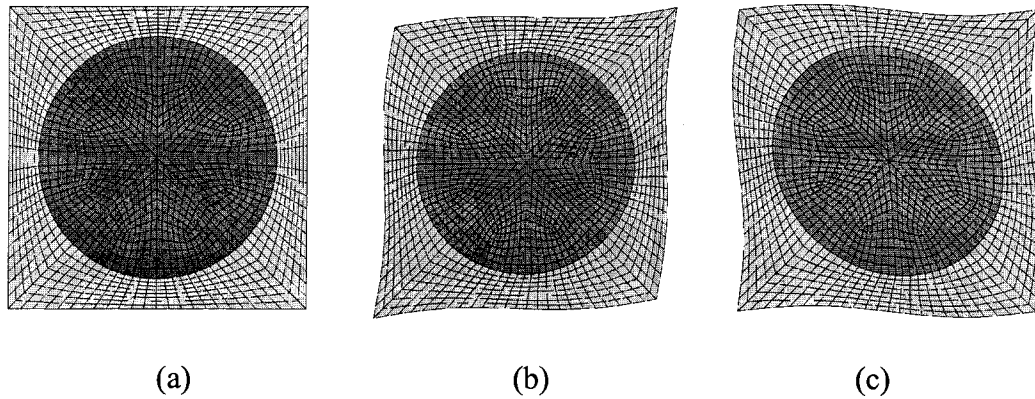


Fig. 2-4 Illustrative example 1: (a) Meshed RUC; (b) Total deformation;  
(c) Periodic part of deformation.

After the solution the displacement field in the RUC is known, thus from Eqn. (2.7)

$$u_i^*(x_1, x_2, x_3) = u_i(x_1, x_2, x_3) - \bar{\epsilon}_{ij}x_j \quad (2.48)$$

Figure 2-4(b) shows the exaggerated deformed shape and Fig. 2-4(c) shows the periodic part of the deformed shape. Note in this example, the origin of the coordinate system is at the centre of the square RUC.

**Example 2**

Figure 2-5 shows an asymmetric RUC with a rectangular inclusion. The problem with loading of  $c_1^1 = c_2^2 = 0$ ,  $c_1^2 = c_2^1 = 0.01$  (Note that  $\Delta x = \Delta y = 1$ ) is solved with a mesh of  $181 \times 181$  four noded elements.

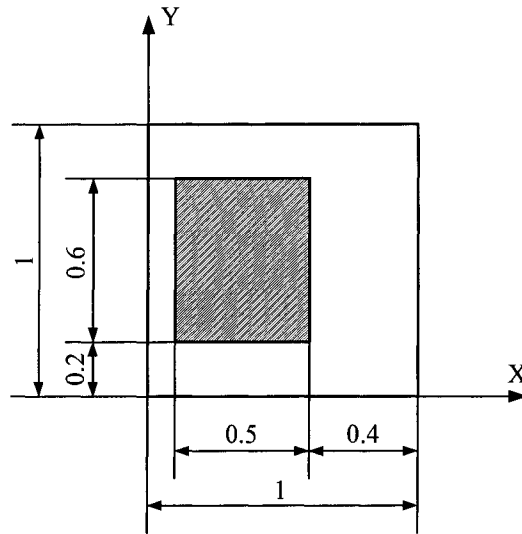


Fig. 2-5 Dimensions of an asymmetric RUC.

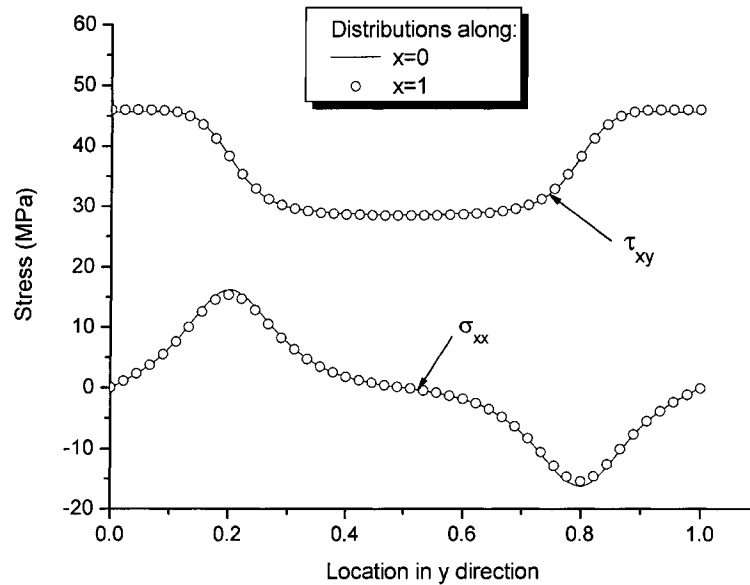


Fig. 2-6 Stress distributions at the two opposite sides of a RUC.

Fig. 2-6 plots the comparison of the distributions of the stress components at two opposite sides of the RUC. It clearly shows that even for asymmetric RUC, the stress continuity conditions are well satisfied.

## 2.3 SYMMETRY CONSIDERATIONS OF A SQUARE RUC

### 2.3.1 *General Procedure and Examples*

When a three dimensional parallelepiped unit cell exhibits a plane of symmetry, the micromechanical analysis with periodic boundary conditions can be reduced to a problem on half of the unit cell with standard boundary conditions on the plane of symmetry. And if the RUC has two or three symmetric planes, the analysis can further be reduced to one-quarter or one-eighth of the original RUC. However, the reduction of the RUC depends not only on the geometry and material of the RUC, but also on the loading applied to the RUC. For multiaxial loading cases, only for some loading cases could symmetry conditions be exploited to reduce the RUC analysis [10]. In this section, we discuss the application of the periodic boundary conditions described in Section 2.2 considering symmetry conditions. The general procedure is first illustrated by simple loading cases, then the consideration on off-axis loading (combined normal loading and shear loading) is described in detail.

In the following, we consider the unit cell  $V$  which is a rectangular parallelepiped delimited by planes  $x_i = \pm L_i$  ( $i = 1, 2, 3$ ). A Cartesian coordinate system can be

established with the origin being the geometric centre of the parallelepiped and the axis along the normal directions of the three orthogonal surfaces of the parallelepiped (see Fig. 2-7).

For RUC analysis, the periodic boundary condition is (Eqn. (2.7)),

$$u_i = \bar{\varepsilon}_{ik} x_k + u_i^*, \quad u_i^* \text{ periodic} \quad (2.49)$$

And the loading of the RUC can be viewed as applying the average strains,  $\bar{\varepsilon}_{ij}$ .

For the RUC with a plane of symmetry,  $x_2 = 0$ , Michel et al [8] showed the following stress and periodic displacement relations for two loading cases, viz.:

**Case 1:**

When the loading is

$$\{\bar{\varepsilon}\} = \{\bar{\varepsilon}_{11}, \bar{\varepsilon}_{22}, \bar{\varepsilon}_{33}, 0, 0, \bar{\varepsilon}_{31}\} \quad (2.50)$$

then

$$u_i^*(x_1, -x_2, x_3) = (-1)^{i+1} u_i^*(x_1, x_2, x_3) \quad (2.51a)$$

$$\sigma_{ij}(x_1, -x_2, x_3) = (-1)^{i+j} \sigma_{ij}(x_1, x_2, x_3) \quad (2.51b)$$

In this case the overall strain (loading)  $\{\bar{\varepsilon}\}$  is the superposition of arbitrary extensions along the three directions of the RUC and of arbitrary shear in the plane (31). Obviously, if only one component in Eqn. (2.50) is not zero, Eqns. (2.51a, b) still apply.

**Case 2:**

When

$$\{\bar{\varepsilon}\} = \{0, 0, 0, \bar{\varepsilon}_{12}, \bar{\varepsilon}_{23}, 0\} \quad (2.52)$$

then

$$u_i^*(x_1, -x_2, x_3) = (-1)^i u_i^*(x_1, x_2, x_3) \quad (2.53a)$$

$$\sigma_{ij}(x_1, -x_2, x_3) = (-1)^{i+j+1} \sigma_{ij}(x_1, x_2, x_3) \quad (2.53b)$$

In this second case the overall strain (loading)  $\{\bar{\epsilon}\}$  is the superposition of pure shears in the planes (12) and (23). Following are two examples showing the reduction of a RUC by using the above relations, Eqns. (2.50)-(2.53).

**Example 1—Extension in three directions:**

In this example, the loading is the combination of  $\bar{\epsilon}_{11}$ ,  $\bar{\epsilon}_{22}$  and  $\bar{\epsilon}_{33}$ . Thus from Eqn. (2-51), on planes  $x_2 = 0$  and  $x_2 = \pm L_2 / 2$  (we only consider the half of the RUC confined by  $x_2 = 0$ , and  $x_2 = L_2 / 2$  for brevity),

$$u_2^*(x_1, 0, x_3) = u_2^*(x_1, L_2 / 2, x_3) = 0 \quad (2.54a)$$

$$\sigma_{12}(x_1, 0, x_3) = \sigma_{12}(x_1, L_2 / 2, x_3) = 0 \quad (2.54b)$$

$$\sigma_{23}(x_1, 0, x_3) = \sigma_{23}(x_1, L_2 / 2, x_3) = 0 \quad (2.54c)$$

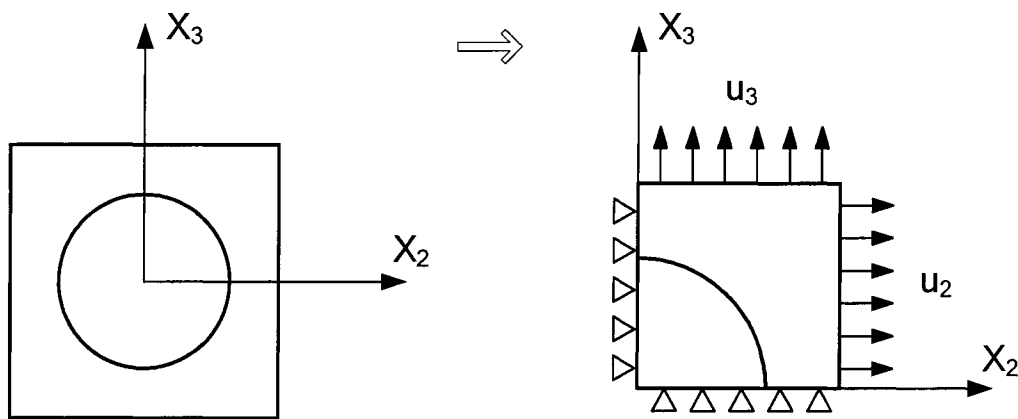


Fig. 2-7 Reduction of RUC under extensions in three directions.

Therefore, from Eqns (2-49) and (2.54), we obtain:

On plane  $x_2 = 0$ :

$$\begin{aligned} u_2 &= 0 \\ \sigma_{12} &= \sigma_{23} = 0 \end{aligned} \quad (2.55)$$

On plane  $x_2 = L_2 / 2$ :

$$\begin{aligned} u_2 &= \bar{\epsilon}_{22}(L_2 / 2) \\ \sigma_{12} &= \sigma_{23} = 0 \end{aligned} \quad (2.56)$$

Therefore, the problem can be solved on a half of the RUC under the above boundary conditions (The boundary conditions on other planes remain unchanged). Repeat the above procedure if the RUC has symmetric planes,  $x_1 = 0$  and  $x_3 = 0$ , we can conclude that the problem can be solved on 1/8 of the RUC using standard boundary conditions. Figure 2-7 shows in 2-D case for simplicity.

**Example 2—Combined shear:**

Now consider the case of combined shears  $\bar{\epsilon}_{12}$  and  $\bar{\epsilon}_{23}$ . The loading and reduction of the RUC is shown in Fig. 2-8. Note in this case, the RUC can only be reduced to one-half of the original size. On planes  $x_1 = \pm L_1 / 2$  and planes  $x_3 = \pm L_3 / 2$ , periodic boundary conditions remain unchanged, and the boundary conditions on planes  $x_2 = 0$  and  $x_2 = \pm L_2 / 2$  are:

On plane  $x_2 = 0$ :

$$\begin{cases} u_1 = 0 \\ u_3 = 0 \\ \sigma_{22} = 0 \end{cases} \quad (2.57)$$

On plane  $x_2 = \pm L_2 / 2$ :

$$\begin{cases} u_1 = \bar{\varepsilon}_{12}(L_2/2) \\ u_3 = \bar{\varepsilon}_{23}(L_2/2) \\ \sigma_{22} = 0 \end{cases} \quad (2.58)$$

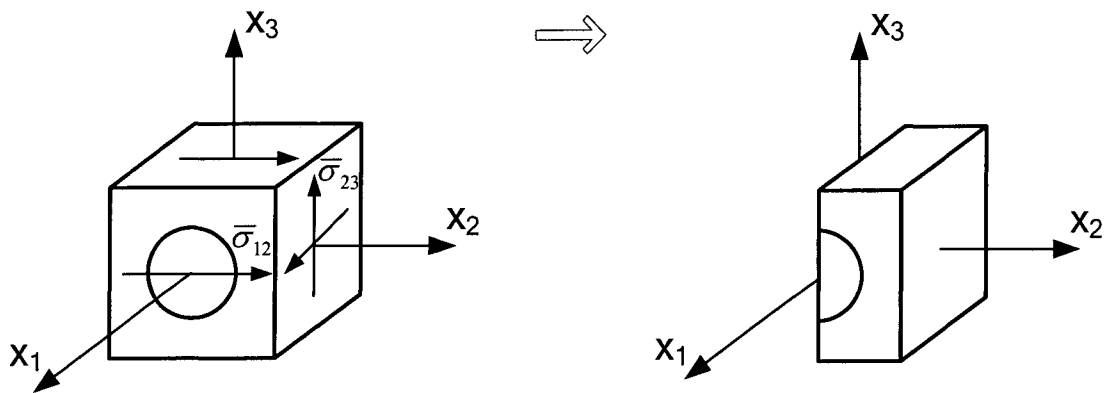


Fig. 2-8 Combined shear loading.

### 2.3.2 Off-axis Loading

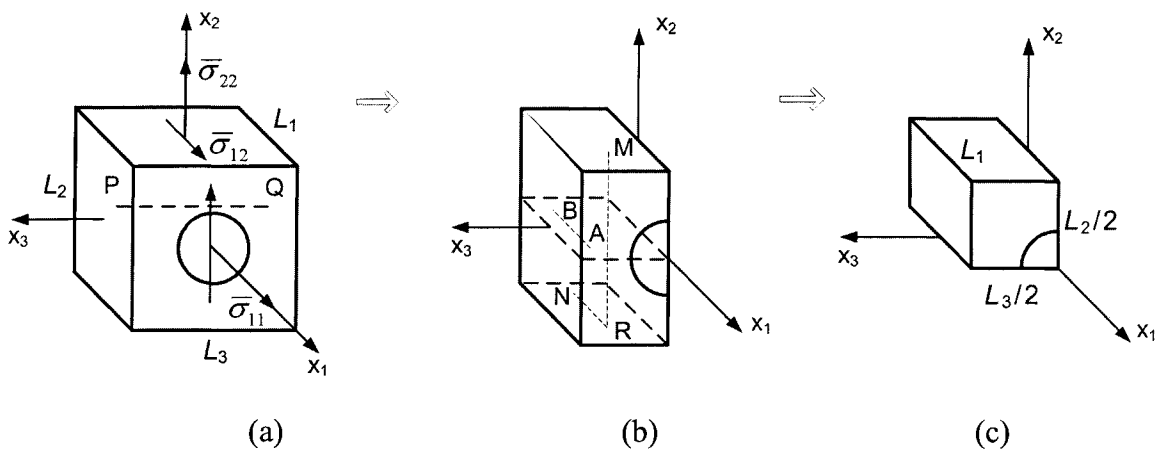


Fig. 2-9 Reduce to one-quarter of the RUC under off-axis loading.

For off-axis loading, the global stress and corresponding strain to be applied to a RUC are (see Chapter 3 and Chapter 4):

$$\{\bar{\sigma}\} = \{\bar{\sigma}_{11}, \bar{\sigma}_{22}, 0, \bar{\sigma}_{12}, 0, 0\}^T \quad (2.59)$$

$$\{\bar{\varepsilon}\} = \{\bar{\varepsilon}_{11}, \bar{\varepsilon}_{22}, \bar{\varepsilon}_{33}, \bar{\varepsilon}_{12}, 0, 0\}^T \quad (2.60)$$

Referring to Fig.2-9, the geometry, material and loading of the present problem has three symmetries, viz. (1) along  $x_1$  axis (fibre direction), the geometry, material, stress/strain, and periodic part of displacement are invariant. (2) a mirror symmetry about the plane  $x_3 = 0$ , and (3) a  $\pi$ -rotation symmetry about the  $x_3$  axis.

In a UDC, local stress  $\sigma_{ij}$ , strain  $\varepsilon_{ij}$ , and periodic part of the displacement is the perturbation of the microstructure, thus they are independent of  $x_1$ , from Eqn. (2.7), the general form of the displacement field can be written as:

$$u_1(x_1, x_2, x_3) = \bar{\varepsilon}_{11}x_1 + 2\bar{\varepsilon}_{12}x_2 + u_1^*(x_2, x_3) \quad (2.61)$$

$$u_2(x_1, x_2, x_3) = \bar{\varepsilon}_{22}x_2 + u_2^*(x_2, x_3) \quad (2.62)$$

$$u_3(x_1, x_2, x_3) = \bar{\varepsilon}_{33}x_3 + u_3^*(x_2, x_3) \quad (2.63)$$

Note a rigid body rotation about  $x_3$  axis,  $u_1 = \bar{\varepsilon}_{12}x_2$ ,  $u_2 = -\bar{\varepsilon}_{12}x_1$ , is added to the displacement field for simplification of the above equations. The stress, strain field will not be changed.

### **Reduce to one-half RUC**

For off-axis loading, Eqns. (2-59) and (2-60), the full-size RUC shown in Fig. 2-9(a)

has a mirror symmetry about plane  $x_3 = 0$ , thus the displacement and stress components of two arbitrary symmetric points satisfy:

$$u_3(x_1, x_2, x_3) = -u_3(x_1, x_2, -x_3) \quad (2.64)$$

$$\sigma_{23}(x_1, x_2, x_3) = -\sigma_{23}(x_1, x_2, -x_3) \quad (2.65)$$

$$\sigma_{31}(x_1, x_2, x_3) = -\sigma_{31}(x_1, x_2, -x_3) \quad (2.66)$$

And for other displacement or stress components:

$$u_i(x_1, x_2, x_3) = u_i(x_1, x_2, -x_3)$$

$$\sigma_{ij}(x_1, x_2, x_3) = \sigma_{ij}(x_1, x_2, -x_3)$$

1) From Eqns. (2.64)-(2.66), on plane  $x_3 = 0$ , we have

$$u_3 = 0, \sigma_{23} = \sigma_{31} = 0 \quad (2.67)$$

2) From Eqn. (2.63) and Eqn. (2.64), for an arbitrary point  $P$  on plane  $x_3 = L_3/2$  and its symmetric point  $Q$  on plane  $x_3 = -L_3/2$ ,

$$u_3(x_1, x_2, L_3/2) - u_3(x_1, x_2, -L_3/2) = \bar{\varepsilon}_{33}L_3$$

$$u_3(x_1, x_2, L_3/2) = -u_3(x_1, x_2, -L_3/2)$$

Therefore, we get

$$u_3(x_1, x_2, L_3/2) = \bar{\varepsilon}_{33}(L_3/2) \quad (2.68)$$

3) From Eqn. (2.65), we have

$$\sigma_{23}(x_1, x_2, L_3/2) = -\sigma_{23}(x_1, x_2, -L_3/2)$$

From the traction compatibility conditions, Eqn. (2.8), for two periodic points, we have

$$\sigma_{23}(x_1, x_2, L_3/2) = \sigma_{23}(x_1, x_2, -L_3/2)$$

Therefore,

$$\sigma_{23}(x_1, x_2, L_3/2) = 0 \quad (2.69)$$

Similarly,

$$\sigma_{31}(x_1, x_2, L_3/2) = 0 \quad (2.70)$$

Thus, under off-axis loading, the RUC shown in Fig. 2-9(a) can be equivalently solved based on the one-half RUC shown in Fig. 2-9(b). The boundary conditions apply to the planes  $x_3 = 0$  and  $x_3 = -L_3/2$  are determined by Eqns. (2.67)-(2.70).

### **Reduce to one-quarter RUC**

The RUC shown in Fig. 2-9(a) or Fig. 2-9(b) also has a  $\pi$ -rotation symmetry about  $x_3$  axis, thus the displacement and stress components of two arbitrary symmetric points meet:

$$u_1(x_1, x_2, x_3) = -u_1(-x_1, -x_2, x_3) \quad (2.71)$$

$$u_2(x_1, x_2, x_3) = -u_2(-x_1, -x_2, x_3) \quad (2.72)$$

$$\sigma_{23}(x_1, x_2, x_3) = -\sigma_{23}(-x_1, -x_2, x_3) \quad (2.73)$$

$$\sigma_{31}(x_1, x_2, x_3) = -\sigma_{31}(-x_1, -x_2, x_3) \quad (2.74)$$

And for other displacement or stress components:

$$u_i(x_1, x_2, x_3) = u_i(-x_1, -x_2, x_3)$$

$$\sigma_{ij}(x_1, x_2, x_3) = \sigma_{ij}(-x_1, -x_2, x_3)$$

1) For two arbitrary  $\pi$ -rotation symmetric points  $A$  and  $B$  on plane  $x_2 = 0$ :

From Eqn. (2.61), and note  $u_1^*$  is independent of  $x_1$ , thus

$$\begin{aligned} u_1(x_1, 0, x_3) - u_1(-x_1, 0, x_3) &= \bar{\varepsilon}_{11}x_1 - \bar{\varepsilon}_{11}(-x_1) + u_1^*(x_1, 0, x_3) - u_1^*(-x_1, 0, x_3) \\ &= 2\bar{\varepsilon}_{11}x_1 \end{aligned}$$

From Eqn. (2.71),

$$u_1(x_1, 0, x_3) = -u_1(-x_1, 0, x_3)$$

Thus from the above two relations, we obtain

$$u_1(x_1, 0, x_3) = \bar{\varepsilon}_{11}x_1 \quad (2.75)$$

Similarly,

$$u_2(x_1, 0, x_3) = 0 \quad (2.76)$$

From Eqn. (2.73),

$$\sigma_{23}(x_1, 0, x_3) = -\sigma_{23}(-x_1, 0, x_3)$$

But along  $x_1$  axis, the local stresses are invariant, thus,

$$\sigma_{23}(x_1, 0, x_3) = \sigma_{23}(-x_1, 0, x_3)$$

Therefore, the above two equations yield

$$\sigma_{23}(x_1, 0, x_3) = 0 \quad (2.77)$$

2) For two arbitrary  $\pi$ -rotation symmetric points  $M$  and  $N$  on planes  $x_2 = \pm L_2/2$ , and an auxiliary point  $R$ , Fig.2-9(b), note  $u_1^*$  of  $M, R$  satisfy periodic condition, and  $u_1^*$  of  $N, R$  are invariant along  $x_1$  axis, thus,

$$u_1^*(x_1, L_2/2, x_3) = u_1^*(-x_1, -L_2/2, x_3) = u_1^*(x_1, -L_2/2, x_3)$$

Therefore from Eqn. (2.61) we have

$$\begin{aligned} & u_1(x_1, L_2/2, x_3) - u_1(-x_1, -L_2/2, x_3) \\ &= \bar{\varepsilon}_{11}x_1 - \bar{\varepsilon}_{11}(-x_1) + 2\bar{\varepsilon}_{12}(L_2/2) - 2\bar{\varepsilon}_{12}(-L_2/2) + u_1^*(x_1, L_2/2, x_3) - u_1^*(-x_1, -L_2/2, x_3) \\ &= 2\bar{\varepsilon}_{11}x_1 + 2\bar{\varepsilon}_{12}L_2 + u_1^*(x_1, -L_2/2, x_3) - u_1^*(-x_1, -L_2/2, x_3) \\ &= 2\bar{\varepsilon}_{11}x_1 + 2\bar{\varepsilon}_{12}L_2 \end{aligned}$$

From Eqn. (2.71),

$$u_1(x_1, L_2/2, x_3) = -u_1(-x_1, -L_2/2, x_3)$$

Thus from the above two relations we have

$$u_1(x_1, L_2/2, x_3) = \bar{\epsilon}_{11}x_1 + 2\bar{\epsilon}_{12}(L_2/2) \quad (2.78)$$

Similarly, for  $u_2$ , we have

$$u_2(x_1, L_2/2, x_3) = \bar{\epsilon}_{22}(L_2/2) \quad (2.79)$$

3) From Eqn. (2.73),

$$\sigma_{23}(x_1, L_2/2, x_3) = -\sigma_{23}(-x_1, -L_2/2, x_3)$$

Consider the three points  $M$ ,  $N$  and  $R$  in Fig. 2-9(b), note  $\sigma_{23}$  of  $M$ ,  $R$  should satisfy the traction continuity conditions, Eqn. (2.8). And  $\sigma_{23}$  of  $N$ ,  $R$  are invariant along  $x_1$  axis, thus,

$$\sigma_{23}(x_1, L_2/2, x_3) = \sigma_{23}(x_1, -L_2/2, x_3) = \sigma_{23}(-x_1, -L_2/2, x_3)$$

From the above two equations, we have

$$\sigma_{23}(x_1, L_2/2, x_3) = 0 \quad (2.80)$$

*The periodic boundary conditions applied to one-quarter RUC (Fig. 2-9c) for off-axis loading are summarized as:*

On planes  $x_1 = \pm L_1/2$ :

$$\begin{cases} u_1(L_1/2, x_2, x_3) - u_1(-L_1/2, x_2, x_3) = \bar{\epsilon}_{11}L_1 \\ u_2(L_1/2, x_2, x_3) - u_2(-L_1/2, x_2, x_3) = 0 \\ u_3(L_1/2, x_2, x_3) - u_3(-L_1/2, x_2, x_3) = 0 \end{cases} \quad (2.81)$$

On plane  $x_2 = 0$ :

$$\begin{cases} u_1(x_1, 0, x_3) = \bar{\epsilon}_{11}x_1 \\ u_2(x_1, 0, x_3) = 0 \\ \sigma_{23}(x_1, 0, x_3) = 0 \end{cases} \quad (2.82)$$

On plane  $x_2 = L_2 / 2$ :

$$\begin{cases} u_1(x_1, L_2 / 2, x_3) = \bar{\varepsilon}_{11} x_1 + 2\bar{\varepsilon}_{12}(L_2 / 2) \\ u_2(x_1, L_2 / 2, x_3) = \bar{\varepsilon}_{22}(L_2 / 2) \\ \sigma_{23}(x_1, L_2 / 2, x_3) = 0 \end{cases} \quad (2.83)$$

On plane  $x_3 = 0$ :

$$\begin{cases} u_3(x_1, x_2, 0) = 0 \\ \sigma_{23}(x_1, x_2, 0) = 0 \\ \sigma_{31}(x_1, x_2, 0) = 0 \end{cases} \quad (2.84)$$

On plane  $x_3 = L_3 / 2$ :

$$\begin{cases} u_3(x_1, x_2, L_3 / 2) = \delta_{33}, \text{ so } \int_{x_3=L_3/2} \sigma_{33} dS = 0 \\ \sigma_{23}(x_1, x_2, L_3 / 2) = 0 \\ \sigma_{31}(x_1, x_2, L_3 / 2) = 0 \end{cases} \quad (2.85)$$

Note that in the  $x_3$  direction, the constant  $\delta_{33}$  in Eqn. (2.85a) is not specified, thus from Section 2.2.4, it ensures that on the plane  $x_3 = L_3 / 2$ , the total normal traction vanishes,

$$\int \sigma_{33} dS = 0$$

Therefore, from Eqn. (2.19), the global stress component (average over the RUC)  $\bar{\sigma}_{33} = 0$ .

### Verification

To verify the above boundary conditions for the one-quarter RUC, a full-size RUC (model A) and a reduced-size RUC (model B) are developed as shown in Fig. 2-10(a) and (b), respectively. Both models are meshed with 8 node brick element with model A has 4592 elements and 7059 nodes and model B has 574 elements and 1226 nodes. The

materials constants used are  $E_f=72400$  MPa,  $\nu_f=0.22$  for inclusion and  $E_m=2600$  MPa, and  $\nu_m=0.4$  for matrix. The verification analysis is performed using ANSYS.

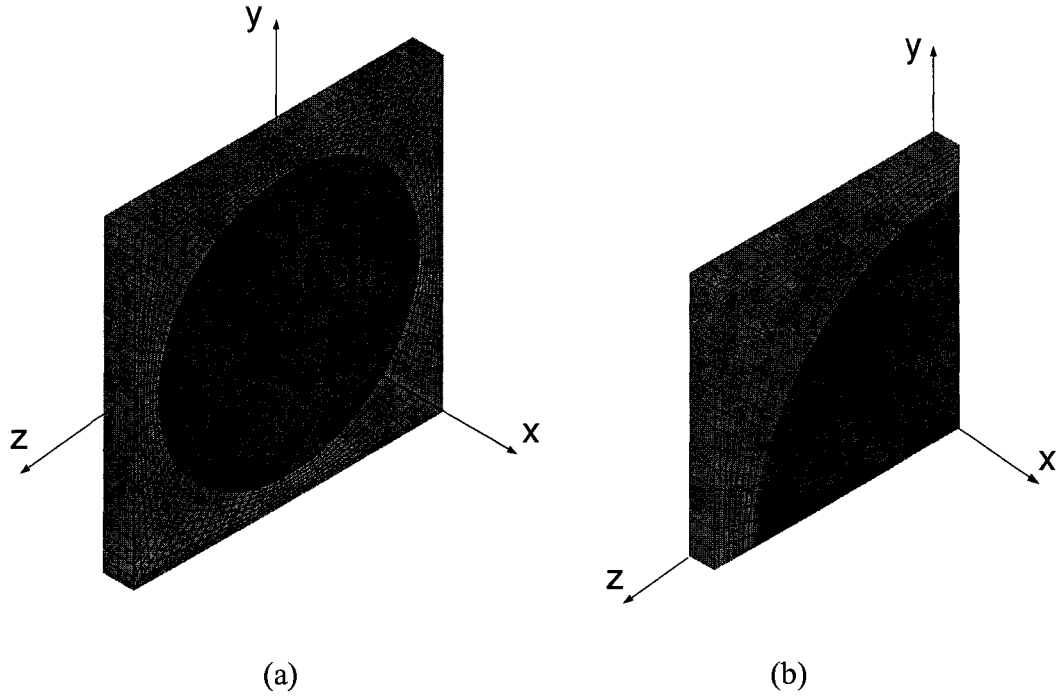


Fig. 2-10 Verification models *A* and *B*:

(a) Full-size RUC; (b) One-quarter RUC.

If the proposed boundary conditions for the RUC model are correct, then the two meshes should produce the same stress/strain field. Note that mesh *A* has two layers of element while *B* has only one layer, this is to verify that in the fibre direction only one layer of element is enough. An arbitrary loading is:

$$\begin{aligned} \{\bar{\varepsilon}\} &= \{\bar{\varepsilon}_{xx}, \bar{\varepsilon}_{yy}, \bar{\varepsilon}_{zz}, \bar{\varepsilon}_{xy}, 0, 0\}^T = \{0.005, 0.01, \bar{\varepsilon}_{zz}, 0.01, 0, 0\}^T \\ \bar{\sigma}_{zz} &= (1/V) \int_V \sigma_{zz} dV = 0 \end{aligned} \quad (2.86)$$

For model *A*, the boundary conditions are from Eqn. (2.15), and for model *B*, the boundary conditions are from Eqns. (2.81-2.85).

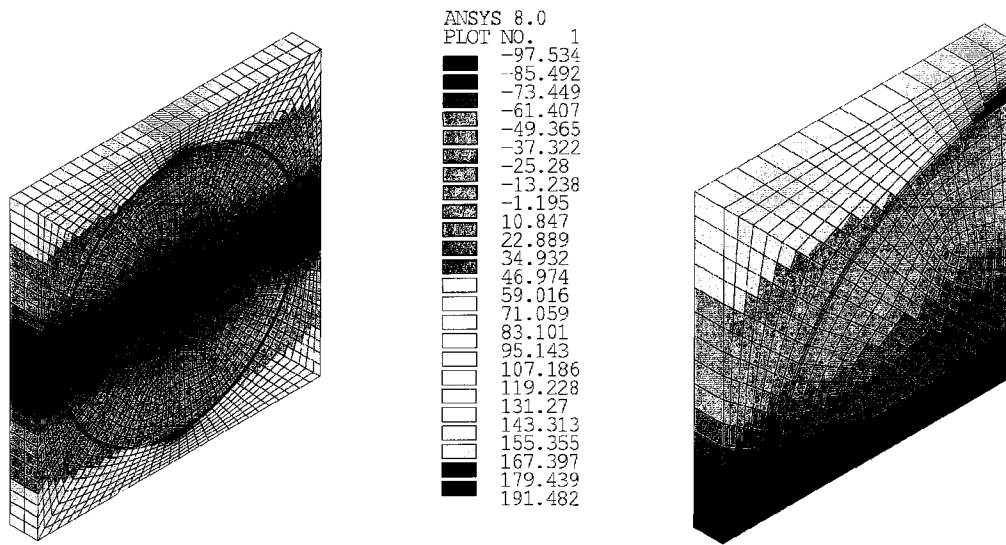
Figure 2-11 shows, for example, the distributions of stress components  $\sigma_{zz}$  and  $\sigma_{xy}$  of the two models. It can be seen from the figure that the distributions of the stress components have two features. Firstly, for both the full size RUC and the reduced size RUC, the distributions of the stress are invariant along the fibre direction ( $x$  direction). Secondly, the distribution in the one-quarter RUC is identical to the distribution in the upper-left quarter (with positive  $x, y, z$  coordinates) of the full RUC. Other stress components have similar results except for stresses  $\sigma_{xz}$  and  $\sigma_{yz}$ , which distribute in the full RUC anti-symmetrically about planes  $y = 0$  and  $z = 0$ . However, in fibre direction, all the six stress components are invariant.

From Fig. 2-11 a it is observed that in the RUC,  $\sigma_{zz}$  is usually not zero, and on the left surface of the RUC (plane  $z = 1$ ), the distribution of  $\sigma_{zz}$  is not uniformly zero. However, from the numerical results, the total normal traction can be calculated from the distribution of  $\sigma_{zz}$ . The numerical result is

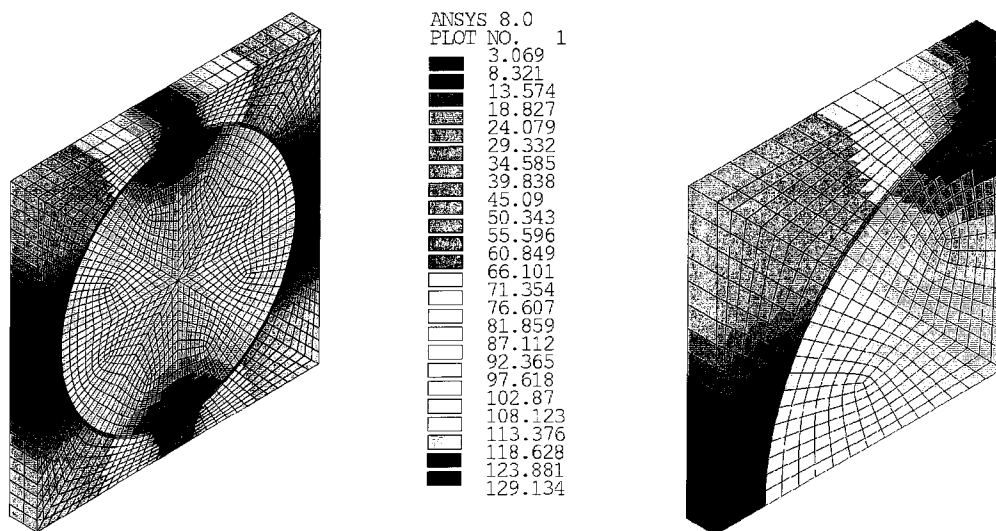
$$\int_{z=1} \sigma_{zz} dS = 0.767386 \times 10^{-12} \approx 0 \quad \text{for full RUC}$$

$$\int_{z=1} \sigma_{zz} dS = 0.280886 \times 10^{-13} \approx 0 \quad \text{for quarter RUC}$$

And therefore the average stress  $\bar{\sigma}_{zz}$  in the RUC is zero.



(a) Distribution of  $\sigma_{zz}$  in the full RUC and quarter RUC



(b) Distribution of  $\sigma_{xy}$  in the full RUC and one-quarter RUC

(c)

Fig. 2-11 Comparison of the distributions of stress.

Table 2-1 lists all the six stress components at arbitrarily selected locations in the full and reduced models. The locations of the selected points are shown in Fig. 2-12 for the one-quarter model. For the full-size model, the corresponding locations in the upper-left quarter are used. Note in the list, for each point, the values in the first line are of the full RUC model, and those in the second line are the values from the one-quarter RUC.

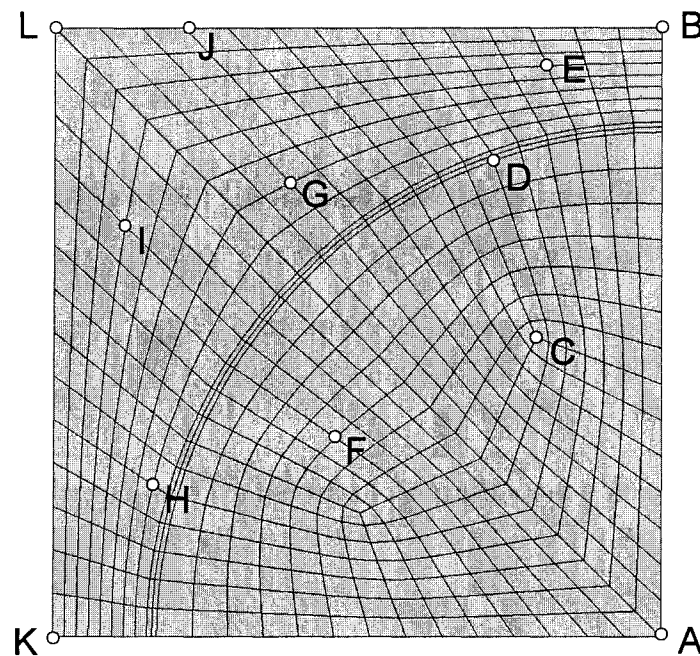


**Fig. 2-12 Selected points for comparison.**

It can be seen from Table 2-1 that the stress values of the two models are identical except at the edge points  $A$ ,  $B$  and  $K$ . From Eqns (2.67), (2.69) and (2.70), the stress components  $\sigma_{yz}$  and  $\sigma_{xz}$  should be zeroes at points  $A$ ,  $B$  and  $K$ , however, in a FEM solution, usually only small numbers will be obtained instead of exact zeroes. From Table 2-1, it is seen that at points  $A$ ,  $B$  and  $K$ , the stress components  $\sigma_{yz}$  and  $\sigma_{xz}$  are very small

Table 2-1 Stress at arbitrarily selected locations

POINT	$\sigma_{xx}$	$\sigma_{yy}$	$\sigma_{zz}$	$\sigma_{xy}$	$\sigma_{yz}$	$\sigma_{xz}$
A	0.401643E+03	0.245522E+03	-0.653280E+02	0.981944E+02	0.509077E-09	0.119458E-08
	0.401643E+03	0.245522E+03	-0.653280E+02	0.981944E+02	-0.277047E-01	-0.183932E-01
B	0.187939E+03	0.302619E+03	0.124104E+03	0.118610E+03	0.301497E-08	0.538535E-09
	0.187939E+03	0.302619E+03	0.124104E+03	0.118610E+03	-0.134164E+00	0.582990E-01
C	0.409201E+03	0.239566E+03	-0.250169E+02	0.105387E+03	-0.805735E+01	-0.759562E+01
	0.409201E+03	0.239566E+03	-0.250169E+02	0.105387E+03	-0.805735E+01	-0.759562E+01
D*	0.287211E+03	0.240142E+03	0.652202E+02	0.107342E+03	-0.331590E+02	-0.531365E+01
	0.287211E+03	0.240142E+03	0.652202E+02	0.107342E+03	-0.331590E+02	-0.531365E+01
E	0.168272E+03	0.262202E+03	0.115353E+03	0.106542E+03	-0.389891E+01	0.480952E+01
	0.168272E+03	0.262202E+03	0.115353E+03	0.106542E+03	-0.389891E+01	0.480952E+01
F	0.394990E+03	0.187219E+03	-0.372659E+02	0.915169E+02	0.182981E+01	-0.120590E+02
	0.394990E+03	0.187219E+03	-0.372659E+02	0.915169E+02	0.182981E+01	-0.120590E+02
G	0.883278E+02	0.129883E+03	0.478118E+02	0.518074E+02	-0.352341E+01	0.202419E+02
	0.883278E+02	0.129883E+03	0.478118E+02	0.518074E+02	-0.352341E+01	0.202419E+02
H	0.426640E+01	0.253313E+02	-0.577903E+02	0.794953E+01	0.290810E+02	0.692185E+01
	0.426640E+01	0.253313E+02	-0.577903E+02	0.794953E+01	0.290810E+02	0.692185E+01
I	0.642034E+02	0.731787E+02	0.442048E+02	0.360217E+02	0.357595E+01	0.641149E+01
	0.642034E+02	0.731787E+02	0.442048E+02	0.360217E+02	0.357595E+01	0.641149E+01
J	0.853789E+02	0.889280E+02	0.813942E+02	0.495667E+02	-0.243899E+00	-0.131148E+00
	0.853789E+02	0.889280E+02	0.813942E+02	0.495667E+02	-0.243899E+00	-0.131148E+00
K	-0.170655E+02	0.116897E+02	-0.974785E+02	0.531061E+01	-0.226460E-08	0.219814E-10
	-0.170655E+02	0.116897E+02	-0.974785E+02	0.531061E+01	0.199569E+00	0.179554E-02
L	0.770590E+02	0.704296E+02	0.790930E+02	0.444523E+02	0.109666E-01	0.680411E-01
	0.770590E+02	0.704296E+02	0.790930E+02	0.444523E+02	0.109666E-01	0.680411E-01

\* Interface node, the values are average values of that in the fibre and matrix.

comparing to the other stress components for both the full model and the quarter-size model. On the other hand, for the full size model, the stress values at the points  $A$ ,  $B$  and  $K$  (nodes) are the averages from all the elements which contain the corresponding node, therefore a very small value is obtained since the stress  $\sigma_{yz}$  and  $\sigma_{xz}$  are anti-symmetric. Furthermore, for the quarter-size model, the stress  $\sigma_{yz}$  and  $\sigma_{xz}$  will approach to very small values with a finer mesh.

Therefore this example validates the proposed boundary conditions for the one-quarter RUC under off-axis loading.

### 2.3.3 Generalized Plane Strain Conditions

As shown in Fig. 2-13, assume  $x_1$  direction is the fibre direction, and the applied load is  $\bar{\epsilon}_{11}$ ,  $\bar{\epsilon}_{22}$ ,  $\bar{\epsilon}_{33}$  and  $\bar{\epsilon}_{23}$  (no out of plane shear). Since all the stresses and strains are independent of  $x_1$ , thus from Eqn. (2-7),

$$u_1(x_1, x_2, x_3) = \bar{\epsilon}_{11}x_1 + u_1^*(x_2, x_3) \quad (2.87)$$

$$u_2(x_1, x_2, x_3) = \bar{\epsilon}_{22}x_2 + \bar{\epsilon}_{23}x_3 + u_2^*(x_2, x_3) \quad (2.88)$$

$$u_3(x_1, x_2, x_3) = \bar{\epsilon}_{23}x_2 + \bar{\epsilon}_{33}x_3 + u_3^*(x_2, x_3) \quad (2.89)$$

Assuming the laminate is very long in  $x_1$  direction, thus for the RUC delimited by planes  $x_1 = \pm L_1$ , plane  $x_1 = 0$  is a plane of symmetry. From Eqn. (2.51a),

$$u_1^*(0, x_2, x_3) = u_1^*(\pm L_1/2, x_2, x_3) = 0 \quad (2.90)$$

Note  $u_1^*$  is invariant along  $x_1$ , thus  $u_1^*(x_1, x_2, x_3) = 0$ . Therefore on an arbitrary plane

$x_1 = \text{const}$ , we have

$$u_1 = \bar{\varepsilon}_{11} x_1 \quad (2.91)$$

and

$$u_2 = u_1(x_2, x_3), \quad u_3 = u_3(x_2, x_3) \quad (2.92)$$

Therefore Eqn. (2.91) and Eqn. (2.92) define a generalized plane strain problem. In *plane strain* conditions, usually the stress in  $x_1$  direction  $\sigma_{11} \neq 0$ , consequently  $\int_{x_1=\text{const}} \sigma_{11} dS \neq 0$ . However, for *generalized plane strain* case, proper boundary conditions can be applied to ensure that  $\int_{x_1=\text{const}} \sigma_{11} dS = 0$ , hence the global stress component in  $x_1$  direction vanishes, i.e.  $\bar{\sigma}_{11} = 0$ . For a unidirectional laminate under loadings in the transverse plane, there is no global stress at the ends in the  $x_1$  direction, thus generalized plane strain condition may be closer to the real case.

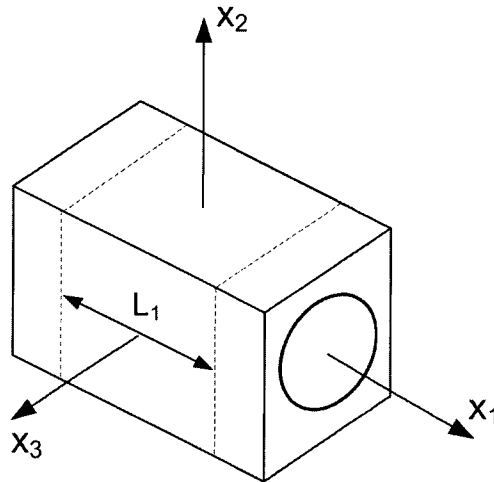


Fig. 2-13 Generalized plane strain.

From the above discussions, under in plane loadings

$$\{\bar{\sigma}\} = \{0, \bar{\sigma}_{22}, \bar{\sigma}_{33}, 0, 0, \bar{\sigma}_{23}\}^T \quad (2.93)$$

$$\{\bar{\varepsilon}\} = \{\bar{\varepsilon}_{11}, \bar{\varepsilon}_{22}, \bar{\varepsilon}_{33}, 0, 0, \bar{\varepsilon}_{23}\}^T \quad (2.94)$$

The problem can be solved on the RUC which is a segment of arbitrary thickness in  $x_1$  direction with the boundary conditions as the following:

On planes  $x_1 = 0$   $x_1 = L_1/2$ :

$$\begin{aligned} u_1(0, x_2, x_3) &= 0 \\ u_1(L_1/2, x_2, x_3) &= \delta_{11} \quad \text{so} \quad \int \sigma_{11} dS = 0 \\ \sigma_{12} &= \sigma_{13} = 0 \end{aligned} \quad (2.95)$$

On planes  $x_2 = \pm L_2/2$ :

$$\begin{aligned} u_2(x_2 = L_2/2) - u_2(x_2 = -L_2/2) &= \bar{\varepsilon}_{22} L_2 \\ u_3(x_2 = L_2/2) - u_3(x_2 = -L_2/2) &= \bar{\varepsilon}_{23} L_2 \\ \sigma_{21} &= 0 \end{aligned} \quad (2.96)$$

On planes  $x_3 = \pm L_3/2$ :

$$\begin{aligned} u_2(x_3 = L_3/2) - u_2(x_3 = -L_3/2) &= \bar{\varepsilon}_{23} L_3 \\ u_3(x_3 = L_3/2) - u_3(x_3 = -L_3/2) &= \bar{\varepsilon}_{33} L_3 \\ \sigma_{31} &= 0 \end{aligned} \quad (2.97)$$

## 2.4 ILLUSTRATIVE EXAMPLES OF MICROMECHANICAL ANALYSIS

In this section, two examples are provided to show the application and validity of the proposed finite element modeling procedure. For simplicity, all the material constituents are assumed to be elastic and the interface between the inclusion (fibre) and matrix are assumed to be perfectly bonded.

### 2.4.1 Example 1

This example compares the unified boundary conditions, Eqn. (2-15), with the “homogeneous boundary conditions” (or plane-remains-plane boundary conditions) [2]. The 2-D model consists of a rectangular reinforcement with a volume fraction of 50%, Fig. 2-14. The elastic moduli and the Poisson’s ratio for the fibre and matrix are  $E_f=72400$  MPa,  $\nu_f=0.22$  for inclusion and  $E_m=2600$  MPa, and  $\nu_m=0.4$  for matrix. For a pure shear deformation mode we apply the following two different sets of boundary conditions to the RUC model:

(a) Periodic boundary conditions, Eqn. (2.15):

$$\begin{aligned} u_{AB} - u_{EF} &= 0, & v_{AB} - v_{EF} &= 0.0018 \\ u_{AE} - u_{BF} &= 0.0018, & v_{AE} - v_{BF} &= 0 \end{aligned} \quad (2.98)$$

$$u_F = v_F = 0 \quad (\text{to eliminate the rigid body motion})$$

where  $u$  and  $v$  are displacement components along  $X$  and  $Y$ , respectively.

(b) Homogeneous boundary conditions:

The following homogeneous boundary conditions were suggested in Ref. [2] to be applied to the boundary surface  $S$  of a repeated unit cell  $V$ :

$$u_i(S) = \bar{\varepsilon}_{ij} x_j \quad (2.99)$$

where  $\bar{\varepsilon}_{ij}$  is the average strain.

For the current example, the above equation reduces to:

$$\begin{aligned} u_{AB} &= 0.0018 y_{AB}, & u_{EF} &= 0.0018 y_{EF} \\ v_{AB} &= 0.0018 x_{AB} = 0.0018, & v_{EF} &= 0.0018 x_{EF} = 0 \\ u_{AE} &= 0.0018 y_{AE} = 0.0018, & u_{BF} &= 0.0018 y_{BF} = 0 \\ v_{AE} &= 0.0018 x_{AE}, & v_{BF} &= 0.0018 x_{BF} \end{aligned} \quad (2.100)$$

Note that the origin of the coordinate system is set at the point  $F$  of the square RUC and the above boundary conditions specify that all displacement components are linearly distributed at the boundaries, i.e. a plane-remains-plane.

### Finite element analysis results

**Case (a):** The deformed shape for this case is shown in the Fig. 2-14(a). One notes that the boundaries do not remain plane after the deformation. The resultant tractions at the boundaries are:

$$\text{At } AE \text{ and } BF : N_{yx} = \pm 6.4831, N_{yy} = 0; \quad \text{at } AB \text{ and } EF: N_{xx} = 0, N_{xy} = \pm 6.4831$$

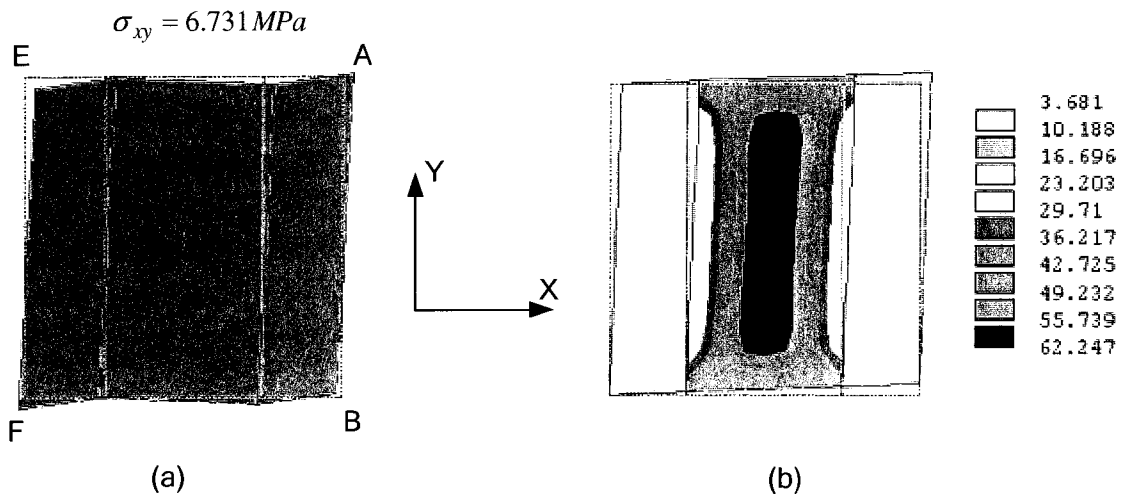


Fig. 2-14 Deformed shape and shear stress distribution of a two dimensional RUC model with different applied boundary conditions: (a) Eqn. (2.98); (b) Eqn. (2.100) (dashed lines show the undeformed shape)

Further examination of the stress distribution indicates that at all boundaries the normal stress components are zero and the shear stresses are uniform in the whole body as shown in Fig. 2-14a, i.e. the RUC is subject to a pure shear load. In addition, not only the displacements but also the stress distributions along the boundaries satisfy the periodic conditions. Therefore, the average shear strain and the average shear stress can be calculated from Eqns. (2.17) and (2.19) resulting in  $\bar{\gamma} = 2\bar{\epsilon}_{xy} = 0.0036$  and  $\bar{\tau} = \bar{\sigma}_{xy} = 6.4831\text{MPa}$ , respectively, and the equivalent shear modulus is  $G=1,801\text{MPa}$ .

**Case (b):** The deformed shape is shown in Fig.2-14(b). The boundary lines remain straight lines. Therefore, the displacement periodicity is satisfied but it is an over-constrained condition in comparison with the results in Fig.2-14(a). Now let us look at the resultant forces and moments at the boundaries. They are:

$$\text{At } AE \text{ and } BF: N_{yx} = \pm 24.335, N_{yy} = 0, M_1 = 10.3494;$$

$$\text{At } AB \text{ and } EF: N_{xx} = 0, N_{xy} = \pm 4.5963, M_2 = 0.4807.$$

Note that in this case the resultant shear forces at the boundaries  $AE$  and  $AB$  are not equal. This indicates that the unit cell is not subject to a pure shear force and other forces (moments) must be applied to the boundaries in order to maintain force and moment equilibrium, see Fig. 2-15(a). Figures 2-15(a) and 2-15(b) also show the distributions of stress components  $\sigma_{xx}$  and  $\sigma_{yy}$ , respectively. It is seen that the  $\sigma_{xx}$  and  $\sigma_{yy}$  give rise to boundary moments  $M_2$  and  $M_1$  to ensure that the unit cell as a whole is in equilibrium. However, the normal traction at the corresponding points on the opposite sides have opposite signs; one is in tension while the other in compression as seen in Fig. 2-15(b) at

points  $C$  and  $D$ . This implies that the traction distribution at the corresponding opposite boundaries does not satisfy the periodic condition and as such a “RUC” model cannot be arranged in a periodic array to represent a composite material. Accordingly, it is clear that the “homogeneous displacement boundary conditions” are not appropriate boundary conditions for the RUC of composite materials subject to a shear load.

The average shear strain and the average shear stress in this case are  $\bar{\gamma} = 2\varepsilon_{xy}^0 = 0.0036$  and  $\bar{\tau} = \bar{\sigma}_{xy} = 24.972\text{MPa}$ , respectively, and the equivalent shear modulus is  $G=6,937\text{MPa}$ . We can see that the homogeneous displacement boundary condition does greatly overestimate the modulus.

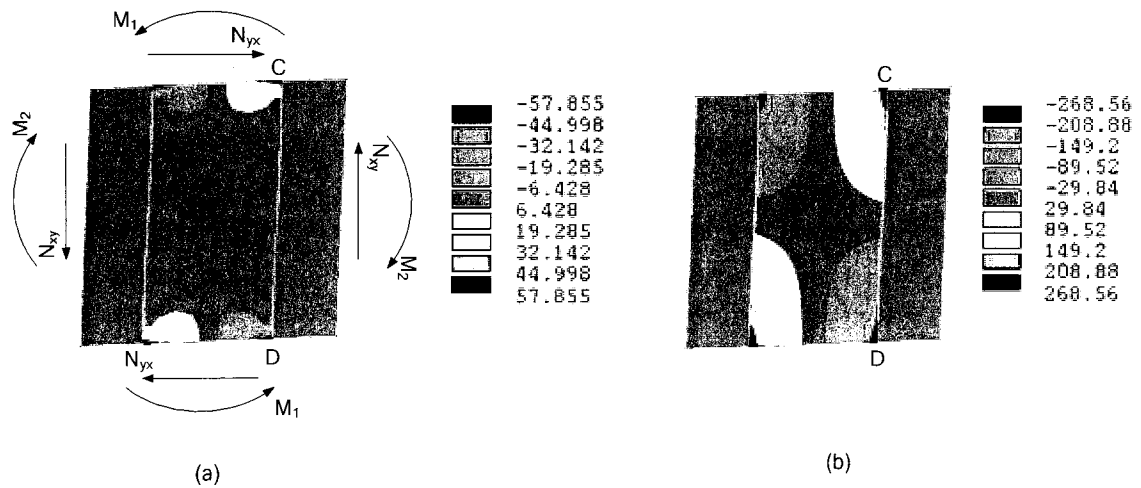


Fig. 2-15 Resultant boundary forces and distribution of stress components by applying homogeneous boundary conditions:

(a) Distribution of stress component  $\sigma_{xx}$ ; (b) Distribution of stress component  $\sigma_{yy}$ .

### 2.4.2 Example 2 (Prediction of Effective Elastic Constants of a UDC)

The meshed RUC model is shown Fig. 2-16. It is meshed with three-dimensional eight-node hexahedral elements. The finite element mesh is constructed with 1881 nodes and 1536 brick elements.

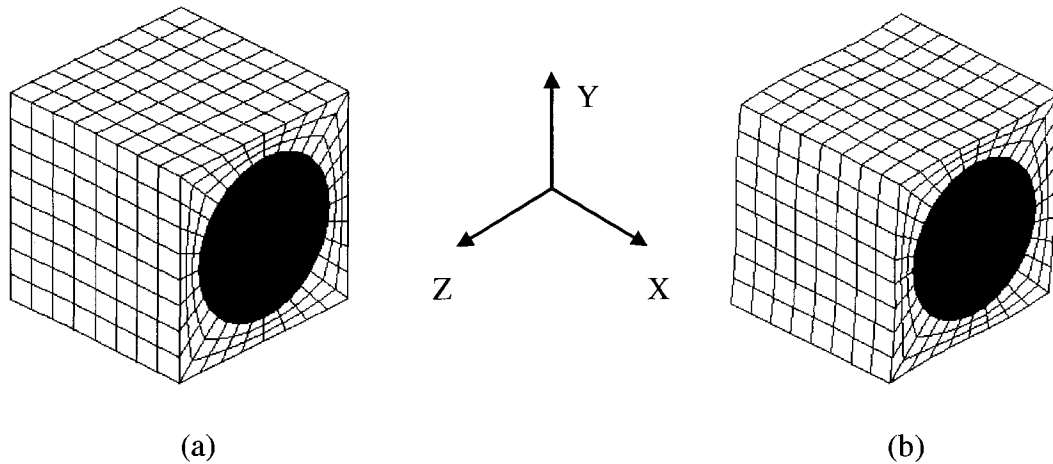


Fig. 2-16(a) The Finite element mesh of the RUC model for the unidirectional laminate;  
(b) Deformed shape under shear.

In this example, the unidirectional composite laminate is composed of aluminum matrix and boron fibre. All the constituent materials are assumed to be isotropic elastic but with different material properties. Table 2-2 lists the materials properties used in the calculations. The fibre volume fraction is 47 %.

Table 2-2 Material properties of fibre and matrix [4]

Material	E (MPa)	$\nu$
Boron	$3.793 \times 10^5$	0.1
Aluminum	$6.83 \times 10^4$	0.3

The unidirectional laminate is assumed to be orthotropic and linearly elastic. In a matrix notation form, the constitutive relation of this effective material can be written as,

$$\{\bar{\varepsilon}\} = [S]\{\bar{\sigma}\} \quad (2.101)$$

where  $[S]$  is the compliance matrix,

$$[S] = \begin{bmatrix} S_{11} & S_{12} & S_{13} & 0 & 0 & 0 \\ S_{12} & S_{22} & S_{23} & 0 & 0 & 0 \\ S_{13} & S_{23} & S_{33} & 0 & 0 & 0 \\ 0 & 0 & 0 & S_{44} & 0 & 0 \\ 0 & 0 & 0 & 0 & S_{55} & 0 \\ 0 & 0 & 0 & 0 & 0 & S_{66} \end{bmatrix} \quad (2.102)$$

After obtaining the  $\bar{\sigma}_{ij}$  and  $\bar{\varepsilon}_{ij}$  for given  $c_i^j$  from Eqns. (2.17) and (2.19) of a RUC, the  $S_{ij}$  can be obtained from Eqn. (2.101). The relation between the engineering elastic constants and  $S_{ij}$  are:

$$\begin{aligned} E_1 &= \frac{1}{S_{11}} & \nu_{12} &= -\frac{S_{12}}{S_{11}} & G_{12} &= \frac{1}{2S_{44}} \\ E_2 &= \frac{1}{S_{22}} & \nu_{13} &= -\frac{S_{13}}{S_{11}} & G_{13} &= \frac{1}{2S_{55}} \\ E_3 &= \frac{1}{S_{33}} & \nu_{23} &= -\frac{S_{23}}{S_{11}} & G_{23} &= \frac{1}{2S_{66}} \end{aligned} \quad (2.103)$$

It should be noted that for a general orthotropic material, nine independent material constants must be determined. However, Eqn. (2.101) contains only six equations; thus two sets of solutions are required. Note that the last three equations will result in the same moduli for the two sets of solutions. Thus, in total there are nine independent equations for nine independent material constants. All the nine constants are, therefore, determined by

solving the nine equations.

The following two sets of  $c_i^j$  are used in the calculation of the unidirectional laminate model ( $\Delta x = \Delta y = \Delta z = 1$ ):

$$\text{Set 1: } c_1^1 = c_2^2 = c_3^3 = 0.012, \quad c_i^j = 0.016 \quad (i \neq j),$$

$$\text{Set 2: } c_1^1 = c_2^2 = 0.018 \text{ all other } c_i^j = 0.$$

The predicted elastic properties of the unidirectional boron/aluminum laminate ( $E_3 = E_2, G_{13} = G_{12}$  and  $\nu_{13} = \nu_{12}$ ) and a comparison with the numerical, analytical and the available experimental data are given in Table 2-3. In the table, the results of Aboudi et al. [22] and Sun and Vaidya [4] are using a square array RUC similar to that used in this thesis. It can be seen that the present results are very close to the results in [4, 22]. The predictions of Sun and Chen [25] and Chamis [26] are based on a mechanics approach involving the use of displacement continuity and force equilibrium conditions. The solution presented by Whitney and Riley [27] is based on the use of the energy balance approach with the aid of classical elasticity theory. It is noted that the analytical results of Hashin and Rosen [28], based on energy variational principles, provide bounds for the elastic moduli, and the average values are used in the table. For  $E_1, G_{12}$  and  $\nu_{12}$  the upper and lower bounds coincide to provide an exact solution. The present predictions agree well with the exact analytical values, as seen from the table.

It can be concluded that the predicted properties are generally in good agreement with the analytical, numerical, and experimental results in the literature.

Table 2-3 Results and comparison for unidirectional boron/aluminum laminate

$$(V_f = 0.47)$$

Elastic								Test data
Constants	Present	Ref. 22	Ref. 4	Ref. 25	Ref. 26	Ref. 27	Ref. 28	(Ref. 29)
$E_1(\text{GPa})$	214	215.4	215	214	214	215	215	216
$E_2(\text{GPa})$	143	144.0	144	135	156	123	135.2	140
$G_{12}(\text{GPa})$	54.2	54.34	57.2	51.1	62.6	53.9	53.9	52
$G_{23}(\text{GPa})$	45.7	45.83	45.9	---	43.6	---	52.3	---
$\nu_{12}$	0.195	0.195	0.19	0.19	0.20	0.19	0.195	0.29
$\nu_{23}$	0.253	0.255	0.29	---	0.31	---	0.295	---

The deformed shape of the RVE under an applied pure shear periodic displacement boundary condition,  $c_2^3 = c_3^2 = 0.016$ , and all other  $c_i^j = 0$ , is shown in Fig. 16(b). Again, it can be seen that the deformed boundary surfaces no longer remain planes.

## 2.5 CONCLUDING REMARKS

The following conclusions are drawn from the study of the present chapter:

- Based on the compatibility conditions for a periodic structure, unified boundary conditions for repeated unit cell (RUC) model are presented which satisfy the periodicity conditions and are suitable for any combination of multiaxial loads.
- The proposed unified boundary conditions satisfy not only the boundary displacement periodicity but also boundary traction periodicity of the RUC model. In a FEM scheme,

the traction conditions are automatically satisfied. The proposed boundary conditions can be conveniently implemented into a finite element code

- A method to evaluate the average stresses and strains has been derived based on the applied boundary conditions. And it shows that the average stress can be calculated from the resultant forces at the boundaries.
- In the proposed boundary conditions, the periodic part of displacement is not explicitly presented, however, the periodic part of deformation can be easily retrieved after the solution.
- The proposed procedure applies to both geometrically symmetric and asymmetric RUCs. For geometrically asymmetric RUC, the entire model should be used in a analysis for multiaxial loading
- For a parallelepiped RUC under different loading conditions, the symmetries of the RUC are exploited to reduce the size of the problem. For a unidirectional laminate under spatial off-axis loading, proper periodic boundary conditions for a one-quarter RUC are derived rigorously.
- A 2-D example shows the “homogeneous boundary conditions” (plane-remains-plane) are not only over-constrained conditions but they may also violate the stress periodicity conditions. Thus, they cannot be used to represent periodical structures of the composite laminae or laminates under loading conditions with shear components.

- 
- Applying two sets of values of the proposed boundary conditions, all elastic moduli for the unidirectional laminates can be predicted simultaneously. The predicted results are in good agreement with the results available in the literature, and the experimental data.
  - The basic relations proposed in this chapter do not depend on the properties of the constituent materials of a composite. Therefore, they can also be applied to nonlinear micromechanical analysis of the composites under multiaxial loads. However, all the derived equations in this chapter are based on small deformation theory.

**BIBLIOGRAPHY**

1. Suquet, P. (1987). Elements of homogenization theory for inelastic solid mechanics. In: Sanchez-Palencia, E., Zaoui, A. (eds). *Homogenization Techniques for Composite Media*. Springer-Verlag, Berlin, 194-275.
2. Aboudi, J. (1991). *Mechanics of Composite Materials, a Unified Micromechanical Approach*. Elsevier Science Publishers, Amsterdam.
3. Nemat-Nasser S., Hori M. (1993). *Micromechanics: Overall Properties of Heterogeneous Materials*. Elsevier Science Publishers, Amsterdam.
4. Sun, C. T., Vaidya, R. S. (1996). Prediction of composite properties from a representative volume element. *Composites Science and Technology*, **56**, 171-179.
5. Li, S. (2000). General unit cells for micromechanical analysis of unidirectional composites. *Composites, Part A: Applied Science and Manufacturing*, **32**, 815-826.
6. Jansson, S. (1992). Homogenized nonlinear constitutive properties and local stress concentrations for composites with periodic internal structure. *International Journal of Solids and Structures*, **29**, 2181-2200.
7. Brockenbrough, J. R., Suresh, S., Wienecke, H. A. (1991). Deformation of metal-matrix composites with continuous fibers: geometrical effects of fibre distribution and shape. *Acta metallurgica et Materialil*, **39**, 735-752.
8. Michel, J. C., Moulinec, H, Suquet, P. (1999). Effective properties of composite materials with periodic microstructure: a computational approach. *Computer Methods*

- in Applied Mechanics and Engineering*, **172**, 109-143.
9. Anthoine, A. (1995). Derivation of the in-plane elastic characteristics of masonry through homogenization theory. *International Journal of Solids and Structures*, **32**, 137-163.
  10. Tang, X. Whitcomb, J. D. (2003). General techniques for exploiting periodicity and symmetries in micromechanics analysis of textile composites. *Journal of Composite Materials*, **37**, 1167-1189.
  11. Yuan, F., Pagano, N. J., Cai, X. (1997). Elastic moduli of brittle matrix composites with interfacial debonding. *International Journal of Solids and Structures*, **34**, 177-201.
  12. Hashin, Z., Shtrikman, S. (1963). A variational approach to the theory of elastic behaviour of multiphase materials. *Journal of Mechanics and Physics of Solids*, **11**, 127-140.
  13. Hill, R. (1963). Elastic properties of reinforced solids: Some theoretical principles. *Journal of Mechanics and Physics of Solids*, **11**, 357-372.
  14. Taliercio, A. (2005). Generalized plane strain finite element model for the analysis of elastoplastic composites. *International Journal of Solids and Structures*, **42**, 2361-2379.
  15. Xia, Z., Zhang, Y., Ellyin, F. (2003). A unified periodical boundary conditions for representative volume elements of composites and applications. *International Journal of Solids and Structures*, **40**, 1907-1921.

16. ADINA User's Manual. (1984). ADINA Engineering, Watertown, MA, USA.
17. ANSYS User's Manual (Version 5.0). (1992). Swanson Analysis System, Inc. Huston, PA., USA.
18. Zhang, Y., Xia, Z., Ellyin, F. (2005). Nonlinear viscoelastic micromechanical analysis of fibre reinforced polymer laminates with damage evolution. *International Journal of Solids and structures*, **42**, 591-604.
19. Zhang, Y., Xia, Z., Ellyin, F. (2005). Viscoelastic and damage analyses of fibre reinforced polymer laminates by micro/meso-mechanical modeling. *Journal of Composite Materials*, (in press).
20. Cook, R. D., Malkus, D. S., Plesha, M. E. (1989). *Concepts and Applications of Finite Element Analysis* (3rd ed.). John Wiley & Sons, New York.
21. Ainsworth, M. (2001). Essential boundary conditions and multi-point constraints in finite element analysis. *Computer Methods in Applied Mechanics and Engineering*, **190**, 6323-6339.
22. Aboudi, J., Pindera, M.-J., Arnold, S. M. (2001). Linear thermoelastic higher-order theory for periodic multiphase materials. *ASME Journal of Applied Mechanics*, **68**, 697-707.
23. Bathe, K. J.(1982). *Finite Element Procedures in Engineering Analysis*. Prentice-Hall, Inc., Englewood Cliffs, New Jersey, USA.

- 
24. Xia, Z., Zhou, C., Yong, Q., Wang, X. (2005). On selection of repeated unit cell model and application of unified periodic boundary conditions in micro-mechanical analysis of composites. *International Journal of Solids and Structures*, (in press).
  25. Sun, C. T., Chen, J. L. (1991). A micromechanical model for plastic behavior of fibrous composites. *Composites Science and Technology*, **40**, 115-129.
  26. Chamis, C. C. (1984). Simplified composite micromechanics equations for hygral, thermal and mechanical properties. *SAMPE Quarterly*, April, 14-23.
  27. Whitney, J. M., Riley, M. B. (1966). Elastic properties of fiber reinforced composite materials. *AIAA Journal*, **4**, 1537-1542.
  28. Hashin, Z., Rosen, B. W. (1964). The elastic moduli of fiber-reinforced materials. *ASME Journal of Applied Mechanics*, **31**, 223-32.
  29. Kenaga, D., Doyle, J. E., Sun, C. T. (1987). The characterization of boron/aluminum in the nonlinear range as an orthotropic elastic plastic material. *Journal of Composite Materials*, **27**, 516-531.

## CHAPTER 3

### MODELING VISCOELASTICITY OF MATRIX AND INTRALAMINAR DAMAGE

#### 3.1 INTRODUCTION

Epoxies are polymerization products with a highly crosslinked network. They are extensively used as the matrix phase in high performance composite materials. Their specific properties depend upon their particular formulation [1]. However, the epoxy matrix, like other thermoset polymers, has a highly nonlinear viscoelastic response. Although the fibres, such as E-glass fibre, behave elastically for most of their stress-strain range, composites still exhibit viscoelasticity. The analysis of Hashin [2] demonstrated that the viscoelastic effect in a unidirectional fibre composite is significant for axial shear, transverse shear and transverse uniaxial stress, for which the influence of matrix is dominant. Zhang et al [3] have studied the evolution of residual stresses/strains in composite laminates. It is shown clearly that the time-dependent viscoelastic properties of the polymer matrix (creep and stress relaxation) will cause a change of the stress/strain values in the fibres due to the interaction between the constituents, although the fibres are purportedly elastic. For the same reason, the damage in composite laminates would also evolve with time. Ellyin et al [4] have presented the evolution of matrix cracking due to its viscoelasticity. Consequently, an effective micromechanical analysis of fibrous composites requires accurate constitutive relations for the matrix material.

Another adverse effect of epoxy matrix is its influence on the damage properties of the composite. As compared with fibres, epoxies are usually weak and are flaw sensitive, under tensile loading, most epoxies fail in a brittle manner [5]. Because of the brittleness

of the epoxy, matrix cracking becomes one of the most important damage mechanisms of a composite.

In most advanced composite materials, there is invariably an interphase between the two main constituents of the reinforced composites. The scale of the interphase may be very small of the order of several microns [6]. Therefore, in many studies the interphase can be treated as an interface. Interphase/interface determines the stress transfer between the reinforcement and matrix, and thus it influences the damage process of laminates if the bonding is weak.

For a unidirectional laminate under tensile loading, the matrix cracking and fibre/matrix interphase damage are the two main damage modes [7]. In most cases, damage process in laminates initiates by the above two mechanisms. And usually, these two damages are referred to as *intralaminar damage*. For multidirectional laminates, intralaminar damage may exist at a loading level much lower than the final failure load or even during the material curing process. The most common example is the loading of the  $0^\circ/90^\circ$  cross-ply laminates along the  $0^\circ$  ply direction. In this case the damage occurs in the  $90^\circ$  plies at a rather low load, however, the laminates can still carry higher load in the  $0^\circ$  direction, although at a reduced stiffness, see, e.g. Hoover et al [8]. Thus for an accurate analysis, it is imperative to consider the prevailing damage mechanisms, especially the intralaminar ones.

Thus there are two key requirements for an effective micromechanical analysis for a fibre reinforced polymeric composite: (a) an accurate constitutive model for the matrix material, and (b) a proper simulation of damage process (damage initiation criterion and post-damage constitutive relation which governs the propagation of the damage). In this

chapter, models for the matrix viscoelasticity, the fibre/matrix interphase damage, and matrix cracking are presented, respectively. The matrix behaviour is described by a recently developed nonlinear viscoelastic constitutive model [9-10]. A brief description of the model is provided in Section 3.2 and examples are given to show the influence of the viscoelasticity of the matrix on the response of the composite. To model the damage (separation) of the fibre/matrix interface, an interphase element is proposed which can be directly applied to a unit cell analysis. The stress-strain relation of the interphase element is derived based on a cohesive law [11-12], which characterizes the dependence of the tractions on the displacement discontinuities across the interface. In addition, a viscous term is added to the cohesive law to overcome the convergence difficulty induced by the so-called snap-back instability in the equilibrium iterations (Section 3.3). To model the matrix cracking, a ‘smeared crack approach’ is employed. In this approach, the cracked solid is assumed to be a continuum that permits a crack description in terms of stress-strain relations. In particular, the proposed post-damage stress-strain relation allows only normal stress and in-plane shear stress components (corresponding to crack orientations) tend to zero (Section 3.4). Applications of the constitutive model and damage models to the analysis of composite laminates will be presented in Chapters 4 and 5.

## **3.2 NONLINEAR VISCOELASTIC MATERIAL MODEL FOR EPOXY**

### ***3.2.1 Nonlinear Visoelastic Model for Epoxy Matrix***

Throughout this thesis, the glass fibres are modeled by the generalized Hooke’s law. However, the epoxy polymer matrix is modeled by a nonlinear viscoelastic model

recently developed by Xia et al. [9]. Here, for the sake of completeness, only a brief description will be given.

For the uniaxial stress state, the model can be represented by a finite number of nonlinear Kelvin elements and a linear spring element, connected in series (Figure 3-1).

The constitutive equations, generalized to the multiaxial stress state, are summarized below:

$$\{\dot{\epsilon}_t\} = \{\dot{\epsilon}_e\} + \{\dot{\epsilon}_c\} \quad (3.1)$$

$$\{\dot{\epsilon}_c\} = \sum_{i=1}^n \left( \frac{[A]}{E_i \tau_i} \{\sigma\} - \frac{1}{\tau_i} \{\epsilon_{ci}\} \right) \quad (3.2)$$

$$\{\dot{\sigma}\} = E[A]^{-1} \{\dot{\epsilon}_e\} \quad (3.3)$$

In the above,  $\{\dot{\epsilon}_t\}$ ,  $\{\dot{\epsilon}_e\}$ ,  $\{\dot{\epsilon}_c\}$ ,  $\{\dot{\sigma}\}$  are the total strain-rate, elastic strain-rate, creep strain-rate, and stress-rate vectors (each contains six components, respectively).  $E$  is an elastic modulus which is assumed to be constant and  $[A]$  is a matrix related to the value of Poisson's ratio, defined by

$$[A] = \begin{bmatrix} 1 & -\nu & -\nu & 0 & 0 & 0 \\ -\nu & 1 & -\nu & 0 & 0 & 0 \\ -\nu & -\nu & 1 & 0 & 0 & 0 \\ 0 & 0 & 0 & 1+\nu & 0 & 0 \\ 0 & 0 & 0 & 0 & 1+\nu & 0 \\ 0 & 0 & 0 & 0 & 0 & 1+\nu \end{bmatrix} \quad (3.4)$$

A time scale factor  $\alpha$  is introduced. It is assumed as the following:

$$\tau_i = (\alpha)^{i-1} \tau_1 \quad (3.5)$$

In this way all  $\tau_i$  are related through the scale factor  $\alpha$ . A time span of order of  $n$  would be covered, if  $n$  Kelvin elements were chosen and the value of  $\alpha$  is taken to be 10.

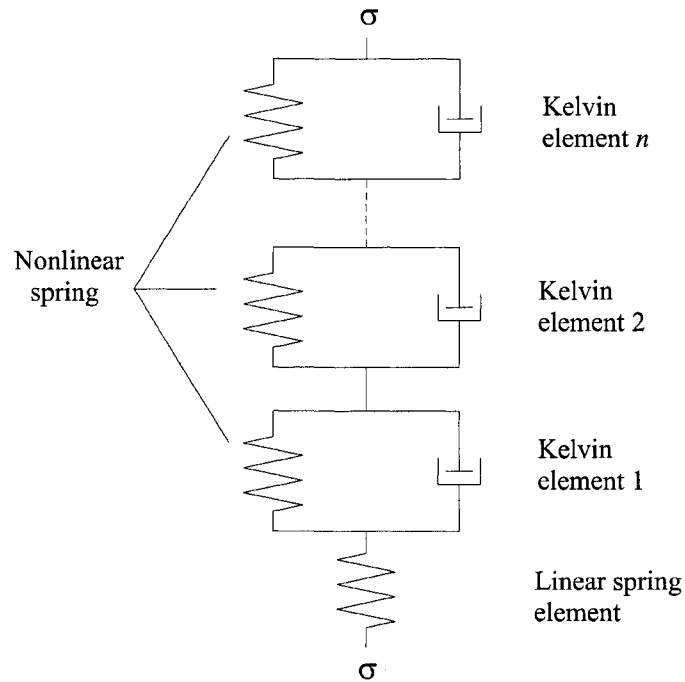


Fig. 3-1 A uniaxial visoelastic model represented by a finite series of Kelvin elements coupled with an elastic spring.

The description of the nonlinear behaviour in the current model is achieved by letting  $E_i$  be functions of the current equivalent stress,  $\sigma_{eq}$ . Furthermore, a single function form for all  $E_i$  is assumed, i.e.

$$E_i = E_1(\sigma_{eq}) \quad (3.6)$$

with

$$\sigma_{eq} = \frac{(R-1)I_1 + \sqrt{(R-1)^2 I_1^2 + 12RJ_2}}{2R} \quad (3.7)$$

where  $I_1 = \sigma_1 + \sigma_2 + \sigma_3$  is the first invariant of the stress tensor,  $J_2 = S_{ij}S_{ij}/2$  is the second invariant of the deviatoric stress tensor and  $R$  is the ratio of compressive to tensile

‘yield stress’. Note that when  $R = 1$ , then Eqn. (3.7) reduces to the von Mises equivalent stress,  $\sigma_{eq} = \sqrt{3J_2}$ .

To delineate the loading/unloading cases for general multiaxial loading paths, a stress memory surface is defined as

$$f_m^\sigma(\sigma_{ij}) - R_{mem}^2 = \frac{3}{2} s_{ij} s_{ij} - R_{mem}^2 = 0 \quad (3.8)$$

where  $s_{ij} = \sigma_{ij} - \frac{1}{3} \sigma_{kk} \delta_{ij}$  are the deviatoric stress components. The radius of the memory surface,  $R_{mem}$ , is determined by the maximum von Mises stress level experienced by the

material during its previous loading history, i.e.  $R_{mem} = \sqrt{\left(\frac{3}{2} s_{ij} s_{ij}\right)_{\max}}$ . Therefore, for a

monotonic loading from the virgin state, the stress memory surface will expand isotropically with an increasing stress level. If  $\sigma_{ij}^t$  is the current stress point,  $d\sigma_{ij}^t$  is the

stress increment at time  $t$ , and  $\left(\frac{\partial f}{\partial \sigma_{ij}}\right)_{\sigma_{ij}=\sigma_{ij}^t}$  represents the direction of the normal to the

memory surface at the current stress point, then a criterion to distinguish the loading/unloading cases is introduced as follows:

- if the current stress point is on the memory surface and  $\left(\frac{\partial f}{\partial \sigma_{ij}}\right)_{\sigma_{ij}^t} \cdot d\sigma_{ij}^t \geq 0$ , this signifies a loading case;
- if the current stress point is on the memory surface and  $\left(\frac{\partial f}{\partial \sigma_{ij}}\right)_{\sigma_{ij}^t} \cdot d\sigma_{ij}^t < 0$ , then a switch from loading to unloading occurs;

- if the current stress point is inside the memory surface, i.e.  $f_m^\sigma(\sigma_{ij}^t) - R_{mem}^2 < 0$ , it is then an unloading case.

For the loading case the spring stiffness of the Kelvin elements is defined as a function of the equivalent stress,  $E_i = E_1(\sigma_{eq})$ . For the unloading case, it is assumed that  $E_i$  remains the same value during the entire unloading process, which is equal to the value of  $E_i$  at the switch point, where unloading takes place.

The values of constants ( $E, \nu, \alpha, \tau_1, R$ ) and the functional form of  $E_1(\sigma_{eq})$  can be determined from uniaxial creep curves at different stress levels following a routine procedure which is described in the above mentioned references.

In this thesis, three types of epoxy are involved, viz, (1) Epon 826/curing agent 9551; (2) Epon 828/curing agent Epon Z; and (3) Epon 815/ curing agent Versamid 140. The viscoelastic model presented here is calibrated using Epon 826/9551 as in [9-10]. To compare the predictions of the present micromechanical model with the off-axis test results reported in [13], where Epon 828/Z and Epon 815/Versamid 140 are used in the two types of laminates, the constants and functional in the viscoelastic model for these two epoxies should be determined. However, due to lack of test data, the constants for Epon 828/Z and Epon 815/Versamid 140 are determined by: (1) the Young's moduli and Poisson's ratio are taken from the test values in [1]; (2) the values of  $\alpha, \tau$  and  $R$  are taken approximately as the values for Epon 826/9551; and (3) the coefficients in the functional  $E_1(\sigma_{eq})$  are estimated such that the predicted uniaxial stress-strain curves of the corresponding epoxies are close to the test curves in [1].

Table 3-1 Material properties and constants of constitutive model

	E-Glass	Epon 826	Epon 828	Epon 815
E (MPa)	72400	3400	3450	2130
$\nu$	0.22	0.42	0.40	0.39
$\alpha$	/	10	10	10
$\tau_1$	/	6.116	6.116	6.116
R	/	1.15	1.15	1.15
$E_1(\sigma_{eq})$	/	$105500e^{\frac{\sigma-22.764}{18.000}}$	$105500e^{\frac{\sigma-22.764}{18.000}}$	$10000e^{\frac{\sigma-40.0}{9.0}}$
$\epsilon_{cr}$	/	0.048	0.09	0.14
$E_t(MPa)$	/	284	345	213

The constants for the epoxy resins, Epon 826/9551, Epon 828/Epon Z, and Epon 815/Versamid 140 are listed in Table 3-1. The elastic properties of E-glass fibre are also listed in the Table 3-1.

### 3.2.2 Implementation into ADINA and Verification Examples

The above viscoelastic constitutive model for epoxy matrix is implemented into the FEA code ADINA through its user defined subroutine [14]. The implementation procedure is straightforward; therefore we only show three verification examples herein. Figure 3-2 shows the predicted results of the model and the comparison with test for Epon 826 (including unloading). And Fig. 3-2 shows the predicted uniaxial stress-strain curves for Epon 828 and Epon 815 (strain rate =  $10^{-3}$ /s).

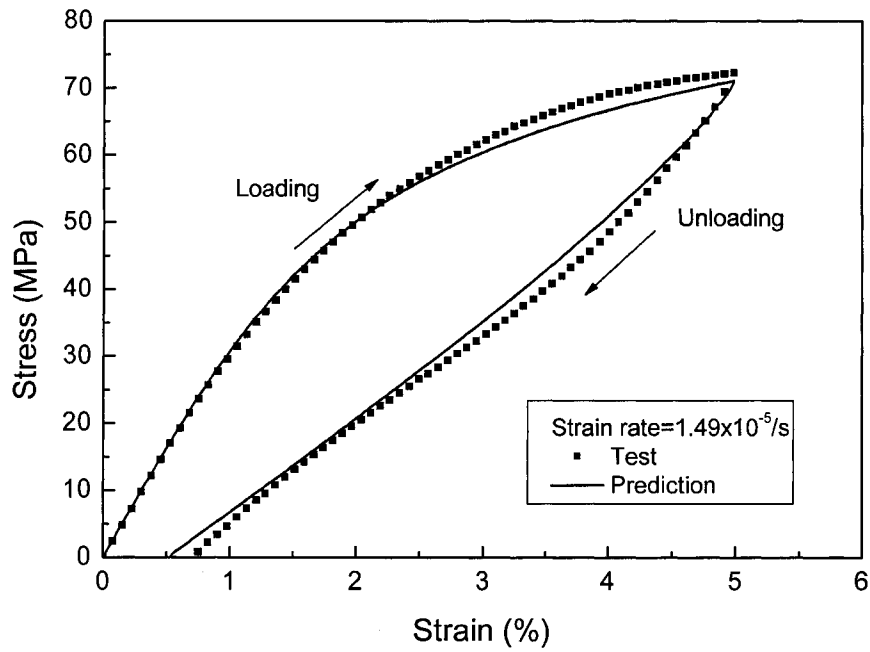


Fig. 3-2 Stress-strain curve of viscoelastic matrix including unloading.

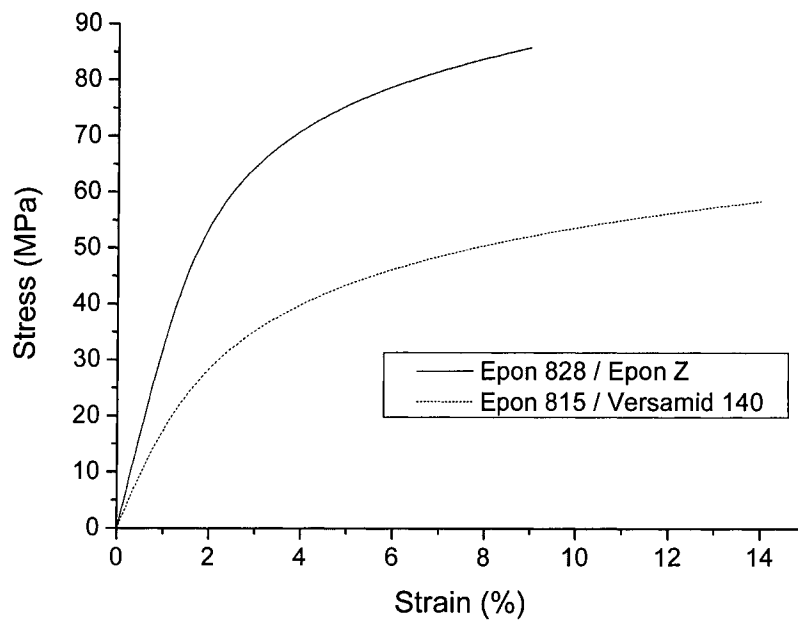


Fig. 3-3 Stress-strain curve of Epon 828 and Epon 815.

Another example shows the transverse response of an RUC under transverse tensile loadings in different loading directions shown in Fig. 3-4. Figure 3-5 portrays the stress-

strain response at a strain rate of  $10^{-3} / s$ . It is observed that the global stress-strain curve of the composite is nonlinear due to the nonlinearity of the matrix.

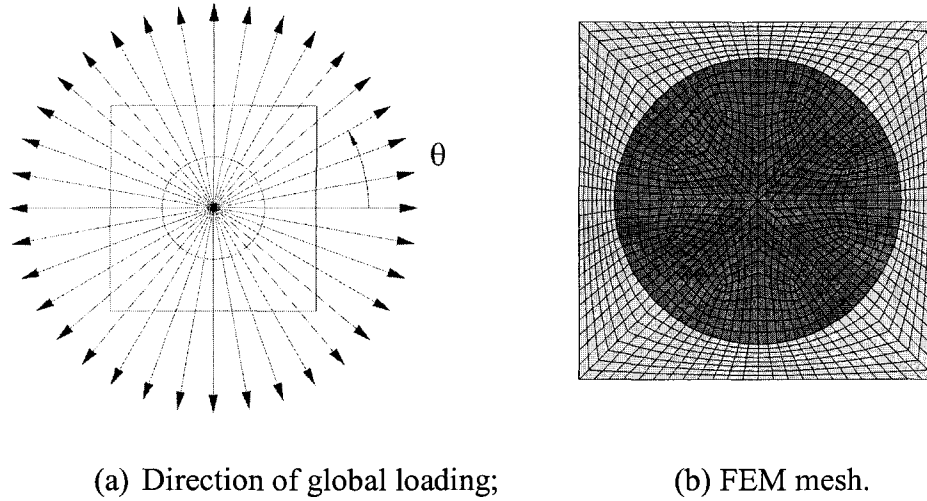


Fig. 3-4 Transverse loading of unidirectional laminate at different orientations.

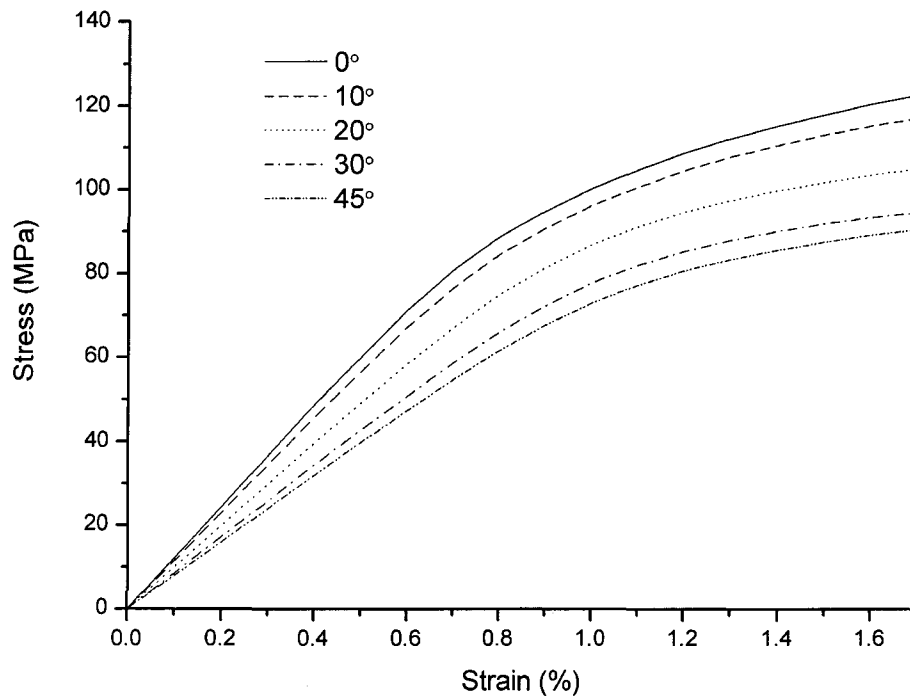


Fig. 3-5 Transverse response of a unidirectional laminate.

### 3.3 COHESIVE DEBONDING LAW AND COHESIVE INTERPHASE ELEMENT

#### 3.3.1 Cohesive Law

The fibre-matrix interphase/interface will be modeled by a cohesive zone model proposed by Tvergaard [11-12]. The behaviour to be captured by a cohesive law is that, as the cohesive surface separates the magnitude of the traction at first increases, reaches a maximum and then it decreases with the increasing separation and finally approaches zero. In the interface coordinate system 1-2-3 shown in Fig. 3-6, let  $[u_1], [u_2]$  and  $[u_3]$  be the *displacement differences* across the interface and  $T_1, T_2$  and  $T_3$  are the corresponding tractions in the 1, 2, and 3 directions, respectively. To account for the combined effect of normal and shear decohesions, a non-dimensional parameter  $\lambda$  is defined as in [11-12]

$$\lambda = \left\{ \left( \frac{[u_3]}{\delta_n} \right)^2 + \left( \frac{[u_2]}{\delta_{t1}} \right)^2 + \left( \frac{[u_1]}{\delta_{t2}} \right)^2 \right\}^{1/2} \quad (3.9)$$

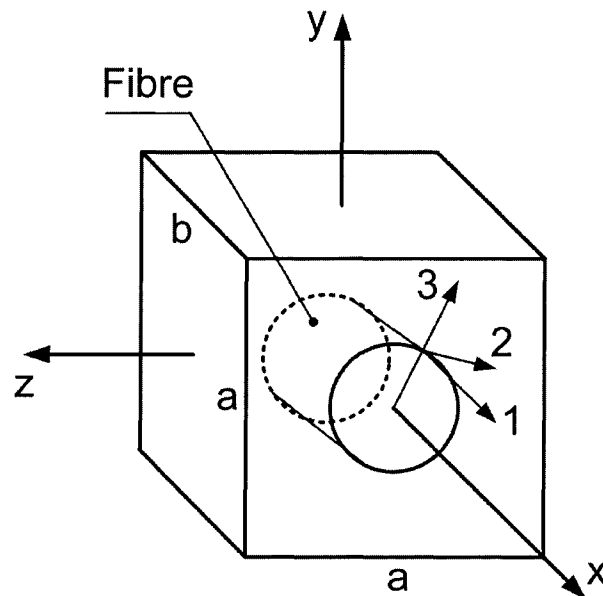


Fig. 3-6 Interface coordinate system.

where  $\delta_n$ ,  $\delta_{i1}$ ,  $\delta_{i2}$  are displacement difference values in the three directions, corresponding to complete separation. Therefore Eqn. (3.9) defines the critical damage condition for combined mode debonding, i.e., the interface completely separates when  $\lambda = 1$  (see Fig. 3-7).

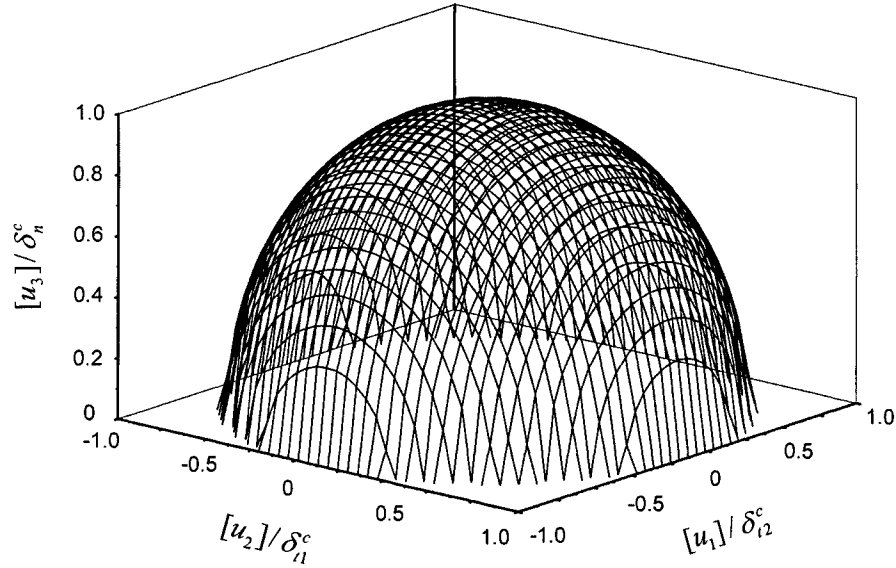


Fig. 3-7 Combined mode debonding criterion.

To determine the tractions a function  $F(\lambda)$  is chosen as in [11],

$$F(\lambda) = \frac{27}{4} \sigma_{\max} (1 - 2\lambda + \lambda^2) \quad \text{for } 0 \leq \lambda \leq 1 \quad (3.10)$$

and the interface tractions are given by the expressions

$$\begin{aligned} T_3 &= \frac{[u_3]}{\delta_n} F(\lambda) \\ T_2 &= \alpha \frac{[u_2]}{\delta_{i2}} F(\lambda) \\ T_1 &= \alpha \frac{[u_1]}{\delta_{i1}} F(\lambda) \end{aligned} \quad (3.11)$$

In the above equations,  $\sigma_{\max}$  is the tensile strength of the interface for pure normal separation (in 3 direction as shown in Fig. 3-6,  $[u_1]=[u_2]\equiv 0$ ,  $\lambda=[u_3]/\delta_n$ ). The tangential strength of the interface for sliding separation (in 1 or 2 direction as shown in Fig. 3-6,  $[u_3]\equiv 0$ ) is designated as  $\alpha\sigma_{\max}$ , in which  $\alpha$  is a dimensionless factor (the ratio of the tangential strength to normal strength of the interface). Function  $F(\lambda)$  determines the shape of the traction/displacement jump curve. Note in some researches, exponential function or straight lines are also used to describe the traction/displacement jump curve.

By choosing the function  $F(\lambda)$  as expressed in Eqn (3.10), the traction/displacement jump relation for *the pure normal separation* will be  $T_3 = \frac{27}{4}\sigma_{\max}\lambda(1-\lambda)^2$ . Therefore we can obtain the normal traction/displacement jump curve which is shown in Fig. 3-8. It can be seen that for the case of purely normal separation, the relation between traction  $T_3$  and displacement jump  $[u_3]$  described by the cohesive law is:  $T_3$  varies from the value 0 at  $[u_3]=0$ , then reaches a maximum value  $\sigma_{\max}$  at  $[u_3]=\delta_n/3$ , and then again drops to 0 at  $[u_3]=\delta_n$ , where complete separation is assumed to occur (Fig. 3-8). By integrating the traction/displacement jump curve over  $\lambda=0$  to 1, the work of separation per unit interface area is obtained to be  $9\sigma_{\max}\delta_n/16$ . Thus, to represent the interfacial debonding behaviour for a given interface the values of the five parameters  $\delta_n$ ,  $\delta_{t1}$ ,  $\delta_{t2}$ ,  $\sigma_{\max}$  and  $\alpha$  have to be chosen such that the maximum traction and the work required for the separation for the combined modes are approximated as closely as possible.

For decreasing  $\lambda$  a type of elastic unloading is used to represent the partly damaged interface [12]:

$$\begin{aligned}
 T_3 &= \frac{[u_3]}{\delta_n} F(\lambda_{\max}) \\
 T_2 &= \alpha \frac{[u_2]}{\delta_{t2}} F(\lambda_{\max}) \quad \text{for } \lambda < \lambda_{\max} \text{ or } \dot{\lambda} < 0 \\
 T_1 &= \alpha \frac{[u_1]}{\delta_{t1}} F(\lambda_{\max})
 \end{aligned} \tag{3.12}$$

Where  $\lambda_{\max}$  is the maximum of  $\lambda$  in the loading history. Furthermore, under normal compression, elastic springs with a high stiffness are used to approximately represent contact (instead of Eqn. (3.11a) or Eqn. (3.12a)), thus taking

$$\begin{aligned}
 T_3 &= \frac{27}{4} \sigma_{\max} \frac{[u_3]}{\delta_n} \\
 \lambda &= \left\{ \left( \frac{[u_2]}{\delta_{t2}} \right)^2 + \left( \frac{[u_1]}{\delta_{t1}} \right)^2 \right\}^{1/2}
 \end{aligned} \tag{3.13}$$

Figure 3-8 shows the normal cohesive law expressed by Eqns. (3.11)-(3.13).

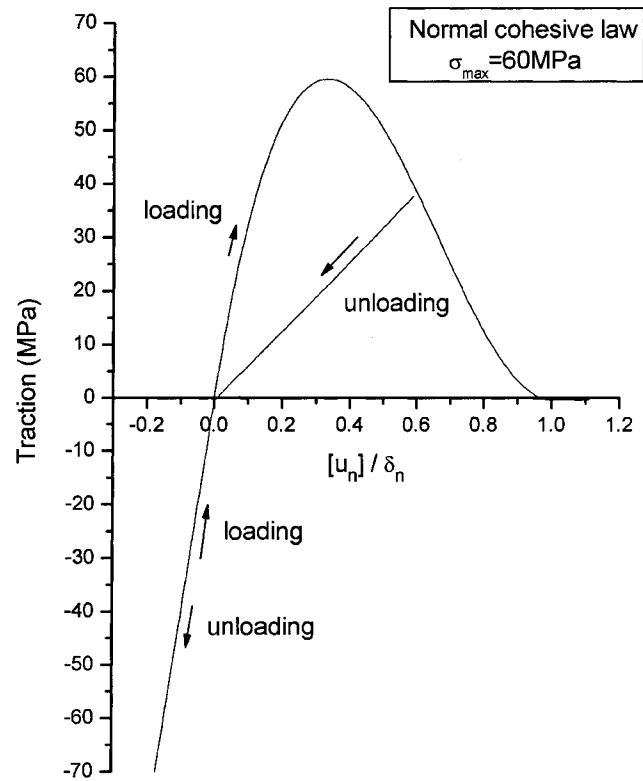


Fig. 3-8 Normal cohesive law.

### 3.3.2 Cohesive Interphase Element

The traction-displacement jump relation is relatively difficult to implement into a commercial finite element code, especially for three-dimensional cases. Instead, in this study the ideal *interface* (zero thickness) is represented by a very thin layer of *interphase* element with thickness of  $h$ . Assuming uniform strains throughout the thickness, then, the strains can be expressed as a function of the displacement jumps as follows (in the local coordinate system 1-2-3 shown in Fig. 3-6):

$$\{\varepsilon_{33} \ \gamma_{23} \ \gamma_{13}\} = \frac{1}{h} \{[u_3] \ [u_2] \ [u_1]\} \quad (3.14)$$

The critical strains are defined from the above equation as

$$\{\varepsilon_{33}^c \ \gamma_{23}^c \ \gamma_{13}^c\} = \frac{1}{h} \{\delta_n \ \delta_{t2} \ \delta_{t1}\} \quad (3.15)$$

Substituting Eqns. (3.14) and (3.15) into the cohesive law expressed by Eqns.(3.11)-(3.13), and replacing the corresponding tractions  $T_3$ ,  $T_2$  and  $T_1$  by the stresses  $\sigma_{33}$ ,  $\tau_{23}$  and  $\tau_{13}$ , a stress-strain constitutive law is obtained as follows:

$$\begin{aligned} \sigma_{33} &= \frac{\varepsilon_{33}}{\varepsilon_{33}^c} F(\lambda) \\ \tau_{23} &= \alpha \frac{\gamma_{23}}{\gamma_{23}^c} F(\lambda) \\ \tau_{13} &= \alpha \frac{\gamma_{13}}{\gamma_{13}^c} F(\lambda) \end{aligned} \quad (3.16)$$

$$\lambda = \left\{ \left( \frac{\varepsilon_{33}}{\varepsilon_{33}^c} \right)^2 + \left( \frac{\gamma_{23}}{\gamma_{23}^c} \right)^2 + \left( \frac{\gamma_{13}}{\gamma_{13}^c} \right)^2 \right\}^{1/2} \quad (3.17)$$

The incremental expressions are obtained from Eqn. (3.16) as

$$\begin{aligned}
\dot{\sigma}_{33} &= \frac{\dot{\varepsilon}_{33}}{\varepsilon_{33}^c} F(\lambda) + \frac{\varepsilon_{33}}{\varepsilon_{33}^c} \frac{\partial F}{\partial \lambda} \dot{\lambda} \\
\dot{\tau}_{23} &= \alpha \frac{\dot{\gamma}_{23}}{\gamma_{23}^c} F(\lambda) + \alpha \frac{\gamma_{23}}{\gamma_{23}^c} \frac{\partial F}{\partial \lambda} \dot{\lambda} \\
\dot{\tau}_{13} &= \alpha \frac{\dot{\gamma}_{13}}{\gamma_{13}^c} F(\lambda) + \alpha \frac{\gamma_{13}}{\gamma_{13}^c} \frac{\partial F}{\partial \lambda} \dot{\lambda}
\end{aligned} \tag{3.18}$$

where

$$\begin{aligned}
\frac{\partial F}{\partial \lambda} &= \frac{27}{2} \sigma_{\max} (-1 + \lambda) \\
\dot{\lambda} &= \frac{1}{\lambda} \left( \frac{\varepsilon_{33}}{\varepsilon_{33}^c} \frac{\dot{\varepsilon}_{33}}{\varepsilon_{33}^c} + \frac{\gamma_{23}}{\gamma_{23}^c} \frac{\dot{\gamma}_{23}}{\gamma_{23}^c} + \frac{\gamma_{13}}{\gamma_{13}^c} \frac{\dot{\gamma}_{13}}{\gamma_{13}^c} \right)
\end{aligned} \tag{3.19}$$

This cohesive constitutive law can be implemented into a FEM code as a stress-strain relationship.

### 3.3.3 Snap-back Instability

In the numerical simulation of the interfacial debonding, the snap-back instability of the stress-strain curve frequently results in convergence difficulties in the calculation. Snap-back of the stress-strain curve indicates the strain decreasing with the decreasing of the stress (under displacement control) [15-16]. In cases when the snap-back instability occurs, special equilibrium iteration algorithm such as ‘arc-length’ method should be used [17-18]. In the arc-length method, a load-displacement constraint equation is incorporated into the Newton-Raphson iterative procedure. However, in the FEM code ADINA used in the present study, this option is not available when a user-defined material constitutive model is used [14]. Thus, in this section, a simple interfacial model is considered to study the snap-back behaviour and a numerical strategy to overcome the convergence difficulties.

### One-dimensional interphase model and analytical solution

A one dimensional interfacial model is shown in Fig. 3-9. It consists of three plane strips representing the fibre, interphase and matrix, respectively. The fibre and the matrix are assumed to be elastic and the interphase model is described by the cohesive law described in Sections 3.3.1 and 3.3.2. This one dimensional model can be solved either analytically or numerically. In the analytical solution, the interphase is idealized as an interface, and the cohesive law expressed by Eqns. (3.11)-(3.13) is used. While in the FEM solution, the interphase is represented by a thin layer of interphase element, and cohesive constitutive relations expressed by Eqns. (3.16)-(3.19) are used. First, let us examine the following analytical solution:

$$\begin{aligned}\bar{\varepsilon} &= \lambda(\delta_n / 2R) + (\bar{\sigma} / \sigma_{\max})(\sigma_{\max} / 2E_m)(1 + E_m / E_f) \\ \bar{\sigma} / \sigma_{\max} &= \frac{27}{4} \lambda(1 - \lambda)^2\end{aligned}\quad (3.20)$$

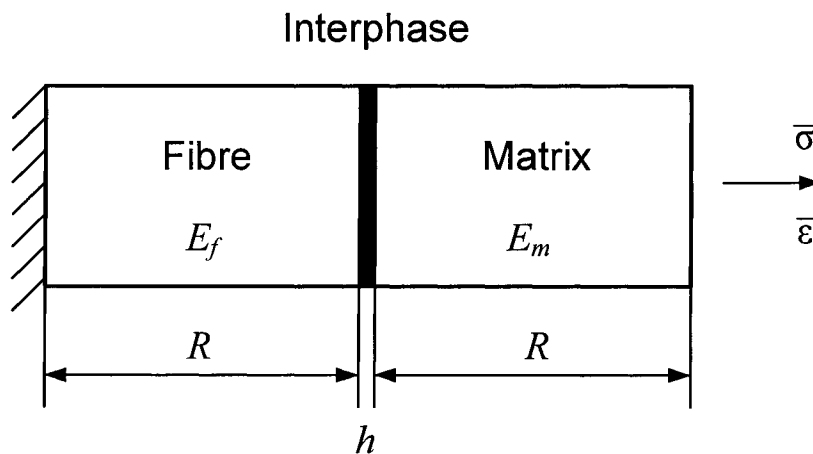


Fig. 3-9 One dimensional interphase model.

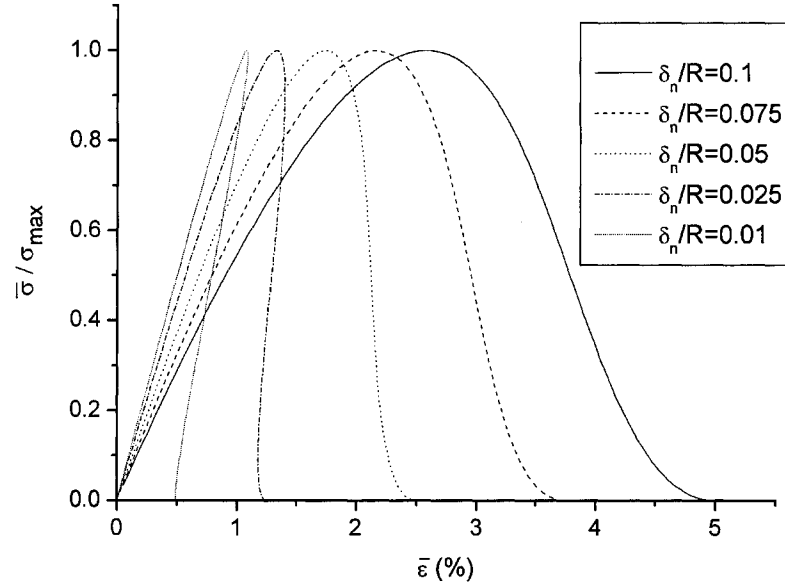


Fig. 3-10 Global stress vs. global strain.

Figure 3-10 portrays the stress-strain curves for the above solution with  $E_m=3450$  MPa,  $E_f=72400$  MPa,  $\sigma_{\max} = 60$  MPa and different ratios of  $\delta_n / R$ . And Fig. 3-11 shows the relation between the interphase separation with the global strain. It can be seen that the stress-strain curves show the 'snap back' instability when  $\delta_n / R = 0.025$  or  $0.01$ . By differentiating Eqn. (3.20), the condition for this instability is, when

$$(\sigma_{\max} / \delta_n) / (E' / R) > 4 / 9 \quad (3.21)$$

where  $E' = E_m E_f / (E_m + E_f)$ .

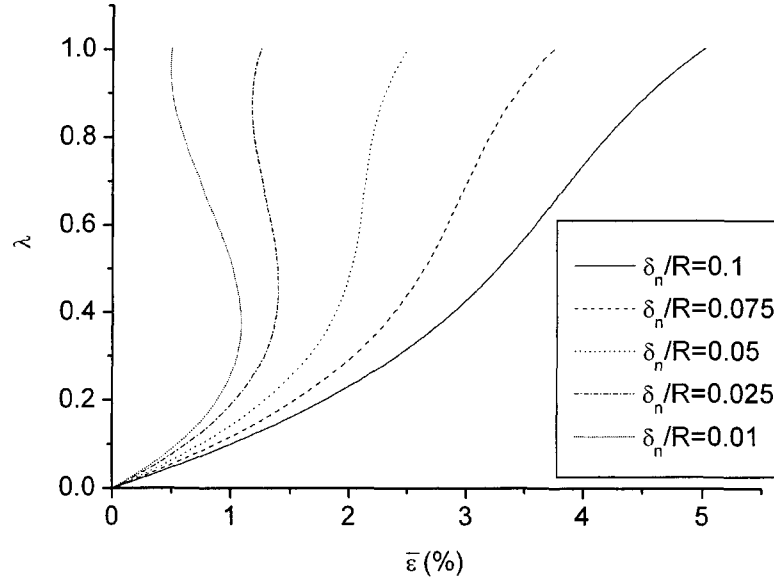


Fig. 3-11 Interface separation vs. global strain.

### **Finite element solution**

In the FEM analyses, for the three ratios of  $\delta_n/R = 0.1, 0.075$  and  $0.05$ , the same global stress-strain curves as that in Fig.3-10 are obtained. However, as for the ratios of  $\delta_n/R = 0.025$  and  $0.01$ , the calculations can be continued only until the maximum global stress is reached and no converged solution can be obtained thereafter. To overcome this difficulty, when the snap-back occurs, an artificial viscous term is introduced, as suggested in Gao and Bower [15]. The modified cohesive law is given by

$$\begin{aligned}
 T_3 &= \frac{[u_3]}{\delta_n} F(\lambda) + \frac{\eta_n}{\delta_n} \frac{d[u_3]}{dt} \\
 T_2 &= \alpha \frac{[u_2]}{\delta_{t2}} F(\lambda) + \frac{\eta_{t2}}{\delta_{t2}} \frac{d[u_2]}{dt} \\
 T_1 &= \alpha \frac{[u_1]}{\delta_{t1}} F(\lambda) + \frac{\eta_{t1}}{\delta_{t1}} \frac{d[u_1]}{dt}
 \end{aligned} \tag{3.22}$$

where  $\eta_n, \eta_{t2}, \eta_{t1}$  are viscous coefficients.

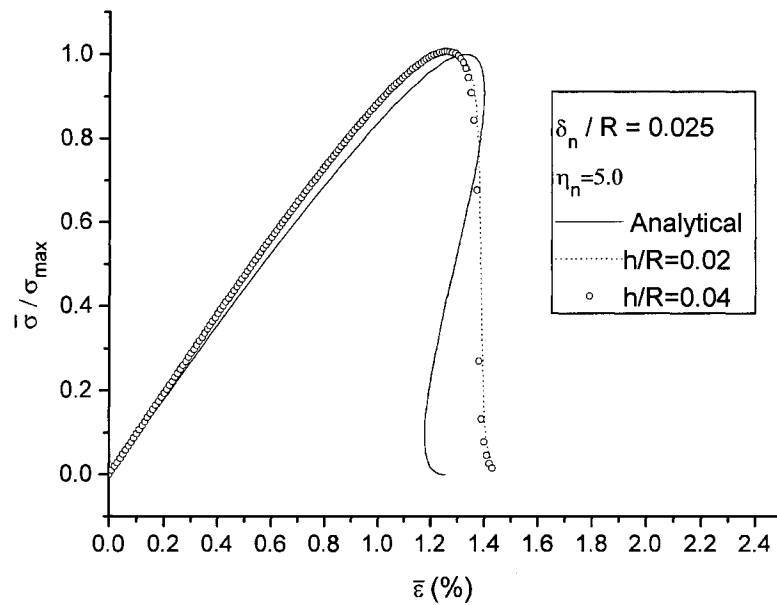


Fig. 3-12 Response with artificial viscosity.

In Fig. 3-12, the FEM numerical solution for  $\delta_n / R = 0.025$  with  $\eta_n = 5.0$  is compared with the analytical solution. It can be seen that the snap-back instability is avoided and the curve after complete separation seems physically more realistic. In addition, the influence of the thickness of the cohesive interphase element,  $h$ , is also shown by comparing the results with two different thicknesses. It is seen that, the influence of the  $h$  is negligible as long as it is sufficiently small. Thus in the analyses of composite laminates in Chapter 4, the thickness of the interphase element will be taken to be 2% of the fibre radius.

### 3.4 MODELING OF MATRIX CRACKING

Upon increasing the applied load, micro-cracks will develop in the matrix. These cracks cause reduction in stiffness of the laminate. In contrast to a predefined single

dominant crack in isotropic materials, the orientation and location or even numbers of cracks in a laminate is unknown, thus makes it difficult to deal with such cracks through the classical fracture mechanics approach. Instead, the so-called ‘smeared crack’ approach [19-21] will be used. In this approach the initiation of the crack is determined by an appropriate damage criterion, and the reduction of load bearing capacity induced by a crack is described by stress-strain softening relationship. Thus the discontinuity caused by a crack is smeared out, and the model can again be implemented into a FEM code conveniently.

### 3.4.1 *Initiation of a Crack*

The first step is to determine the initiation of a crack using an appropriate damage criterion. Generally, a damage criterion is a function of stress/strain components, for example, the maximum stress criterion, equivalent stress criterion, maximum strain criterion, etc. Experimental investigation has indicated that the main fracture mechanism of an epoxy resin is brittle tensile failure [5] and the maximum principal strain theory is in good agreement with test data for matrix crack initiation in fibre reinforced epoxy laminates [22-23]. Thus, at each step and at each matrix sampling point, the principal strains are computed. A local (crack) coordinate system O-1-2-3 is established in which the three axes are along the directions of the three principal strains ( $\varepsilon_1 \geq \varepsilon_2 \geq \varepsilon_3$ ), see Fig. 3-13. The maximum principal strain damage criterion is then specified by

$$\varepsilon_1 \geq \varepsilon_{cr} \quad (3.23)$$

And when this condition is met, then a crack in the plane perpendicular to the direction of the  $\varepsilon_1$  is deemed to have initiated.

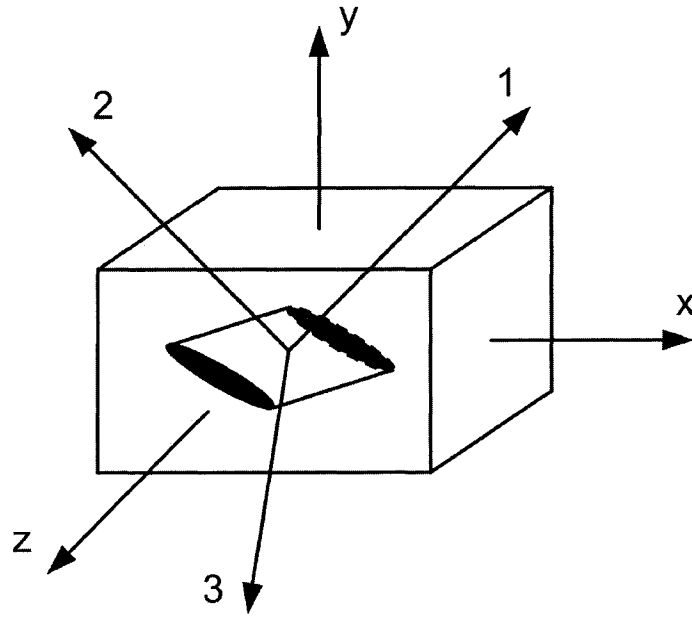


Fig. 3-13 Global and local coordinate systems of a crack.

### 3.4.2 Post-damage Constitutive Model

Once a crack is formed, it is assumed that it cannot transfer normal and shear stresses across the crack plane, i.e.,  $\sigma_{11}$ ,  $\sigma_{12}$  and  $\sigma_{13} \rightarrow 0$ . The subscript 1 denotes the Cartesian axis perpendicular to the crack plane while 2 and 3 are in the crack plane (Fig. 3-13). However, the ability to transfer the other stress components is not affected by the crack formation. Let the stress and strain vectors in the local (crack) coordinate system be designated by

$$\begin{aligned} \{\sigma\}^{cr} &= \{\sigma_{11}, \sigma_{22}, \sigma_{33}, \sigma_{12}, \sigma_{23}, \sigma_{31}\}^T \\ \{\varepsilon\}^{cr} &= \{\varepsilon_1, \varepsilon_2, \varepsilon_3, \gamma_{12}, \gamma_{23}, \gamma_{31}\}^T \end{aligned} \quad (3.24)$$

and the stress and strain vectors in the global (O-x-y-z) coordinate system are

$$\begin{aligned}\{\sigma\}^{gl} &= \{\sigma_{xx}, \sigma_{yy}, \sigma_{zz}, \sigma_{xy}, \sigma_{yz}, \sigma_{zx}\}^T \\ \{\varepsilon\}^{gl} &= \{\varepsilon_{xx}, \varepsilon_{yy}, \varepsilon_{zz}, \gamma_{xy}, \gamma_{yz}, \gamma_{zx}\}^T\end{aligned}\quad (3.25)$$

Thus, the post-damage constitutive model in the crack coordinate system is:

$$\{\Delta\sigma\}^{cr} = E_t [D] \{\Delta\varepsilon\}^{cr} - \chi [B] \{\sigma\}^{cr} \quad (3.26)$$

or written in its full form:

$$\begin{pmatrix} \Delta\sigma_{11} \\ \Delta\sigma_{22} \\ \Delta\sigma_{33} \\ \Delta\sigma_{12} \\ \Delta\sigma_{23} \\ \Delta\sigma_{31} \end{pmatrix}^{cr} = E_t \begin{pmatrix} \beta Z_1 & 0 & 0 & 0 & 0 & 0 \\ 0 & Z_1 & Z_2 & 0 & 0 & 0 \\ 0 & Z_2 & Z_1 & 0 & 0 & 0 \\ 0 & 0 & 0 & \beta Z_3 & 0 & 0 \\ 0 & 0 & 0 & 0 & Z_3 & 0 \\ 0 & 0 & 0 & 0 & 0 & \beta Z_3 \end{pmatrix} \begin{pmatrix} \Delta\varepsilon_1 \\ \Delta\varepsilon_2 \\ \Delta\varepsilon_3 \\ \Delta\gamma_{12} \\ \Delta\gamma_{23} \\ \Delta\gamma_{31} \end{pmatrix}^{cr} - \chi \begin{pmatrix} 1 & 0 & 0 & 0 & 0 & 0 \\ 0 & 0 & 0 & 0 & 0 & 0 \\ 0 & 0 & 0 & 0 & 0 & 0 \\ 0 & 0 & 0 & 1 & 0 & 0 \\ 0 & 0 & 0 & 0 & 0 & 0 \\ 0 & 0 & 0 & 0 & 0 & 1 \end{pmatrix} \begin{pmatrix} \sigma_1 \\ \sigma_2 \\ \sigma_3 \\ \sigma_{12} \\ \sigma_{23} \\ \sigma_{31} \end{pmatrix}^{cr} \quad (3.27)$$

In the above,

$$Z_1 = \frac{1-\nu}{(1+\nu)(1-2\nu)}, \quad Z_2 = \frac{\nu}{(1+\nu)(1-2\nu)}, \quad Z_3 = \frac{1}{2(1+\nu)}, \quad (3.28)$$

$E_t$  is the modulus of the epoxy under uniaxial tensile loading at the instant of damage,  $\beta$  is a small number which represents the loss of the stiffness in these three particular stress directions and the constant  $\chi$  allows the three stress components to be reduced to near zero values in a sufficiently short time duration.

In Ref. [10], a series of uniaxial tensile tests on pure epoxy specimens (Epon 826/9551) at a strain rate of  $10^{-4} \text{ s}^{-1}$  indicated a failure strain of 4.8%, therefore, the value of  $\varepsilon_{cr} = 4.8\%$  is used in this analysis. Also,  $E_t = 284 \text{ MPa}$  is taken as the tangent modulus prior to failure of the epoxy resin under the uniaxial tensile loading. For Epon

828/Z and Epon 815/V140, the constant  $\varepsilon_{cr}$  is taken from the test in [1], and  $E_t$  is taken as  $E/10$ . The constants  $\varepsilon_{cr}$  and  $E_t$  for the three epoxies are also listed in Table 3-1.

For example, the values of  $\beta$  and  $\chi$  are taken to be 0.001 and 0.05, respectively, in the calculation for Epon 826/9551. With such a choice of the values of the constants in Eqn. (3.27), the above constitutive relation would reduce the stress components across the crack plane to a very small value in a short time (zero is the asymptotic limit). The matrix element then cannot carry loads in the corresponding direction; thus, simulating the damage process.

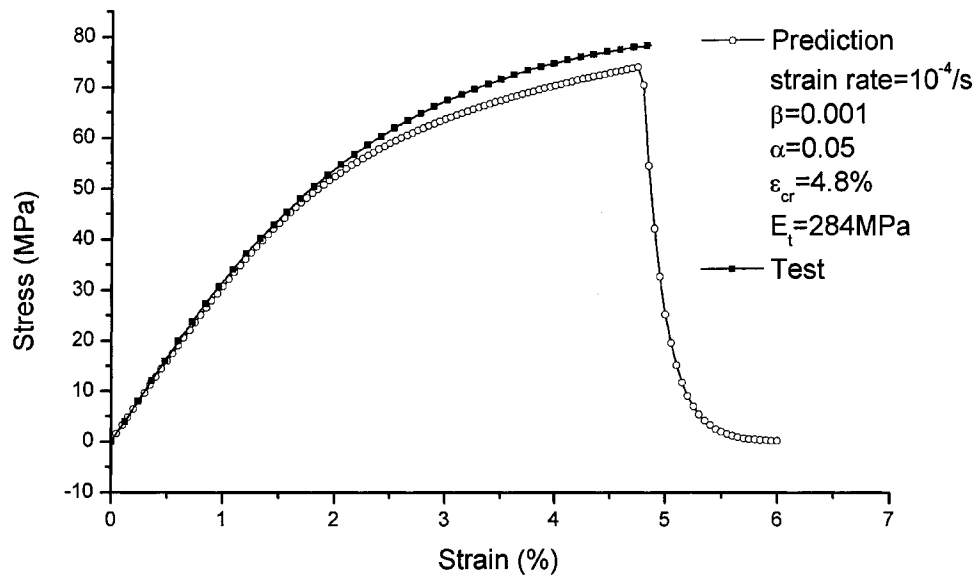


Fig. 3-14 The response of a matrix element including damage process.

Figure 3-14 shows the response of a matrix element before and after damage. Also shown is the test result [10] of epoxy specimens under uniaxial tensile loading at a strain rate of  $10^{-4}\text{s}^{-1}$ . It can be seen that the response before failure is in good agreement with the test data. These values will be used in the following analysis for composite laminates.

### 3.4.3 Coordinate System Transformation

The crack orientation in a 3-D composite unit cell may vary at different locations; therefore, it would be convenient to have the post-damage relation transformed to the global coordinate system, where the FEA is carried out. Let the direction cosines of the principal strains  $\varepsilon_i$  ( $i=1, 2, 3$ ) be denoted by  $(\ell_i \ m_i \ n_i)$ . Therefore, the transformation matrix between the local and global coordinate systems can be written as,

$$[T] = \begin{bmatrix} \ell_1^2 & m_1^2 & n_1^2 & \ell_1 m_1 & m_1 n_1 & n_1 \ell_1 \\ \ell_2^2 & m_2^2 & n_2^2 & \ell_2 m_2 & m_2 n_2 & n_2 \ell_2 \\ \ell_3^2 & m_3^2 & n_3^2 & \ell_3 m_3 & m_3 n_3 & n_3 \ell_3 \\ 2\ell_1 \ell_2 & 2m_1 m_2 & 2n_1 n_2 & \ell_1 m_2 + \ell_2 m_1 & m_1 n_2 + m_2 n_1 & n_1 \ell_2 + n_2 \ell_1 \\ 2\ell_2 \ell_3 & 2m_2 m_3 & 2n_2 n_3 & \ell_2 m_3 + \ell_3 m_2 & m_2 n_3 + m_3 n_2 & n_2 \ell_3 + n_3 \ell_2 \\ 2\ell_3 \ell_1 & 2m_3 m_1 & 2n_3 n_1 & \ell_3 m_1 + \ell_1 m_3 & m_3 n_1 + m_1 n_3 & n_3 \ell_1 + n_1 \ell_3 \end{bmatrix} \quad (3.29)$$

The stress and strain transformation is given by

$$\{\Delta\varepsilon\}^{cr} = [T]\{\Delta\varepsilon\}^{gl}, \quad \{\Delta\sigma\}^{cr} = [T]^{-T}\{\Delta\sigma\}^{gl}, \quad \{\sigma\}^{cr} = [T]^{-T}\{\sigma\}^{gl} \quad (3.30)$$

In the above, the superscript  $T$  is the transpose of a matrix, and superscript  $-T$  is the transpose of the inverse of a matrix, i.e.,  $[T]^{-T} = ([T]^{-1})^T$ . Substituting Eqn. (3.30) into Eqn. (3.26), the post-damage constitutive equation in the global coordinate system is

$$\{\Delta\sigma\}^{gl} = E_t [D'] \{\Delta\varepsilon\}^{gl} - \chi [B'] \{\sigma\}^{gl} \quad (3.31)$$

with

$$\begin{aligned} [D'] &= [T]^T [D] [T] \\ [B'] &= [T]^T [B] [T]^{-T} \end{aligned} \quad (3.32)$$

Note both  $[D']$  and  $[B']$  are  $6 \times 6$  matrix. Using Eqns. (3.29) and (3.30), the expression of the elements of the two matrices read

$$\begin{aligned} d'_{ij} &= t_{1i} t_{1j} \beta Z_1 + (t_{2i} Z_1 + t_{3i} Z_2) t_{2j} + (t_{2i} Z_2 + t_{3i} Z_1) t_{3j} + (t_{4i} t_{4j} \beta + t_{5i} t_{5j} + t_{6i} t_{6j} \beta) Z_3 \\ &\quad (i, j = 1, \dots, 6) \end{aligned} \quad (3.33)$$

$$\begin{aligned}
 b'_{ij} &= t_{1i}t_{1j} + \frac{1}{2}t_{4i}t_{4j} + \frac{1}{2}t_{6i}t_{6j} \quad (i = 1, \dots, 6, j = 1, 2, 3) \\
 b'_{ij} &= 2t_{1i}t_{1j} + t_{4i}t_{4j} + t_{6i}t_{6j} \quad (i = 1, \dots, 6, j = 4, 5, 6)
 \end{aligned}
 \tag{3.34}$$

For the stress-strain relationship of interphase element, the coordinate systems transformation between the interface coordinate system and the global coordinate system can be obtained similarly.

### 3.5 CONCLUDING REMARKS

- A nonlinear viscoelastic constitutive model is implemented into the FEM code ADINA. Example shows that the viscoelasticity of the epoxy has a significant influence on the composite response in the transverse direction.
- The interphase element developed based on the cohesive law is capable of modeling mixed mode (both normal and tangential) separations of the interface. The interphase element is convenient for implementation in a FEM code since an equivalent stress-strain relationship is used.
- Snap-back instability involved in the simulation of the interphase damage is illustrated by a 1-D example and a simple strategy is adopted to overcome the induced convergence difficulties.
- A smeared crack approach is proposed to model the initiation and propagation of the matrix cracking in a composite. Stress-strain relationships are used to describe a crack, thus making it convenient to implement into a commercial FEM code.

**BIBLIOGRAPHY**

1. Lorenzo, L., Hahn, H. T. (1986). Effect of ductility on the fatigue behavior of epoxy resins. *Polymer Engineering and Science*, **26**, 274-284.
2. Hashin, Z. (1966). Viscoelastic fiber reinforced materials. *AIAA Journal*, **4**, 1141-1147.
3. Zhang, Y., Xia, Z., Ellyin, F. (2004). Evolution and influence of residual stresses/strains of fibre reinforced laminates. *Composites Science and Technology*, **64**, 1613-1621.
4. Ellyin, F., Xia, Z., Chen, Y. (2002). Viscoelastic micromechanical modeling of free edge and time effects in glass fibre/epoxy cross-ply laminates. *Composites, Part A*, **33**, 399-409.
5. Bandyopadhyay, S. (1990). Review of the microscopic and macroscopic aspects of fracture of unmodified and modified epoxy resins. *Materials Science and Engineering*, **A125**, 157-184.
6. Daniel, I. M., Ishai, O. (1994). *Engineering Mechanics of Composite Materials*. Oxford University Press, New York, Oxford.
7. Smith, B. W. (1987). Fractography for continuous fiber composites. In *Engineered Materials Handbook, Volume 1, Composites*. ASM International, Metals Park, Ohio, USA, pp786-793.
8. Hoover, J. W., Kujawski, D., Ellyin, F. (1997). Transverse cracking of symmetric and unsymmetric glass-fiber/epoxy-resin laminates. *Composites Science and Technology*, **57**, 1513-1526.

9. Xia, Z., Hu, Y., Ellyin, F. (2003). Deformation behaviour of an epoxy resin subject to multiaxial loadings, part II: constitutive modeling and predictions. *Polymer Engineering and Science*, **43**, 734-748.
10. Hu, Y. (2002). *Multiaxial Behavior and Viscoelastic Constitutive Modeling of Epoxy Polymers*. PhD thesis, Department of Mechanical Engineering, University of Alberta, Canada.
11. Tvergaard, V. (1990). Effect of fibre debonding in whisker-reinforced metal. *Material Science and Engineering*, **A125**, 203-213.
12. Tvergaard, V. (1990). Analysis of tensile properties for a whisker-reinforced metal-matrix composite. *Acta Metallurgica*, **38**, 185-194.
13. Ishai, O. (1971). Failure of unidirectional composites in tension. *Journal of the Engineering Mechanics Division, Proceedings of the ASCE*, **97**, 205-222.
14. ADINA User's Manual, (1984). ADINA Engineering, Watertown, MA, USA.
15. Gao, Y. F., Bower, A. F. (2004). A simple technique for avoiding convergence problems in finite element simulations of crack nucleation and growth on cohesive interfaces. *Modelling and Simulation in Materials Science and Engineering*, **12**, 453-463.
16. Yang, Z. J., Proverbs, D. (2004). A comparative study of numerical solutions to non-linear discrete crack modelling of concrete beams involving sharp snap-back. *Engineering Fracture Mechanics*, **71**, 81-105.
17. Crisfield, M. A. (1981). A fast incremental-iterative solution procedure that handles snap-through. *Computers and Structures*, **13**, 55-62.
18. Ragon, S. A., Grüdäl, Z., Watson L. T. (2002). A comparison of three algorithms for

- tracing nonlinear equilibrium paths of structural systems. *International Journal of Solids and Structures*, **39**, 689–698.
19. Rots, J.G., Borst, R.D. (1989). Analysis of concrete fracture in “direct” tension. *International Journal of Solids and Structures*, **25**, 1381-1394.
20. Rots, J. G. (1991). Smearred and discrete representations of localized fracture. *International Journal of Fracture*, **51**, 45-59.
21. Jadhav, V. R., Sridharan, S. (2002). Micro-mechanical modeling of polymer based unidirectional composites: use of bulk properties of matrix with the smeared crack model. *Journal of Composite Materials*, **36**, 2735-2762.
22. Hoover, J. W., 1999. *Transverse Cracking of  $[\pm\theta,90_3]_S$  Composite Laminates*. MSc. thesis, Department of Mechanical Engineering, University of Alberta, Canada.
23. El Kadi, H. A. (1993). *Analysis and Failure of Laminated Fibre Reinforced Composites*. PhD thesis, Department of Mechanical Engineering, University of Alberta, Canada.

## CHAPTER 4

### MICROMECHANICAL ANALYSIS OF OFF-AXIS UNIDIRECTIONAL LAMINATES WITH INTRALAMINAR DAMAGE

#### 4.1 INTRODUCTION

Both macromechanical and micromechanical approaches can be used to model the mechanical response of the composite laminates, with or without an assumed damage occurrence. However, damage in the composite laminates evolve at a microscopic level and it would be desirable that a micromechanical approach be used, in which the fibre, matrix, and interphase/interface are explicitly accounted for in the model [1-2]. Assuming a uniform distribution of fibres, a representative volume element (RVE) or a repeated unit cell (RUC) can be used to conduct micromechanical studies [3]. By using the micromechanical approach, not only the effective properties of the composites can be obtained, but also various damage at the microscopic level can be predicted provided proper damage initiation criteria and evolution rules are available. Some recent micromechanical studies of laminates involving matrix cracking or interphase damage are reported, e.g., in [2, 4-10], among others. It is worthwhile to note that several researchers introduced cohesive interface cracking models into the micromechanical RUC analysis. A significant advantage of the cohesive cracking model is that both the initiation and propagation of the damage can be properly simulated [7-9]. While in the modeling of matrix cracking, the smeared crack method is used in [10]. This approach permits a description of the crack in terms of stress-strain relations; therefore, it is convenient to implement into a FEM code [11].

Most micromechanical analyses so far are confined to uniaxial loadings along the material principal directions, as reviewed by Pagano and Yuan [1]. For off-axis loadings, only limited attention has been paid. Examples of recent studies for off-axis loadings are Zhu and Sun [12] for thermoplastic matrix composites and Aghdam et al. [13] for metal matrix composites. However, in these researches, no damage models are involved.

In this chapter, the initiation and evolution of the intralaminar damage (matrix/fibre interface debonding and matrix cracking) and its effect on the global stress-strain relation of composite laminates are predicted by finite element micromechanical analysis. A three-dimensional RUC model based on a periodic fibre array is established, and appropriate periodic boundary conditions for combined shear and normal stress loading are applied. To model both the normal and tangential separations of the fibre/matrix interface, a thin layer of interphase elements is introduced in the unit cell model. The stress-strain relation of the interphase element is derived based on a cohesive law [7-8], which characterizes the dependence of the tractions on the displacement discontinuities across the interface. In addition, a viscous term is added to the cohesive law to overcome the convergence difficulty induced by the so-called snap-back instability in the numerical iterations. To model the matrix cracking, a 'smeared crack approach' [10-11] has been employed. In this approach the cracked solid is assumed to be a continuum which permits a crack description in terms of stress-strain relations, thus making it computationally more convenient to implement into the finite element displacement method. The rate-dependent behaviour of epoxy is described by a recently developed nonlinear viscoelastic constitutive model [14]. As application examples, two unidirectional laminates (E-glass fibre/Epon 828 and E-glass/Epon 815) under off-axis tensile loading are analyzed. Results show that the initiation and evolution of the intralaminar damage can be well

simulated. And the predicted global stress-strain curves are also in good agreement with the experimental results.

## 4.2 OFF-AXIS TENSILE LOADING OF UNIDIRECTIONAL LAMINATES

To conduct the micromechanical analysis of a unidirectional laminate under off-axis loading, a unit cell model should be extracted from the microstructure from the laminates and appropriate boundary conditions be applied to the unit cell. For nonlinear analysis, proper iteration is needed to simulate the loading conditions. These aspects will be described in the following sections.

### 4.2.1 Unit Cell of a Unidirectional Laminate

Assuming fibre distribution is periodic across the cross-section, a repeated unit cell (RUC) can be isolated from the composite laminates. The periodic fibre sequences commonly used are the square array and the hexagonal array [3]. In this chapter, the square array of fibre distribution is assumed, resulting in a rectangular parallelepiped RUC containing one fibre, as shown in Fig.4-1(b).

The cross section of the unit cell is a square with sides  $a$ , and thickness in the fibre direction is  $b$  (Fig.4-1(b)). The radius of the fibre,  $R$ , is determined by the fibre volume fraction  $V_f$  of the composite such that  $V_f = \pi R^2 / a^2$ .

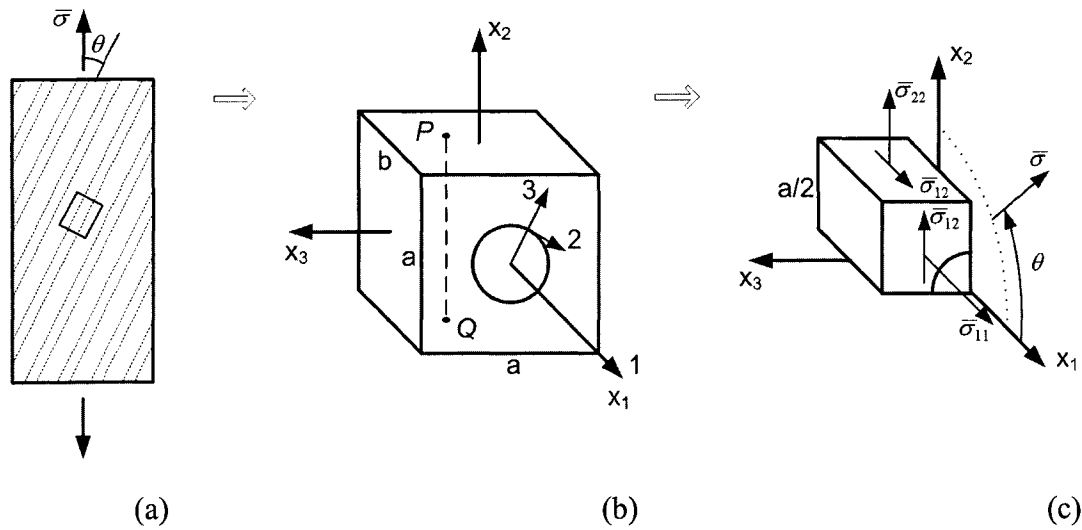


Fig. 4-1 Unidirectional laminates and unit cell model:

- (a) A unidirectional laminate under off-axis loading; (b) Unit cell for a square fibre array;  
 (c) Quarter of a unit cell.

#### 4.2.2 Periodic Boundary Conditions

The off-axis tensile loading applied to a unidirectional laminate can be decomposed into a set of multiaxial loading in the material principal directions of a lamina, as shown in Fig. 4-1(c).

$$\begin{aligned}
 \bar{\sigma}_{11} &= \bar{\sigma} \cos^2 \theta \\
 \bar{\sigma}_{22} &= \bar{\sigma} \sin^2 \theta \\
 \bar{\sigma}_{12} &= \bar{\sigma} \sin \theta \cos \theta
 \end{aligned} \tag{4.1}$$

Therefore the global stress and corresponding strain vectors can be written as:

$$\{\bar{\sigma}\} = \{\bar{\sigma}_{11}, \bar{\sigma}_{22}, 0, \bar{\sigma}_{12}, 0, 0\}^T \tag{4.2}$$

$$\{\bar{\varepsilon}\} = \{\bar{\varepsilon}_{11}, \bar{\varepsilon}_{22}, \bar{\varepsilon}_{33}, \bar{\varepsilon}_{12}, 0, 0\}^T \tag{4.3}$$

To impose the above global loadings to the RUC, appropriate periodic boundary conditions should be applied. The periodic boundary conditions can be expressed as the

displacement and traction compatibility relations between the two opposite surfaces of the RUC (see Chapter 2). Designating  $P$  and  $Q$  as two arbitrary corresponding points (with the same in-plane coordinates) on the two opposite surface of the RUC, Fig. 4-1(b), the general form of the periodic boundary conditions reads

$$u_i(P) - u_i(Q) = [x_j(P) - x_j(Q)] \bar{\varepsilon}_{ij} \quad (4.4)$$

$$\sigma_{ij}(P)n_j(P) = -\sigma_{ij}(Q)n_j(Q) \quad (4.5)$$

where  $n_j$  are the unit out normals of the RUC surface.

In practical numerical applications, Eqns. (4.4) and (4.5) can be greatly simplified as one solves the RUC problem using a FEM procedure and considers the symmetry conditions. In Chapter 2, a detailed derivation of the periodic boundary conditions for the one-quarter RUC, Fig. 4-1(c), under the combined shear and normal loading was provided considering the geometric, material, and loading symmetries. In such a way, the computation time required can be significantly reduced, especially for the current nonlinear problem. The applied boundary conditions to the one-quarter model are summarized as Eqns. (2.81) to (2.85) in Chapter 2.

### 4.2.3 Off-axis Loading Algorithm

In an off-axis loading of unidirectional laminate under strain control, the global strain in the loading direction (see Fig.4-1 (a) and (c)) is

$$\bar{\varepsilon} = \bar{\varepsilon}_{11} \cos^2 \theta + \bar{\varepsilon}_{22} \sin^2 \theta + 2\bar{\varepsilon}_{12} \cos \theta \sin \theta \quad (4.6)$$

For each time step,  $\Delta t$ , the strain increment is given by

$$\Delta \bar{\varepsilon} = \dot{\bar{\varepsilon}} \Delta t \quad (4.7)$$

where  $\dot{\bar{\epsilon}}$  is the applied global strain rate. To simulate the off-axis loading, an iterative procedure is required to ensure that proper proportions of the increments of  $\bar{\epsilon}_{11}$ ,  $\bar{\epsilon}_{22}$ ,  $\bar{\epsilon}_{12}$  are applied, so that Eqn. (4.1) is satisfied at each step. The iteration procedure is as follows [2]:

- (i) For each time step  $\Delta t$ , we have the trial increments of  $\bar{\epsilon}_{11}$ ,  $\bar{\epsilon}_{22}$ ,  $\bar{\epsilon}_{12}$ , which satisfy Eqn. (4.6).
- (ii) The solution gives the stress distribution in the unit cell, so the global stress components can be calculated from

$$\{\bar{\sigma}\} = \frac{1}{V} \int_V \{\sigma(x_1, x_2, x_3)\} dV \quad (4.8)$$

where  $V$  is the volume of the unit cell.

- (iii) Equation (4.1) is checked and, if it is satisfied (within certain error limit), then one proceeds to the next step. If not, new increments of  $\bar{\epsilon}_{11}$ ,  $\bar{\epsilon}_{22}$ ,  $\bar{\epsilon}_{12}$  are obtained and steps (i) to (iii) are repeated.

For a small time step, it could be assumed that the increments of  $\bar{\epsilon}_{11}$ ,  $\bar{\epsilon}_{22}$ ,  $\bar{\epsilon}_{12}$  are proportional to the corresponding increments of average stress components, then the new increments of  $\bar{\epsilon}_{11}$ ,  $\bar{\epsilon}_{22}$ ,  $\bar{\epsilon}_{12}$  can be estimated from the average stresses, Eqn. (4.8). Numerical calculation indicated that the required increments of  $\bar{\epsilon}_{11}$ ,  $\bar{\epsilon}_{22}$ ,  $\bar{\epsilon}_{12}$  could be obtained through a few iterations.

#### 4.2.4 Finite Element Analysis of the Unit Cell

Usually, an analytical solution of the unit cell problem presented in the previous sections is difficult to obtain, thus a numerical approach is required. In this study, the finite element method is used to conduct the analysis.

As application examples, two unidirectional laminates, E-glass/Epon 828(curing agent Z) and E-glass/Epon 815(curing agent Versamid 140), under off-axis tensile loading are analyzed, respectively. These examples are chosen because a detailed experimental study (Ishai [15]) has been conducted for the two laminates under off-axis loadings.

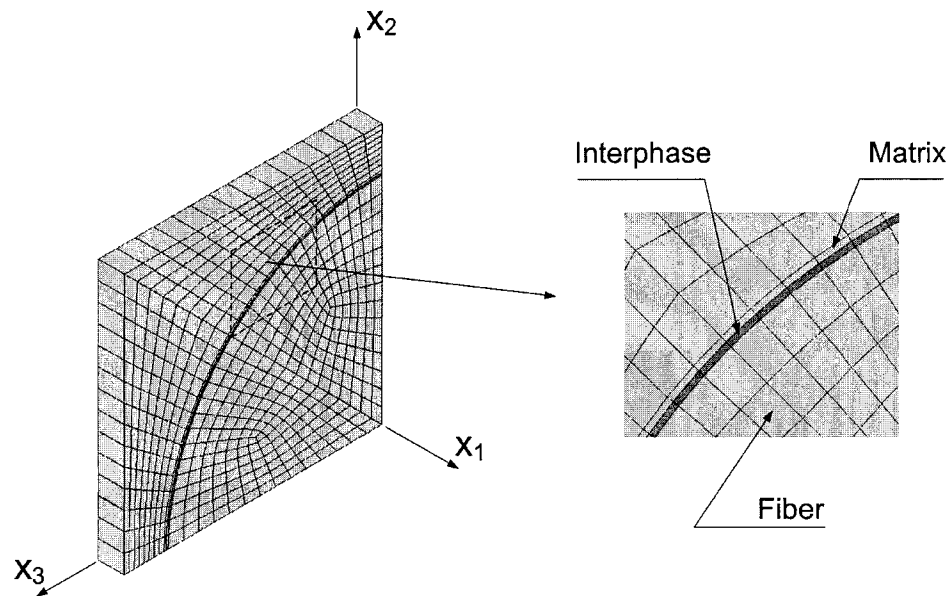


Fig. 4-2 Finite element mesh of the RUC model.

The cohesive stress-strain relations for the interphase element, the matrix cracking model and the viscoelastic constitutive model of the epoxy resin have been implemented into the FEM code ADINA as a user-defined material subroutine. The calculations were conducted on a SGI Origin 2000 computer system. Figure 4-2 shows the finite element meshes of the RUC model with 8 node brick elements. The mesh consists of 1226 nodes

and 574 elements. A thin layer of interphase element around the fibre ( $h/R = 0.02$ ,  $h$  and  $R$  are the thickness of the interphase element and the radius of the fibre, respectively) is shown in the inset.

### **Mesh convergence**

To determine if the mesh (Mesh A) shown in Fig. 4-2 is sufficient to obtain converged results, a finer mesh (mesh B) shown in Fig. 4-3 is used to conduct the convergence study. The mesh B is also constructed with 8-noded brick element, however, this finer mesh consists of 3884 nodes and 1872 elements.

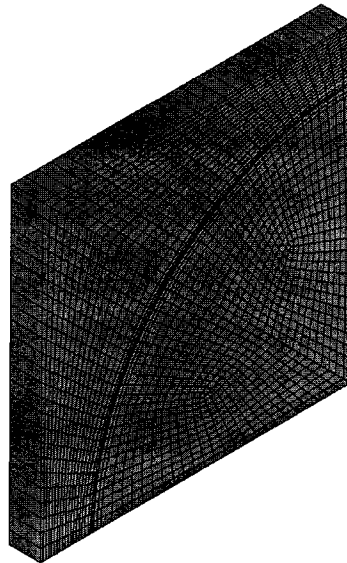


Fig. 4-3 Finer mesh for RUC (Mesh B).

E-glass/Epon 828 unidirectional laminate is analyzed using the aforementioned two meshes. The material constants for E-glass (linear elastic) and Epon 828 (nonlinear viscoelastic) are listed in Table 3-1. Evolution of interphase damage is simulated using

the interphase model described in Section 3.3, Chapter 3. The constants used in the interphase model are shown in the legend of Fig. 4-4.

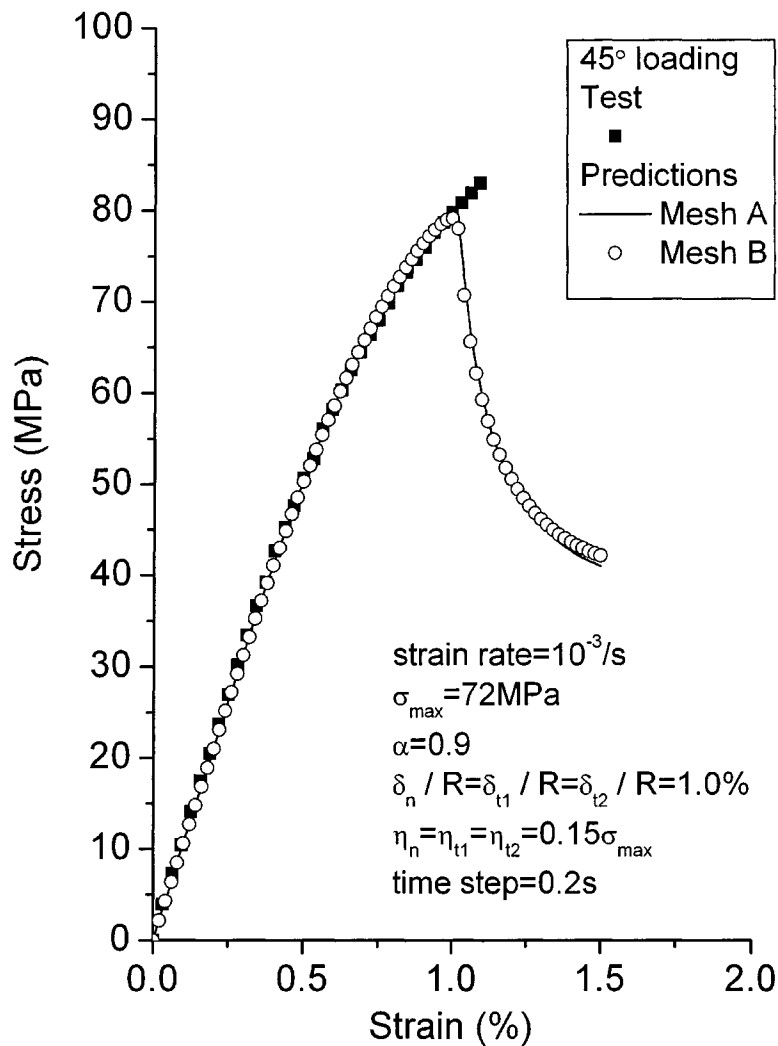


Fig. 4-4 Comparison of the results of two meshes and the test.

Figure 4-4, for example, shows the predicted stress-strain curve of 45° off-axis loading of glass/Epon 828 unidirectional laminates. It can be seen that predictions from the two meshes are very close. Therefore mesh A, i.e. the mesh shown in Fig. 4-2 will be used in the following sections to conduct the analysis. Note that in the fibre direction ( $x_1$

direction), only one layer of elements is sufficient, since all the stress and strain components are invariant along the fibre direction. Note the test data from [15] are also plotted in the figure.

### 4.3 ANALYSIS OF GLASS/EPON 828 LAMINATES

#### 4.3.1 Test Results

Detailed test results can be found in [15]. It is noted that the global stress-strain curves for four off-axis angles ( $90^\circ$ ,  $45^\circ$ ,  $30^\circ$ , and  $20^\circ$ ) under a strain rate of about  $10^{-3}/s$  were obtained from these tests. Furthermore, the tests revealed the damage mechanisms for the unidirectional laminates. For the E-glass/Epon 828 laminates, the bonding between the fibre and matrix was relatively weak and interfacial debonding was the dominant failure mechanism for all the off-axis orientations.

Figure 4-5 shows the fractographs of the failed unidirectional laminate specimens under  $90^\circ$ ,  $45^\circ$  and  $20^\circ$  off-axis loadings for the glass/Epon 828 laminates. In the picture, those vertical striped zones with relatively smooth surfaces indicate complete separations between the fibres and the epoxy matrix, while those zones with 'wrinkles' are damaged surface regions of the epoxy matrix. Note these fractographs are the scanning electron microscopy (SEM) pictures of the final failure surfaces of the specimen, thus there is always some fractured zones produced from the separation of the matrix. However, it can be seen that the interphase/interface separation is the primary damage mode for glass/Epon 828 laminates.

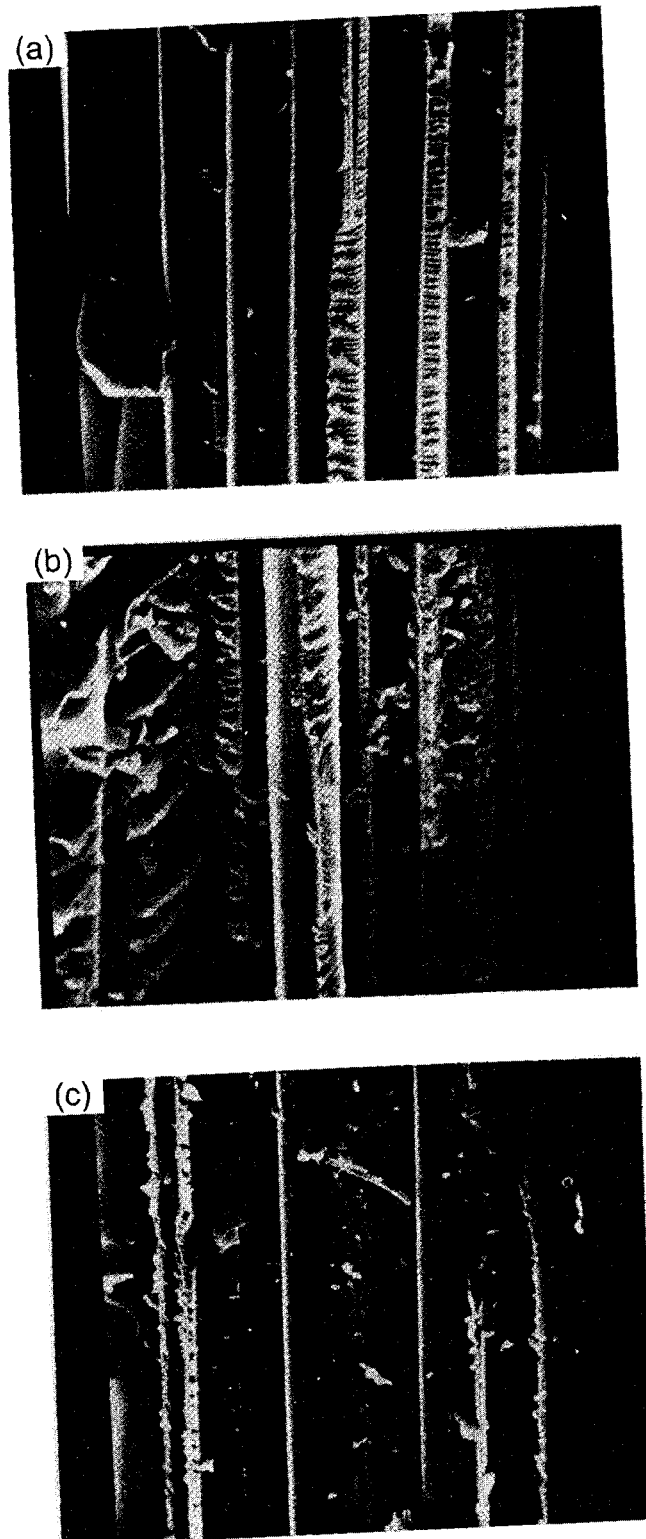


Fig. 4-5 Fractographs of glass/Epon 828 coupon specimens under off-axis loadings:

(a) 90° loading; (b) 45° loading; (c) 20° loading (adopted from [15]).

### 4.3.2 Material Constants

In the current FEM analysis the glass fibre is assumed to be linear elastic with elastic constants listed in Table 3-1. The nonlinear viscoelastic model described in Chapter 3 is used to model the constitutive response of the epoxy matrix. The material constants needed for the viscoelastic model are also listed in Table 3-1.

The constants for the interphase damage model and the matrix damage model are mainly determined by numerical tests. The following constants for the cohesive model are used for the E-glass/Epon 828 system:

$$\sigma_{\max} = 72 \text{MPa}, \delta_n / R = \delta_{t1} / R = \delta_{t2} / R = 1.0\%, \alpha = 0.9 \quad (4.9)$$

For the Epon 828 matrix, the constants used for the matrix damage model are:

$$\varepsilon_{cr} = 0.09, E_t = 0.1E, \beta = 0.001, \chi = 0.02 \quad (4.10)$$

Note  $\varepsilon_{cr} = 0.09$  is the uniaxial tensile test value for Epon 828/Z in [16].

To compare with the test results in Ishai [15], uniaxial tensile loads at different off-axis angles were applied to the unidirectional laminates at a constant strain rate of  $10^{-3} \text{ s}^{-1}$ .

### 4.3.3 Numerical Results for Glass/Epon 828 Laminates

#### Prediction of Global Stress-strain Curves

Figure 4-6 shows the predicted global stress-strain curves and the comparison with the test results of Ishai [15]. All the calculations used the same set of material constants as shown in Table 3-1 and the off-axis angles considered were  $90^\circ$ ,  $45^\circ$ ,  $30^\circ$ ,  $20^\circ$ , as in the test. It can be seen that stress-strain curves of the laminates with four different angle orientations are well predicted by the present micromechanical analysis. In the calculations for all the four off-axis angles (glass/Epon 828 laminates),

$\eta_n / \sigma_{\max} = \eta_{t1} / \sigma_{\max} = \eta_{t2} / \sigma_{\max} = 0.15$  were used to avoid the convergence problems caused by the snap-back instabilities.

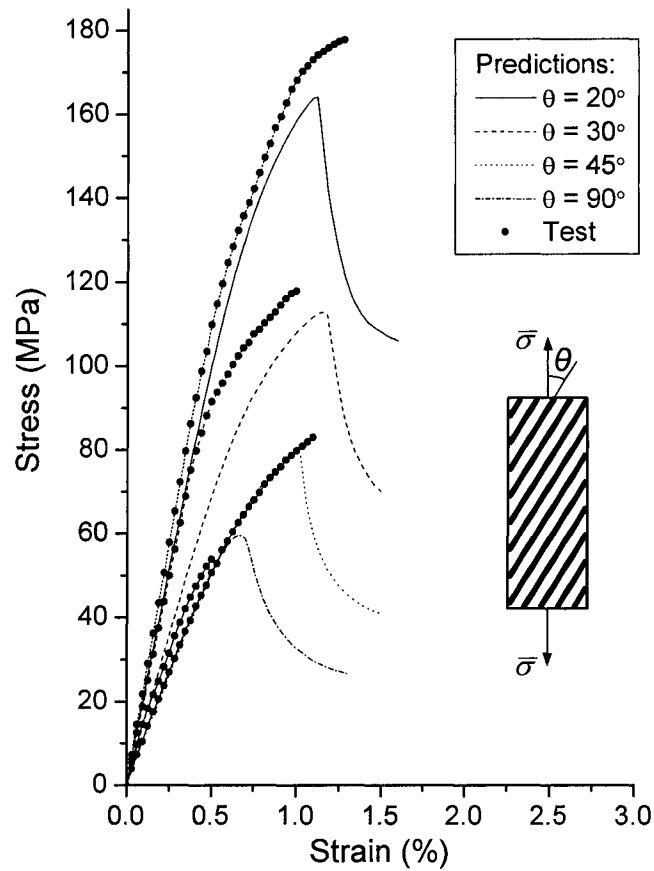


Fig. 4-6 Global stress-strain curve of glass/Epon 828 laminates under off-axis loadings.

### Strength vs. off-axis orientations

Taking the peak of the predicted stress-strain curve as the strength of an off-axis laminate, one obtains the tensile strength  $\bar{\sigma}_s$  of unidirectional laminates vs. the off-axis orientation  $\theta$ , as shown in Fig. 4-7. Note to obtain the predicted curve in the figure, more off-axis angles besides  $\theta = 90^\circ, 45^\circ, 30^\circ, 20^\circ$ , are calculated using the same set of material constants. Thus the off-axis angles calculated are  $\theta = 90^\circ, 80^\circ, 70^\circ, 60^\circ, 45^\circ, 30^\circ$ ,

20°, 10°, 5°, and 0°. The test values ( $\theta = 90^\circ, 60^\circ, 45^\circ, 30^\circ, 20^\circ,$  and  $10^\circ$ ) are also from Ishai [15]. It is seen that the predictions agree well with the test results.

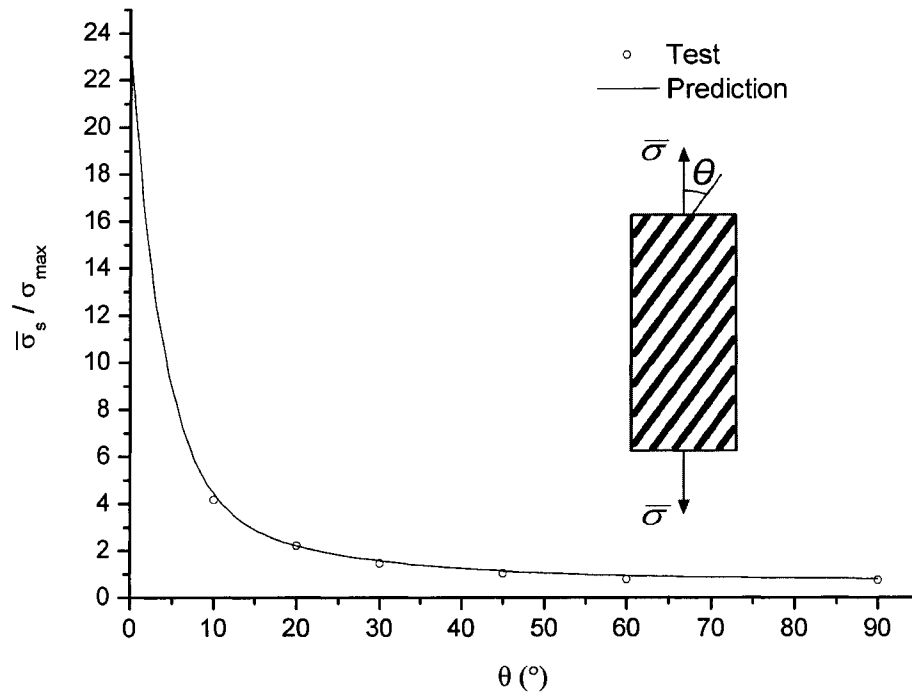


Fig. 4-7 Strength of unidirectional laminates vs. off-axis orientations ( $\sigma_{max} = 72MPa$ ).

It should be noted that, for  $90^\circ \geq \theta \geq 5^\circ$ , the FEM results indicate that the damage initiates as the interphase separation. However, for the prediction of  $\theta = 0^\circ$  (longitudinal loading), the numerical result indicates that both the matrix damage and interphase damage criteria are not met up to global strain  $\bar{\epsilon}_{11} \geq 2.5\%$ . Therefore a fibre damage criterion is adopted. This criterion assumes that the fibre is damaged when the axial strain of the fibre exceeds a prescribed maximum value,  $\epsilon_{f_{max}}$ . For the E-glass fibre used in this investigation,  $\epsilon_{f_{max}} = 2.3\%$  is assumed [17].

### Microscopic Deformation and Interphase Damage Initiation

The microscopic deformation including the interphase damage behaviour can be directly obtained from the current analysis. Figures 4-8(a) and (b) show the deformed RUC and the separation of the interphase for  $90^\circ$  and  $45^\circ$  off-axis loadings, respectively. The deformations of  $30^\circ$  and  $20^\circ$  loadings are similar to that of the  $45^\circ$  loading. As shown in Fig. 4-8(a), for the  $90^\circ$  (transverse) loading, the maximum separation of the interphase is normal to the interphase with  $[u_3] \neq 0$ ,  $[u_1] = [u_2] = 0$ . For  $45^\circ$  off-axis loading, the interphase damage shows a mixed mode: opening normal to the interphase and sliding in the 1 direction, i.e. in this case,  $[u_3] \neq 0$ ,  $[u_1] \neq 0$ , but  $[u_2] = 0$  as shown in Fig. 4-8(b). Note also that for transverse loading, the deformed surfaces of the RUC remains rectangular, while for  $45^\circ$  off-axis loading, the surfaces originally perpendicular to the fibre do not remain plane after the deformation.

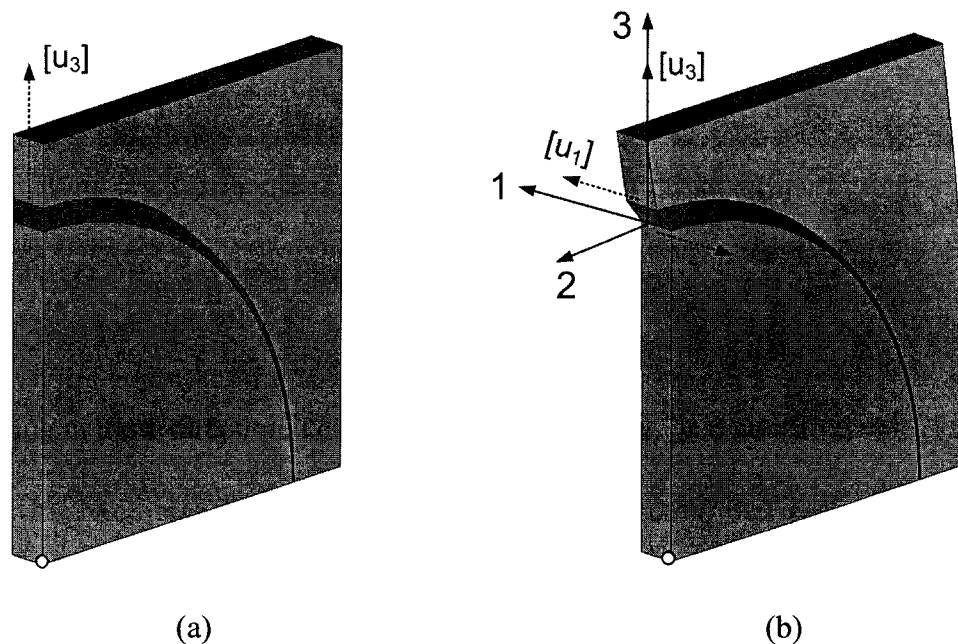


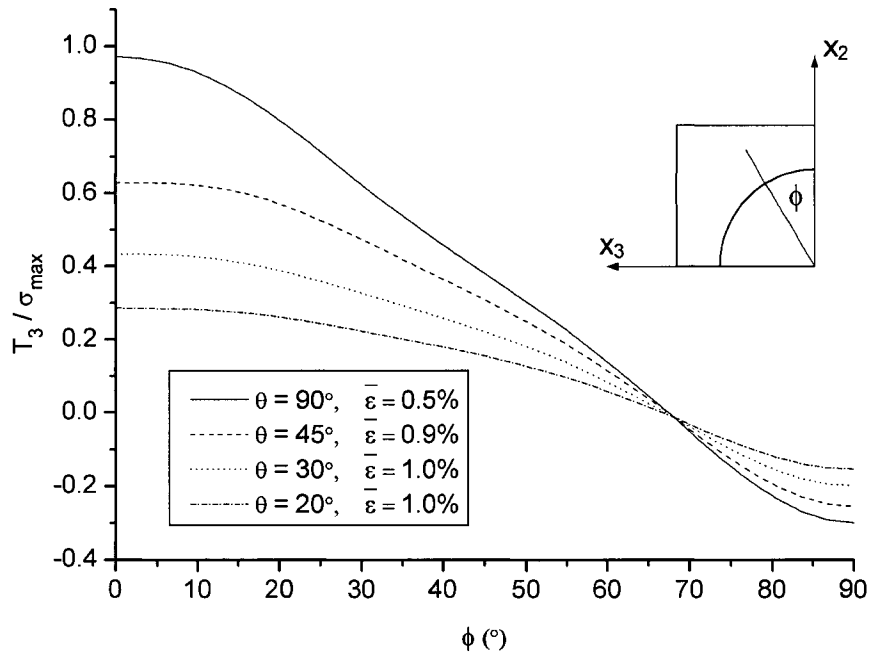
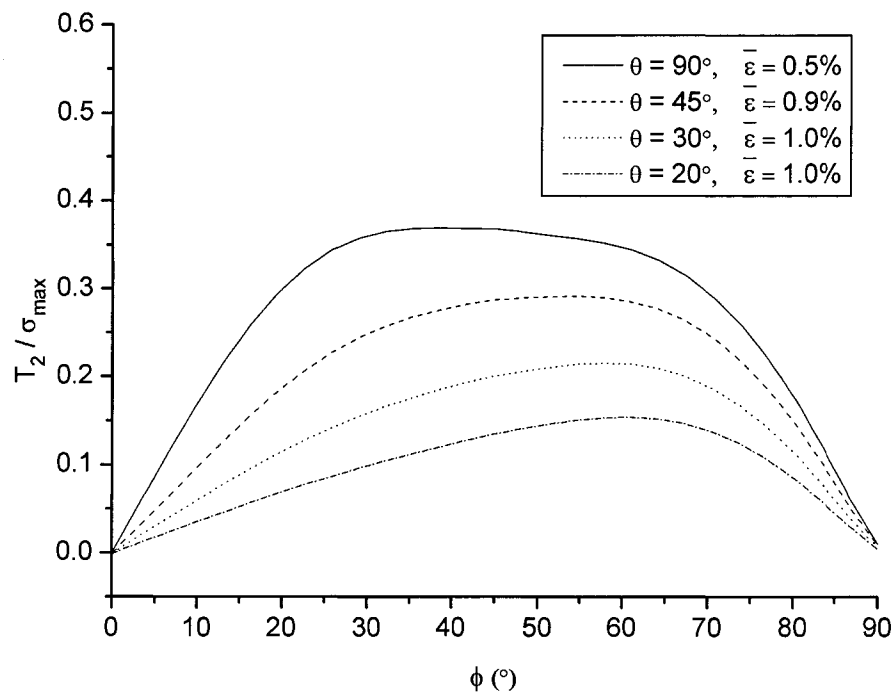
Fig. 4-8 Deformed shape of the RUC and interphase damage for different off-axis angles:

(a)  $90^\circ$  loading; (b)  $45^\circ$  loading.

Figures 4-9 to 4-11 plot distribution of the tractions in the interphase for the four fibre angles at the instant prior to but close to the peak point of the stress-strain curves. For  $90^\circ$ ,  $45^\circ$ ,  $30^\circ$ , and  $20^\circ$  off-axis angles, the corresponding global strains are  $\bar{\epsilon} = 0.5\%$ ,  $0.9\%$ ,  $1.0\%$ , and  $1.0\%$ , respectively.

It can be seen from Figs. 4-9 to 4-11 that, along the circumferential direction of the interphase (see inset in Fig. 4-9 for angle  $\phi$ ), the normal traction  $T_3$  and sliding traction  $T_1$  for all the four off-axis angles have maximum values at  $\phi=0^\circ$ , thus indicates that the interphase debonding will initiate at  $\phi = 0^\circ$ . However, the proportions of tractions  $T_3$  and  $T_1$  are different for different off-axis angles  $\theta$ . When  $\theta = 90^\circ$  (transverse loading), the tractions  $T_2$  and  $T_1$  are very small at  $\phi = 0^\circ$ , while  $T_3 / \sigma_{\max}$  is close to 1 as indicated by Fig. 4-9, thus the initiation of the damage is mainly caused by the traction  $T_3$ . When  $\theta = 45^\circ$ ,  $T_3 / \sigma_{\max} \approx 0.6$ ,  $T_1 / \sigma_{\max} \approx 0.7$  (at  $\phi=0^\circ$ ), thus both tractions  $T_3$  and  $T_1$  contribute to the initiation of the interphase damage, resulting in the interphase separates with the combined normal opening and the sliding along the fibre direction.

Figure 4-12 portrays the distributions of the maximum principal strain near the interphase (in the matrix elements adjacent to interphase elements shown in Fig. 4-2) for the four off-axis angles. Note these curves are also plotted at the same global strains as those in Figs. 4-9 to 4-11. Thus comparison of the maximum principal strain and the interphase traction at the approximate same location will indicate the probable damage initiations (matrix cracking or interphase separation) at the next loading level. Therefore the two intralaminar damage modes can be distinguished. Of course the accurate judgment will be based on the damage criteria. For the present glass/Epon 828 laminates, numerical results indicate that the damage mode is interphase separation.

Fig. 4-9 Distribution of  $T_3$  (Epon 828 laminates).Fig. 4-10 Distribution of  $T_2$  (Epon 828 laminates).

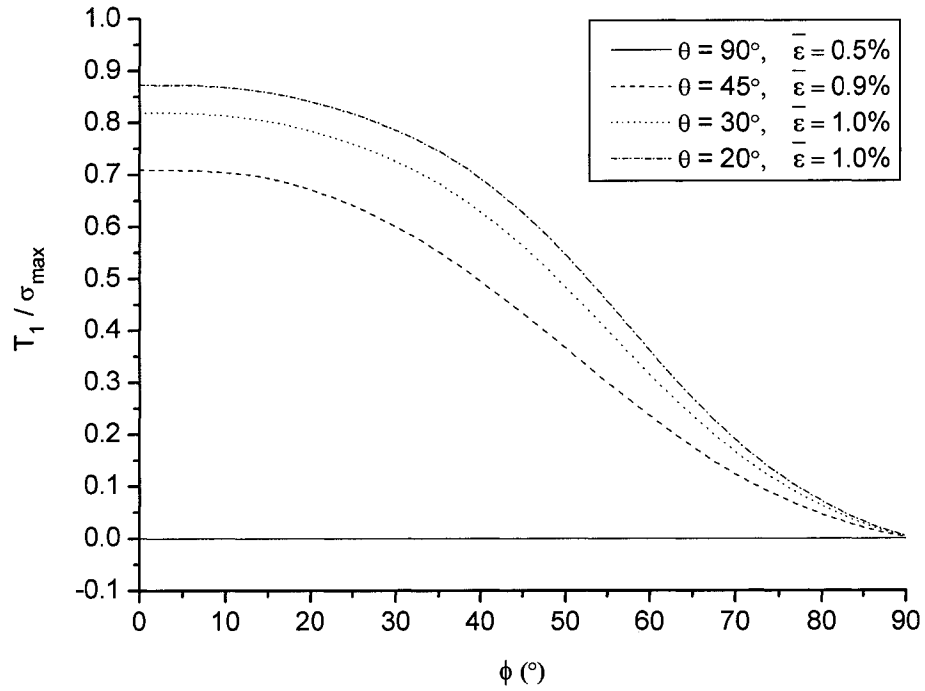


Fig. 4-11 Distribution of  $T_1$  (Epon 828 laminates).

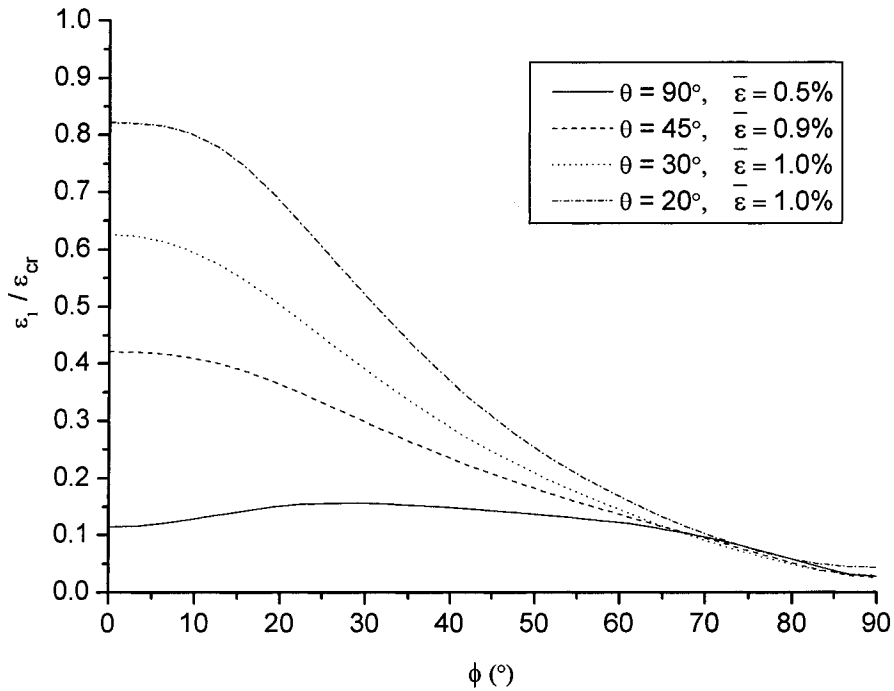


Fig. 4-12 Distribution of the first principal strain near the interphase (Epon 828 laminates).

### Evolution of interphase damage

The propagation of the interphase damage can also be depicted by the interphase traction distributions in the RUC. For transverse loading, for example, Figure 4-13 shows the distribution of the interphase tractions at different loading levels. At  $\bar{\varepsilon} = 0.5\%$ , the traction  $T_3$  reaches the maximum value at  $\phi = 0^\circ$ , thus the interphase starts separating at this point. The traction decreases with the increase of the separation, thus the normalized traction decreases to about 65% at global strain of 0.7% and at global strain of 0.8%, the total separation occurs, i.e. the traction drops to zero. With further increase of loading to 0.9% and 1.1%, the damaged zone propagates further along the circumferential direction. The interphase damage propagates to an angle of  $\phi = 40^\circ$  at the global strain of  $\bar{\varepsilon} = 1.1\%$ .

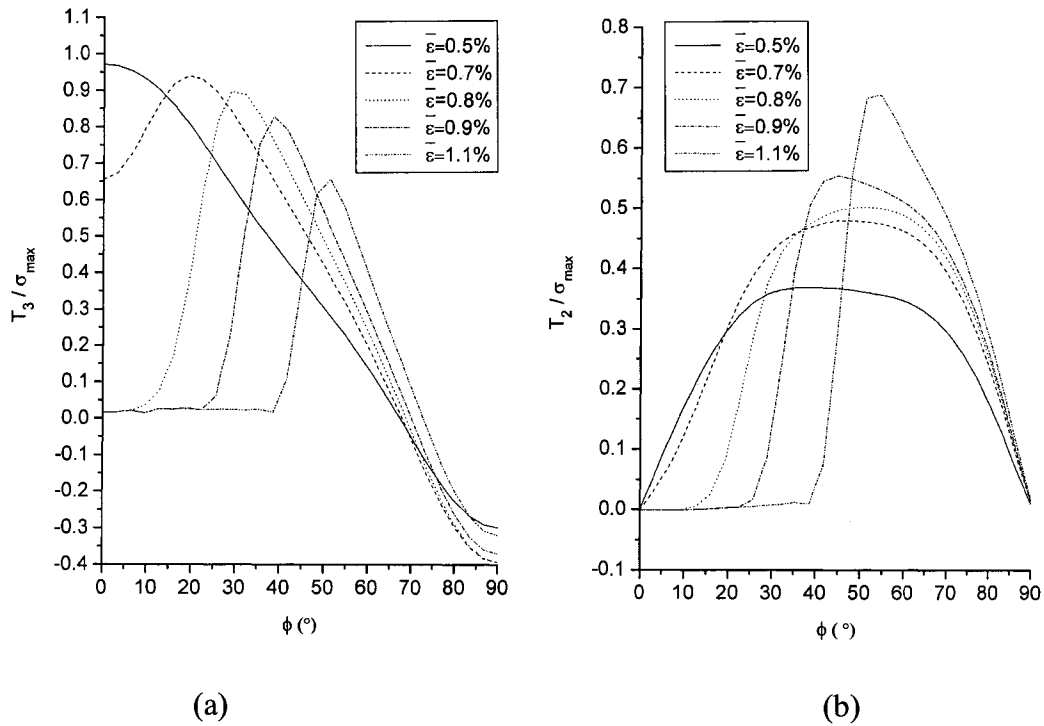


Fig. 4-13 Traction distributions in interphase prior to and after damage:

(a) Traction  $T_3$ ; (b) Traction  $T_2$ .

## 4.4 ANALYSIS OF GLASS/EPON 815 LAMINATES

### 4.4.1 Test Results

For the E-glass/Epon 815 laminates, there were two damage modes [15]: For off-axis angles of  $10^\circ < \theta < 60^\circ$ , matrix failure prevailed; and for off-axis angles of  $60^\circ < \theta < 90^\circ$ , interfacial debonding was the predominate damage mode. In the global stress-strain curves, matrix failure was characterized by a plateau and the final failure occurred after large deformations. Figure 4-14 shows the fractographs of the failed unidirectional laminate specimens under  $90^\circ$ ,  $45^\circ$  and  $20^\circ$  off-axis loadings for the glass/Epon 815 laminates. For  $90^\circ$  loading shown in Fig. 4-14a, those vertical stripped zones with relatively smooth surfaces indicate complete separations between the fibres and the epoxy matrix, while those zones with 'wrinkles' are damaged surface of epoxy matrix. Thus the damage is mainly the interphase separation, or at least it is the mixed interphase damage and matrix damage. For  $45^\circ$  and  $20^\circ$  off-axis loadings shown in Fig. 4-14b and c, however, there are almost *no* smooth zones, thus the matrix damage is the primary damage mode.

Also, stress-strain curves for off-axis angles  $\theta = 90^\circ$ ,  $45^\circ$ ,  $30^\circ$ , and  $20^\circ$  are obtained under strain rate of about  $10^{-3}/s$ .

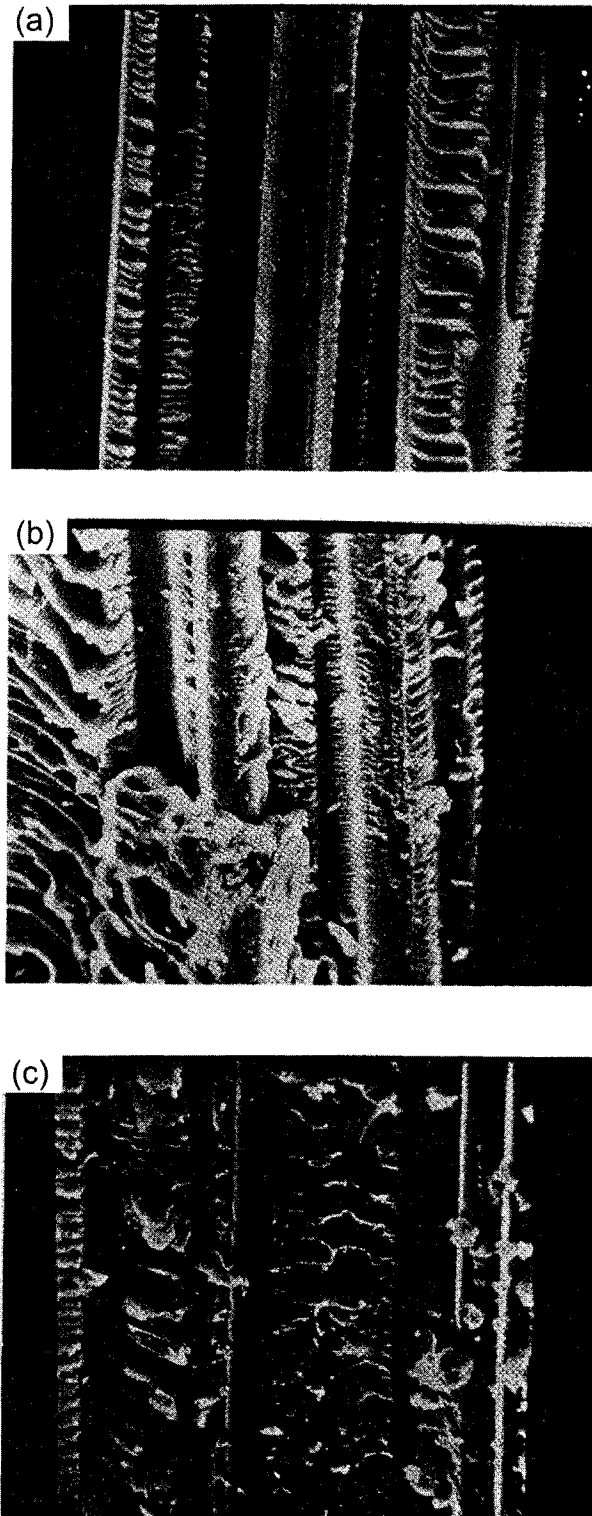


Fig. 4-14 Fractographs of glass/Epon 815 coupon specimens under off-axis loadings:

(a)  $90^\circ$  loading; (b)  $45^\circ$  loading; (c)  $20^\circ$  loading (adopted from [15]).

#### 4.4.2 Material Constants

The elastic constants for the E-glass fibre and the material constants needed for the viscoelastic model for Epon 815/Versamid 140 are listed in Table 3-1. The constants for the cohesive model for E-glass/Epon 815 are:

$$\sigma_{\max} = 80\text{MPa}, \delta_n / R = \delta_{t1} / R = \delta_{t2} / R = 1.5\%, \text{ and } \alpha = 1.0 \quad (4.11)$$

And for the Epon 815/Versamid 140, the constants used for the matrix damage model are:

$$\varepsilon_{cr} = 0.14, E_t = 0.1E, \beta = 0.001, \chi = 0.02 \quad (4.12)$$

Again, to compare with the test results in Ishai [15], uniaxial tensile loads at different off-axis angles were applied to the unidirectional laminates at a constant strain rate of  $10^{-3}$  /s.

#### 4.4.3 Numerical Results

The calculations for the glass/Epon 815 unidirectional laminates are similar to that for the glass/Epon 828 unidirectional laminates. All the calculations used the same set of material constants as shown in Table 3-1 and the off-axis angles considered were  $90^\circ$ ,  $45^\circ$ ,  $30^\circ$ ,  $20^\circ$ , as in the test. However, in all the four off-axis angles for glass/Epon 815, numerical results shows that no snap-back instabilities occurred during the calculation, thus,  $\eta_n = \eta_{t1} = \eta_{t2} = 0$ .

#### Global stress-strain curves

Figure 4-15 shows the predicted global stress-strain curves and the comparison with the test results. It can be seen again that the stress-strain curves under different loading angles are well predicted. However, for the glass/Epon 815 laminates, numerical results

show that for  $90^\circ$  loading, the damage mode is interphase damage; while for  $45^\circ$ ,  $30^\circ$ , and  $20^\circ$  loading angles, the damage mode is matrix cracking. This result is in agreement with the general conclusion of Ishai [15].

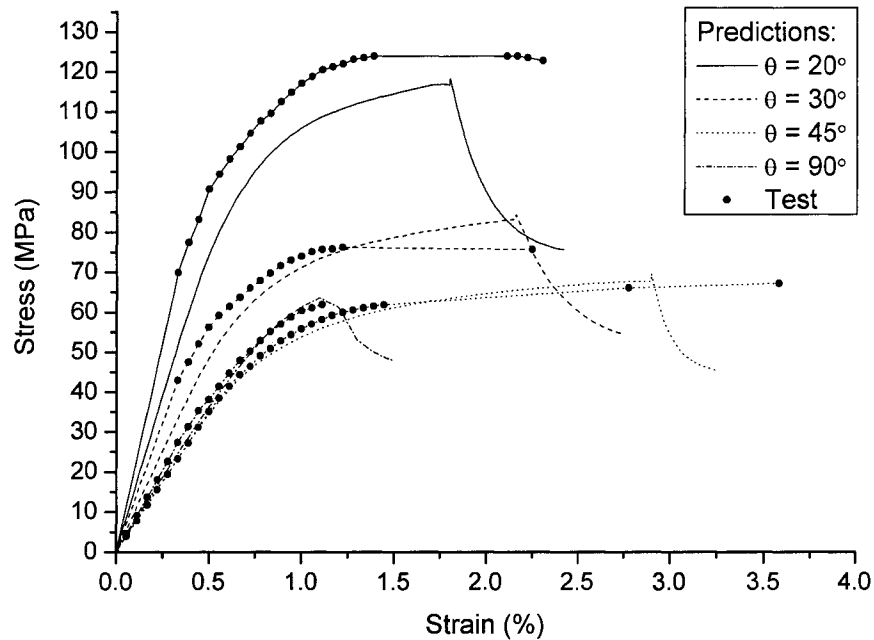
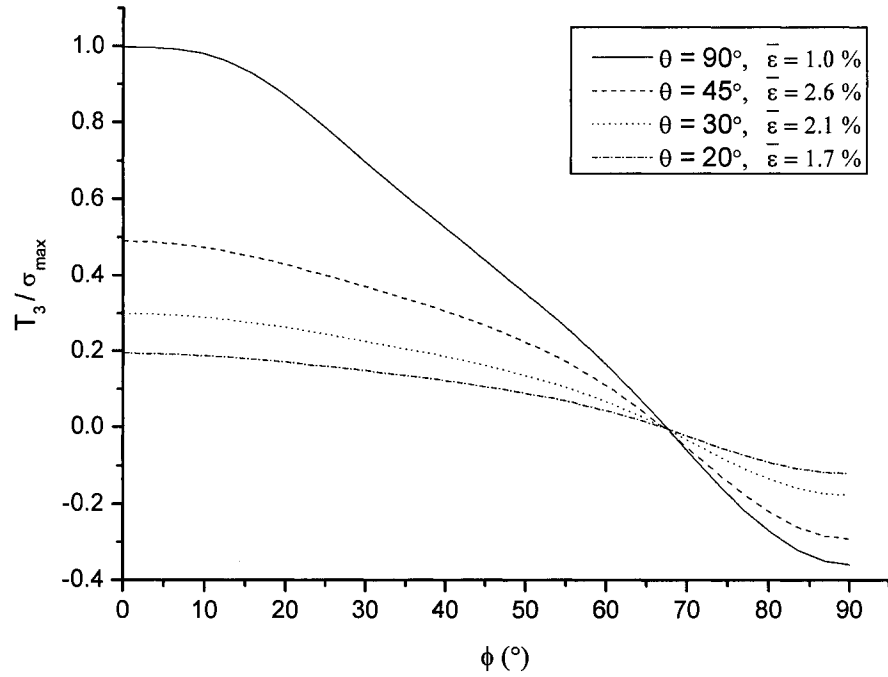
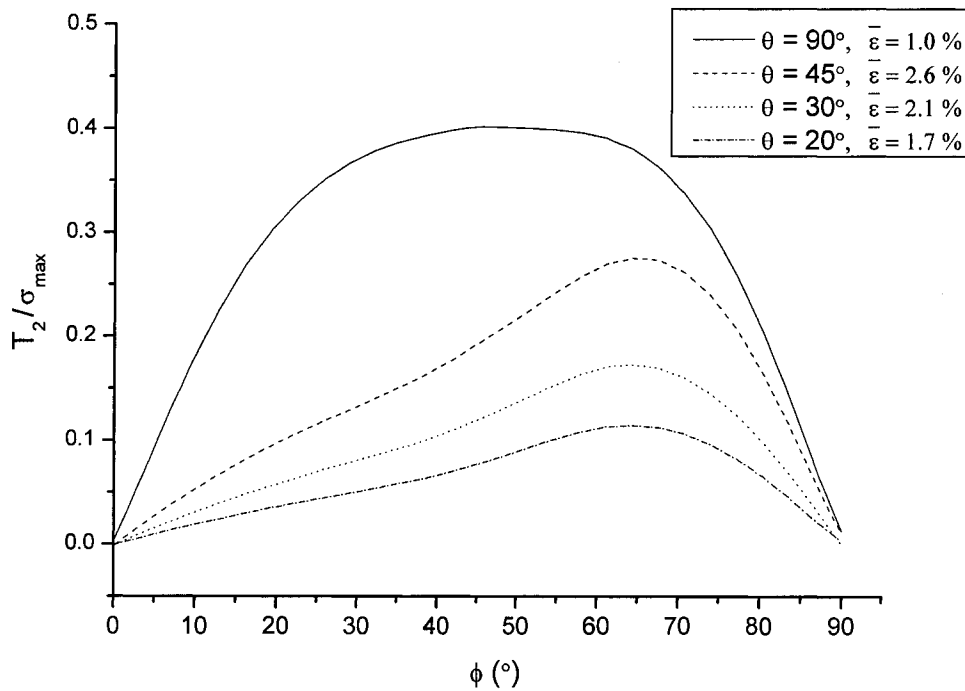


Fig. 4-15 Global stress-strain curve of glass/Epon 815 laminates under off-axis loadings.

### Prediction of damage

The initiation and evolution of the damage can be analyzed analogously to that of the glass/Epon 828 laminates. Figures 4-16 to 4-18 plot the distributions of the interphase tractions prior to damage. And Fig. 4-19 shows the distribution of the first principal strain in the matrix. For  $90^\circ$ ,  $45^\circ$ ,  $30^\circ$ , and  $20^\circ$  off-axis angles, the corresponding global strains are  $\bar{\epsilon} = 1.0\%$ ,  $2.6\%$ ,  $2.1\%$ , and  $1.7\%$ , respectively. From these distributions, the initiation of the damage upon further loadings can be predicted.

Fig. 4-16 Distribution of  $T_3$  (Epon 815 laminates).Fig. 4-17 Distribution of  $T_2$  (Epon 815 laminates).

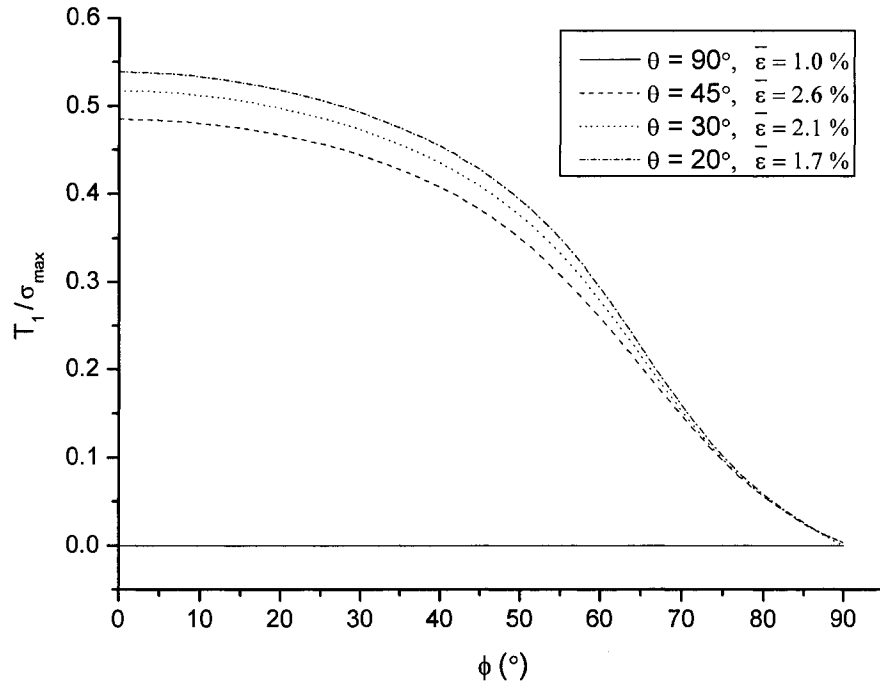


Fig. 4-18 Distribution of  $T_I$  (Epon 815 laminates).

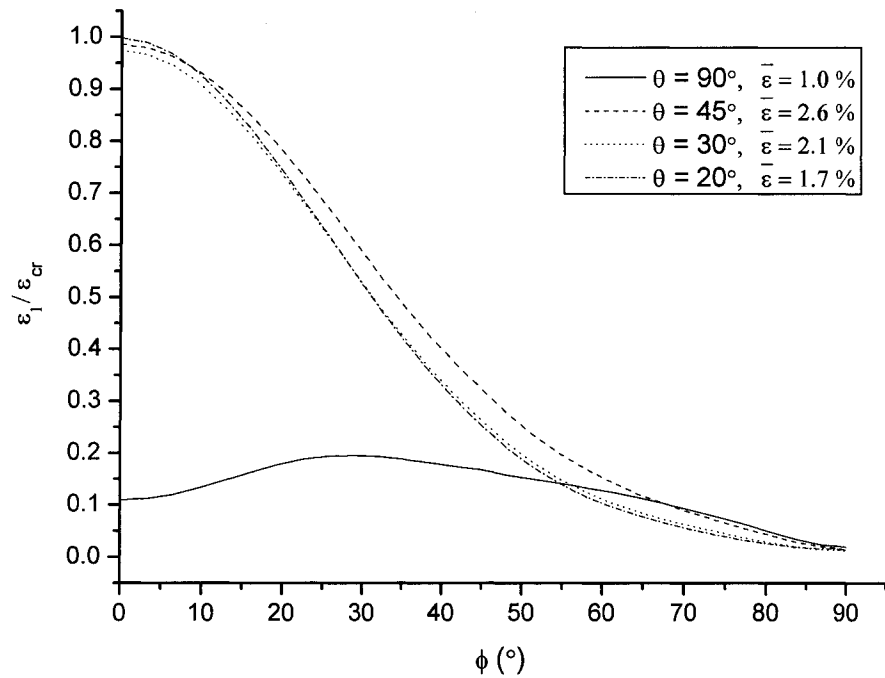


Fig. 4-19 Distribution of the first principal strain near the interphase (Epon 815 laminates).

For  $\theta = 90^\circ$ , Fig. 4-16 shows that traction  $T_3$  nearly reaches  $\sigma_{\max}$  at  $\phi = 0^\circ$ , while from Fig. 4-19, the first principal strain is very small at  $\phi = 0^\circ$ . Thus it implies that upon further loading, the damage will initiate at  $\phi = 0^\circ$  as interphase damage. For  $\theta = 45^\circ$ ,  $30^\circ$  and  $20^\circ$ , Figs. 4-16 to 4-18 indicate that the tractions  $T_1$ ,  $T_2$ , and  $T_3$  are rather small, while from Fig. 4-19, the first principal strains for all the three cases are close to the critical value at  $\phi = 0^\circ$ . Thus it implies that upon further loading, the matrix damage will initiate at  $\phi = 0^\circ$ .

It can be concluded that in the case of glass/Epon 815, for  $90^\circ$  off-axis loading, the damage initiates as the interphase separation; while for  $45^\circ$ ,  $30^\circ$ , and  $20^\circ$  off-axis loadings, the damage mode is matrix cracking. This is in agreement with the test results reported in [15]. Furthermore, it shows that the matrix cracking and interphase damage can be distinguished.

#### 4.5 CONCLUDING REMARKS

The fibre/matrix interphase damage and matrix cracking modeling have been simultaneously incorporated into the micromechanical finite element analysis for the fibrous composite materials. Both the macroscopic and microscopic responses of unidirectional laminates under off-axis loadings are well predicted based on the properties of the constituents and that of the interphase. In particular, the following conclusions can be drawn from the current investigation:

- The interphase element developed based on the cohesive law is capable of modeling both normal and tangential separations of the interface. Thus the entire response including damage initiation and evolution of the composite can be simulated. The

interphase element is convenient to implement into a FEM code since an equivalent stress-strain relationship is used.

- Two intralaminar damage modes can be distinguished by the present analysis. For E-glass/Epon 828 unidirectional laminates under transverse loading, the interphase damage initiates as the normal opening while for the off-axis loadings combined mode of normal opening and in-plane sliding is predicted. For E-glass/Epon 815 laminates under transverse loading, the damage mode is interphase separation; however, for 45°, 30°, and 20° off-axis loadings, the damage is matrix cracking. Those predictions on the damage mechanisms are in agreement with the experimental observations.
- Using the same set of material constants, the global stress-strain curves at different off-axis angles are predicted and they are in good agreement with the experimental results.

**BIBLIOGRAPHY**

1. Pagano, N. J., Yuan, F. G. (2000). The significance of effective modulus theory (homogenization) in composite laminate mechanics. *Composites Science and Technology*, **60**, 2471-2488.
2. Zhang, Y., Xia, Z., Ellyin, F. (2005). Nonlinear viscoelastic micromechanical analysis of fibre reinforced polymer laminates with damage evolution. *International Journal of Solids and structures*, **42**, 591-604.
3. Sun, C. T., Vaidya, R. S. (1996). Prediction of composite properties from a representative volume element. *Composites Science and Technology*, **56**, 171-179.
4. Zhu, H., Sankar B.V., Marney R.V. (1998). Evaluation of failure criteria for fiber composites using single element micromechanics. *Journal of Composite Materials*, **32**, 766-782.
5. Zhu, H., Achenbach, J. D. (1991). Radial matrix cracking and interphase failure in transversely loaded fiber composites. *Mechanics of Materials*, **11**, 347-356.
6. Yuan, F. G., Pagano, N. J., Cai, X. (1997). Elastic moduli of brittle matrix composites with interfacial debonding. *International Journal of Solids and structures*, **34**, 177-201.
7. Tvergaard, V. (1990a). Effect of fiber debonding in whisker-reinforced metal. *Material Science and Engineering*, **A125**, 203-213.
8. Tvergaard, V. (1990b). Analysis of tensile properties for a whisker-reinforced metal-matrix composite. *Acta Metallurgica*, **38**, 185-194.
9. Legarth, B. N. (2004). Unit cell debonding analyses for arbitrary orientation of plastic anisotropy. *International Journal of Solids and structures*, **41**, 7267-7285.

10. Jadhav, V. R., Sridharan, S. (2002). Micro-mechanical modeling of polymer based unidirectional composites: use of bulk properties of matrix with the smeared crack model. *Journal of Composite Materials*, **36**, 2735-2762.
11. Rots, J. G. (1991). Smeared and discrete representations of localized fracture. *International Journal of Fracture*, **51**, 45-59.
12. Zhu, C., Sun, C. T. (2003). Micromechanical modeling of fiber composites under off-axis loading. *Journal of Thermoplastic Composite Materials*, **16**, 333-344.
13. Aghdam, M. M., Pavier, M. J., Smith, D. J. (2001). Micro-mechanics of off-axis loading of metal matrix composites using finite element analysis. *International Journal of Solids and Structures*, **38**, 3905-3925.
14. Xia, Z., Hu, Y., Ellyin, F. (2003). Deformation behaviour of an epoxy resin subject to multiaxial loadings, part II: constitutive modeling and predictions. *Polymer Engineering and Science*, **43**, 734-748.
15. Ishai, O. (1971). Failure of unidirectional composites in tension. *Journal of the Engineering Mechanics Division, Proceedings of the ASCE*, **97**, 205-222.
16. Lorenzo, L., Hahn, H. T. (1986). Effect of ductility on the fatigue behavior of epoxy resins. *Polymer Engineering and Science*, **26**, 274-284.
17. Zhang, Y., Xia, Z., Ellyin, F. (2005). Viscoelastic and damage analyses of fibre reinforced polymer laminates by micro/meso-mechanical modeling. *Journal of Composite Materials*, (in press).

## CHAPTER 5

### MICRO/MESO-MECHANICAL ANALYSIS OF ANGLE-PLY AND CROSS-PLY LAMINATES

#### 5.1 INTRODUCTION

Experimental results show that under the same uniaxial loading the fibrous composite laminates with different fibre architecture have quite different stress-strain response and damage behaviour [1]. For a unidirectional laminate under  $45^\circ$  off-axis loading, the stress-strain curve is an almost linear one and the specimen fractures along the  $45^\circ$  fibre direction at an applied low global strain value. For a  $[0^\circ/90^\circ]_{ns}$  cross-ply laminate, the global stress-strain curve consists of two linear portions. The knee between the two straight lines corresponds to the load level causing transverse cracking of the matrix in the laminate. And the final failure of the specimen is due to the fracture of fibres in the  $0^\circ$  plies. It is quite instructive to study the behaviour of  $[\pm 45^\circ]_{ns}$  angle-ply laminate. The stress-strain curve indicates a gradual transition from a linear portion to a part with low tangent modulus similar to the “yielding” behaviour in metals. At a relatively low global strain value the stress-strain response is comparable to that of the unidirectional  $45^\circ$  angle-ply laminate. However, the specimen does not fail until the global strain reached quite a large value of approximately 15% (for glass fibre reinforced epoxy laminates [1]). To predict such a drastically different response of the  $[\pm 45^\circ]_{ns}$  angle-ply laminate poses a considerable challenge in the mechanical modeling of composites. In this case it becomes imperative, that a micromechanical model be adopted since damage evolution plays an important role. In such a model damage initiation and evolution can be properly

simulated in the individual constituents of the composite laminate at the microscopic scale, e.g. see Pagano et al. [2], Raghavan et al. [3] and Kim et al. [4].

In this chapter, three-dimensional meso/micro-mechanical unit/multi-cell models are established for three different laminates in a unified procedure. The composite system studied is E-glass/epoxy matrix with fibre volume fraction of 52.5%. The coupon specimens of the three laminates were made from a prepreg of 3M Company [5]. Experimental and numerical studies showed that the epoxy polymer matrix can be described by the nonlinear viscoelastic constitutive model in Chapter 3 and the fibre is assumed to behave elastically.

The analysis of unidirectional laminates under off-axis loading was described in Chapter 4. To facilitate the micromechanical analysis for angle-ply and cross-ply laminates, a meso/micro rhombohedral two cell model has been developed for the  $[\pm\theta]_n$  angle-ply laminates. The in-plane elastic moduli for  $[\pm\theta]_n$  angle-ply laminates are predicted to verify the model (Section 5.2).

For the three laminates investigated in this Chapter, studies show that bonding between the fibre and matrix is strong and perfect bonding conditions can be assumed. Thus matrix cracking remains the main intralaminar damage mechanism. The ‘smeared crack approach’ presented in Chapter 3 is employed to simulating the matrix cracking in the three laminates. The finite element predictions of the three types of laminates subject to uniaxial tensile loading are presented, viz. (1) unidirectional laminate under 45° off-axis loading, (2)  $[0^\circ/90^\circ]_{ns}$  cross-ply laminate under transverse loading and, (3)  $[\pm 45^\circ]_{ns}$  angle-ply laminates under tensile loading. The numerical results indicate the local and global responses of the laminates including the damage evolution. The predicted results

are compared with the experimental data with similar composite lay-ups, and the agreement is found to be good (Section 5.3).

Residual stress/strain may lead to the development of damage and may also have an adverse effect on the mechanical behaviour of the composites. The influence of residual stress/strain is investigated in section 5.4. The initiation and evolution of the residual stress/strain are first analyzed using time-dependent and temperature-dependent material constants. The meso/micro-mechanical analysis of a cross-ply laminate indicates that the damage initiation and evolution under subsequent mechanical loading are greatly influenced by the residual stress/strain.

## 5.2 MESO SCALE MODELING FOR ANGLE-PLY LAMINATES

### 5.2.1 *Meso Scale Unit Cell Modeling*

The meso/micro-mechanical model is set up based on the extension of periodic RUC technique for a unidirectional laminate. Fig. 5-1 indicates the manner in which a two cell model is developed for a thick angle-ply  $[\pm\theta]_n$  laminate. From the periodicity of the fibre array, we can cut a rhombohedral cell consisting of two layers, each with a single fibre in the direction  $+\theta$  and  $-\theta$ , respectively. The angle-ply laminate can thus be seen as a periodical array of this two-cell model [6]. This type of two-cell model or possibly multi-cell model will be referred as meso-scale unit cell model (MUC).

It should be noted that in Fig. 5-1, the angle  $\theta$  is measured from  $X$  axis ( if measured from the  $Y$  axis, it will be  $90^\circ - \theta$ , therefore this model can also be seen as a MUC for the  $[\pm(90 - \theta)]_n$  laminates. For example, the MUCs for the  $[\pm 30]_n$  laminates and the  $[\pm 60]_n$  laminates are the same.

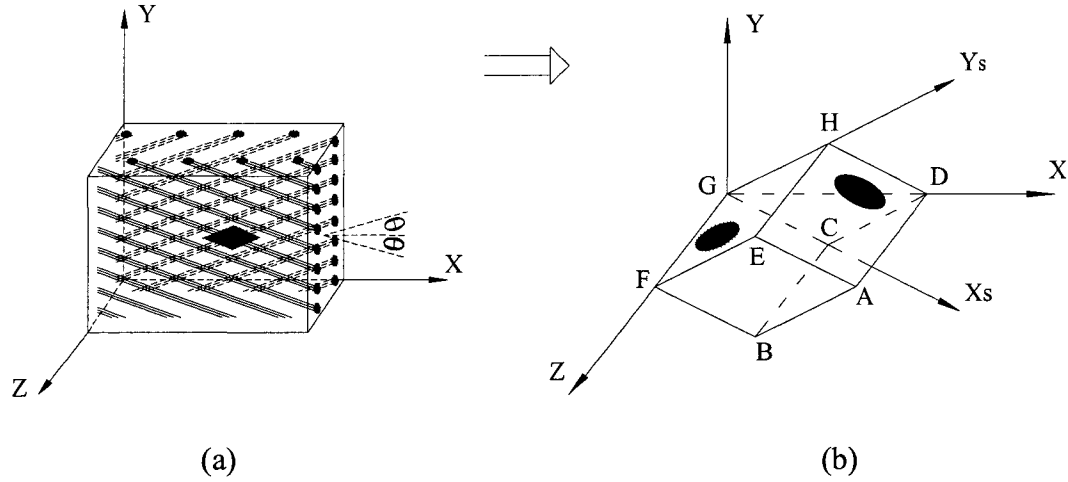


Fig. 5-1 Meso-scale cell models for angle-ply laminates:  
 (a) Angle-ply laminates; (b) Meso scale unit cell model.

To facilitate the analysis, a skew coordinate system as shown in Fig. 5-2 is introduced. We denote this skew coordinate system as  $O - X_s Y_s Z_s$ , with the same origin as that of the orthogonal coordinate system  $O - XYZ$ , and the axes  $X_s, Y_s$  are parallel to the fibre directions (direction of  $\pm\theta$ ). In this system, the coordinates and the displacement components are designated as  $(x_s, y_s, z_s)$ , and  $(u_{x_s}, u_{y_s}, u_{z_s})$ , respectively. From Fig.5-2, we can obtain the transformation between the two coordinate systems as follows:

$$\begin{cases} x_s \\ y_s \\ z_s \end{cases} = \frac{1}{\sin 2\theta} \begin{bmatrix} \sin \theta & -\cos \theta & 0 \\ \sin \theta & \cos \theta & 0 \\ 0 & 0 & \sin 2\theta \end{bmatrix} \begin{cases} x \\ y \\ z \end{cases} \quad (0 < \theta < \frac{\pi}{2}) \quad (5.1)$$

$$\begin{cases} u_{x_s} \\ u_{y_s} \\ u_{z_s} \end{cases} = \frac{1}{\sin 2\theta} \begin{bmatrix} \sin \theta & -\cos \theta & 0 \\ \sin \theta & \cos \theta & 0 \\ 0 & 0 & \sin 2\theta \end{bmatrix} \begin{cases} u_x \\ u_y \\ u_z \end{cases} \quad (0 < \theta < \frac{\pi}{2}) \quad (5.2)$$

Referring to Fig. 5-1(b), we assume that  $S$  is the area of side surface (ABCD),  $\ell$  is the length of the side AB,  $h$  is the height of the multi-cell model (AD),  $S_f$  is the area of the cross section (AEFB), the volume of the MUC is  $V$ , the fibre volume fraction is  $V_f$  and  $R$

is the radius of the fibre. The following relations between these geometric parameters can be obtained:

$$h = 2\ell \sin 2\theta$$

$$S_1 = \ell^2 \sin 2\theta$$

$$S = 2\ell^2 \sin 2\theta \quad \left(0 < \theta < \frac{\pi}{2}\right) \quad (5.3)$$

$$V = 2\ell^3 \sin^2 2\theta$$

$$R = \ell \sin 2\theta \sqrt{\frac{V_f}{\pi}}$$

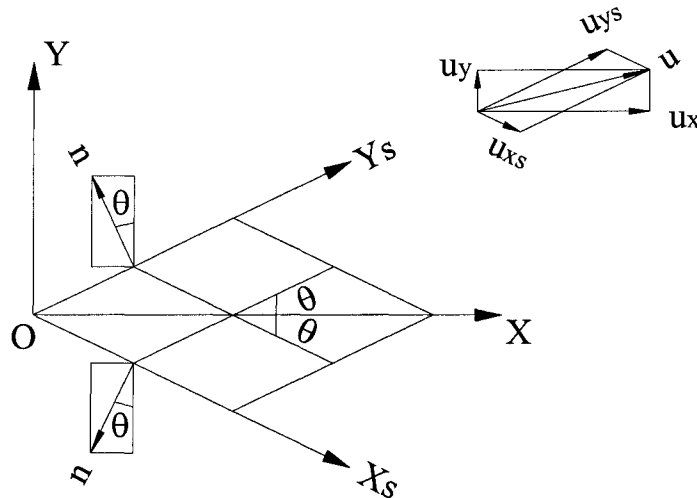


Fig. 5-2 The two coordinate systems.

Similarly to the derivation of the unified boundary conditions for the rectangular RUC in Chapter 2, for angle-ply laminates represented by the rhombohedral MUC shown in Fig. 5-1(b), from Eqn. (2-7) and Eqn. (5-2), a unified form of boundary conditions can be written as (in the skew coordinate system  $O-X_s Y_s Z_s$ ):

$$u_{is}^{j+}(x_s, y_s, z_s) - u_{is}^{j-}(x_s, y_s, z_s) = c_i^j \quad (5.4)$$

In the above equation, all indices have the same meaning as in the Eqn. (2.15, Chapter 2) except that they are now defined in the skew coordinate system. Specifically, the indices  $i, j=1, 2, 3$  correspond to  $X_s, Y_s, Z_s$ ; and  $j^+, j^-$  correspond to the surfaces with normals along the positive and negative  $X_s, Y_s, Z_s$  directions, respectively.

If only in-plane loads are considered ( $c_1^3 = c_3^1 = c_2^3 = c_3^2 = 0$ ) and by using the relation between the displacement components in the skew coordinate system and in the orthogonal  $O-XYZ$  coordinates, Eqns. (5.1) and (5.2), the displacement boundary conditions in the  $O-XYZ$  coordinates can be written as (note that the coordinates are expressed in the skew coordinate system in the following equations for clarity):

On planes  $ABCD$  ( $x_s = \Delta x_s$ ) and  $EFGH$  ( $x_s = 0$ ):

$$\begin{aligned} [u_x(\Delta x_s, y_s, z_s) - u_x(0, y_s, z_s)] \sin \theta - [u_y(\Delta x_s, y_s, z_s) - u_y(0, y_s, z_s)] \cos \theta &= c_1^1 \sin 2\theta \\ [u_y(\Delta x_s, y_s, z_s) - u_y(0, y_s, z_s)] \cos \theta + [u_x(\Delta x_s, y_s, z_s) - u_x(0, y_s, z_s)] \sin \theta &= c_1^2 \sin 2\theta \quad (5.5) \\ u_z(\Delta x_s, y_s, z_s) &= u_z(0, y_s, z_s) \end{aligned}$$

On planes  $ADHE$  ( $y_s = \Delta y_s$ ) and  $BCGF$  ( $y_s = 0$ ):

$$\begin{aligned} [u_x(x_s, \Delta y_s, z_s) - u_x(x_s, 0, z_s)] \sin \theta - [u_y(x_s, \Delta y_s, z_s) - u_y(x_s, 0, z_s)] \cos \theta &= c_2^1 \sin 2\theta \\ [u_y(x_s, \Delta y_s, z_s) - u_y(x_s, 0, z_s)] \cos \theta + [u_x(x_s, \Delta y_s, z_s) - u_x(x_s, 0, z_s)] \sin \theta &= c_2^2 \sin 2\theta \quad (5.6) \\ u_z(x_s, \Delta y_s, z_s) &= u_z(x_s, 0, z_s) \end{aligned}$$

On planes  $BAEF$  ( $z_s = \Delta z_s$ ) and  $CDHG$  ( $z_s = 0$ ):

$$\begin{aligned} [u_x(x_s, y_s, \Delta z_s) - u_x(x_s, y_s, 0)] \sin \theta - [u_y(x_s, y_s, \Delta z_s) - u_y(x_s, y_s, 0)] \cos \theta &= 0 \\ [u_y(x_s, y_s, \Delta z_s) - u_y(x_s, y_s, 0)] \cos \theta + [u_x(x_s, y_s, \Delta z_s) - u_x(x_s, y_s, 0)] \sin \theta &= 0 \quad (5.7) \\ u_z(x_s, y_s, 0) &= 0 \\ u_z(x_s, y_s, \Delta z_s) &= c_3^3 = \text{const.} \end{aligned}$$

Note that for the in-plane loading case, the constant  $c_3^3$  is not required to be specified. Its value will be obtained through the FEM analysis. To eliminate the rigid body motion, the displacement components,  $u_x$ ,  $u_y$  of the center point of the MUC are assumed to be zero.

To apply the the above Eqns. (5.5)-(5.7) in the FEM analysis, the mesh in opposite boundary surfaces should be the same. For each pair of displacement component at the two corresponding nodes with identical in-plane coordinates on the two boundary surfaces a constraint equation is imposed. Although a large number of the constraint equations needs to be applied, it is usually easy to produce all those equations by using certain automatic schemes embedded in a FEM package.

Based on definitions of the average strain and stress, Eqns. (2.9) and (2.10) of Chapter 2, and noting the geometric description of the MUC given by Eqns. (5.3), a relation between the avearge strains and the constants  $c_i^j$ , and the average stresses and resultant tractions on the boundary surfaces are found as follows:

$$\begin{aligned}\bar{\varepsilon}_{xx} &= \frac{1}{2l}(c_1^1 + 2c_1^2 + c_2^2) \\ \bar{\varepsilon}_{yy} &= \frac{1}{2l}(c_1^1 - 2c_1^2 + c_2^2) \\ \bar{\varepsilon}_{xy} &= \frac{1}{l \sin 2\theta}(c_2^2 - c_1^1) \\ \bar{\varepsilon}_{zz} &= \frac{c_3^3}{h}\end{aligned}\tag{5.8}$$

$$\begin{aligned}\bar{\sigma}_{xx} &= \frac{P_x^{AB} + P_x^{AE}}{2S \sin \theta} \\ \bar{\sigma}_{yy} &= \frac{P_y^{AE} - P_y^{AB}}{2S \cos \theta} \\ \bar{\sigma}_{xy} &= \frac{P_x^{AE} - P_x^{AB}}{2S \cos \theta} = \frac{P_y^{AB} + P_y^{AE}}{2S \sin \theta}\end{aligned}\quad (5.9)$$

Note Eqns. (5-8) and (5-9) are defined in the coordinate system  $O-XYZ$ . In Eqns. (5.9), each resultant traction  $P$  has two indices. The subscript  $x$  or  $y$  indicates that the traction is along the  $X$  or  $Y$  direction; and the superscript  $AB$  or  $AE$  is a short designation for plane  $ABCD$  or  $AEHD$  (see Fig. 5-1b). For example,  $P_x^{AB}$  is the total traction of plane  $ABCD$  along the  $X$  direction, its value can be obtained from the FEA solution:

$$P_x^{AB} = \int_{ABCD} \sigma_{xx}(x, y, z) \cos \theta \, dS + \int_{AEHD} \sigma_{xy}(x, y, z) \sin \theta \, dS \quad (5.10)$$

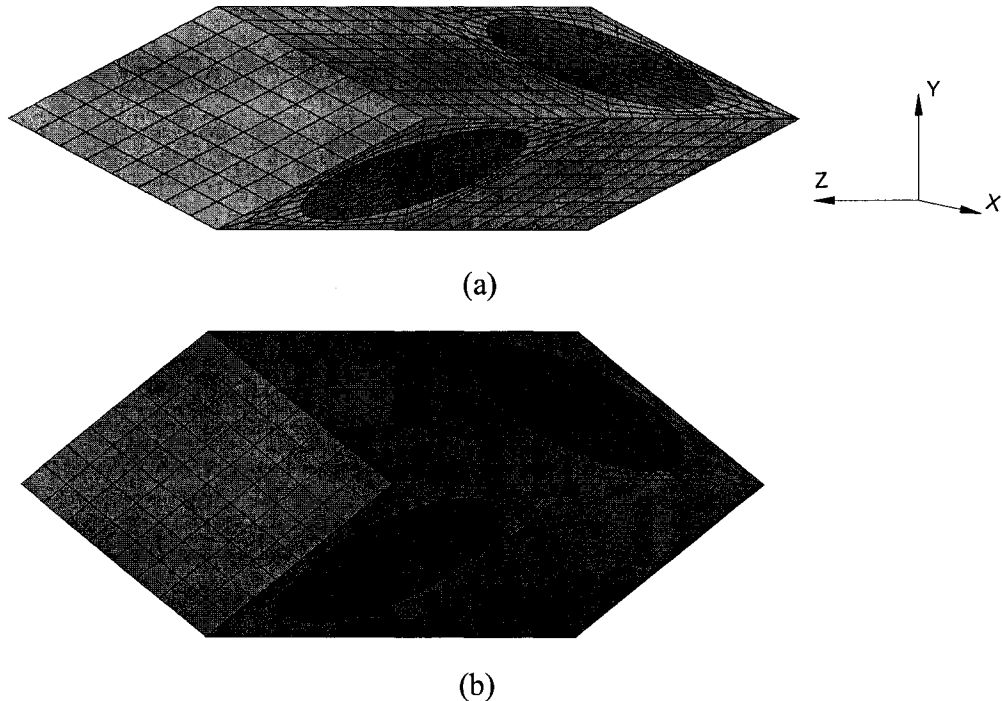


Fig. 5-3 Meshed MUC for angle-ply laminates:

(a) Meshed MUC for  $\pm 15^\circ$  ( $\pm 75^\circ$ ); (b) Meshed MUC for  $\pm 30^\circ$  ( $\pm 60^\circ$ ).

Figure 5.3 shows the meshed MUCs for  $\pm 15^\circ$  ( $\pm 75^\circ$ ) and  $\pm 30^\circ$  ( $\pm 60^\circ$ ) laminates, each having 3681 nodes and 3072 elements. The MUC for  $\pm 45^\circ$  laminates will be shown later (Fig. 5-7).

### 5.2.2 Prediction of In-plane Moduli

From the microstructure of the laminate, it is reasonable to assume that the laminate is orthotropic in the sense of overall response, i.e., for average stresses and average strains, we have

$$\begin{Bmatrix} \bar{\epsilon}_{xx} \\ \bar{\epsilon}_{yy} \\ \bar{\epsilon}_{xy} \end{Bmatrix} = \begin{bmatrix} S_{11} & S_{12} & 0 \\ S_{12} & S_{22} & 0 \\ 0 & 0 & S_{66} \end{bmatrix} \begin{Bmatrix} \bar{\sigma}_{xx} \\ \bar{\sigma}_{yy} \\ \bar{\sigma}_{xy} \end{Bmatrix} \quad (5.11)$$

In a procedure similar to that described in Chapter 2, two sets of  $c_1^1, c_2^2, c_1^2$  are specified to obtain the elastic constants in Eqn. (5.11). The in-plane elastic moduli can be obtained from:

$$E_x = \frac{1}{S_{11}}, E_y = \frac{1}{S_{22}}, \nu_{xy} = -\frac{S_{12}}{S_{11}} \text{ and } G_{xy} = \frac{1}{2S_{66}} \quad (5.12)$$

Figures 5-4 and 5-5 show the predicted  $E_x$  and  $G_{xy}$  for angle-ply laminates with varying angles and a comparison with the results obtained by using the classical laminate theory (CLT). Note that the micromechanical results are based on the properties of the two constituents (fibre and matrix, Table 5-1), while the CLT results are based on the global properties of the lamina [7], Table 5-2.

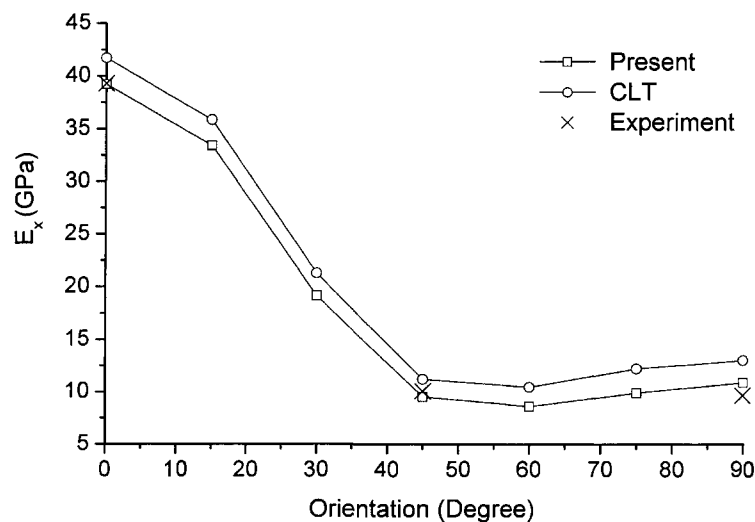
Table 5-1 Properties of constituents [5]

Material	E (MPa)	$\nu$
E-glass	$7.25 \times 10^4$	0.22
Epoxy	$2.6 \times 10^3$	0.4

Table 5-2 Properties of a lamina [7]

E-glass/epoxy lamina (3M-1003)	
$E_1$ (GPa)	41.7
$E_2$ (GPa)	13.0
$\nu_{12}$	0.3
$G_{12}$ (GPa)	3.4

From Figs. 5-4 and 5-5, it is seen that the differences between the results of the CLT and the present micromechanical model are rather small. And from the limited experiment points [1, 5], it seems that the present micromechanical results are in good agreement with the experimental data.

Fig. 5-4  $E_x \sim \theta$  curves for angle-ply laminates.

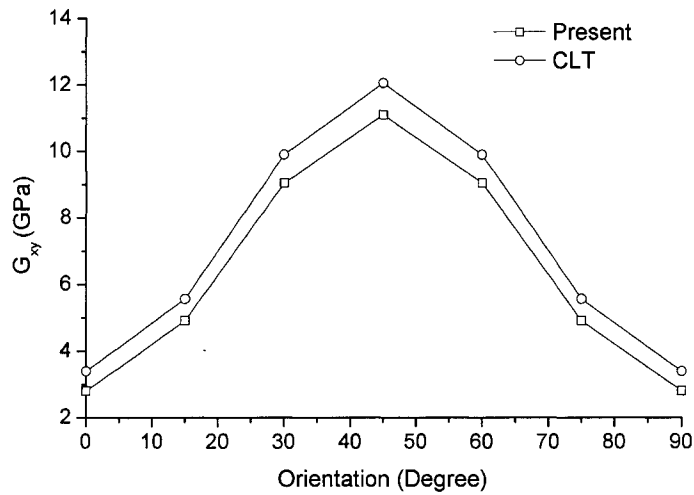


Fig. 5-5  $G_{xy} \sim \theta$  curves for angle-ply laminates.

### 5.3 MESO/MICRO-MECHANICAL ANALYSIS OF THREE LAMINATES

#### 5.3.1 RUC/MUC Model and Loading

Figures 5-6(a) and 5-6(b) show a  $45^\circ$  off-axis loading of a unidirectional laminate and uniaxial loading of a  $[\pm 45^\circ]_{ns}$  angle-ply laminate, respectively.

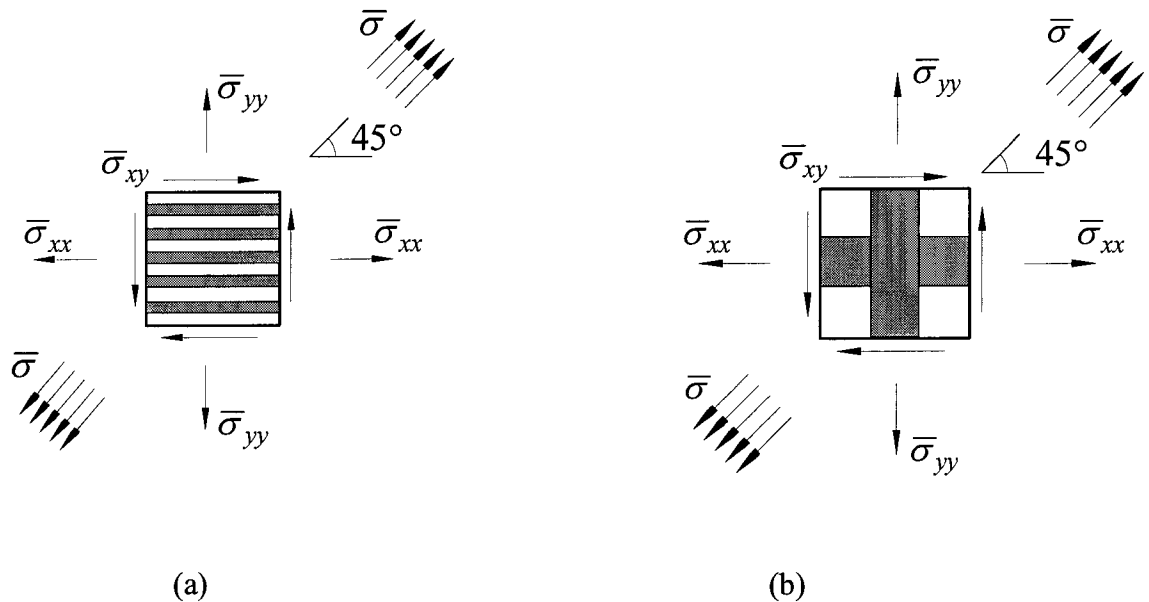


Fig. 5-6 Two types of laminates under uniaxial tensile loading ( $\bar{\sigma}$ ):

(a) A unidirectional laminate; (b) A  $[\pm 45^\circ]_{ns}$  angle-ply laminate.

Note that for the  $[\pm 45^\circ]_{ns}$  angle-ply laminate we assign the Y-axis in the  $+45^\circ$  fibre direction and the X-axis in the  $-45^\circ$  fibre direction. The Z-axis is in the thickness direction of the laminate. The tensile load  $\bar{\sigma}$  applied to these two types of laminates can be decomposed into a set of multiaxial loading in the coordinate system O-XYZ shown in Figures 5-6 and 5-7. From the transformation of stress components, for both Figs. 5-6 (a) and 5-6 (b), we have

$$\bar{\sigma}_{xx} = \bar{\sigma}_{yy} = \bar{\sigma}_{xy} = \frac{1}{2} \bar{\sigma} \quad (5.13)$$

The response of  $45^\circ$  unidirectional laminate and the  $[\pm 45^\circ]_{ns}$  angle-ply laminate under the equivalent multiaxial loads will be analyzed here by a micromechanical method. Figures. 5-7(a) and 5-7(b) show the micro/meso-mechanical representations of unidirectional laminates and  $[\pm 45^\circ]_{ns}$  angle-ply laminates.

The models in Fig. 5-7 are meshed with 8-nodes brick elements with 1536 elements, 1881 nodes for the unidirectional laminate and 4096 elements, 4833 nodes for the  $[\pm 45^\circ]_{ns}$  angle-ply laminate.

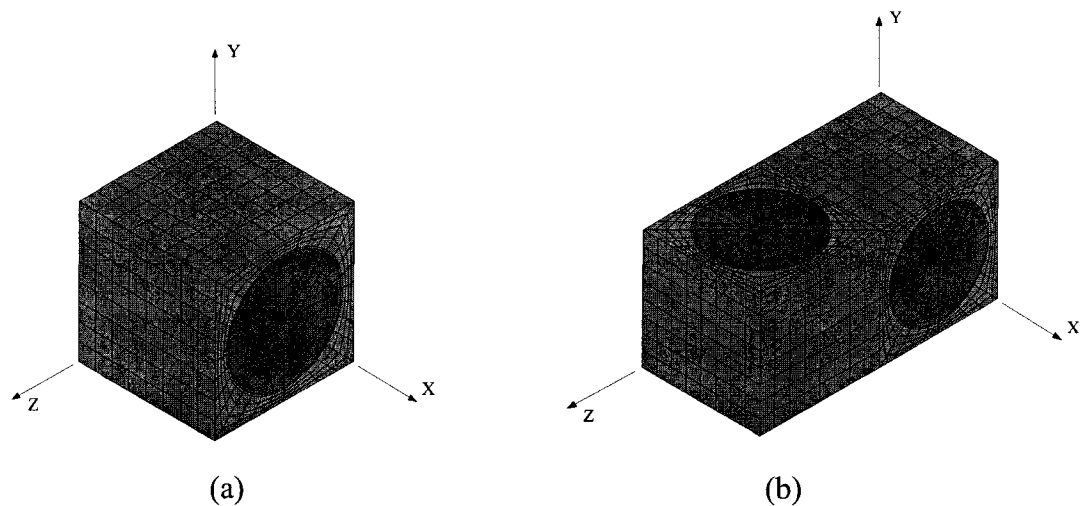


Fig. 5-7 RUC/MUC models of two composite laminates:  
(a) A unidirectional laminate; (b) A  $[\pm 45^\circ]_{ns}$  angle-ply laminate.

### 5.3.2 Boundary Conditions

For the  $45^\circ$  unidirectional laminates and angle-ply laminates subjected to the above in-plane loading, the applied global strain components are  $\bar{\epsilon}_{xx}$ ,  $\bar{\epsilon}_{yy}$ ,  $\bar{\epsilon}_{zz}$  and  $\bar{\epsilon}_{xy}$ , therefore the boundary conditions can be obtained from the general periodic boundary conditions described in Chapter 2. Note that the same model in Fig. 5-7 (b) for  $[\pm 45^\circ]_{ns}$  angle-ply laminate can also be used for the analysis of  $[0^\circ/90^\circ]_{ns}$  cross-ply laminates, since the direction of the fibres of the two layers are perpendicular. However, different forms of boundary conditions should be used. For cross-ply laminates under transverse tensile loading, the 'plane keeps plane' boundary conditions are adopted. Referring to Fig. 5-7, the boundary conditions for a cross-ply laminate under transverse loading (along X-axis) can be specified as,

On plane  $X=0$ ,  $Y=0$  and  $Z=0$ , symmetric conditions are specified,

$$u(0, y, z) = 0, \quad v(x, 0, z) = 0, \quad \text{and} \quad w(x, y, 0) = 0, \quad \text{respectively} \quad (5.14)$$

On plane  $X=1$ ,  $Y=1$ , and  $Z=2$

$$u(1, y, z) = c_1^1, \quad v(x, 1, z) = \delta_1, \quad \text{and} \quad w(x, y, 2) = \delta_2 \quad (5.15)$$

Note that  $c_1^1$  is specified as the node displacement on the plane  $X=1$ , which results in a global strain  $\bar{\epsilon}_{xx} = c_1^1$  applied to the cell, while on plane  $Y=1$ , and  $Z=2$ , the corresponding displacement components for each point are equal to a constant, but the constant is not specified.

For the  $45^\circ$  unidirectional laminate and  $\pm 45^\circ$  laminates, the iteration algorithm for off-axis loading described in Chapter 4 is required to conduct the analysis.

### 5.3.3 Models for Material and Damage and Constants

For the composite system in this Chapter, the glass fibre is assumed to be linear elastic with elastic constants listed in Table 3-1. The nonlinear viscoelastic model described in Chapter 3 is used to model the constitutive response of the epoxy matrix. The material constants for the epoxy matrix are approximately taken as those of the Epon 826, which are also listed in Table 3-1.

For the three laminates studied in this Chapter, perfect bonding between the fibre and matrix is assumed. Thus matrix cracking remains the main intralaminar damage mechanism. The 'smeared crack approach' presented in Chapter 3 is employed to simulating the matrix cracking in the three laminates. The constants used for the matrix damage model are:

$$\varepsilon_{cr} = 0.048, E_t = 284MPa, \beta = 0.001, \chi = 0.05 \quad (5.16)$$

Note  $\varepsilon_{cr} = 0.048$  and  $E_t = 284MPa$  are the uniaxial tensile test values for Epon 826 in [8].

At each step of the calculation, the average axial strain of the fibre is monitored, if it exceeds a prescribed maximum value, i.e.

$$\bar{\varepsilon}_{fa} \geq \varepsilon_{f \max} \quad (5.17)$$

Then the fibre is assumed to have fractured and the calculation is then terminated. For the glass fibre used in this calculation,  $\varepsilon_{f \max} = 2.3\%$  is assumed [9].

Uniaxial tensile loads were applied to the aforementioned three laminates at a constant strain rate of  $10^{-4} \text{ s}^{-1}$ . In the following sections, both global and local responses will be presented for the three types of laminates, viz. (1) a unidirectional laminate under  $45^\circ$

off-axis loading, (2) a  $[\pm 45^\circ]_{ns}$  angle-ply laminate under uniaxial tensile loading, and (3) a  $[0^\circ/90^\circ]_{ns}$  cross-ply laminate under transverse tensile loading.

### 5.3.4 Prediction of Stress-strain Curves of the Three Types of Laminates

Figures 5-8 and 5-9 show the global stress-strain responses of the three types of laminates and the comparison with test results. All the calculations use the same set of material constants. The test specimens were made of “Scotchply 1003” prepregs from the 3M Company. The test data of cross-ply laminates is from the technical data of the 3M Company [5] and that of the  $[\pm 45^\circ]_{ns}$  angle-ply laminates and unidirectional laminates under  $45^\circ$  off-axis loading are from [1]. It can be seen that drastically different responses of the three types of laminates are well predicted by the micro/meso-mechanical analysis. Note that for the cross-ply laminate, the results indicate that at a global strain of 2.3%, the fibre in the  $0^\circ$  ply breaks at the average stress of 470 MPa. However, for the other two laminates, no fibre fracture occurs within the strain range of the present calculations.

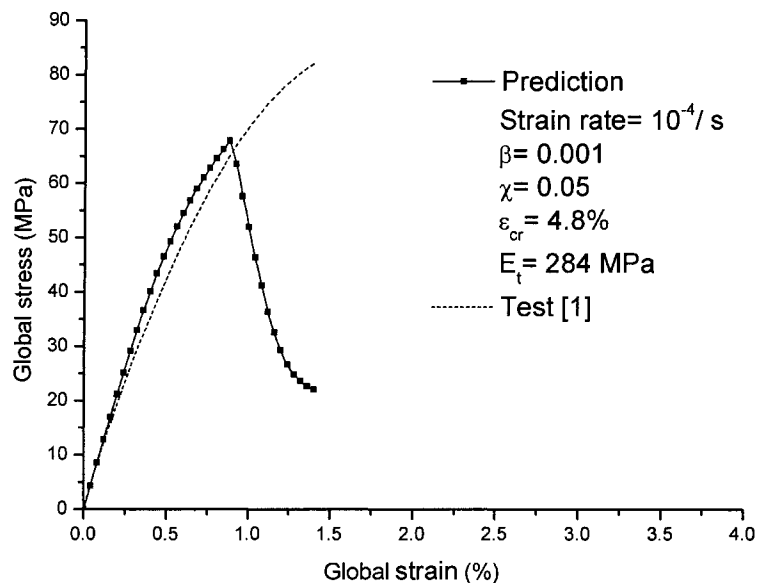


Fig. 5-8 Predicted global stress-strain curve of a unidirectional laminate.

For the unidirectional laminate, it is seen that the predicted trend is in good agreement with the test results, Figure 5-8. The predicted initial stiffness is 10.1 GPa, and the maximum load is 68 MPa, while the corresponding test results are 10.1 GPa and 82 MPa. The effect of viscoelastic behaviour of the matrix is manifested by the nonlinearity of the stress-strain curve, which is noticeable once the stress exceeds 40 MPa (about 0.5% strain). Since damage has not yet occurred at this load level (damage initiation will be presented later), therefore this nonlinearity is mainly caused by the viscoelasticity of the epoxy matrix.

The results for cross-ply and angle-ply laminates are shown in Figure 5-9. For the cross-ply laminate, the bilinear stress-strain curve is predicted with two stages of modulus, which are approximately 25.5 GPa and 17.4 GPa. Corresponding test values are 25.5 GPa and 15.6 GPa, respectively. The knee between the two straight lines corresponds to the load level causing transverse cracking of matrix in the laminate. And the final failure of the specimen is due to the fracture of fibres in the  $0^\circ$  plies. From the technical data of the 'Scotchply', the test value of tensile strength of cross-ply laminate is 480 MPa, and the present prediction of 470 MPa is very close to that of the test.

The unique nonlinear stress-strain curve for the  $[\pm 45^\circ]_{ns}$  laminate is also well predicted. For example, the predicted initial stiffness of 10.1 GPa agreed very well with the test value of 10.1 GPa. In contrast to a unidirectional laminate under  $45^\circ$  off-axis loading which failed at a relatively low global strain of 0.9%, at the same strain level, the  $[\pm 45^\circ]_{ns}$  laminate is capable of carrying the applied load albeit at a reduced stiffness. However, prior to the 'yielding' point, the stress-strain curve also manifested a nonlinear response. Since the damage has not yet occurred at this load level (50 MPa), this nonlinearity is

mainly caused by the viscoelasticity of the epoxy matrix. Note that the nonlinearity of the stress-strain curve has different causes at different strain levels: at lower strain levels, it is mainly caused by the viscoelasticity of the matrix, while at higher strain values, it is mainly influenced by the damage evolution in the matrix. Note, however, that the simulation is carried out only up to about 2.3% applied global strain. Thereafter, it is difficult to continue the simulation, since the local deformation is very large and the present FEM model is based on the small deformation formulation.

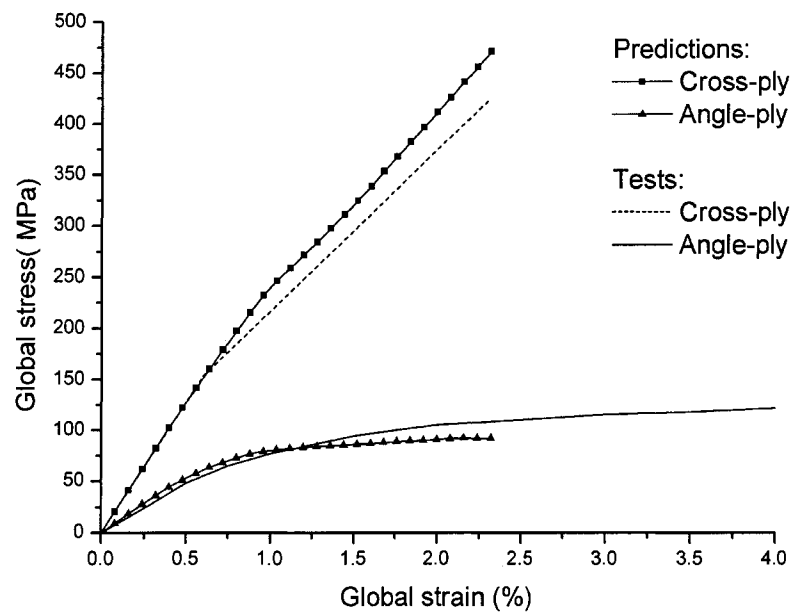


Fig. 5-9 Predicted global stress-strain curves of a  $[0/90^{\circ}]_{ns}$  cross-ply laminate and a  $[\pm 45^{\circ}]_{ns}$  angle-ply laminate.

### 5.3.5 Prediction of the Ply Level Response

The average in-plane stress components of each ply in the laminates can also be easily determined from the current analysis. Since the stress field in the repeated unit cell or multi-cells is known, the average stress is calculated according to Eqn. (2.9) but over the corresponding unit cube as shown in Fig. 5-7(b). Figure 5-10 shows the evolution of the

ply-level in-plane stresses for  $[\pm 45^\circ]_{ns}$  angle-ply laminates. Referring to Fig. 5-6(b) and Fig. 5-7(b), due to symmetry the average stresses of the  $45^\circ$  ply and the  $-45^\circ$  ply have the relation:

$$(\bar{\sigma}_{xx})_{-45} = (\bar{\sigma}_{yy})_{45}, \quad (\bar{\sigma}_{yy})_{-45} = (\bar{\sigma}_{xx})_{45}, \quad (\bar{\sigma}_{xy})_{-45} = (\bar{\sigma}_{xy})_{45} \quad (5.18)$$

Therefore only the evolution of the stress components of  $45^\circ$  ply  $(\bar{\sigma}_{xx}, \bar{\sigma}_{yy}, \bar{\sigma}_{xy})_{45}$  is shown. Prior to damage initiation at global strain of about 0.9%, the stress components  $(\bar{\sigma}_{xx}, \bar{\sigma}_{yy}, \bar{\sigma}_{xy})_{45}$  all increase with the increase of the global strain, and Eqn. (5.13) is satisfied. After the initiation of damage, the three stress components evolve in a different manner:  $(\bar{\sigma}_{xx})_{45}$  and  $(\bar{\sigma}_{yy})_{-45}$  decrease steadily which implies that in the transverse direction of each ply the capability to sustain tensile loading diminishes. However,  $(\bar{\sigma}_{yy})_{45}$  and  $(\bar{\sigma}_{xx})_{-45}$  components increase at a higher rate than that prior to damage. This indicates that after damage, each ply carries more loading in the fibre direction. In fact, the global stress of the laminate in the X-direction can be written as

$$(\bar{\sigma}_{xx})_{lamin ate} = \frac{1}{2}(\bar{\sigma}_{xx})_{45} + \frac{1}{2}(\bar{\sigma}_{xx})_{-45} \quad (5.19)$$

Therefore, after the initiation of matrix damage, the laminates can still carry load in the X- and Y-directions, although the contributions of each lamina are different ( $\bar{\sigma}_{yy}$  for  $45^\circ$  ply and  $\bar{\sigma}_{xx}$  for  $-45^\circ$  ply). Note also that the shear stress  $(\bar{\sigma}_{xy})_{45}$  or  $(\bar{\sigma}_{xy})_{-45}$  changes gradually; thus, the laminate's global load evolves gradually at approximately the same rate as that of the shear stress, see Figure 5-10.

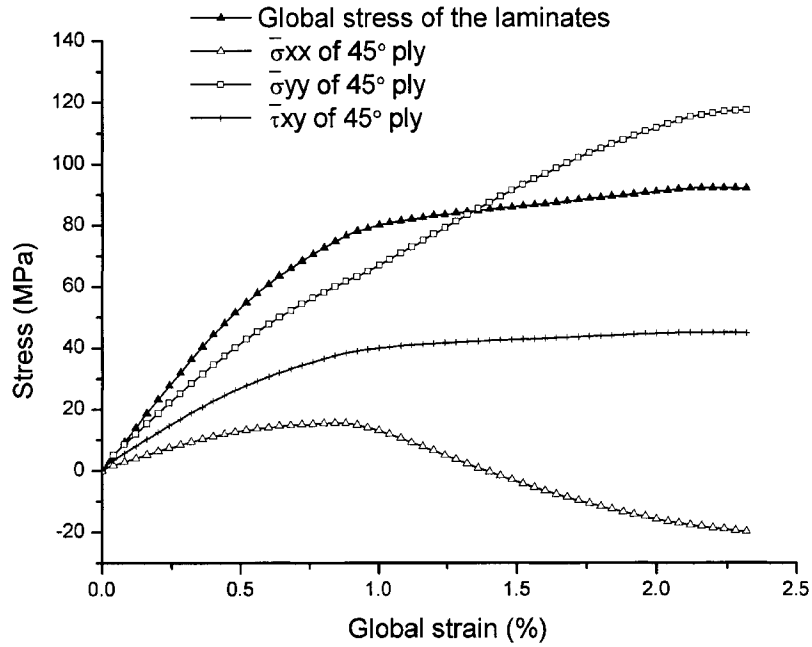


Fig. 5-10 Global stress-strain curve at the laminate level and ply level stresses (angle-ply).

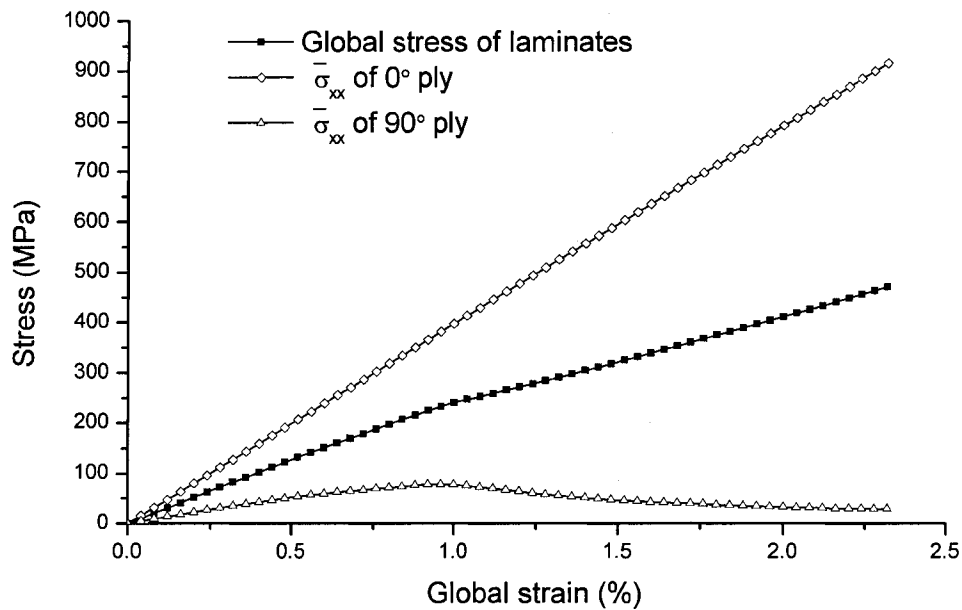


Fig. 5-11 Global stress-strain curve at the laminate level and ply level stresses (cross-ply).

Figure 5-11 shows the average (global) stress-strain curve for each ply of the cross-ply laminates. The evolution of load carrying capacity of each ply and the entire laminate as a

function of the global strain is demonstrated. Prior to the initiation of damage in the 90° ply, both 90° and 0° plies contribute to the load carrying of the laminate, however, after the damage, the load carrying capacity of the 90° ply drops to a small value, whereas the 0° ply continues to carry the load at almost the same rate.

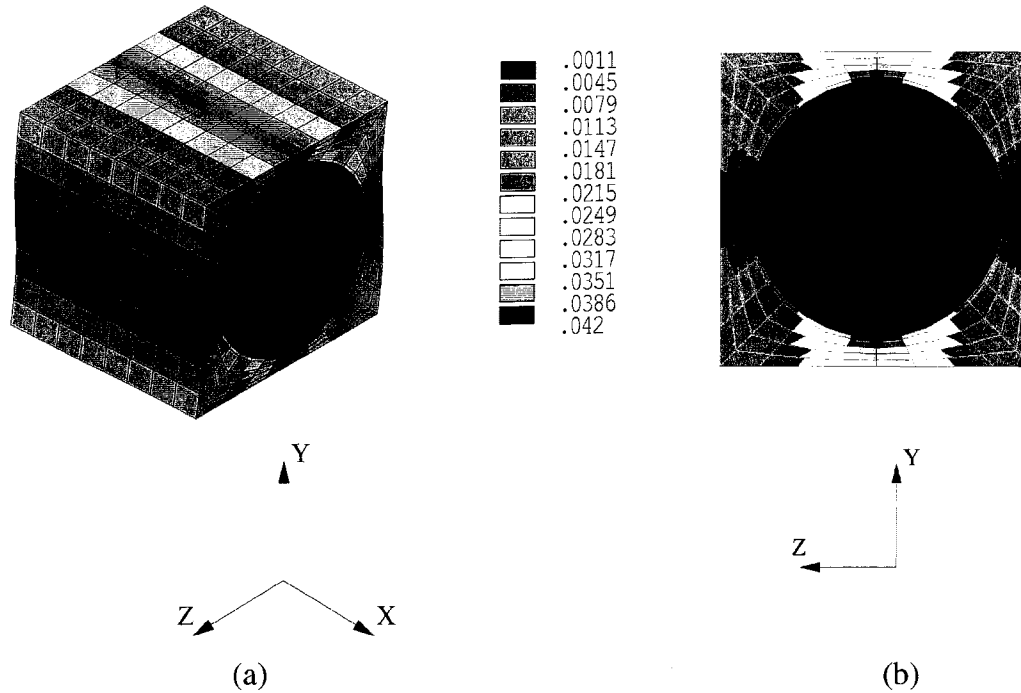


Fig. 5-12 First principal strain distribution in the unit cell:  
(a) Isometric 3D view; (b) Front 2D view.

### 5.3.6 Microscopic Response

It is the local stress/strain distribution which determines the damage initiation. Figure 5-12 shows the distribution of the maximum principal strain at an applied global strain of 0.8 % for the unidirectional laminate. For the angle-ply laminates, Fig. 5-13 shows the distribution of the stress components  $\sigma_{xy}$  at an applied global strain of 0.8 %. The distribution of the maximum principal strain is depicted in Fig. 5-14. As seen in Figs 5-12 to 5-14, the stress and strain distribution along the fibre direction (Y-axis for +45° ply

and X-axis for  $-45^\circ$  ply, respectively) is constant. An examination of the distributions of other stress/strain components results in the same conclusion.

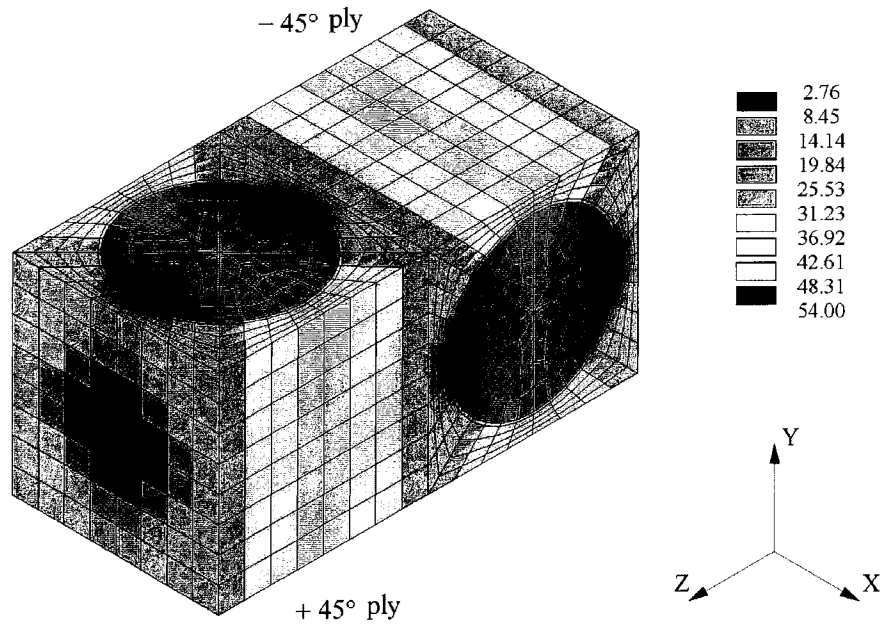


Fig. 5-13 Distribution of the local shear stress,  $\sigma_{xy}$  in a  $[\pm 45^\circ]_{ns}$  laminate.

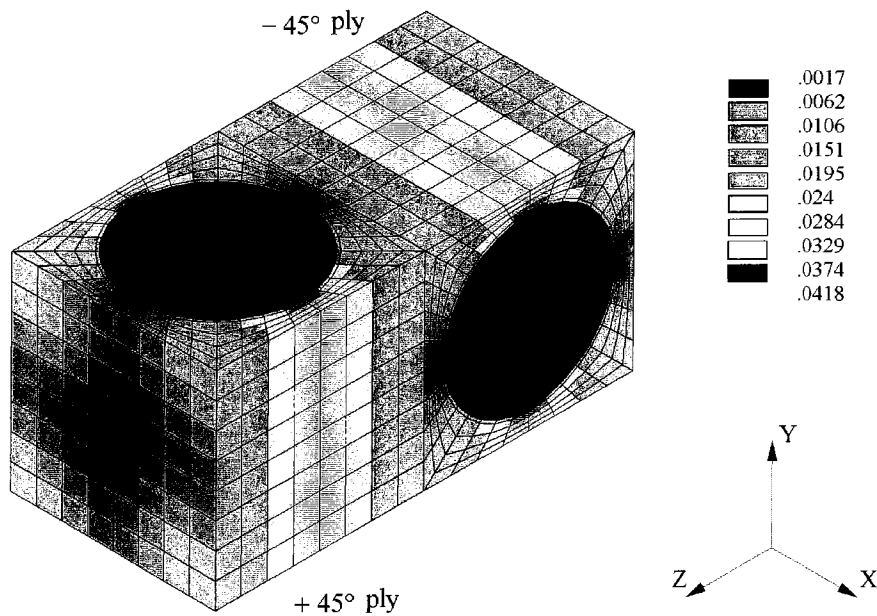


Fig. 5-14 Distribution of the maximum principal strain in a  $[\pm 45^\circ]_{ns}$  laminate.

It is seen that the maximum value of principal strain occurs in the matrix near the fibre/matrix interface extending along the fibres (Figure 5-12 for unidirectional laminate and Figure 5-14 for angle-ply laminate, respectively). Thus, upon further loading, there will be two symmetric 'narrow bands' of matrix cracking along the fibre direction in each lamina. The stress/strain distribution for the cross-ply laminates will also indicate the critical regions in the laminates, however for the sake of brevity these will not be shown herein.

Figure 5-15 displays the angle change of the fibres of the  $[\pm 45^\circ]_{ns}$  angle-ply laminate at a global strain of  $\bar{\epsilon} = 0.8\%$ . The numerical values of the angle change can be estimated from the displacement of the center of the fibre, and this is plotted in Fig. 5-16 which shows the angle change  $\Delta\theta$  vs. the applied global strain up to 2.5%. It is worthwhile to mention that Sun and Zhu [10] included the angle change of the fibre in their analysis of angle-ply laminates based on classical laminate theory and concluded that it is also a factor contributing to the nonlinear behaviour. Here the change of the angle is directly determined by the micro/meso-mechanical approach.

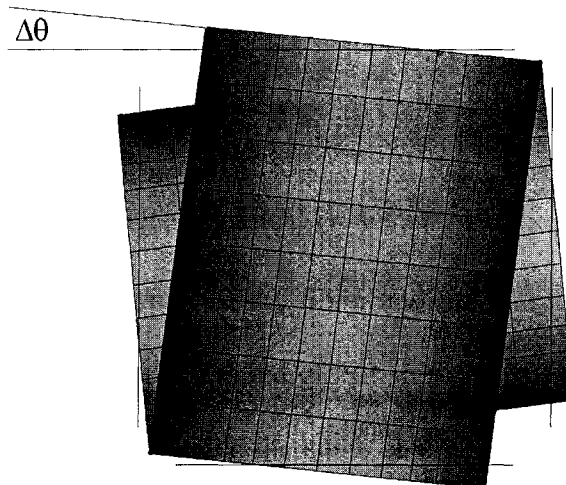


Fig. 5-15 Change in the fibre orientation resulting from load application.

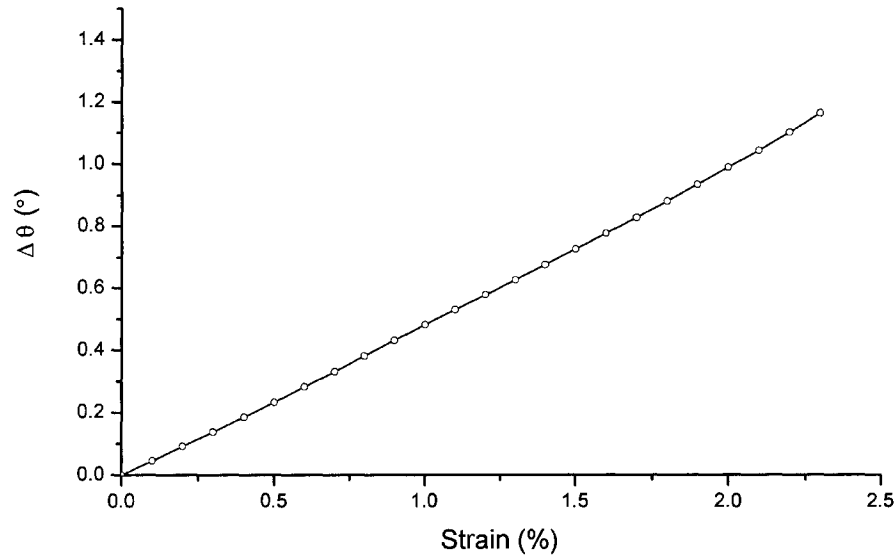


Fig. 5-16 Fibre orientation change vs. the applied global strain.

### 5.3.7 Evolution of Matrix Damage

The evolution of the damage zone (matrix cracking) can also be determined by the current analysis. Figures 5-17 to 5-19 show the evolution of the damaged zone with the applied global strain for the three types of laminates. Note that the cells are cut along the Y-direction at the mid-plane of the ply to more clearly show the damaged zone along the fibres direction. For a unidirectional laminate under a  $45^\circ$  off-axis loading (Fig. 5-17), damage initiated at an applied global strain of  $\bar{\epsilon} = 0.9\%$ , in the form of two 'narrow bands' in the matrix near the interface along the fibre direction, Fig. 5-17(a). Upon further loading the bands expand around the circumference of the fibre. Note that the direction of global load is along the diagonal of the square cross-section. The matrix cracking is not transverse to the tensile loading, but along the fibre direction.

For a cross-ply laminate under transverse loading along X-axis (Fig. 5-18), a different damage form is noted. Initially there are two damage bands in the matrix of the 90° ply, and shortly after, there is another pair of damage bands which are around the fibre/matrix interface. Upon further loading only the latter two damage bands propagate around the fibre/matrix interface in 90° plies. All the damaged zones are restricted to the 90° ply, and the damaged bands are in the fibre direction of 90° ply, i.e. they are perpendicular to the applied loading. For an angle-ply laminate (Fig. 5-19), at an applied global strain of  $\bar{\epsilon} = 0.9\%$ , damage initiates in the form of two 'narrow bands' in the matrix near the interface along the fibre direction for each ply, Fig. 5-19(a). Upon further loading the bands expand around the circumference of the fibres, Figs. 5-19(b) to 5-19(d). Note that the direction of the global load is along the diagonal of the square cross-section. Thus the predicted orientation of the 'cracks' is not perpendicular to the load; rather it is in the direction of fibres.

This prediction of the orientation of matrix cracking is in agreement with that observed in the tests. In the tests of the three corresponding coupon specimens under tensile loading, the cracks in the specimen and the main final fracture of the specimen were along the fibre directions [11-12].

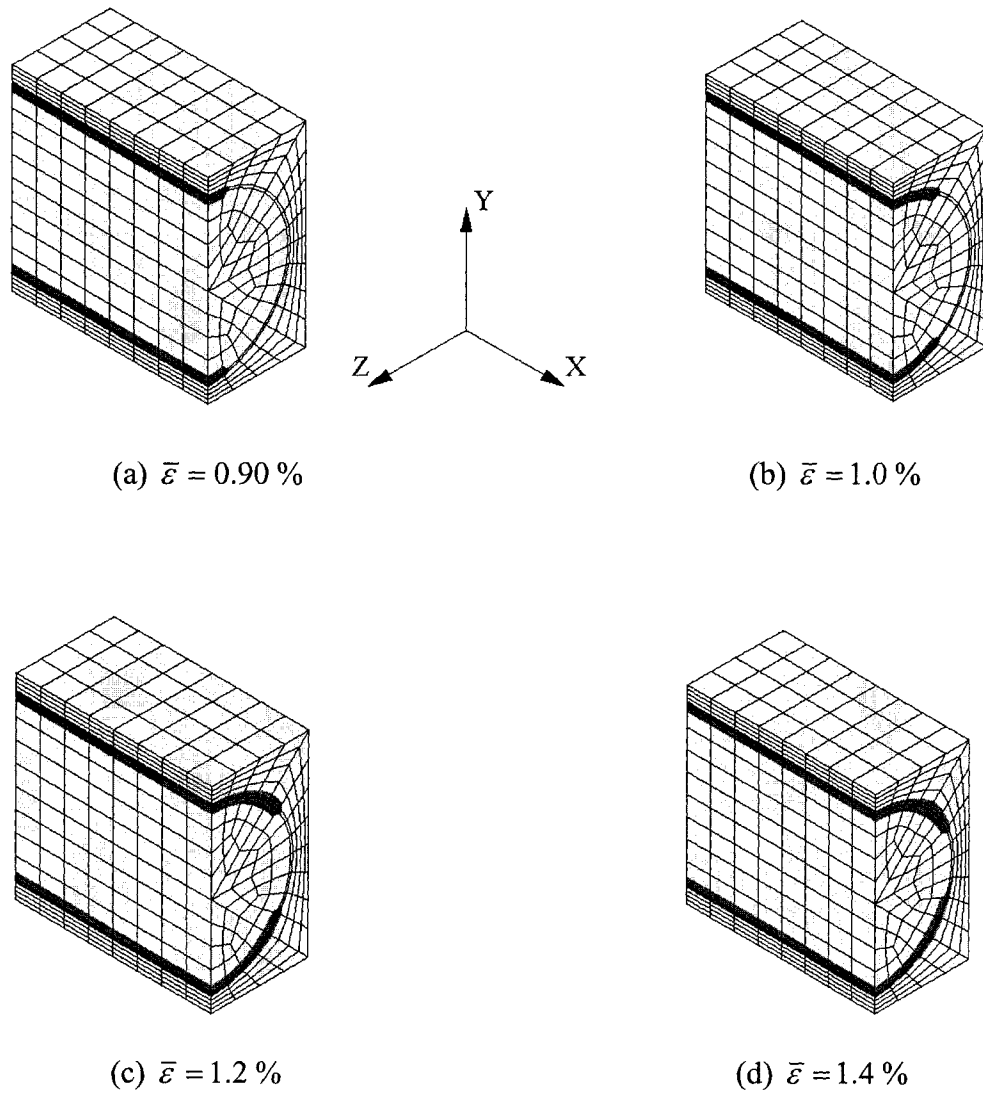


Fig. 5-17 Evolution of the damaged zone (unidirectional laminate).

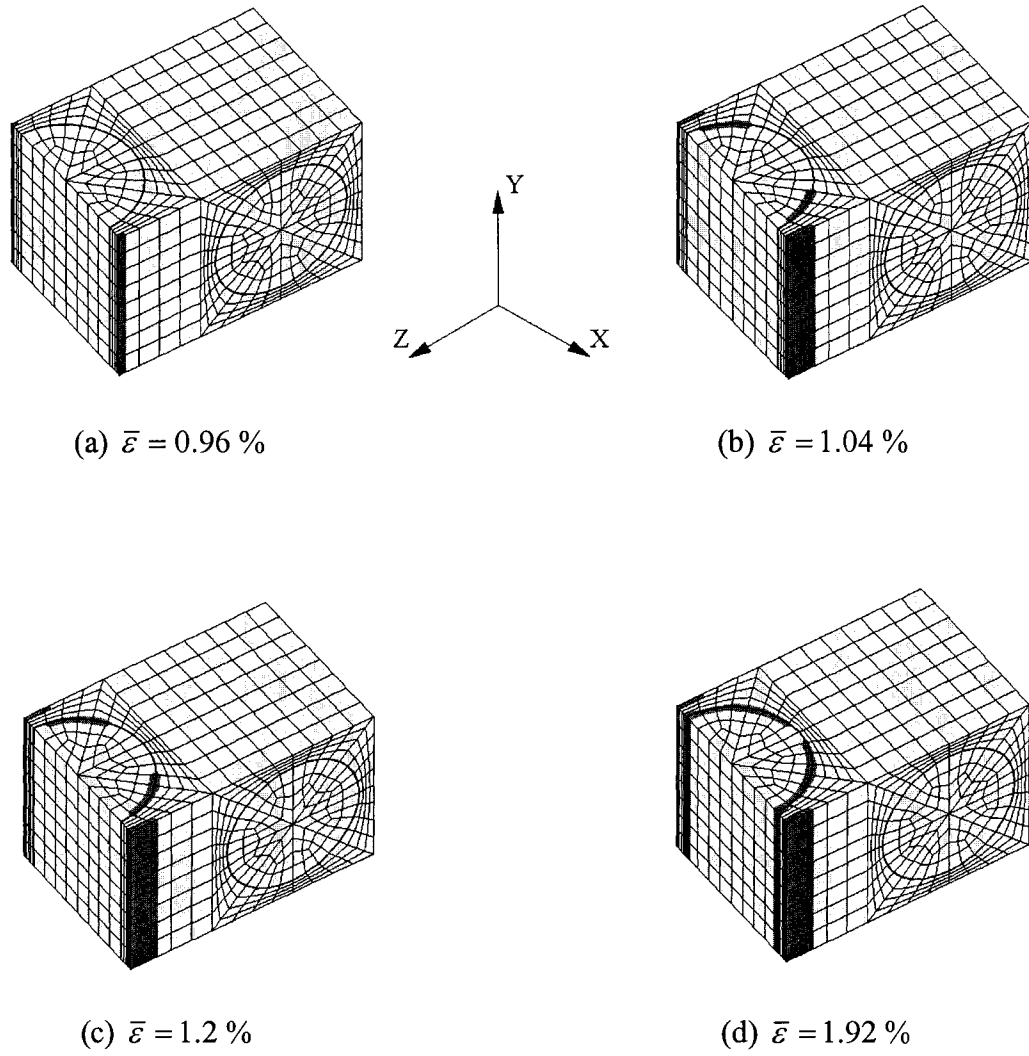


Fig. 5-18 Evolution of the damaged zone (cross-ply laminate).

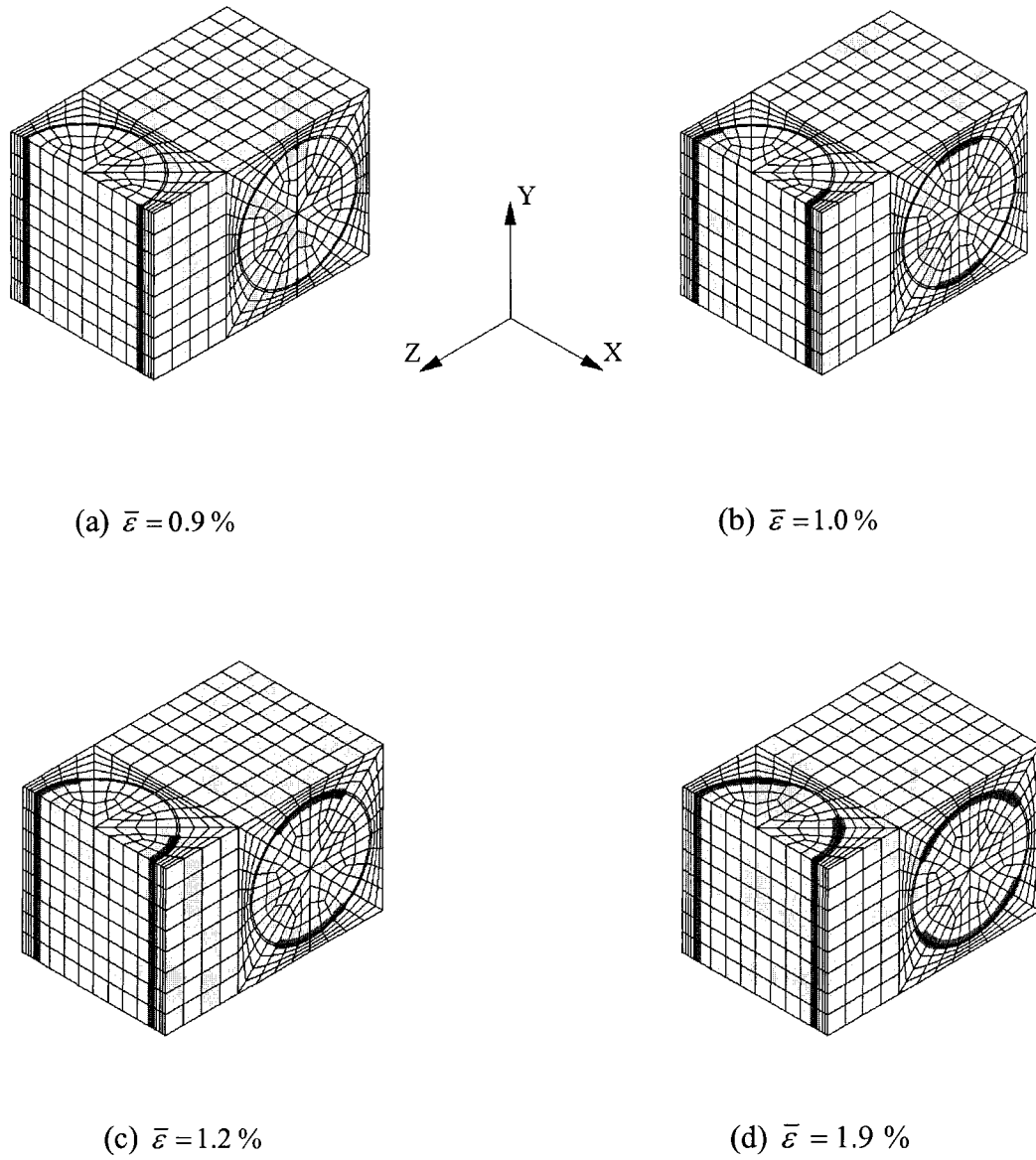


Fig. 5-19 Evolution of the damaged zone (angle-ply laminate).

## 5.4 ANALYSIS OF RESIDUAL STRESS AND ITS INFLUENCES

### 5.4.1 Temperature Dependent Material Constants

In this section, the evolution of curing induced residual stress/strain and their influence on the damage behaviour of a cross-ply laminate are investigated. The MUC model used in this section is shown in Fig. 5-20. The nonlinear viscoelastic constitutive model for the epoxy matrix is a version of that used in [13-15]. The material constants in the model are calibrated at room temperature based on an EPON 828 epoxy system, see Xia and Ellyin [15].

For the epoxy resin used in this investigation, the glass transition temperature is 110° C. The curing temperature, 149° C, is higher than the glass transition temperature. Thermal transition temperatures, for example, the glass transition temperature,  $T_g$ , and the melting temperature,  $T_m$ , strongly affect the mechanical properties of polymers and their composites. The morphology of the polymer is also a determining factor [16-18]. Therefore, it would be more reasonable to consider the dependency of the material constants on temperature.

For the cross-linked epoxy polymer matrix considered in this study, the following relations are used:

- (a) Poisson's ratio is assumed to be temperature independent [17].
- (b) We consider the change of Young's modulus over the temperature range from curing to room temperature. The total temperature range can be divided into three regions. When  $T \geq T_g + \Delta T_2$ , the matrix is in liquid or rubbery state [17], and  $E$  is assumed to have a very small value, for example, for some polymers it is of the order of a few *MPa*, or  $E(T) \approx (0.001 \sim 0.01)E(T_r)$ , where  $E(T_r)$  is the modulus at room temperature. The

transition region around  $T_g$  is assumed to be  $T_g - \Delta T_1 \leq T \leq T_g + \Delta T_2$ , in which,  $E$  varies greatly. When  $T \leq T_g - \Delta T_1$ , the matrix is in solid state, and  $E$  changes slightly. Exponential functions are used for the last two regions, and the constants are determined approximately by using the data for similar polymers in Refs. [16-17]:

$$\begin{aligned}
 E(T) &= E(T_r) \exp\left(-k_1 \frac{T - T_r}{T_g - \Delta T_1 - T_r}\right) & T \leq T_g - \Delta T_1 \\
 E(T) &= E(T_g - \Delta T_1) \exp\left(-k_2 \frac{T - T_g + \Delta T_1}{\Delta T_1 + \Delta T_2}\right) & T_g - \Delta T_1 \leq T \leq T_g + \Delta T_2 \\
 E(T) &= 0.01E(T_r) & T \geq T_g + \Delta T_2
 \end{aligned} \tag{5.19}$$

For the current matrix we have, approximately,

$$\begin{aligned}
 T_g &= 110^\circ C, \quad T_r = 23^\circ C, \quad \Delta T_1 = \Delta T_2 = 35^\circ C, \\
 E(T_r) &= 2600 \text{ MPa}, \quad E(T_g - \Delta T_1) = 0.7E(T_r), \quad E(T_g + \Delta T_2) = 0.01E(T_r) \\
 k_1 &= 0.357 \text{ and } k_2 = 4.249.
 \end{aligned}$$

(c) For  $a_i$  in Eqn. (3) in Ref. [15] we assume,

$$\begin{aligned}
 a_i(T) &= a_i(T_r) \exp\left(k_1 \frac{T - T_r}{T_g - \Delta T_1 - T_r}\right) & T \leq T_g - \Delta T_1 \\
 a_i(T) &= a_i(T_r) \exp\left(k_2 \frac{T - T_g + \Delta T_1}{\Delta T_1 + \Delta T_2}\right) & T_g - \Delta T_1 \leq T \leq T_g + \Delta T_2 \\
 a_i(T) &= a_i(T_r) \times 10^2 & T \geq T_g + \Delta T_2
 \end{aligned} \tag{5.20}$$

where  $a_i(T_r)$  is the value at room temperature, see Eqn. (3) in Ref. [15]. The constant  $b_i$  is assumed to be temperature independent.

(d) The coefficient of thermal expansion (CTE) is assumed to change linearly with temperature with a slope of

$$K = \frac{\alpha_g - \alpha(T_r)}{T_g - T_r} \quad (5.21)$$

where  $\alpha(T_r) = 63 \times 10^{-6} / ^\circ\text{C}$ , and  $\alpha_g$  is the CTE just above the  $T_g$ . From Ref. [17],  $\beta_v T_g \approx 0.16$  ( $\beta_v$  is the volumetric CTE, and  $T_g$  is in Kelvin temperature), therefore,

$$\alpha_g = \frac{1}{3} \beta_v = \frac{1}{3} \times \frac{0.16}{273 + 110} = 139 \times 10^{-6} / ^\circ\text{C}.$$

#### 5.4.2 Generation and Evolution of Thermal Residual Stresses and Strains

The distribution of residual stress  $\sigma_{zz}$  induced by cooling from the curing temperature  $149^\circ\text{C}$  to  $23^\circ\text{C}$  at a cooling rate of  $1.4^\circ\text{C}/\text{min}$  is shown in Fig. 5-20. The result is based on the temperature-dependent material constants as specified in the previous section and the residual stress distribution is at that instant when the temperature reaches the ambient one. It can be seen that the maximum tensile stress is  $33.68 \text{ MPa}$  in the matrix near the interface and the maximum compressive stress is  $61.89 \text{ MPa}$  in the fibre. For the  $[0^\circ/90^\circ]$  cross-ply laminate the stress component  $\sigma_{xx}$  has the same maximum values and distribution as  $\sigma_{zz}$ . To find bounds on the magnitude of residual stresses generated, two other types of analysis are carried out. First, a slower cooling rate of  $0.15^\circ\text{C}/\text{min}$  is specified. Second, it is assumed that the polymer matrix properties during cool-down are temperature-independent. For the slower cooling rate of  $0.15^\circ\text{C}/\text{min}$ , the distribution is similar to that of Fig. 5-20 but with a maximum tensile stress of  $27.22 \text{ MPa}$  in the matrix and a maximum compressive stress of  $50.44 \text{ MPa}$  in the fibre. Therefore, a faster cooling rate results in higher residual stresses. When the material constants at room temperature are used for the entire temperature range, much higher values of residual stresses are

obtained. The maximum tensile stress for the later case is 42.69 MPa and that of the compressive stress is 77.7 MPa for the cooling rate of 1.4°C/min, and the corresponding values for the slower rate of 0.15°C/min are 32.01 MPa and 59.04 MPa. Since the modulus of an epoxy material increases with the decrease of temperature, the results from the temperature-independent constants overestimate the residual stresses in the composite laminate. An elastic solution is obtained by using elastic material constants  $E = 2600\text{MPa}$  and  $\nu = 0.4$  for epoxy. For this elastic solution, the maximum tensile stress in the matrix is 52 MPa and the maximum compressive stress in the fibre is 101 MPa, irrespective of the rate of cooling.

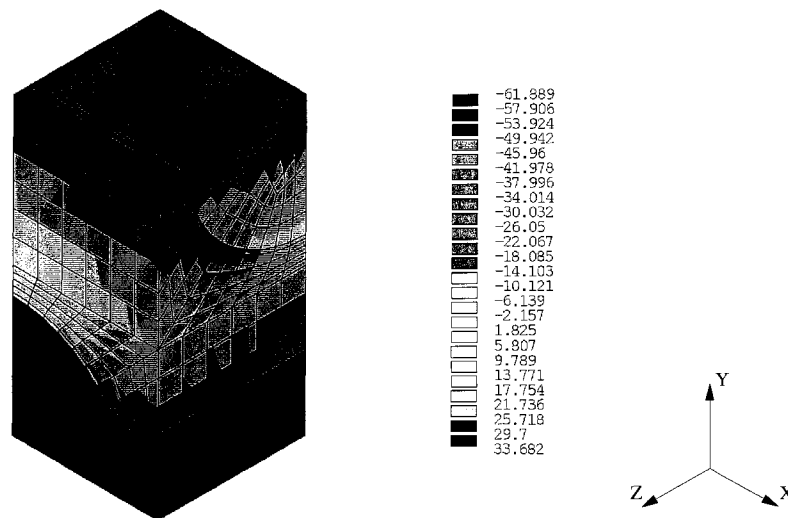


Fig. 5-20 Residual stress ( $\sigma_{zz}$ ) distribution in the model.

Following cooling to room temperature, creep and relaxation take place simultaneously due to the viscoelastic properties of the epoxy matrix. The change of the stresses/strains in the matrix causes a change of the stresses/strains in the elastic fibre in order to reach a new state of balance for the cross-ply laminate. The numerical analysis was carried out for 2500 minutes ( $\approx 42$  hrs) while the temperature was held at 23°C.

Figures 5-21 and 5-22 show the evolution of the maximum tensile stress in the matrix and the maximum compressive stress in the fibre, respectively. The time 0 in the figures corresponds to the instant when the cooling temperature reached 23°C. In the legend of the figures, “TD” refers to the results with *temperature dependent* material constants, and “TI” refers to the results with *temperature independent* material constants.

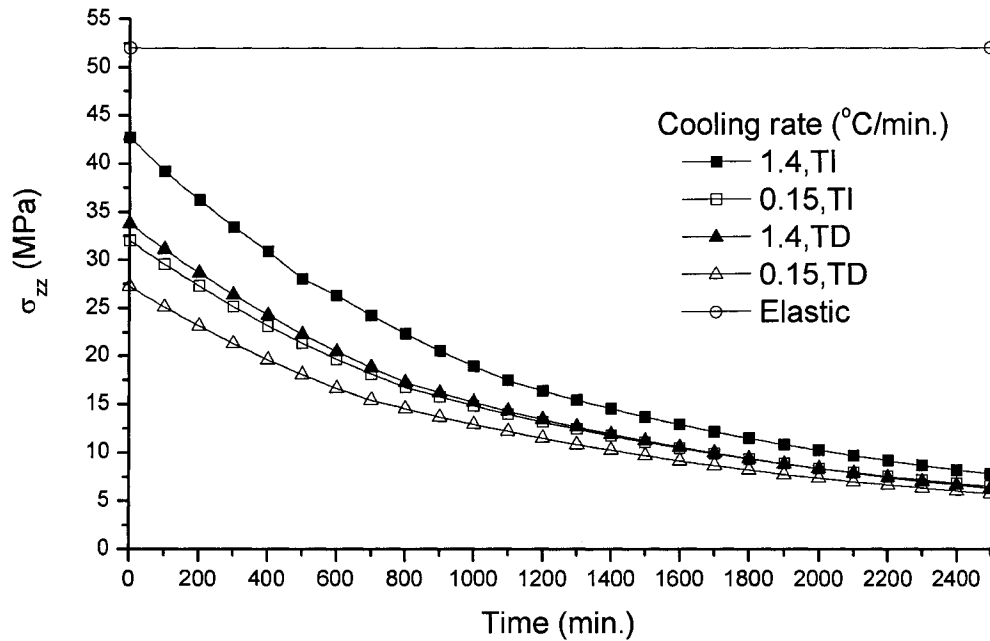


Fig. 5-21 Evolution of the maximum tensile stress in the matrix for various cooling rates and material properties.

It can be seen that both tensile and compressive stresses are decreasing with time. The cooling rate affects the initial residual stress values. However, irrespective of the cooling rate, the residual stresses asymptotically tend to small values. For example, after 2500 minutes, the maximum tensile stresses are 6.32 MPa and 5.76 MPa, and the maximum compressive stresses are 10.12 MPa and 9.40 MPa, for the cooling rates of 1.4°C/min and 0.15°C/min, respectively. For the purpose of comparison, the results of temperature-

independent constants are also presented in the figures. They show a similar trend and the residual stress values after 2500 minutes for both the fast and slow cooling rates are not much different than those of the temperature-dependent ones.

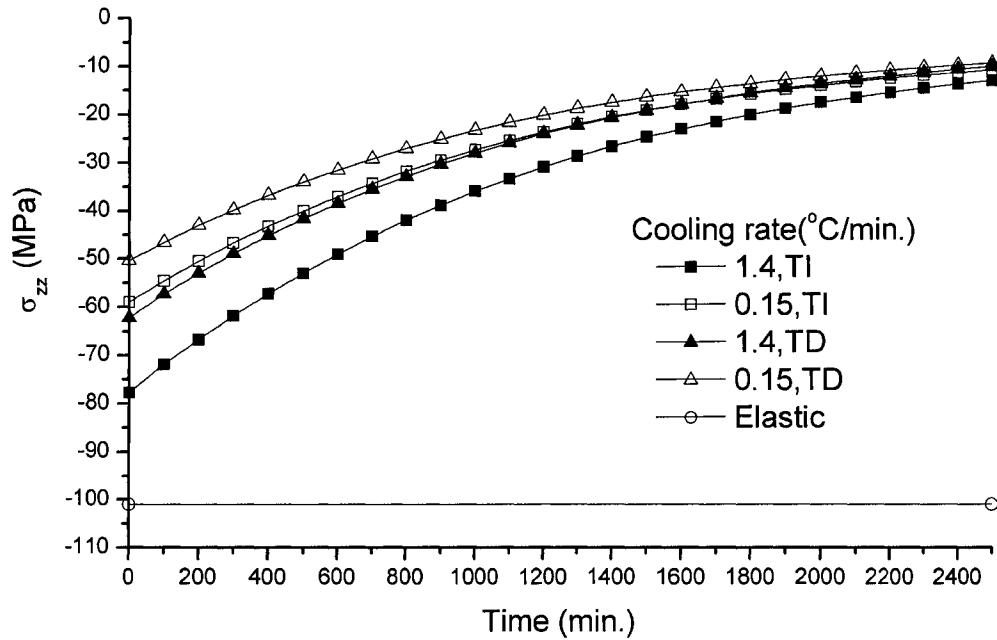


Fig. 5-22 Evolution of the maximum compressive stress in the fibre for various cooling rates and material properties.

In the micromechanical analysis of composites, it is assumed that the global stress and strain are defined by the average values over the volume of the cell as follows [6, 19],

$$\{\bar{\sigma}\} = \frac{1}{V} \int_V \{\sigma\} dV, \quad \{\bar{\varepsilon}\} = \frac{1}{V} \int_V \{\varepsilon\} dV \quad (5.22)$$

where  $V$  is the volume of the multi-cell model.

From the FEM results we can also obtain the average residual stresses in each ply, for example, for the 90°ply (fibre along X-direction), we have

$$\{\bar{\sigma}\}_{90} = \frac{1}{V_{90}} \int_{V_{90}} \{\sigma\} dV = \frac{\sum \{\bar{\sigma}_i\} V_i}{\sum V_i} \quad (5.23)$$

where  $V_i$  is the volume of  $i$ th element,  $\{\bar{\sigma}_i\}$  is the average stress of  $i$ th element. The latter is simply the average of the stress values at all 8 nodes of each element.

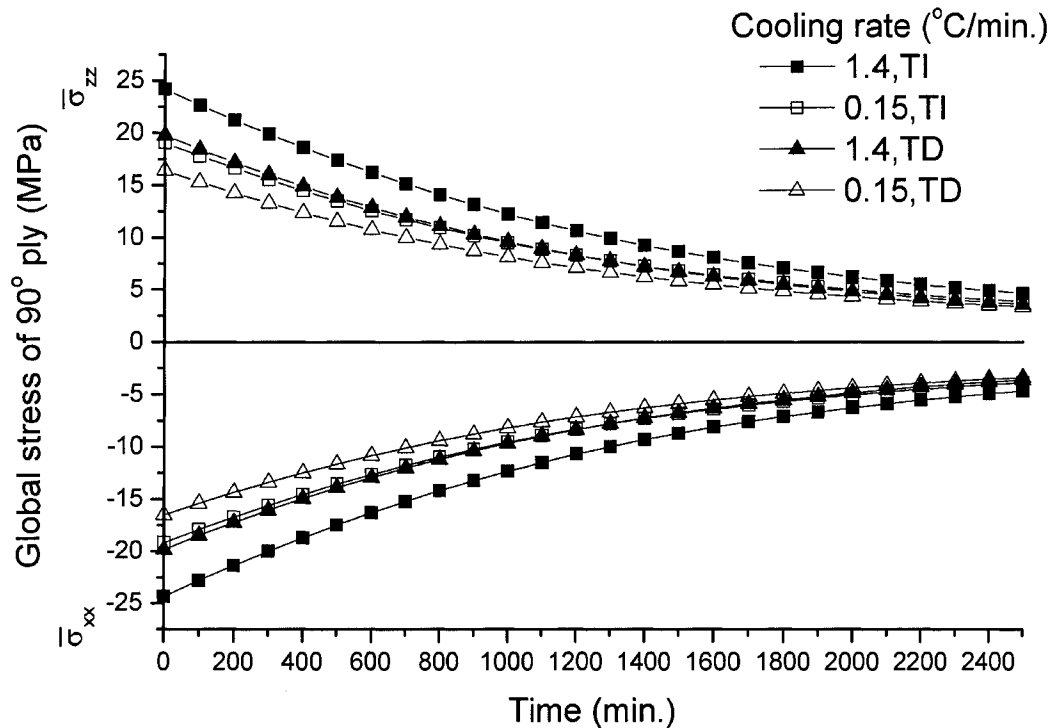


Fig. 5-23 Evolution of the global (average) stress  $\bar{\sigma}_{xx}$  and  $\bar{\sigma}_{zz}$  in the 90° ply.

Figure 5-23 shows the evolution of the average stress components  $\bar{\sigma}_{xx}$  and  $\bar{\sigma}_{zz}$  of the 90°ply. Again, the time 0 in the figure corresponds to the instant when the cooling temperature just reaches 23°C, and at this instant the stresses have the highest values. The average residual stresses in the ply decrease with time and tend to small asymptotic values after a period of time. It can be seen that the two in-plane stress components are equal but with opposite signs, negative in the fibre direction ( $\bar{\sigma}_{xx}$ ) and positive in the transverse direction ( $\bar{\sigma}_{zz}$ ). It should also be noted that for the 0° ply, the global stress

components  $(\bar{\sigma}_{xx})_0 = -(\bar{\sigma}_{xx})_{90}$  and  $(\bar{\sigma}_{zz})_0 = -(\bar{\sigma}_{zz})_{90}$ , i.e. the global (average) thermal residual stress of the cross-ply laminate is zero as expected.

The shrinkage of the laminate can be illustrated by the average strain (global strain). It should be noted that Eqn. (5.22) is valid for both mechanical and/or thermal loadings. Thus, by micromechanical analysis of a cell, one can get the macroscopic strains and stresses of the composite. By using Gauss's theorem, the average strain in the cell can be expressed as an integral around the boundary surfaces [6, 19]. For the current  $[0^\circ/90^\circ]_n$  cross-ply laminate the average shrinkage strain is the same in the X- and Z-axes directions and can be obtained from the following equation:

$$\bar{\varepsilon}^L = -\bar{\varepsilon}_{zz} = -\frac{1}{V} \int_V \varepsilon_{zz} dV = -\frac{1}{V} \int_V \frac{\partial w}{\partial z} dV = -\frac{1}{V} \int_S w n_z dS \quad (5.24)$$

where  $S$  is the outside surface of the multi-cell model,  $w$  is displacement in  $z$  direction and  $n_z$  is the normal unit vector. Using the boundary condition similar in Eqn. (5.13), we obtain:

$$\bar{\varepsilon}^L = \frac{-w(0,0,1)}{L} \quad (5.25)$$

where  $L$  is the length of the micro-mechanical model in the  $Z$ -direction and  $w(0,0,1)$  is the displacement of the surface  $Z=1$ . Figure 5-24 shows the evolution of the average shrinkage strain with time. It is noted that a fast cooling rate results in a higher shrinkage strain when the laminate is cooled to room temperature. The thermal shrinkage strain gradually recovers and asymptotically tends to a smaller value irrespective of the cooling rate. Again, the result from the temperature-independent material constants shows a similar trend to that of the temperature-dependent material constants, however, the magnitude of the shrinkage strain is overestimated.

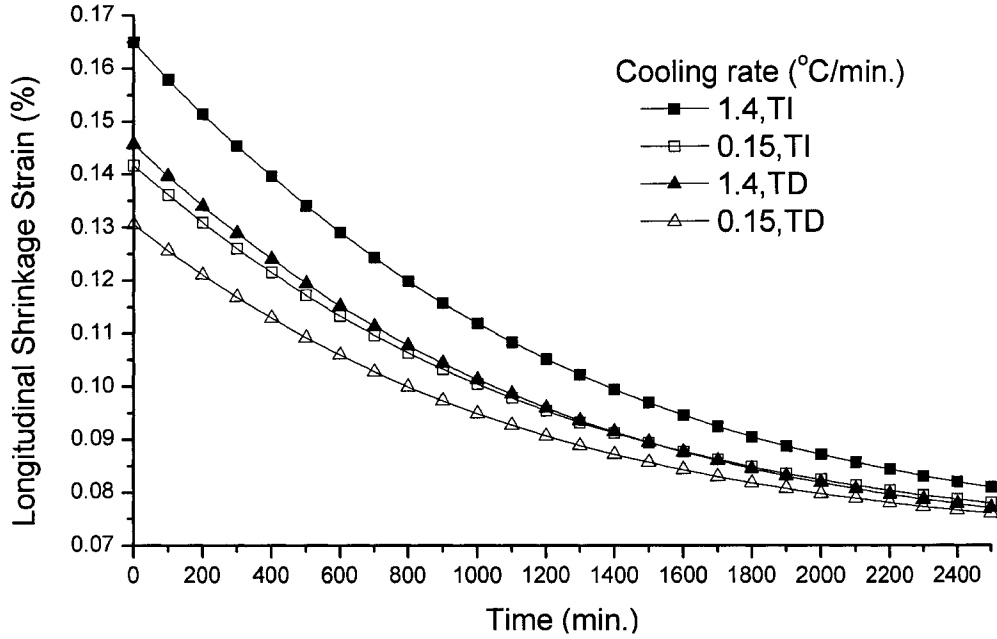


Fig. 5-24 The evolution of shrinkage strain  $\bar{\varepsilon}^L$  for two cooling rates and two material properties.

### 5.4.3 Mechanical Part of the Total Strain

The above results show that the residual stresses (both local stresses and the average stress in each ply) and the average shrinkage strain tend to small values after a certain period of time. However, this is not the case for the local strains. Here we are interested in the mechanical part of the total strains because this part is produced due to the mismatch of the thermal strains between the fibre and the matrix. At each point within the MUC, the total strain  $\{\varepsilon_t\}$ , mechanical part of the strain (residual strain),  $\{\varepsilon_m\}$  and the thermal strain,  $\{\varepsilon_{th}\}$  have the following relation:

$$\{\varepsilon_m\} = \{\varepsilon_t\} - \{\varepsilon_{th}\} \quad (5.26)$$

Figure 5-25 shows the distribution of the first principal strain of the strain vector  $\{\varepsilon_m\}$  in the MUC at 2700 minutes after cooling to room temperature at 1.4°C/min by using

temperature dependent material constants. It can be seen that the highest residual principal strain reaches 3.5% in the matrix near the fibre/matrix interface – a rather high value. The location of the maximum strain is unchanged during the evolution of shrinkage strain.

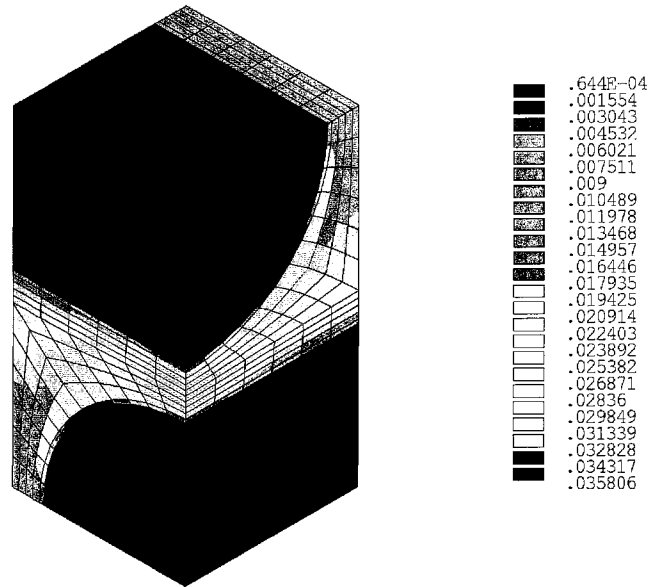


Fig. 5-25 The distribution of the first principal strain.

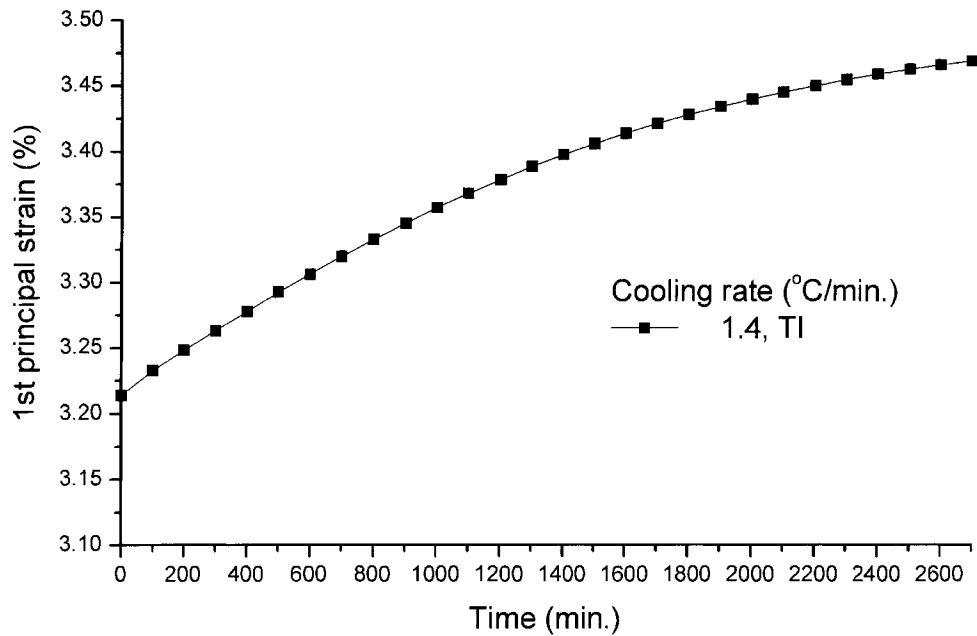


Fig. 5-26 The evolution of the maximum principal strain in the matrix.

The evolution of the maximum residual strain with time is shown in Fig. 5-26. It can be seen that the 1st principal strain *increases* with time and tends to an asymptotic value. The increase of the local residual strains can be attributed to a combined action of the relaxation of the stresses and the creep of the strains. The local material is constrained to a certain degree by surrounding materials, therefore, the relaxation and the creep processes can occur simultaneously. The creep rate decreases with the decreasing stress, and tends to zero when the local stress becomes low enough.

#### **5.4.4 Results of Subsequent Uniaxial Tensile Loading**

The previous results indicate that the residual stresses (both local stress and average stress in each ply) and the average shrinkage strain tend to small values after a certain period of time; however, the local residual strains in the multi-cell model are still quite significant. To study the influence of residual stresses/strains on the response of the laminate under subsequently applied mechanical loads, the damage evolution in the matrix under a uniaxial tensile loading in Z-direction (Fig. 5-20) is investigated. The analysis is carried out in the meso/micro-mechanical model with the residual stress/strain state. After keeping the laminate at room temperature for 2700 min, a global tensile strain  $\bar{\epsilon}_{zz}$  is superimposed to the model. This is achieved by specifying a displacement at the surface  $Z=1$ . The load is applied up to  $\bar{\epsilon}_{zz}=1.5\%$  (superimposed value) at a strain rate of  $10^{-5} s^{-1}$ . At each time step the damage zone of the matrix is determined using the criterion and post-damage relation described in Chapter 3.

The evolution of damage zones (represented by black color) in matrix is shown in Fig. 5-27(a). When the global strain  $\bar{\epsilon}_{zz}=0.2\%$ , damage begins near the fibre/matrix interface

in  $90^\circ$  ply (fibre along X-direction), and upon further loading it propagates in two directions. One is a growth in the hoop direction of the interface, and the other one is along the axial direction of the interface (X-direction). At  $\bar{\varepsilon}_{zz}=0.5\%$ , another damage (transverse crack) initiates at the upper edge of the surface  $Z=1$ . This damage zone on the plane  $Z=1$  does not grow further with the increased strain, but the damaged zone along the fibre/matrix interface propagates further along the X-direction and goes through the MUC at about  $\bar{\varepsilon}_{zz}=1.0\%$ . It is noted that in the lower part of the MUC ( $0^\circ$  ply, where the fibre is in the loading direction) no damage has as yet occurred.

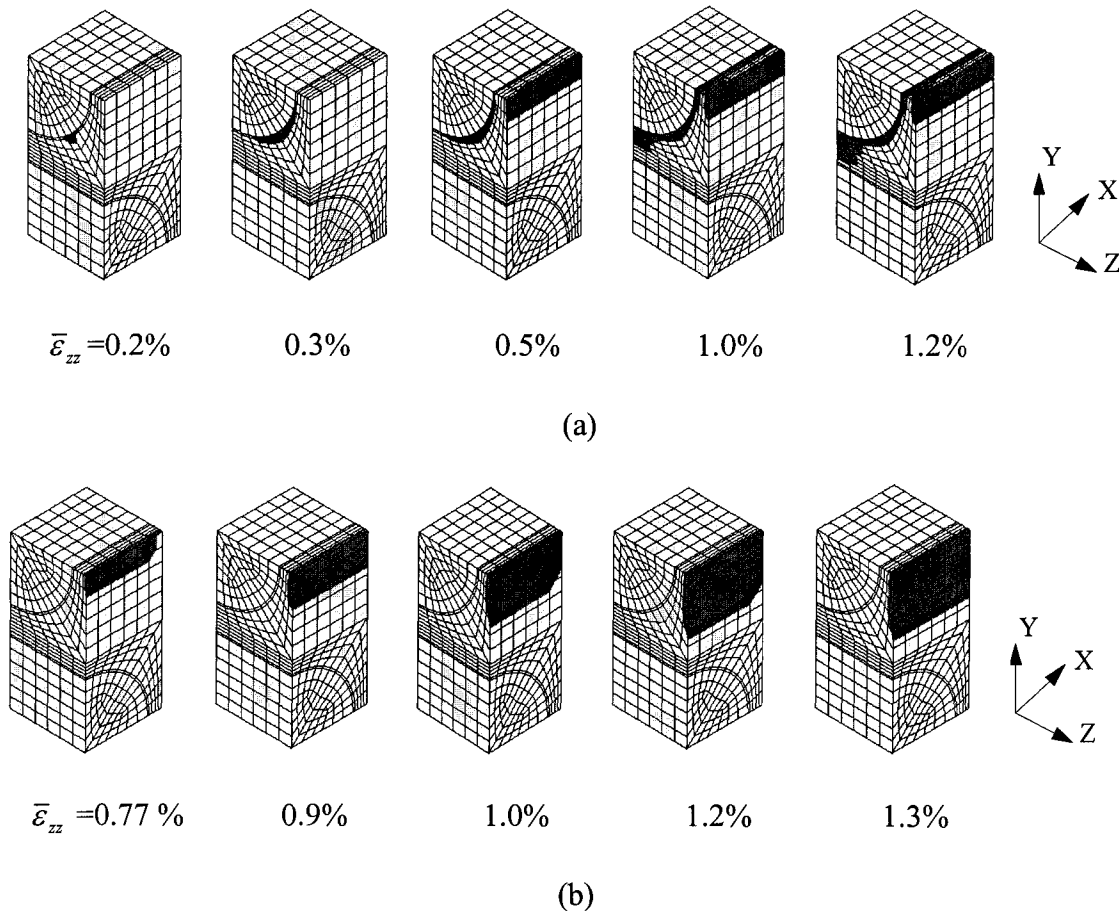


Fig. 5-27 Damage evolution in cross-ply laminates:

(a) With residual stress/strain; (b) Without residual stress/strain.

For the sake of comparison, Fig. 5-27(b) shows the damage evolution under the same uniaxial tensile loading but neglecting the residual stress/strain introduced in the cooling process. It can be seen that at the global strain of 0.77% damage band (transverse cracking) is first formed along the X-direction. Thereafter, the band extends across the thickness of 90° layer and finally it is blocked by the 0° layer. Therefore, the location and the strain level at which damage initiates and the evolution of the damage are different in these two cases. This indicates that although the residual stresses relax to small values after a period of time, the local residual strains could still have a significant influence on the response of the laminate under subsequently applied mechanical loads.

## 5.5 CONCLUDING REMARKS

Following conclusions are drawn from the current investigation.

- The meso-scale representation and mechanical analysis of cross-ply and angle-ply laminates provide an alternate approach for these laminates. Elastic results show that the predictions based on the meso-scale model of the laminates agree well with the classical laminate theory.
- The predicted global stress-strain curves of the three types of laminates are in good agreement with the experimental observations. In particular, the predicted results indicate the unifying nature of the micro/meso-mechanical approach for both the unidirectional and angle-ply laminates using the same material constants.
- The results of the ply level stress indicate that after damage, the load carrying capacity is decreased only in directions perpendicular to the fibre. Thus it explains the varying stress-strain responses of laminates with different types of fibre architecture.

- The predicted orientation of the matrix cracking is in agreement with the macroscopic test observations and the evolution path is properly simulated by the micro/meso-mechanical analysis. It is shown that the matrix cracking for the cross-ply laminates are confined to the 90° ply, hence, the analysis highlights the different mesoscopic response of a cross-ply laminate compared to that of an angle-ply one.
- The evolution of thermal residual stress/strain induced during curing process and their influence on the subsequently applied mechanical loading have been analyzed through a viscoelastic finite element analysis for cross-ply laminates. The generation of the residual stresses strongly depends on the cooling rate and the model with temperature independent material constants over-predicts the residual stresses.
- A stress relaxation process takes place in polymer composites after the temperature has dropped to the ambient one. The residual stresses decrease with time. In addition, they asymptotically tend to a small value irrespective of the cooling rates.
- The maximum shrinkage is reached at the completion of the cooling process. A higher cooling rate results in a higher shrinkage strain. However, most of the shrinkage strain is recovered with time and it asymptotically tends to a small value irrespective of the cooling rates.
- Although the residual stresses and the global shrinkage strain are small after a period of time, the local residual strains could still have a significant influence on the response of the laminate under subsequently applied mechanical loading. The location and the global strain level of which damage initiates, and the evolution of the damage are different for cases with or without consideration of the residual stresses/strains.

**BIBLIOGRAPHY**

1. Ellyin, F., Kujawski, D. (1995). Tensile and fatigue behaviour of glass fibre/epoxy laminates. *Construction and Building Materials*, **9**, 425-430.
2. Pagano, N. J., Yuan, F. G. (2000). The significance of effective modulus theory (homogenization) in composite laminate mechanics. *Composites Science and Technology*, **60**, 2471-2488.
3. Raghavan, P., Moorthy, S., Ghosh, S., Pagano, N. J. (2001). Revisiting the composite laminate problem with an adaptive multi-level computational model. *Composites Sciences and Technology*, **61**, 1017-1040.
4. Kim, S. J., Lee, C. S., Yeo, H. J. (2002). Direct numerical simulation of composite structures. *Journal of Composite Materials*, **36**, 2765-2785.
5. 3M Minnesota Mining & Manufacturing CO., *Technical Data of 'Scotchply' Reinforced Plastic Type 1002 & 1003*. St. Paul, Minnesota, USA.
6. Xia, Z., Zhang, Y., Ellyin, F. (2003). A unified periodical boundary condition for representative volume elements of composites and applications. *International Journal of Solids and Structures*, **40**, 1907-1921.
7. Hoover, J. W. (1999). *Transverse Cracking of  $[\pm\theta, 90_3]_S$  Composite Laminates*. MSc. thesis, Department of Mechanical Engineering, University of Alberta, Canada.
8. Hu, Y. (2002). *Multiaxial Behaviour and Viscoelastic Constitutive Modeling of Epoxy Polymers*. PhD thesis, Department of Mechanical Engineering, University of Alberta, Canada.

9. Zhang, Y., Xia, Z., Ellyin, F. (2005). Viscoelastic and damage analyses of fibre reinforced polymer laminates by micro/meso-mechanical modeling. *Journal of Composite Materials*, (in press).
10. Sun, C. T., Zhu, C. (2000). The effect of deformation-induced change of fibre orientation on the nonlinear behavior of polymeric composite laminates. *Composites Science and Technology*, **60**, 2337-2345.
11. Daniel, I. M., Ishai, O. (1994). *Engineering Mechanics of Composite Materials*. Oxford University Press, New York, Oxford.
12. El Kadi, H. A. (1993). *Analysis and Failure of Laminated Fibre Reinforced Composites*. PhD thesis, Department of Mechanical Engineering, University of Alberta, Canada.
13. Chen, Y., Xia, Z., Ellyin, F. (2001). Evolution of residual stresses induced during curing processing using a viscoelastic micromechanical model. *Journal of Composite Materials*, **35**, 522-542.
14. Zhang, Y., Xia, Z., Ellyin, F. (2004). Evolution and influence of residual stresses/strains of fibre reinforced laminates. *Composites Science and Technology*, **64**, 1613-1621.
15. Xia, Z., Ellyin, F. (1998). Time-dependent behaviour and viscoelastic constitutive modeling of an epoxy polymer. *Polymers and Polymer Composites*, **16**, 75-83.
16. Barker, A. J., Vangerko, H. (1983). Temperature dependence of elastic constants of CFRP. *Composites*, **14**, 52-56.
17. Van Kervelen, D. W. (1972). *Properties of Polymers, Correlations with Chemical Structures*. Elsevier, Amsterdam.

- 
18. Tant, M. R., Connell, J. W., McManus, H. L. N. (editors). (1995). *High-temperature Properties and Applications of Polymeric Materials*. ACS Symposium Series 603, American Chemical Society, Washington, DC.
  19. Sun, C. T., Vaidya, R. S. (1996). Prediction of composite properties from a representative volume element. *Composites Science and Technology*, **56**, 171-179.

## CHAPTER 6

### SUMMARY

#### 6.1 SUMMARY AND CONCLUSIONS

The main works and conclusions through this Ph. D research project can be briefly summarized as the following.

Based on the general form of periodic conditions, a unified form of boundary conditions is proposed for the FEM analysis of RUC models subjected to multiaxial loads. Using Lagrange's multiplier method, it is demonstrated that by imposing displacement difference constraints (in the form described in Chapter 2), the traction continuity conditions can be satisfied automatically. Thus the proposed periodic boundary conditions can be conveniently specified in a standard structural FEM scheme.

With the aid of the Gauss's theorem, a method to evaluate the average stresses and strains has been derived based on the applied boundary conditions and the resultant forces at the boundaries. It is shown that by using effective properties of a 'homogenized' media, the strain energy stored in the effective media is equal to the strain energy stored in the composite material. For a unidirectional laminate subjected to general off-axis loading, the periodic boundary conditions for a one-quarter RUC are derived by exploiting the symmetries in geometry, in material and in loading conditions. The comparison with a full-size RUC model demonstrated the validity of the formulation.

The matrix behaviour is described by a recently developed nonlinear viscoelastic constitutive model which has further been implemented into the FEM code ADINA through its user-defined subroutine. Since the nonlinear viscoelasticity is introduced at

the constituent level, the influences on the response of unidirectional and angle-ply laminates under mechanical loading, evolution of the residual stress/strain induced by curing, and the evolution of damage can be well simulated.

Through representing the interphase/interface by a thin layer of element, the proposed interphase/interface separation model can be directly applied to the micro/meso unit-cell analyses. The stress-strain relation of the interphase element is derived based on a cohesive law. The model can handle both the normal and tangential separation of the interphase, thus mixed mode interphase damage can be predicted by the model. Furthermore, the interphase damage model is easily to implement into FEM scheme since an equivalent stress-strain relationship is used.

The so-called snap-back instability involved in the numerical simulation of the interphase damage is illustrated by a 1-D example analytically and numerically. In addition, a viscous term is added to the cohesive law to overcome the convergence difficulty induced by the snap-back instability in the equilibrium iterations.

To model the matrix cracking, a ‘smeared crack approach’ is employed. In this approach, the cracked solid is assumed to be a continuum that permits a crack description in terms of stress-strain relations. In addition, the proposed post-damage stress-strain relation allows only normal and in-plane shear stress components (corresponding to crack orientations) tend to zero.

An iteration algorithm is established to simulate the global off-axis loading under strain control conditions. Since off-axis tensile loading to a UDC is equivalent to multiaxial loadings in the material principal directions, at each loading step, appropriate ratios of increments of strain components should be applied to ensure the resultant of the

stress components acting along the off-axis direction.

The proposed meso scale analysis method for the  $[\pm\theta]_n$  angle-ply laminates can be regarded as an extension of the micromechanical approach of unidirectional laminates and it provides an alternative way to the analysis of multi-directional laminates. Thus the mechanical properties of the laminates and damage evolution can be directly related to the properties of the constituents.

Two types of unidirectional laminate (E-glass/Epon 828 and E-glass/Epon 815) are analyzed with the intralaminar damage. For macroscopic response, it is shown that the predictions on both the global stress-strain curves and ultimate strength at different off-axis angles are in very good agreement with the corresponding test results. For microscopic response, it is illustrated that the initiation and propagation of the interphase damage and matrix cracking, can be well simulated. In addition, the two types of intralaminar damage modes can be distinguished in the analyses.

For cross-ply laminates, initiation and evolution of curing induced residual stress/strain and the effect of the residual stress/strain on the subsequent mechanical loading are investigated. Temperature-dependent material constants at the range from the curing temperature to room temperature are estimated approximately. The results indicate that elastic model and temperature-independent material constants over-estimated the residual stresses. It is also shown that the residual stress will relax and the residual strain will increase with time due to the viscoelasticity nature of the polymer matrix and they will asymptotically reach stable values. For the subsequent tensile loading of a cross-ply laminate with residual stress/strain, it is observed that both the location and load level at which matrix cracking initiates and propagates depend on the residual stress/strain

distribution.

In summary, a comprehensive and reliable micro/meso-mechanical analysis approach for composite laminates has been established. The approach is able to deal with material nonlinear viscoelasticity and multiaxial loading, is able to simulate initiation and growth of different damage modes in composite laminates including interface debonding, matrix cracking and fiber fracture. Presented application examples to different types of laminates (unidirectional, cross-ply and angle-ply) under different loading scenarios (uniaxial, off-axial and thermal loading) have demonstrated the feasibility of the approach. Satisfactory agreements between the predictions of the approach and available experimental or analytical results have confirmed the validity of the method. Moreover, FEM modules of major importance to this method, such as viscoelastic material model, interface damage model and smeared matrix crack model have been developed and successfully incorporated into a commercial FEM code, which provides great potential for more applications of the proposed micro/meso-mechanical analysis approach.